Optimized Dark Matter Searches in Deep Observations of Segue 1 with MAGIC

Ph.D. Dissertation
Universitat Autònoma de Barcelona

Jelena Aleksić
jelena@ifae.es

May 2013

Suprvised by

Dr. Manel Martinez Rodriguez
Dr. F. Javier Rico Castro
Dr. Enrique Fernández Sánchez

Contents

Introduction

There is an impressive amount of evidence, on all scales, favouring the existence of dark matter – an invisible, non-baryonic component of the Universe that accounts for almost 85% of its total mass density. Although its existence was for the first time postulated more than 80 years ago, the nature of dark matter still remains a mystery. Finding and understanding the answer to this question is one of the most important and exciting tasks of modern science.

In the context of our current cosmological view of the Universe, dark matter is considered to be a new type of massive particle, that interacts weakly with ordinary matter and radiation. In addition, this new particle is most likely cold, non-baryonic, produced thermally in the early Universe and stable on cosmological scales. Our search for dark matter particle is carried out in parallel by three different approaches: detection of dark matter produced in colliders, direct detection of dark matter scattering off ordinary matter in underground experiments, and indirect search with space and ground-based observatories for Standard Model particles created in dark matter annihilation or decay.

This last strategy is the subject of this Thesis. Results presented here are from indirect searches for dark matter in dwarf spheroidal galaxy Segue 1, carried out with the Imaging Air Cherenkov Telescopes called MAGIC. The objective is to recognize highly energetic photons, produced in annihilation or decay of dark matter particles, by some characteristic spectral features unique for gamma rays of dark matter origin. An dedicated analysis approach, called the *full likelihood method*, has been developed to optimize the sensitivity of the analysis for such dark matter signatures.

The outline of the Thesis could be summarized as follows:

- **Chapter 1** introduces the dark matter paradigm: what are the astrophysical and cosmological evidence supporting the existence of dark matter, and how can they be reconciled with our current image of the evolution of the Universe. The Chapter ends with review of some of the best motivated candidates for dark matter particle, with detailed discussion about those that are of particular interest for this work.

- **Chapter 2** is devoted to dark matter searches. It begins with presentation of different strategies currently employed by various experiments and their most worth noting results, to continue with more detailed description of indirect searches. Special attention is devoted to the highly energetic photons as search messengers: what signal should be expected, where to look for it and with which instruments.

- **Chapter 3** introduces this work's tool for dark matter searches – the MAGIC Telescopes. Chapter is divided into two parts: one, describing the technical properties of the system, and the other, characterizing its standard analysis chain.

- **Chapter 4** presents the original scientific contribution of this work – the development of the full likelihood approach, an analysis method optimized for recognition of spectral features expected from photons of dark matter origin. First, the method is introduced, then characterized for the pre-defined sets of conditions and its performance evaluated for particular spectrum examples.

- **Chapter 5** brings the results of this work. First, the motivation behind the Segue 1 galaxy as the optimal dark matter candidate for searches with MAGIC is presented. Then, details of the carried observations and data reduction are summarized. This is followed by the full likelihood analysis of the data. Finally, this Chapter ends with the constraints obtained from this work for different models of dark matter annihilation or decay.

Brief summary of the most relevant points of this Thesis is presentes in Conclusions.

Introductión

Existe una impresionante cantidad de evidencia, a todas las escalas, en favor de la existencia de la materia oscura – la componente del Universo invisible, no bariónica, que representa casi el 85% de su masa total. Aunque su existencia se postuló por primera vez hace más de 80 aos, la naturaleza de la materia oscura sigue siendo hoy en día un misterio. Encontrar y entender la respuesta a esta pregunta es una de las tareas más importantes y emocionantes de la ciencia moderna.

En el contexto de nuestra visión cosmológica actual del Universo, la materia oscura es considerada como un nuevo tipo de partícula, que interactúa débilmente con la materia ordinaria y la radiación. Además, esta nueva partícula es probablemente fría (no relativista), no bariónica, producida térmicamente en el Universo temprano y estable en escalas cosmológicas. Nuestra búsqueda de la partícula de materia oscura se lleva a cabo en paralelo con tres enfoques diferentes: la detección de la materia oscura producida en colisionadores, la detección directa de materia oscura por su interacciones en los experimentos subterráneos, y la búsqueda indirecta en el espacio de tierra y los observatorios de Partículas del modelo estándar creados en la aniquilación de materia oscura o la decadencia.

Esta última estrategia es el tema de esta tesis. Los resultados presentados aquí son de búsquedas indirectas de la materia oscura en la galaxia esferiodal enana Segue 1, realizadas con los telescopios MAGIC de luz Cherenkov. El objetivo es reconocer los rayos gamma altamente energéticos producidos en la aniquilación o la desintegración de las partículas de materia oscura. Para ello, utilizamos algunas de las características espectrales únicas de los rayos gamma procedentes de dichos procesos. Un método de análisis específico, llamado el *método de full likelihood*, ha sido desarrollado para optimizar la la sensibilidad del análisis para las señales de materia oscura.

El esquema de la Tesis se podría resumir de la siguiente manera:

- **Capítulo 1** presenta el paradigma de la materia oscura: cuáles son las evidencias astrofísicas y cosmológicas que sustentan la existencia de la materia oscura y cómo pueden conciliarse con nuestra actual imagen de la evolución del Universo. El capítulo termina con una revisión de algunos de los candidatos más motivados para partícula de materia oscura, con una discusión detallada sobre aquellos que son de especial interés para este trabajo.

- **Capítulo 2** está dedicado a describir las búsquedas de materia oscura. Se inicia con la presentación de las diferentes estrategias que emplean actualmente los diversos experimentos, incluyendo los resultados más destacaddos, para continuar con la descripción más detallada de las búsquedas indirectos. Se presta especial atención a las

fotones de alta energía como mensajeros de búsqueda, contestando a las preguntas de qué seal se debe esperar, dónde buscarla y con qué instrumentos.

- **Capítulo 3** presenta el instrumento utilizado en este trabajo para las búsquedas de materia oscura – los telescopios MAGIC. El capítulo se divide en dos partes: la primera describe las propiedades técnicas del sistema; la segunda, la caracterización de su cadena de análisis estándar.

- **Capítulo 4** presenta la contribución científica original de este trabajo – el desarrollo del método de full likelihood, un método de análisis optimizado para el reconocimiento de las características espectrales que se esperan de los fotones originados por la materia oscura. En primer lugar, se presenta formalmente el método, y a continuación se procede a la caracterización de su comportamiento para un conjunto predefinido de condiciones, y se evalúa su rendimiento para determinadas formas espectrales.

- **Capítulo 5** presenta los resultados de este trabajo. En primer lugar, la motivación tras la selección de la galaxia Segue 1 como el candidato óptimo para las búsqueda de materia oscura con MAGIC. A continuación, se resumen los detalles de las observaciones realizadas y de la reducción de datos. Sigue el análisis de datos usando el método de full likelihood. Por último, el capítulo termina con los límites obtenidos en este trabajo para diferentes modelos de aniquilación o desintegración de la materia oscura.

Se presenta breve resumen de los puntos ms relevantes de esta Tesis en las conclusiones.

1

Dark Matter Paradigm

The notion of dark matter has been present for almost a century, but the question about its nature is still unanswered. Observational evidence and cosmological predictions assure that dark matter represents almost 85% of the matter content of our Universe, and almost 25% of its total energy budget. Discovering its essence is one of the most important and exciting tasks of modern science.

This Chapter is devoted to a brief introduction of the dark matter concept as well as the experimental results and theoretical predictions that support this paradigm. Additionally, some of the most widely considered candidates for the dark matter particle are presented.

1.1 Observational Evidence

Although works of Öpik (1922) [1] and of Oort (1932) [2] were implying that the luminous components of the galaxies were not sufficiently massive to explain their dynamics, it was Zwicky that first adopted the concept of dark matter in 1933 [3]. Through studies of individual galaxies in the Coma cluster, he concluded that their radial velocities were too high for the system to be gravitationally stable and not disperse – unless there was a dominant, invisible, *missing mass* keeping it together.

In the decades that followed, more observational evidence supporting the dark matter paradigm was gathered on all scales. This Section briefly describes some of the most relevant results.

1.1.1 Dynamics of Galaxies and Galaxy Clusters

One of the most compelling and direct evidences for the existence of dark matter are the rotation curves of the galaxies, i.e. circular velocities of visible stars and gas given as a function of their radial distances from the galaxy center.

In a stably bound system with spherical distribution of mass objects (stars, galaxies, etc.), the virial theorem relates the total time-averaged kinetic and potential energies, so that for an element of the system, rotating around the center at distance r, velocity distribution is derived as $v(r) \propto M(r)^{1/2} r^{-1/2}$, with $M(r)$ being the mass of the system within the radius r. In the innermost regions of the elliptical galaxies and the bulges of the spheroidal ones, mass distribution can be considered spherical and of constant density, so that $M(r) \propto r^3$ and $v(r) \propto r$. As one moves towards the galaxy outskirts, the stars become scarce and very spread apart, so it is expected that $M(r) \approx const.$ and $v(r) \propto r^{-1/2}$. However, the observations have shown that circular velocities do not decrease with the increasing distance from the galactic center: instead, rotation curves show an unexpected flat behavior that extends far beyond the edges of the luminous components (Figure 1.1) [4, 5]. This implies that mass distributions of galaxies cannot be as concentrated as their light distributions, i.e. *mass does not trace light.*

This departure from predictions of Newtonian gravity is apparent on greater scales as well: mass of a galaxy cluster, estimated from the velocities of its constituting galaxies, is much larger than the mass seen directly as galaxies and hot gas in the cluster.

The discrepancy is solved if a dominant dark matter halo embedding the galaxies and galaxy clusters is added to the whole system. A common way to express the estimated amount of dark matter needed for the dynamical equilibrium is through the mass-to-light ratio (M/L), commonly given in solar units, $M_\odot/L_\odot$. Mass is estimated from the dynamics of the system and gravitational lensing (§1.1.2), while the light is inferred from the photometric observations. For spiral galaxies, for instance, M/L is of $\mathcal{O}(10)$. On larger scales, for galaxy clusters, this ratio is of $\mathcal{O}(100)$. The most dark matter dominated systems known so far are the dwarf Spheroidal (dSph) galaxies, the low-surface-brightness objects that show unusual velocity dispersions and indicate a complete domination of dark over luminous matter at any radii, with M/L reaching values of $\mathcal{O}(1000)$.

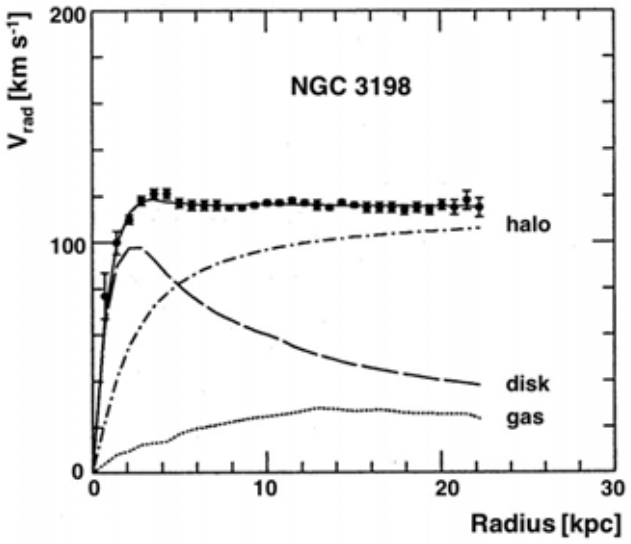

Figure 1.1: Rotation curve for galaxy NGC 6503. Also shown are the velocity contributions from the visible baryonic components, gas (dotted line) and galaxy disk (dashed line), as well as the dark matter contribution (dot-dashed line) required to match the observations. Adapted from [5].

1.1.2 Gravitational Lensing

According to the predictions of General Relativity, gravitational fields deflect the light path of photons and modify the apparent flux and shape of astronomical sources. As a consequence, mass concentrations modify the space-time metric and act as lenses, causing background objects to seem distorted to the observer. This effect can be used to gravitationally ascertain the existence of mass even when it emits no light and, furthermore, even probe its nature to the certain extent [6]. Gravitational lensing is primarily sensitive to the amount of matter of the lensing body and, in accordance to its effects, distinction is made between the strong, weak and microlensing.

The strong lensing regime is produced by very massive objects, such are galaxies and galaxy clusters. Resulting images are often multiplied, stretched to arcs and even rings, allowing for relatively effortless estimations of the total mass and even some reconstruction of the mass distribution of the lens. Studies of strong lensing indicate that galaxies and clusters of galaxies are dark matter dominated, with M/L increasing with the mass as well as the radius [7]. However, since strong lensing only relies on the gravitational optics, and is (almost) independent on the dynamical state of the lens, it can provide robust and reliable mass estimate only inside a small region. For the areas beyond, weak lensing effects should be considered instead.

Weak gravitational lensing is a cumulative effect produced by the overall distribution of matter in the Universe. It acts as a distortion grid that modifies the shape of all sources, but rather insignificantly – the changes can not be detected in the individual galaxies. Nevertheless, the weak lensing effects can be perceived by averaging over numerous population of distant galaxies in deep astronomical images, and the results have been successfully translated into masses of numerous galaxy clusters [8].

When used together, weak and strong lensing probe the structure and the dynamical properties of dark halos from the innermost regions to the borderline periphery. One of the most spectacular results from lensing effects, that not only favors the dark matter paradigm but

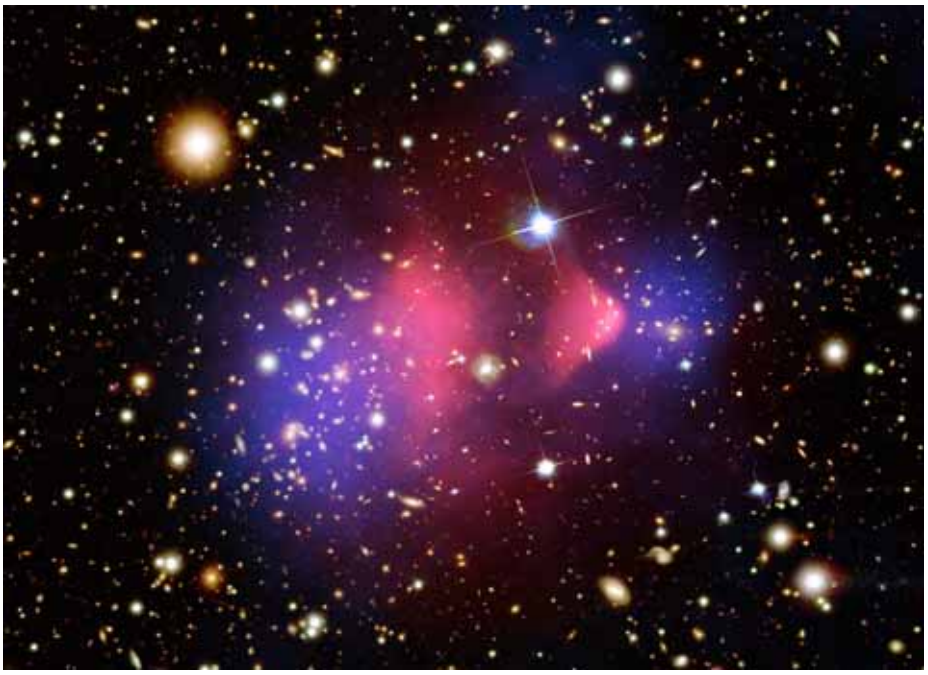

Figure 1.2: Hubble Space Telescope and Chandra-XRO composite image of 1E0657-56 (the Bullet cluster), formed in collision of two galaxy clusters. The X-ray emitting gas, accounting for the most of the baryonic matter of the system, is colored red, while the dark matter distribution, reconstructed from the gravitational lensing, is shown in blue color. Credit: NASA.

sheds some light on its nature as well, is the case of the "Bullet" cluster of galaxies [9, 10]. Its baryon distribution observed in X-rays by Chandra and gravitational mass mapped from the joined weak and strong lensing indicate that the Bullet cluster formed in a violent collision of two galaxy clusters. Two massive substructures, that are offset with respect to the baryon components, imply that the dark matter halos of the merging clusters passed through each other, succumbing only to weak and gravitational interactions, while the baryonic contents were slowed down by the electromagnetic force. As a result, the baryonic and dark matter portions of each of the clusters were decoupled (Figure 1.2). These findings strongly favour the dark matter existence, seen how otherwise the cluster galaxy population would not be following, but coinciding with the mass distribution. Furthermore, this case also suggests the collisionless nature of dark matter particles.

Lastly, the microlensing occurs when a small, stellar-like dark object acts as a lens, amplifying the flux intensity of the background objects. Observations of such effects play a role in constraining the contribution of the dark baryonic bodies (like dark stars and MAssive Compact Halo Objects (MACHOs)) to the total dark matter content of the Universe [11].

1.2 Λ Cold Dark Matter Model

If the observational findings presented in §1.1 are justified by the existence of dark matter, a cosmology is needed that can successfully incorporate this dark matter in the evolution and current image of our Universe. The most valid explanation so far is offered by the Λ Cold Dark Matter (ΛCDM) model, also referred to as the Concordance Cosmological Model

(CCM). The ΛCDM is based on both sound theoretical foundations and good agreement with the observational results (for a review, see, e.g. [12] and references within).

This Section gives some details on the ΛCDM formalism and its parameters. Also presented are the most relevant evidence that favor this model, as well as its flaws and possible cosmological alternatives.

1.2.1 The Λ Cold Dark Matter Formalism

The ΛCDM builds upon the Big Bang theory: approximately 10^{10} years ago, the Universe began expanding from an infinitesimally small and infinitesimally dense point. During the rapid inflation that followed, fundamental particles were formed, but not yet the matter, and the Universe was opaque and filled with hot plasma and powerful radiation. As the expansion continued, the temperature and density decreased, particles joined into atoms and the structure formation, initiated from the quantum fluctuations previously generated in the inflation field, began. The Universe composition turned out to be radiation (photons), matter (leptons, hadrons and dark matter) and dark energy.

The ΛCDM is founded on general relativity and it assumes that the following principles apply: Earth does not occupy a preferential place in the Universe (*Copernican principle*) and on the sufficiently large scales the Universe is homogeneous and isotropic (*Cosmological principle*). The most general space-time metric satisfying these conditions is the Friedmann-Robertson-Walker metric:

$$ds^2 = -c^2dt^2 + a(t)^2\left(\frac{dr^2}{1-kr^2} + r^2d\Omega^2\right), \tag{1.1}$$

where $a(t)$ is the cosmic scale factor and k is the spatial curvature constant, that can take values of 0, -1 and +1 for the flat, negatively curved and positively curved Universe, respectively.

On the other hand, from the Einstein equations, relation between the geometry and the density content of the Universe is given as:

$$G^{\mu\nu} \equiv R^{\mu\nu} - \frac{1}{2}g^{\mu\nu}R = -\frac{8\pi G}{c^4}T^{\mu\nu} - \Lambda g^{\mu\nu}, \tag{1.2}$$

that is, the geometry of space-time is affected by the matter and the matter distribution is influenced by the space-time geometry. In eq.(1.2), $G^{\mu\nu}$ is the Einstein tensor, $R^{\mu\nu}$ and R are the Ricci tensor and scalar, respectively, $g^{\mu\nu}$ is the space-time metric, $T^{\mu\nu}$ stands for the energy-momentum tensor and Λ represents the cosmological constant.

By solving eq.(1.2) with eq.(1.1), and considering the time components of the field equations, the temporal evolution of the Universe is expressed as

$$H^2 \equiv \left(\frac{\dot{a}}{a}\right)^2 = \frac{8\pi G\rho_{\rm tot}}{3} - \frac{kc^2}{a^2}, \tag{1.3}$$

also known as the Friedmann equation, where H is the Hubble parameter and $\rho_{\rm tot}$ is the total density of the Universe. In ΛCDM, the $\rho_{\rm tot}$ is divided among three main components: matter (baryonic and dark, $\rho_{\rm m} = \rho_{\rm b} + \rho_{\rm dm}$), radiation ($\rho_{\rm r}$) and dark energy ($\rho_\Lambda$):

$$\rho_{\rm tot} = \rho_{\rm m} + \rho_{\rm r} + \rho_\Lambda. \tag{1.4}$$

For a Universe with a spatially flat metric ($k = 0$), the total energy density from eq.(1.3) becomes *critical density*:

$$\rho_{\rm c} \equiv \frac{3}{8\pi G} H_0^2, \tag{1.5}$$

where H_0 is the Hubble constant, i.e. the value of the Hubble parameter today ($H_0 = 69.32 \pm 0.80$ km s^{-1} Mpc^{-1} [13]). Normalized to the critical density, eq.(1.4) becomes

$$\Omega \equiv \frac{\rho_{\rm tot}}{\rho_{\rm c}} = \Omega_{\rm m} + \Omega_{\rm r} + \Omega_\Lambda = 1 + \frac{kc^2}{(a_0 H_0)^2}, \tag{1.6}$$

with Ω denoting the *density parameter*, commonly used in the cosmology. Additionally, the curvature contribution from eq.(1.6) can be rewritten as

$$\Omega_k = \frac{\rho_{\rm k}}{\rho_{\rm c}} = -\frac{kc^2}{(a_0 H_0)^2}, \tag{1.7}$$

and from there eq.(1.6) becomes

$$\Omega_{\rm m} + \Omega_{\rm r} + \Omega_\Lambda + \Omega_{\rm k} = 1. \tag{1.8}$$

At the present epoch ($a = 1$), components contributing to the energy density of the Universe are:

- non-relativistic matter ($\Omega_{\rm m,0}/a^3$), with equation of state $p = 0$;
- radiation ($\Omega_{\rm r,0}/a^4$), with equation of state $p = \rho/3$, and
- dark energy ($\Omega_{\Lambda,0}$), with constant energy density $p = -\rho$.

In the context of the cosmological studies, the scale factor a is often expressed through the redshift, as $1/a = 1 + z$.

1.2.2 Cosmic Microwave Background

Probably the biggest confirmation of the validity of the ΛCDM comes from its success in predicting the initial candidates for structure formation, which culminated in the discovery of the temperature fluctuations in the cosmic microwave background (CMB).

CMB represents a relic from the earliest stages of the development of the Universe. It is an almost black body (T = 2.725 K), isotropic radiation, composed of photons frozen-out at the mass-radiation decoupling era and cooled down by the expansion of the Universe. The experimental confirmation of CMB in 1965 [14] served as evidence for the validity of the Big Bang theory. However, CMB was also expected to provide information on the Universe during the epoch of recombination: ΛCDM predicts that the acoustic sound waves – forming in the photon-baryon fluid as a result of conflict between the photon pressure and baryonic gravitational potential – froze when the photons decoupled. At the present epoch, these fluctuations should be seen as a series of peaks and troughs in the observed angular power spectrum, whose positions and amplitudes can be used to constrain variety of cosmological parameters.

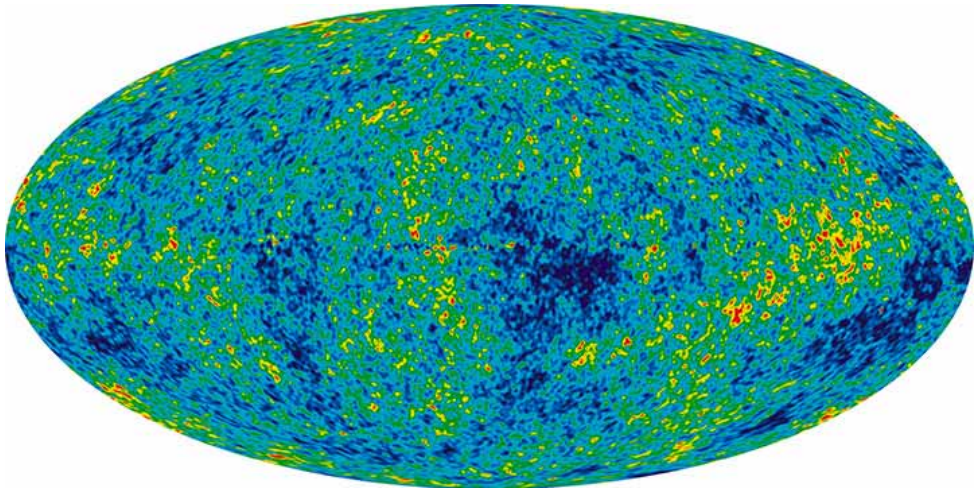

Figure 1.3: The 9-year anisotropy map from WMAP, showing the temperature fluctuations in the early Universe. The covered temperature range is of $\pm$ 200 μK. Credit: NASA / WMAP Science Team.

Indeed, such anisotropies (at the scale of 10^{-5} K) have been seen, most recently by the Wilkinson Microwave Anisotropy Probe (WMAP) satellite [16]. Figure 1.3 shows a whole sky map of the temperature anisotropy, obtained from 9 years of WMAP CMB radiation measurements [15]. The corresponding temperature and the temperature-polarization spectra, with the extremely precise ΛCDM fit to the data, are given in Figure 1.4. From the analysis of these measurements, the cosmological parameters were obtained, and the currently best-fit values of density parameters are [13]:

$$\Omega_{\rm b} = 0.0463 \pm 0.0009,$$
$$\Omega_{\rm dm} = 0.2402 \pm 0.0088,$$
$$\Omega_{\Lambda} = 0.7135 \pm 0.0095.$$

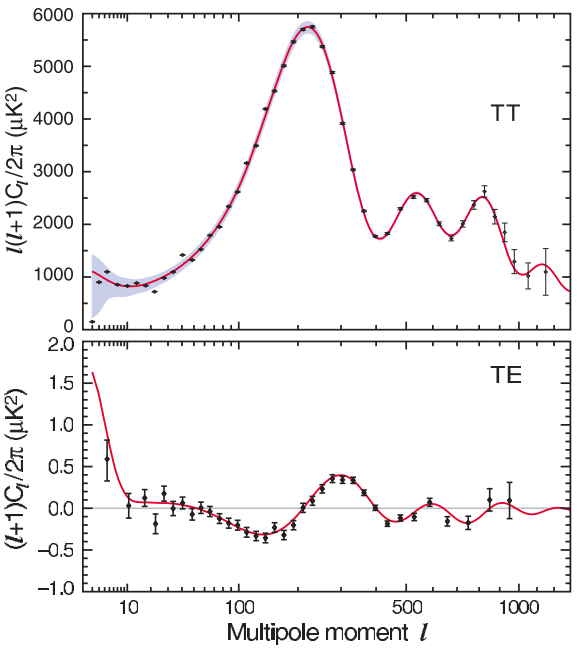

Figure 1.4: The 9-year WMAP temperature (**top**) and temperature polarization power-spectra (**bottom**). The first acoustic peak is related to the total fraction of matter at the recombination era. The best-fit flat model is depicted by the solid lines. Figures extracted from [15].

These values clearly indicate that the Universe today is dominated by the dark energy, that drives its accelerated expansion and contributes to the $\rho_{\rm tot}$ with ∼72%. The remaining energy content is composed of matter, out of which more than 80% is dark. The current contribution of the radiation to the total density is less than 0.1%.

Surprisingly, the visible density from stars, gas and dust only accounts for ∼20% of $\Omega_{\rm b}$. Therefore, most of the baryons are also dark. X-ray studies reveal that part of this baryonic dark matter is formed by intergalactic gas in galaxy clusters, as well as long filaments of warm-hot intergalactic medium connecting galaxies and galaxy clusters. Also, MACHOs contribute to the total dark baryonic mass budget.

1.2.3 Large Structure Formation

Another relevant confirmation of the essential validity of ΛCDM comes from the remarkable agreement between the predictions of numerical simulations, based on the ΛCDM, and the actual measurements by redshift surveys of the large scale structures of the Universe.

In the ΛCDM context, the structure formation initiated from the primordial perturbations in the gravitational potential, presumed to be seeded by quantum fluctuations in the inflation era. As the Universe evolved from this initial inflationary state, regions with density higher than the average background density (expressed in terms of density contrast, $\delta(x) = (\rho(x) - \langle\rho\rangle)/\langle\rho\rangle$) were able to grow due to the gravitational collapse. During the matter-dominated epoch, these tiny density fluctuations grew linearly, as $(1+z)^{-1}$, until $\delta(x) \sim 1$. The fluctuations then entered the non-linear regime, collapsed and the formation of the gravitationally bound structures began [17].

If the Universe were baryonic, the growth of density perturbations on scales lesser than the Jeans mass would be inhibited prior to recombination by the coupling of matter and radiation. From CMB temperature fluctuations (§1.2.2), it is known that the largest δ in baryonic matter at the time of recombination had an amplitude of $\sim 10^5$; in a matter-dominated Universe, δ could not have grown more than a factor 10^3 since, which is insufficient to form the present-day structures with $\delta \gg 1$. The existence of dark matter provides a simple solution to this problem: dark matter decouples while the bosons and fermions are still in the thermal equilibrium and strongly interacting. That way, the density fluctuations in dark matter begin growing earlier than in the ordinary matter. After the recombination, baryons collapse into the already existing gravitational wells formed by the dark matter overdensities, therefore following the dark matter distribution. And given the overwhelming fraction of dark matter in the total mass budget of the Universe, the dark matter component stands out as the driving factor behind the structure formation.

And what can structure formation say about the nature of dark matter particles? For particles to form a structure, it is necessary that their free-streaming paths are smaller than the fluctuation scale – otherwise, particles do not feel the gravitational pull from the fluctuations and can freely scatter, diluting the density and preventing any structure formation at the given scale. Based on the effect they have on the structure formation, three different types of particle dark matter particle have been postulated: hot, cold and warm dark matter.

- *Hot dark matter* particles are expected to have very large free-streaming lengths, due to their relativistic nature at the freeze-out. This implies that density fluctuations below the Mpc scales would be erased. The supercluster-scale structures would have to form first, and then fragment into smaller objects. This, so-called *top-down* scenario, is strongly disfavored by the observations. Therefore, hot dark matter can not be the dominant dark matter type [18].

- *Cold dark matter* particles would be non-relativistic with small free-streaming lengths, thus allowing formation of Earth-like masses. Such particles support the hierarchical structure formation – from smaller to larger sizes (the *bottom-up* scenario). Cold dark matter hypothesis is supported by both observations and simulations [19].

- *Warm dark matter* particles are the intermediate solution between the hot and cold dark matter. Their free-streaming lengths are of galaxy sizes [20], suggesting bottom-up formation at larger scales, and top-down scenario at smaller ones.

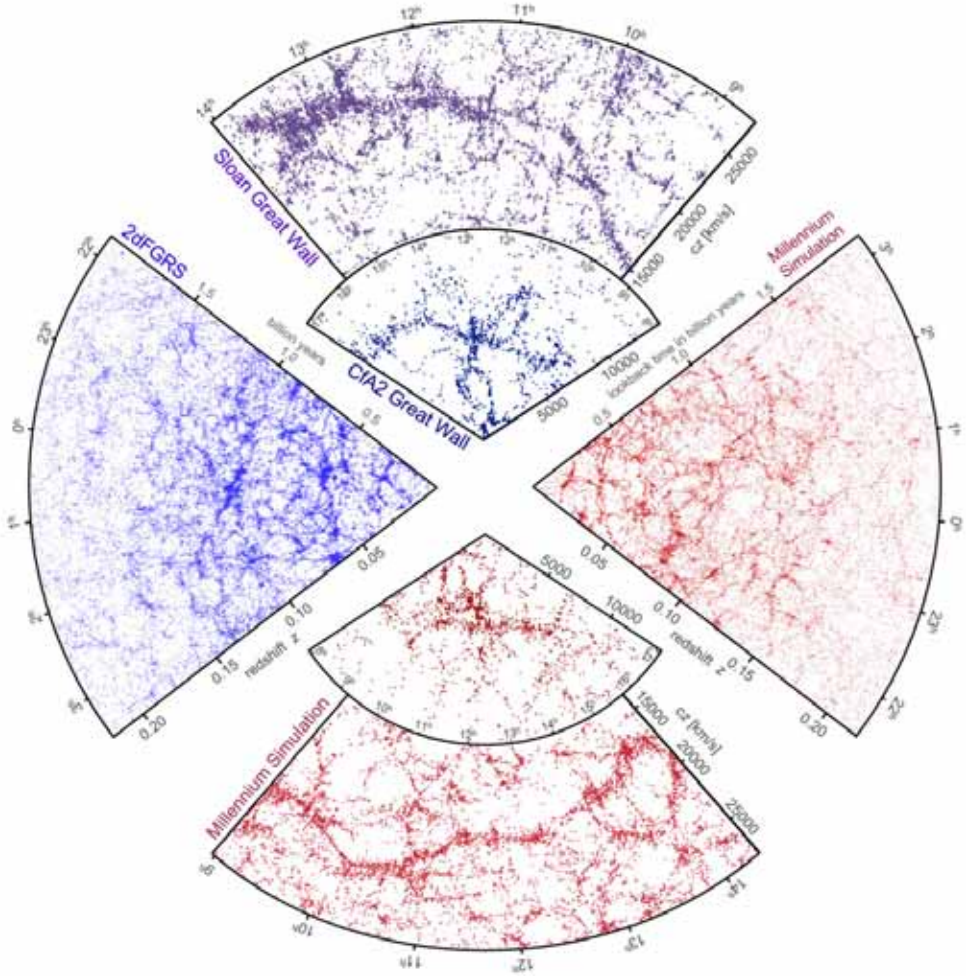

Figure 1.5: The large scale structure of the Universe, mapped by the 2dF Galaxy Redshift Survey [21], the Sloan Digital Sky Survey [22] and the CfA Redshift Survey [23]. Each point represents a galaxy as a function of right ascension and redshift. Also shown are the corresponding N-body Millenium simulations [24] of the ΛCDM structure formation. Credit: VIRGO/Millenium Simulation Project.

As already mentioned, validity of the cosmological models can be tested through the N-body simulations. These numerical studies attempt to reproduce the current image of the Universe at large scales, as well as the formation of galactic halos for chosen cosmological circumstances. So far, the best agreement between the simulations and measurements is achieved for the ΛCDM model, with cold and weakly interacting dark matter (Figure 1.5). N-body simulations are also used to generate mock galaxy catalogues and maps that yield the observed correlations and clustering of galaxies, and precise values of the cosmological parameters, in combination with the CMB maps and other cosmological probes.

1.2.4 Challenges to the ΛCDM

Despite the exceptional agreement between the ΛCDM and majority of the cosmological data, there are still some observational results that can not be accurately justified by the model (see, e.g. [25] and references within). Details on few of the most striking issues challenging the ΛCDM concept are presented below.

Dark matter halos Dark matter-dominated halos of galaxies are considered to be another generic success of ΛCDM, as mapped out by rotation curves (§1.1.1). However, the detailed predicted properties of halos do not seem to be well matched to observations in the inner regions of many disk galaxies [26]. The expected dark matter cusps (density $\rho \propto r^{-\alpha}$, with $1 < \alpha < 1.5$) are not found in most low surface brightness dwarfs observed at high resolution [27]. Whether this issue can be understood by more detailed, better resolution simulations that include the full interactions between the baryons and dark matter, remains to be seen. At the moment, theory fails to provide a compelling explanation.

The missing satellite problem N-body simulations suggest that, in the hierarchical structure formation, dark matter halos are created clumpy, with substructure persisting through the successive mergers. One consequence of the substructure is a large population of satellite galaxies, approximately increasing in abundance with decreasing mass. That, however, contradicts the observations, as the number of detected dwarf galaxies is within an order of magnitude lower than expected from simulations [28]. This problem has two possible solutions. One is that the smaller dark matter halos do exist, but are simply not massive enough to have attracted sufficient baryonic matter and are therefore almost optically invisible. Indeed, in the last decade a number of ultra-faint dwarfs has been discovered, with $M/L \sim 1000$ [29]. Other solution involves complex interactions between dwarfs and large galaxies, with dwarfs ending tidally stripped apart and extremely difficult to identify.

More challenging discrepancies include large scale velocity flows, low multipoles in the CMB and the quasars optical alignment. However, whether the solution of these issues lies in the domain of fundamental gravity, particle physics or astrophysics, these problems are not sufficient to abandon the ΛCDM concept. Rather, at this point it can be concluded that ΛCDM successfully matches the Universe on large scales, while on small scales it has (possibly) some difficulties in confronting the observations.

1.2.5 Alternative Cosmologies

The above mentioned shortcomings of the ΛCDM have motivated development of alternative cosmological explanations. Based on assumptions that dark matter is not cold or weakly interacting, or even postulating that dark matter does not exist at all, majority of these alternative cosmologies provide solutions to singular problems, while at the same time create new inconsistencies. Until date, neither of the proposed cosmologies offers evolutionary image of the Universe as completely as the ΛCDM does. However, for the sake of completeness, the best-justified of these alternatives are briefly described.

Modified Newtonian Dynamics (MOND) claims that the actual gravity deviates from the Newtonian one, thus eliminating the need for existence of dark matter [30]. According to MOND, below a certain gravity scale the effects of gravitational force are magnified. This would explain the observed flattening of the rotation curves, as well as the Tully-Fisher relation, stating that the total mass in visible stars and gas in a disk galaxy is proportional to the fourth power of the asymptotic rotational velocity. However, MOND fails to explain the dynamics of large objects like galaxy clusters, as well as the gravitational lensing effects without adding an additional component of the matter. More over, MOND can not account for any relativistic phenomena.

Tensor-Vector-Scalar (TeVeS) gravity is developed as the relativistic generalization of MOND [31]. TeVeS works in the weak-field limit and possesses all good qualities of the MOND theory. In addition, TeVeS can explain gravitational lensing effects, although in a way non-consistent with the galaxy rotation curves. Major drawbacks of the TeVeS gravity model are the incompatibility with stellar evolution theory and the inability to explain the Bullet cluster phenomena (§1.1.2).

Other non-standard cosmological models include the Gödel Universe [32], the Quasi-Steady state cosmology [33], the Brans-Dickie cosmology [34], the Einstein-de Sitter Universe [35], etc.

1.3 Dark Matter Candidates

Despite the overwhelming observational evidence for the existence of dark matter, the nature of its constituent is still unknown. The wealth of recent astrophysical and cosmological data, however, imposes significant constraints on the dark matter properties. In context of ΛCDM, the dark matter particle should:

- match the dark matter relic density, $\Omega_{\rm dm}h^2 = 0.112 \pm 0.006$[1]. If that is the case, dark matter particle will also be stable on cosmological scale;
- be neutral – otherwise, it could couple with photons and therefore would not be dark;
- interact only weakly and gravitationally: the couplings with electromagnetic sector, as well as strong interactions are highly suppressed and ruled out by the observations;
- play the leading role in the structure formation in the Universe, as the fluctuations in the dark matter density are dominating the evolution of the perturbations in the matter-dominated era;
- be consistent with the Big Bang Nucleosynthesis and not contradict the observed abundances of light elements;
- not affect the stellar evolution;
- be experimentally verifiable and consistent with the constraints derived by different methods of dark matter searches (Chapter 2).

This Section presents some of the best-motivated dark matter particle candidates.

1.3.1 Weakly Interacting Massive Particles

Weakly Interacting Massive Particles (WIMPs) are the most studied dark matter candidates. WIMPs are postulated as non-baryonic, stable and weakly interacting, but their greatest appeal is that they are found in many particle physic theories, that they naturally have the correct relic density, and that they can be detected in many ways [36, 37].

[1] In the multicomponent dark matter scenarios, the relic density for a given partice can be lower than the total $\Omega_{\rm dm}h^2$.

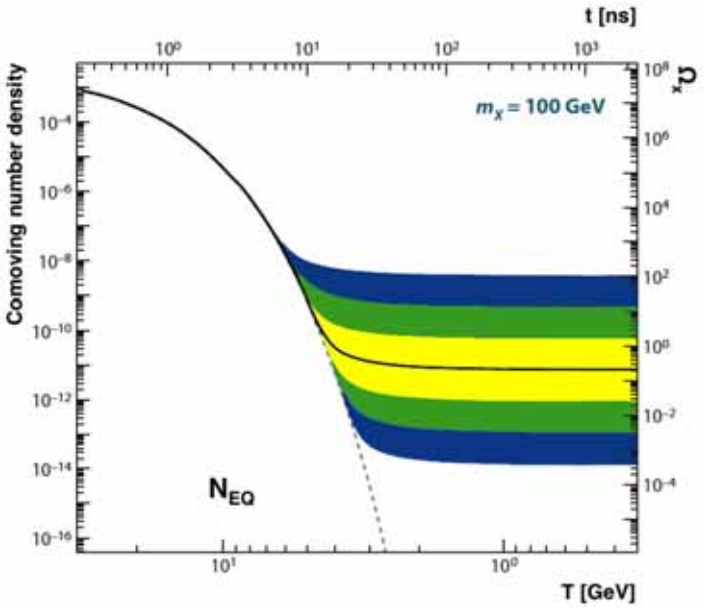

Figure 1.6: The comoving number density (**left**) and the resulting thermal relic density (**right**) of a 100 GeV annihilating dark matter particle as a function of temperature (**bottom**) and time (**top**). The solid black line corresponds to the annihilation cross section that yields the correct relic density, and the blue, green and yellow regions are for cross sections that differ by 10, 100 and 1000 (respectively) from this value. The dashed gray line is the number density of a particle that remains in thermal equilibrium.

WIMPs are presumed to be the thermal relics of the Big Bang. When Universe starts to cool off, and its temperature drops below the mass of the dark matter particle m_X, WIMPs decouple from the thermal equilibrium. Their production ceases and their number begins to drop exponentially, as $e^{-m_X/T}$. However, as the Universe is also expanding, the dark matter gas becomes so diluted that WIMPs can not found each other to annihilate. The WIMPs then "freeze-out", with their number asymptotically approaching a constant – their thermal relic density (Figure 1.6). The fact that the predicted WIMP relic density corresponds to the measured relic density of dark matter is referred to as the *WIMP miracle*. In numbers, this translates to

$$\Omega_X h^2 = \frac{s_0}{\rho_c/h^2}\left(\frac{45}{\pi g}\right)^{1/2}\frac{m_X}{T_{fo}M_{pl}}\frac{1}{\langle\sigma_{ann}v\rangle} \approx \frac{10^{-27}\text{cm}^3\text{s}}{\langle\sigma_{ann}v\rangle}, \tag{1.9}$$

where Ω_X is the density parameter of the WIMP, s_0 is the current entropy density of the Universe, ρ_c is the critical density, h is the scaled Hubble constant, g stands for the relativistic degrees of freedom at the freeze-out, and T_{fo} for the temperature at the freeze-out. Lastly, M_{pl} is the Planck mass and $\langle\sigma_{ann}v\rangle$ is the thermally averaged product of the annihilation cross section and velocity.

For WIMPs the freeze-out occurred for $T_{fo} \simeq m_X/20$, which sets the mass of a WIMP in a few GeV - few TeV range. Hence, at the time of decoupling, these particles were non-relativistic, and thus they are suitable to play the role of the cold dark matter.

However, such particle – a WIMP - does not exist within the framework of the Standard Model (SM). Hence, one must go beyond the borders of SM and into the realm of some new physics to try to find a WIMP. Some of these new theories and their WIMP candidates are described below. Accent is set on those particles that are of relevance for this work; for the

others, references for further reading are provided.

1.3.1.1 Supersymmetric Dark Matter

The Supersymmetry (SUSY) extension of the SM postulates that, for every SM particle there is a new, as-yet-undiscovered partner particle, with the same set od quantum numbers and gauge interactions but the spin, which is increased for 1/2. SUSY represents an elegant, theoretically sound scenario that relates fermions and bosons, thus providing a more unified picture of the particle world (see, e.g. [38, 39]). More importantly, SUSY provides possible solutions to some of the burning problems of the SM, like:

- *hierarchy problem*, linked to the enormous difference between the electroweak and Plank energy scales, is stabilized with SUSY, through the radiative corrections to the Higgs boson mass (and thus to the masses of the rest of the SM particles, [40]);
- *unification of the gauge couplings* of the SM, is possible if the SUSY particles (sparticles) are included in the renormalization-group equations [41];
- *natural dark matter candidate* is provided by SUSY: the Lightest SUSY Particle (LSP) is expected to be heavy, neutral and stable, fitting in perfectly in the ΛCDM paradigm as the dark matter constituent [42].

SUSY Realisations A general SUSY extension contains many unknown parameters. To make progress, it is typical to consider specific models in which simplifying assumptions unify many parameters, and then study to what extent the conclusions may be generalized.

The Minimal Supersymmetric Standard Model (MSSM) [43] extends the SM particles with two extra Higgs doublets, to account for the u and d quark masses, plus the complete set of SUSY partners. If the SUSY were not broken, the sparticles would be of the same masses as their SM partners, and their detection would be achieved by now. Breaking of the symmetry, on the other hand, produces some critical effects on the proton lifetime, shortening it down to values lower than the age of the Universe, which contradicts the observations. To remedy the issue, a new symmetry, called R-parity, is introduced. R-parity allows for the SUSY breaking, and its value is defined as $R \equiv (-1)^{3B+2L+2s}$, where B, L and s stand for the baryon, lepton and the spin number, respectively. SM particles have R-Parity of +1, and their SUSY partners of -1. That way, the R-parity is a conserved quantum number in any reaction – SM particles can only decay to SM particles and sparticles only decay to sparticles. A significant consequence of R-parity preservation is that the lightest sparticle is stable and a viable dark matter candidate. On the other hand, main drawback of MSSM (in terms of practicality) is that has over 120 free parameters.

The constrained Minimal Supersymetric Standard Model (cMSSM) [44] reduces the number of needed parameters to only five: the universal gaugino mass $m_{1/2}$, the universal scalar mass m_0 (sfermions and Higgs masses), the universal trilinear coupling A_0, ratio of the vacum expectation values of the two Higgs fields $\tan\beta$, and the sign of μ, where μ is the higgsino mass parameter. This significant reduction (compared to the MSSM) in the dimensions of the parameter space is accomplished primarily by relaxing the condition of universality of the soft SUSY breaking parameters at a certain energy scale, such as grand unification scale, which is consistent with some well-established SM observations, like the absence of the CP-violating terms and flavour-changing neutral currents.

The minimal SUper-GRAvity Model (mSUGRA) [45] is a special case of the cMSSM, when the SUSY breaking is mediated by the graviton and the graviton mass is fixed so $m_{3/2} = m_0$. Other MSSM realizations include the Non-Universal Higgs Masses model [46], phenomenological MSSM (pMSSM, [47], etc.

SUSY dark matter candidates Among the new particles that SUSY introduces, the electrically neutral ones with weak interactions are the natural dark matter candidates: the spin 3/2 fermion *gravitino* ($\widetilde{G}$), the spin 1/2 fermions called *neutralinos* (χ_1, χ_2, χ_3, χ_4), and the spin 0 scalars *sneutrinos* ($\widetilde{\nu}_e$, $\widetilde{\nu}_\mu$, $\widetilde{\nu}_\tau$).

The sneutrinos are not good dark matter candidates, as both their annihilation and scattering cross sections are large, so they are underabundant or excluded by null results from direct detection experiments, for all masses near m_{weak}. Gravitinos qualify as the dark matter particle in some particular scenarios, like the gauge mediated SUSY, where they are stable and lightest particles. Although theoretically well-motivated, $\widetilde{G}$ may be difficult to detect: as it interact only gravitationally, the main source of gravitinos would be the decay of the next-to-lightest SUSY particles. Thus, the dark matter characterization in the gravitino scenario would require detection of the signatures of the progenitor particle.

Neutralinos, on the other hand, are very favored as the dark matter constituents. Neutralinos are mass eigenstates produced in mixing of the neutral spin 1/2 fermions: bino ($\widetilde{B}$), wino ($\widetilde{W}_3$) and two higgsinos ($\widetilde{H}_1^0$ and $\widetilde{H}_2^0$) [42]. The lightest of the resulting particles, $\chi \equiv \chi_1$ is a natural WIMP dark matter candidate. Neutralino is a Majorana fermion, i.e. its own antiparticle, which in turn means that it can self-annihilate into (detectable) SM particles, such are:

- *Fermions:* neutralinos annihilate into fermion pairs via s-channel, through the exchange of Z or Higgs bosons, or via t-channel, through the sfermion exchange. In either case, the amplitude of the process is proportional to the mass of the fermion product. Consequently, the annihilation into fermions is dominated by heavy particles, like $\tau^+\tau^-$, $b\bar{b}$ and $t\bar{t}$ (for sufficiently high masses).

- *Photons:* direct annihilation into photons can ocurre at one loop level, as $\chi\chi \to \gamma\gamma$ and $\chi\chi \to Z\gamma$. These processes are strongly suppressed, but not impossible; photons produced this way would be detected as sharp lines at energies $E_\gamma = m_\chi$ (for $\gamma\gamma$) and $E_\gamma = m_\chi + m_Z^2/m_\chi^2$ (for $Z\gamma$), representing the undoubtable evidence of dark matter detection. Photons can also be produced in the so-called internal QED bremsstrahlung [48]: if neutralinos annihilate into leptons, the annihilation exchange particle is a charged sparticle that can emit a photon. This photon helps restore the helicity in the annihilation processes of type $\chi\chi \to l^+l^-\gamma$, thus allowing for previously forbidden interactions. Photons produced this way are expected to carry a significant amount of energy ($E_\gamma > 0.6m_\chi$) and to produce a characteristic bump at the end of the differential photon energy spectrum.

- *Gauge bosons:* in the low-velocity regime, pure gaugino-like neutralinos can annihilate into Z and $W^\pm$ bosons via t-channel, while pure higgsino-like and mixed neutralinos would produce these particles via s-channel.

- *Higgs boson:* neutralinos can annihilate into pair of Higgs bosons or a Higgs and a gauge bosons. The most favoured channels are the annihilation into light neutral Higgs and a Z boson ($\chi\chi \to h^0Z$), into a heavy Higgs and a Z boson ($\chi\chi \to H^0Z$), into a

charged Higgs and a W boson ($\chi\chi \rightarrow H^{\pm}W^{\pm}$), and into a light Higgs and a pseudoscalar Higgs (($\chi\chi \rightarrow h^0 A_0$).

Details on methods and current progress of the searches for SUSY dark matter will be presented in Chapter 2. However, it should be mentioned that the latest results from Large Hadron Collider (LHC) [49] have struck serious blows to the SUSY credibility. No proof of new physics has been found so far. The newly discovered Higgs(-like) boson [50] behaves pretty much as the SM predicts, while none of the proposed SM extensions claims a completely "standard" Higgs. Furthermore, no hints of any anomalous behaviour was detected in the extremely rare B_s meson decay [51]. Still, not all hope for the SUSY is lost: introduction of new parameters can adjust the model (to a certain extent) to the current experimental constraints. More conclusive results could probably be expected in 2014, when LHC will begin to operate at the higher energy regime [52] (up to 14 TeV, compared to the current 8 TeV limit).

1.3.1.2 Universal Extra Dimensions

An alternative possibility for the new weak-scale physics are extra dimensions. The idea originated from work of Kaluza and Klein almost a century ago [53, 54], and since then it acquired many modern descendants, of which the strongest foundations has the theory of Universal Extra Dimensions (UED) [55].

In UED, all particles propagate in flat, compact extra dimensions of size 10^{-18} m or smaller. Every SM particle has an infinite number of partner particles of the same spin, with one at every Kaluza-Klein (KK) level n with mass $\sim nR^{-1}$, with R referring to the compactified radius of the extra dimension. Unlike SUSY, UED do not solve the gauge hierarchy problem; in fact, their couplings become large and nonperturbative at energies far below the Planck scale. However, UED are considered as plausible models under the assumption that they are a low-energy approximation to a more complete theory that resolves the hierarchy problem and is well-defined up to the Planck scale.

The simplest UED models preserve a discrete, KK parity, which implies that the lightest KK particle (LKP) is stable and a possible dark matter candidate. The LKP is typically a B^1, a level 1 partner of the hypercharge gauge boson. Investigations of the B^1 regions with the correct thermal relic density indicate that the required LKP mass is in the 600 GeV - 1.4 TeV range, a slightly heavier than for the neutralinos. Other possibilities for the LKP are KK 'neutron', KK 'Z' and KK Higgs.

1.3.1.3 Other WIMP Candidates

Neutralino can be considered as a prototyp of a WIMP, and KK dark matter an instructive alternative. There are many other examples, however. Some of the electroweak theories and their accompanying WIMP candidates include large extra dimensions with branons as particles [56], little Higgs theories with T-odd particles [57] and warped extra dimensions with excited states [58]. As with all WIMPs, these dark matter candidates are produced through thermal freeze-out and are cold and collisionless, but their implications for detection may differ significantly.

1.3.2 Non-WIMP Dark Matter

As already mentioned, there is a wast collection of dark matter candidates. As this work is primarily focused on the search for WIMP particles, some of the other candidates are only briefly reviewed in this Section.

1.3.2.1 Sterile Neutrinos

The fact that neutrinos have non-zero mass is a solid experimental evidence for a new physics beyond the SM. For the neutrinos to get mass through the same mechanisms that generate masses for quarks and charged leptons, a new, right-handed neutrinos should be added. These, so -called *sterile neutrinos* are weakly-interacting Majorana fermions. The lightest of sterile neutrinos, with mass predicted to be in the keV range, is compatible with warm dark matter (§1.2.3), but could also be considered as cold candidate, depending on the production mechanism. Additionally, sterile neutrinos may provide solution for the baryon asymmetry [59] and, in the warm dark matter scenario, the missing satellites problem [60].

As a consequence of the mixing between the sterile and active neutrinos (ν_s and ν, respectively), the former become unstable. The main decay channel for the lightest sterile neutrino is $\nu_s \to 3\nu$; from there, assuming the ν_s mass of $m_{\nu_s} \sim \mathcal{O}(1\text{ keV})$, the expected lifetime of the sterile neutrinos is estimated to 10^{17} years, meaning that these particles are cosmologically stable [61]. Through the described decay, the sterile neutrinos are extremely difficult to detect, given the low energy of the resulting active neutrinos. An alternative way of detection could be pursued for a subdominant decay channel that can provide a distinctive photon line, $\nu_s \to \gamma\nu$. Such line would contribute at energies of $E_\gamma = m_{\nu_s}/2$, and it would be broadened due to the velocity dispersion of sterile neutrino population. Therefore, compact regions with significan accumulations of sterile neutrinos could produce a detectable X-ray flux line in the 0.1-100 keV energy range.

1.3.2.2 SuperWIMPs

In the superWIMP framework for dark matter, WIMPs freeze-out in the early Universe (as described in §1.3.1), but later decay to superWIMPs, particles that form the dark matter that exists today [62]. Because superWIMPs are very weakly interacting, they have no impact on WIMP freeze-out, and the WIMPs decouple with a thermal relic density $\Omega_X \sim \Omega_{dm}$. Assuming that each WIMP decay produces one superWIMP, the relic density of superWIMP is

$$\Omega_{sX} = \frac{m_{sX}}{m_X}\Omega_X. \tag{1.10}$$

SuperWIMPs therefore inherit their relic density from WIMPs, and for $m_{sX} \sim m_X$, the WIMP miracle also applies and the superWIMPs are produced in the desired amount to constitute much or all of dark matter.

Because superWIMPs are very weakly interacting, they are impossible to detect in conventional direct and indirect dark matter searches. However, their extraordinary weak couplings imply that the decays of WIMPs to superWIMPs may be very late and have an observable impact on Big Bang Nucleosynthesis, the Planckian spectrum of the CMB, small-scale structure and the diffuse photon spectrum.

The superWIMP scenario is realized in many particle physics models. The prototypical example is gravitino, which exists in all SUSY theories. Other examples of superWIMP dark

matter candidates include KK gravitinos in UED scenarios, axinos and quintessinos in SUSY theories, and many other.

1.3.2.3 Axions

The axion particle was proposed as a solution to the strong CP problem of the SM [63]. It is a light, neutral and weakly interacting, spin 0 boson that represents a natural dark matter candidate. For axions to live longer than the age of the Universe, their mass can not exceed $m_a \leq 20$ ev. Axions can be produced thermally, like light gravitinos and sterile neutrinos, and in that scenario they would be the hot dark matter (§1.2.3. However, in order to achieve the correct relic density, the axion mass would have to be $m_a \sim 80$ eV; such particles can not be the bulk of the dark matter. Alternative is a non-thermal axion production, consequential to the spontaneous Peccei-Quinn (PQ) symmetry breaking. In that case, axion can be a viable, cold dark matter particle, with mass in the $10^{-6} - 10^{-2}$ eV range, and with properties dependent on whether the PQ phase transition occurred before or after the inflation epoch.

In the presence of electromagnetic fields, axions are predicted to couple with photons in such a way that a conversion is possible, leading to the so-called photon-axion oscillations. This effect may imprint a distinctive signature in the observed spectra of distant gamma-ray sources, which in turn has direct implications of axion discovery and characterization.

1.3.2.4 Hidden Dark Matter

Hidden dark matter is postulated as dark matter that has no SM gauge interactions [64]. Hidden sector differs from the visible one, as it can have its own matter content and gauge forces. Therefore, for the correct relic density to be achieved, for the hidden dark matter the WIMP miracle is generalized to the *WIMPless miracle*: dark matter naturally has the correct relic density, but does not necessarily have a weak-scale mass or weak interactions. Matter in hidden sector interacts only gravitationally. Still, in the scenarions that involve existence of connector sectors, that mediate between the SM and the hidden sector, certain (detectable) astrophysical implications are possible.

2

Dark Matter Searches

The last decades have been marked by ever-growing efforts to discover the true nature of dark matter. Numerous experiments have been devised in attempt to catch a glimpse of the elusive dark matter particle, however, to date, no undeniable results can be claimed. Based on the approach, three main detection techniques can be distinguished: production of dark matter in particle accelerators, direct detection through dark matter scattering off ordinary matter, and indirect detection of secondary, SM particles produced in dark matter annihilation or decay.

This Chapter describes the basic principles behind each of these approaches, as well as their latest experimental results. As implied from the title of this work, indirect searches will be discussed in more detail – from the technique and expected spectral signatures, to suitable targets, existing observatories and the most interesting results.

2.1 Production at Particle Colliders

Possible detection of new physics in particle collider experiments may shed some light on the nature of dark matter. If WIMP (§1.3.1) is the dark matter particle, it could be created in a collider whose luminosity and center-of-mass energy are sufficiently large. The produced WIMPs would, of course, be invisible, but their presence might be deduced indirectly, by measuring the outcome of the collisions (see, e.g. [65] and references within).

Missing transverse energy refers to the energy carried away by a body leaving the detector unseen. It is reconstructed from the momentum conservation law: the momenta of incoming projectiles in the direction orthogonal to the beam is zero, so the final products of the collision must balance their momenta in the transverse plain. When this does not happen, possible explanation is production of dark matter particles[1].

Different mechanisms for WIMP production at colliders have been proposed. In particular case of SUSY (§1.3.1.1), the best detection prospects would arise from the creation of heavier superparticles that in turn decay into quark and gluon jets and pair(s) of neutralinos. Such events should be seen at LHC (and its detectors ATLAS [66] and CMS [67]); however, failure to detect them so far has put serious strains on the most simplified SUSY models [68]. The latest limits from ATLAS on mSUGRA model [69] allow for the exclusion of a large region of the parameter space (Figure 2.1). Still, complete rejection or confirmation of SUSY will most likely have to wait until 2015, when LHC will begin operating at its full energy potential of 14 TeV [52].

Collider experiments also offer the possibility of probing the UED models (§1.3.1.2). The expected signatures in this case are strikingly similar to those of SUSY, and involve jets, leptons and missing energy. In the hypothetical case of the discovery of new physics, SUSY and UED particles would be distinguished by their different spins or by different number of partners for each SM particle (infinite tower of particles for UED versus one partner for SUSY).

Also possible is the direct production of WIMP particle pair accompanied by emission of a photon or a jet from the initial state. Such mono-photon and mono-jet events, respectively, together with the missing transversal energy carried away by the WIMPs, would represent striking signatures of dark matter presence. In linear colliders, disentanglement of such signals from the background is possible, as the initial state particles have definite energy and may be polarized, which provides useful diagnostics. For the hadron colliders, however, these features are missing, since energies of the gluons and quarks, that actually interact in the collision, are not fixed. Consequently, in the LHC, mono-jet and mono-photon signals are highly obscured by the background. Still, limits for such events can be made, and they are directly comparable to the constraints of direct search experiments [70].

Production and detection of a dark matter particle in colliders would reveal significant information, like its mass, annihilation and direct detection cross section, as well as the value of its thermal relic density. Nevertheless, such set of characteristics would have to be independently confirmed by direct and indirect detection experiments before identifying the new particle as dark matter.

For more details on collider searches, refer to [65].

[1] Other explanations include the escape of high energy neutrino or imperfect reconstruction of the momenta (if the missing transverse energy is not too large and significantly different from zero.)

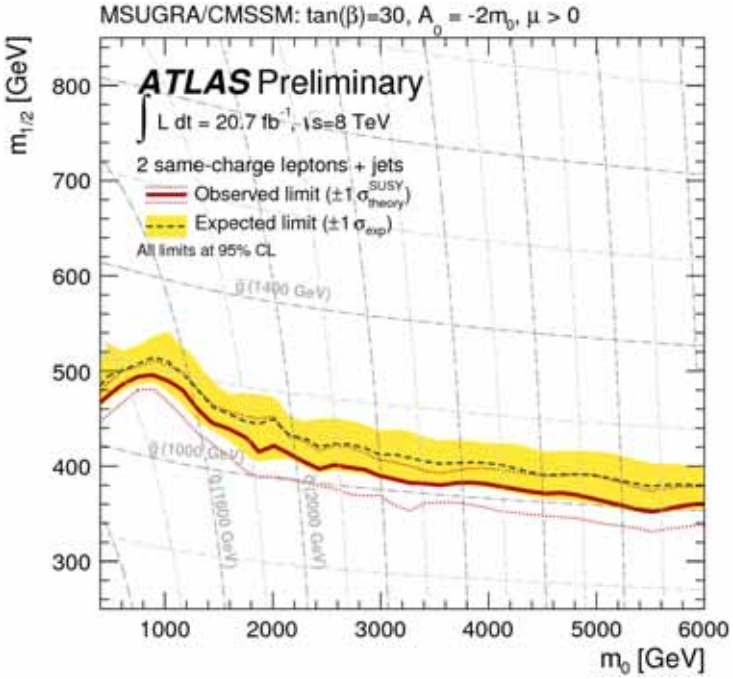

Figure 2.1: ATLAS exclusion limits over the mSUGRA/cMSSM parameter space after 20.7 fb^{-1} of accumulated data. The yellow band around the expected limit shows the $\pm 1\sigma$ uncertainty region, including all statistical and systematic uncertainties except the theoretical uncertainties, on the SUSY cross section. The $\pm 1\sigma$ SUSY lines around the observed limit are obtained by changing the SUSY cross section by $\pm 1\sigma$. Taken from [69].

2.2 Direct Detection

If dark matter is made of WIMPs, then the WIMP flux expected on Earth is of the order of 10^5 cm^{-2} s^{-1} for a particle of $m_\chi = 100$ GeV [71]. This flux is sufficiently large to have a small, but potentially determinable fraction of WIMPs interact with ordinary matter. Direct detection experiments aim to discover dark matter by measuring the nuclear recoils caused by elastic scattering of the WIMPs off baryonic targets. Assuming that the velocity distribution of WIMPs with respect to the Solar System is of order of 100 km s^{-1}, the expected recoil energy, transfered from a GeV-mass WIMP to a heavy nucleus, is typically of order of tens of keV. The energy exchanged in these interactions can be deposited in the detector through ionization, scintillation or heat (photon) production.

All the information about dark matter microscopic properties is codified into the differential elastic scattering cross section, generally separated into a spin-independent and spin-dependent contributions. The spin-independent term comes from scalar and vector couplings to quarks, and its value basically scales as the square number of nucleons. On the other hand, the spin-dependent term comes from axial-vector coupling to quarks, and it is dependent on the nuclear angular momentum. For different dark matter models relation between these two contributions may differ, and although both have to be taken into account, the scalar component dominates for heavy targets, which is the case for most direct detection experiments.

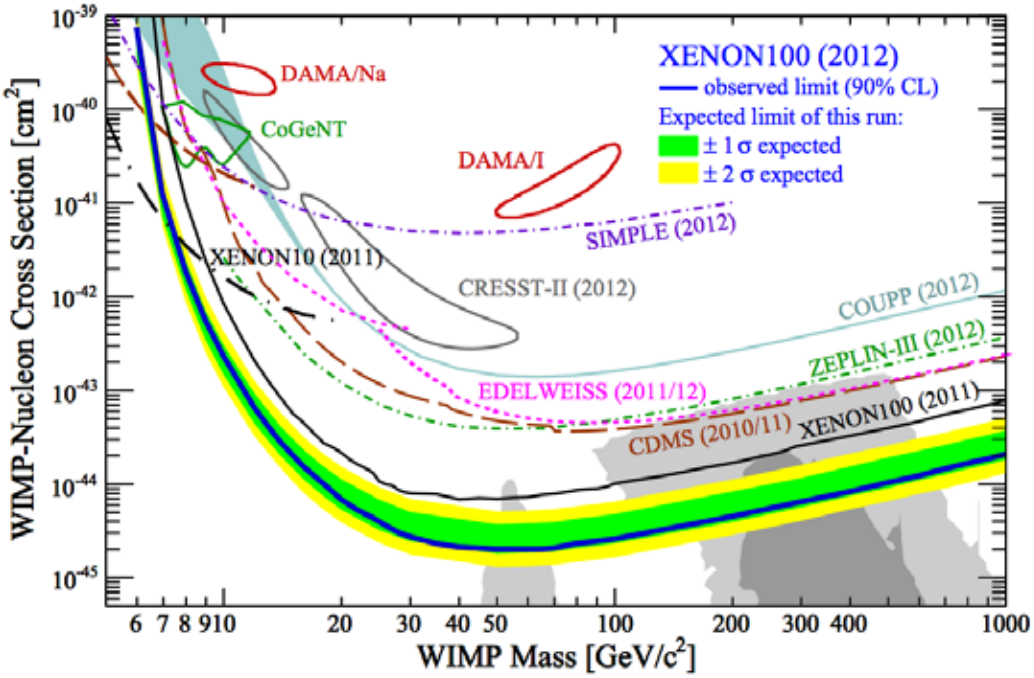

Figure 2.2: Result on spin-independent WIMP-nucleon scattering from XENON100, from 225 live days. The expected sensitivity is shown by the green/yellow band ($1\sigma/2\sigma$) and the resulting exclusion limit (90% c.l.) in blue. For comparison, other experimental limits (90% c.l.) and detection claims (2σ) are also shown, together with the regions ($1\sigma/2\sigma$) preferred by cMSSM models. Taken from [75].

Since the expected elastic cross section is of order of $\sigma \sim 10^{-43}$ cm^2, the rate of nuclear interactions is extremely low (less than 1 event per kg per day). That makes the background characterization and control the greatest challenges of direct detection experiments. Better performance is ensured by choosing large detection target, composed of extremely radiopure elements; same philosophy steers the selection of the rest of the detector parts. Furthermore, the target material is often surrounded by a high-density metal shielding, and special care is taken to minimize the electronic noise. In order to suppress the unwanted background originating from cosmic rays (mainly muons), the installations of the experiments are typically located deep under ground.

By the time this work was written, hints of dark matter signal have been reported by experiments like DAMA/LIBRA [72] and CoGeNT [73]; however, neither was conclusive enough on its own and could not be reproduced by other experiments. Moreover, the most stringent limits over the spin-independent interaction cross section, measured by the XENON100 experiment [74] and of order $\sim 10^{-45}$ cm^2 [75], already exclude both the DAMA/LIBRA and the CoGeNT favored regions. XENON100 also provides the highest sensitivity for the spin-dependent cross section, of order $\sim 10^{-40}$ cm^2 [76].

The future of the direct detection instruments goes along the line of increasing the mass of the target materials above one tone, lowering the ambiental temperature down to few mK, and measuring the signals from ionization, scintillation and heat production within the same detector. Efforts on several of such future experiments, like EURECA [77], DARWIN [78] and XENON1T [79], are already under way.

For more information on direct detection searches, see e.g. [71] and references within.

2.3 Indirect Detection

Indirect searches exploit the possibility that dark matter particles can annihilate or decay, producing SM particles detectable through a variety of modern ground and space-based observatories. The resulting SM products are expected to carry valuable information that could give clues about the properties of dark matter particle. Furthermore, indirect searches are probing the astrophysical distribution of dark matter, which is not possible with direct and collider approaches. The main obstacle to this search method is the (usually) overwhelming abundance of astrophysical background, which makes the disentanglement of SM particles that are of dark matter origin from those that are not a rather complex task.

The premise of dark matter particle annihilating or decaying is based on the assumption that this particle is not absolutely stable, but *stable on cosmological scales*, i.e. its lifetime is longer than the age of the Universe and its annihilation rate is sufficiently small so that the total dark matter budget is not significantly reduced.

Indirect searches look for signatures of dark matter through the stable final SM products: photons, neutrinos, electrons, protons and their corresponding antiparticles. The expected signal depends on the properties of dark matter particle, on type of the resulting final state SM particle, as well as on how and where it was produced. This work focuses on searches for gamma-ray signatures of dark matter annihilation or decay. The remaining of this Chapter describes the calculation of the expected photon flux, the suitable targets and types of gamma-ray observatories used for indirect searches. But first, for the sake of completeness, the most interesting detectable products are listed in the following Section.

2.3.1 Messengers for Indirect Dark Matter Searches

Photons are particularly interesting products of dark matter annihilation or decay, as they travel in straight lines and are practically unabsorbed in the local Universe. Because they point back to the place of their creation, astrophysical foregrounds can be significantly reduced by looking for signals in regions with high dark matter density. Furthermore, the resulting photon spectrum should bare some characteristic features (§2.3.2.3), unique and universal for dark matter annihilation or decay, whose detection would represent the 'smoking gun' of indirect searches. For WIMP-type dark matter, emission of photons is expected in the gamma-ray energy range. More details on the gamma-ray-based searches are provided in the following Sections.

Neutrinos, like photons, are not deflected by magnetic fields and thus can be traced back to their source of origin. Their neutralness, however, is at the same time the main obstacle for their detection: neutrinos do not couple with electromagnetic sector and their interactions with matter are weak. Thus, it is difficult to recognize rare neutrino interaction with nucleons in the Earth from those of atmospheric neutrinos producing muons above the horizon. In order to better control the background, neutrino telescopes are usually placed deep under ground (like Super-Kamiokande [80]), or under water (ANTARES [81]) or ice (IceCube [82]).

Neutrinos are expected to produce in large amounts in dark matter annihilation or decay. If primary products from of these processes are heavy leptons, their consequent decay into lighter ones will be accompanied by neutrino emission. If the primary products are gauge bosons, neutrinos are also produced in they decay into lepton ($W^{\pm}, Z$) and quark pairs (Z).

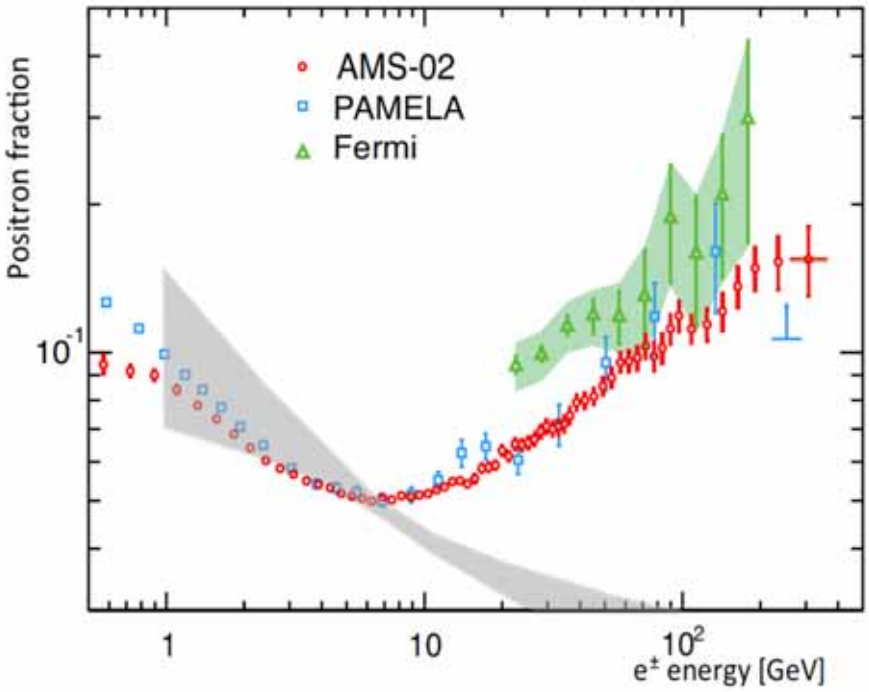

Figure 2.3: The positron fraction in high-energy cosmic rays. The measurement from the AMS extends over a wider energy range and has much lower uncertainty than the earlier measurements from the PAMELA [85] and Fermi-LAT satellites [86]. The AMS measurement confirms an excess in the high-energy positron fraction, above what is expected from positrons produced in cosmic-ray interactions. (The grey band indicates the expected range in the positron fraction, which is based on calculations in [87]). Taken from [88].

In addition, if Z boson is among the primaries, it can decay directly into a pair of neutrinos. Direct annihilation into a neutrino pair is possible as well.

Neutrinos can also be produced by dark matter that gets captured by deep gravitational wells, such as the Sun, and that annihilates at significant rate if gathered in great concentrations. Detection of an neutrino excess from the direction of the Sun could indicate dark matter origin [83]. Same reasoning can be applied to dark matter captured by the Earth, but detection prospects are much weaker that in the case of the Sun.

The currently best limits on dark matter annihilation cross section from neutrino searches come from IceCube observation of the Galactic Center [84]: for $m_\chi \sim 200$ GeV, $\langle \sigma_{\text{ann}} v \rangle$ for direct annihilation into neutrinos is $\sim 10^{-23} \text{cm}^3\text{s}^{-1}$, while the lower limit on lifetime of the dark matter particle in the decaying scenario is $\tau \sim 10^{22}$ s.

Charged cosmic rays diffuse through galactic magnetic field from their production site to the Solar System, so, unlike photons and neutrinos, they can not be traced back to the place of their origin. It therefore makes sense to search for dark matter signal as an anomalous component in cosmic rays in the entire Galactic Halo, instead of focusing on particular single region.

Given that dark matter annihilation or decay results in creation of the same amounts of matter and antimatter, latter products are especially attractive from the point of indirect searches, since for them the astrophysical background is much lower. In this sense, distributions of positrons and antiprotons are very promising places to look for deviations from

conventional flux. In the last years, there have been a number of reports on unusual features in the electron-positron spectrum at high energies. The PAMELA experiment [89] found an interesting rise in the positron fraction ($e^+/(e^+ + e^-)$) at energies up to 100 GeV [85], a behaviour in contradiction to the expected decline predicted by models for cosmic-ray propagation [87] (Figure 2.3). This result was corroborated by measurements of the all-electron ($e^+ + e^-$) spectrum by Fermi-LAT (§2.3.4.1) for energies up to 200 GeV [86]. Latest news on this subject come from the high precision results of AMS-02 [90] that extend up to 350 GeV [88]: these measurements confirm the rise for energies up to ∼250 GeV, above which there is a hint of spectrum flattening (this is in disagreement with Fermi-LAT findings, Figure 2.3). However, none of the numerous proposed theories involving dark matter [91, 92] can successfully justify the observed excess; on the other hand, a more conventional explanation, with particles being accelerated by the nearby pulsars [93], is much more plausible. Another stable product from dark matter annihilation or decay are the antiprotons. Antiprotons may be created from decay of primary products, like quarks and bosons; however, current measurements of the antiproton flux show no deviation from the predictions for local astrophysical sources [94]. Antideutrinos are another possible messengers: if of dark matter origin, their spectrum should be much flatter than the standard astrophysical component.

For more detailed description on indirect searches with cosmic antimatter, refer to e.g. [95] and references within.

2.3.2 Photon Flux from Dark Matter

As already mentioned, dark matter annihilation or decay into SM particles is expected to produce gamma-ray signal with some distinctive features that can be used to obtain information about both the dark matter nature and its spatial distribution. Detection of such signatures would aid the disentanglement of dark matter signal from the astrophysical backgrounds, and potentially allow an unambiguous identification of the dark matter particle. This Section gives brief introduction on calculation of the expected photon flux on Earth, followed by modeling of dark matter distribution and details on characteristic spectral shapes resulting from different annihilation/decay final states.

Dark Matter Annihilation The most general form of the expected differential dark matter photon flux is given as a product of two terms:

$$\frac{d\Phi(\Delta\Omega)}{dE} = \frac{d\Phi^{\mathrm{PP}}}{dE} \times J(\Delta\Omega). \tag{2.1}$$

The particle physic term, $d\Phi^{\mathrm{PP}}/dE$, solely depends on the chosen dark matter model – it is completely determined for the given theoretical framework and its value is the same for all sources. The astrophysical term, $J(\Delta\Omega)$, on the other hand, depends on the observed source (its distance and geometry), the dark matter distribution at the source region and the properties of the instrument.

In the case of annihilating dark matter, the first term takes form:

$$\frac{d\Phi^{\mathrm{PP}}}{dE} = \frac{1}{4\pi} \frac{\langle \sigma_{\mathrm{ann}} v \rangle}{2m_\chi^2} \frac{dN}{dE}, \tag{2.2}$$

where $\langle \sigma_{\mathrm{ann}} v \rangle$ is the thermally averaged product of the total annihilation cross-section and the velocity of the dark matter particles; dN/dE is the differential gamma-ray yield per anni-

hilation, summed over all the n possible channels that produce photons, where each channel has its particular branching ratio Br:

$$\frac{dN}{dE} = \sum_{i=1}^{n} \mathrm{Br}_i \frac{dN_i}{dE}. \tag{2.3}$$

The spectral information (i.e. the spectral shape) is described by the dN/dE contribution. In order to account for the effects the properties of the instrument have on the *emitted* spectral distribution (which will not be the same as the *detected* one), the above expression has to be convoluted with the response function of the detector (§3.3.7.1).

As for the astrophysical factor J_{ann}, it is given as the integral over the squared radial dark matter density profile $\rho(r)$ over the line of sight l and the solid angle $\Delta\Omega$:

$$J_{\mathrm{ann}}(\Delta\Omega) = \int_{\Delta\Omega}\int_{los} \rho^2(r(l,\Omega))dld\Omega. \tag{2.4}$$

In practice, the correct expression for J accounts for the finite angular resolution of the instrument, by convoluting the above expression with the angular resolution of the detector:

$$J_{\mathrm{ann}}(\psi,\Delta\Omega) = \int_{\Delta\Omega}\int \frac{d\Sigma(\psi'-\psi)}{d\Omega'}d\Omega' \int_{los} \rho^2(r(l,\psi'))dl, \tag{2.5}$$

where $d\Sigma(\psi'-\psi)/d\Omega'$ is the gamma-ray PSF of the instrument (§3.3.7.1).

Finally, the integral flux from dark matter annihilation (above a certain energy E_0) reads:

$$\Phi(>E_0,\Delta\Omega) = \frac{1}{4\pi}\frac{\langle\sigma_{\mathrm{ann}}v\rangle}{2m_\chi^2}\int_{E_0}^{m_\chi}\frac{dN}{dE}dE\int_{\Delta\Omega}\int_{los}\rho^2(r(l,\Omega))dld\Omega. \tag{2.6}$$

Dark Matter Decay Assuming that dark matter particles are not completely stable (that is, their stability is valid on cosmological scale), a small fraction of them could be decaying at the present epoch into detectable final states. Like in the case of annihilation, the expected gamma-ray flux has the general form given by the eq.(2.1); however, the particle physics and the astrophysical term are different. The particle physics term depends on the lifetime of the particle τ_χ:

$$\frac{d\Phi^{\mathrm{PP}}}{dE} = \frac{1}{4\pi}\frac{1}{m_\chi\tau_\chi}\frac{dN}{dE}, \tag{2.7}$$

while the astrophysical term scales linearly with the dark matter density:

$$J_{\mathrm{dec}}(\Delta\Omega) = \int_{\Delta\Omega}\int_{los}\rho(r(l,\Omega))dld\Omega. \tag{2.8}$$

The total flux within a solid angle $\Delta\Omega$ is then calculated in a manner similar to eq.(2.6).

2.3.2.1 Dark Matter Density Profile

In the above described calculations of the photon flux, the greatest uncertainty arises from the poorly determined dark matter density distribution. This distribution is not directly observable and can only be constrained by N-body simulations and stellar and gas kinematics.

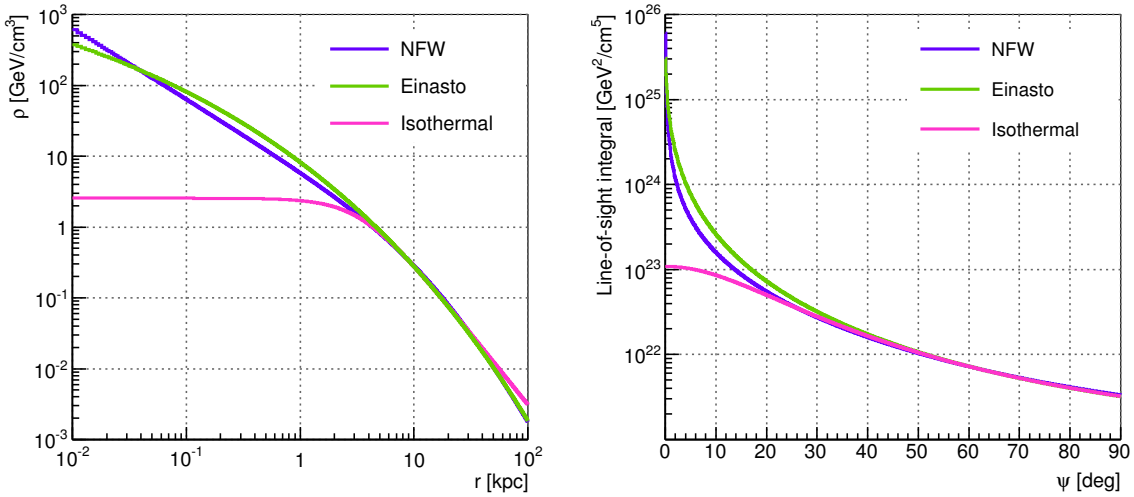

Figure 2.4: Left: comparison of the radial density for NFW (violet), Einasto (green) and isothermal (pink) profiles. **Right**: line-of-sight integral (J) as a function of the angle ψ from the center of the halo shown for the density on the left figure. The calculations assume parameter values provided in [96].

The density profile of a dark matter halo is determined by a number of astrophysical processes, such as the initial gravitational relaxation of dark matter, its interaction with baryons, and potentially the weak interactions of WIMPs with themselves and other particles. And while inclusion of all of these factors in the N-body simulations with sufficiently high resolution is a notoriously difficult task, some "simpler" configurations have already provided abundant information that can be used for studies and modeling of the dark matter halo.

The N-body simulations recreating the hierarchical formation of CDM halos thorough gravitational interactions have shown that the spherically-averaged (smoothed) dark matter halo distribution is well described by a universal profile. Navarro, Frank and White [97] have made a fit to this profile, applicable over 20 decades in mass range:

$$\rho_{\mathrm{NFW}}(r) = \rho_s \left(\frac{r}{r_s}\right)^{-1} \left(1+\frac{r}{r_s}\right)^{-2}, \tag{2.9}$$

where r_s is the scale radius and ρ_s is the characteristic density. For $r \ll r_s$, the NFW profile has a central power-law cusp with $\rho_{\mathrm{NFW}} \propto r^{-1}$, and at large radii ($r \gg r_s$) it declines as $\rho_{\mathrm{NFW}} \propto r^{-3}$ (Figure 2.4). The J factor is primarily sensitive to the behaviour of the density profile in the cusp region; however, the current CDM simulations have limited capability to model the dark matter distribution on such scales. The recent sample of Aquarius simulations [98], which resolve down to less than 1% of the halo viral radius for $\sim 10^{12}$ $\mathrm{M}_\odot$ halos, shows that the asymptotic slope, predicted by the NFW, is not yet achieved, and that the profile becomes more and more shallow towards the center of the halo. These results favor the Einasto profile [99] as a better fit:

$$\rho_{\mathrm{Ein}}(r) = \rho_s \exp\left[-\frac{2}{\alpha}\left(\left(\frac{r}{r_s}\right)^{\alpha} - 1\right)\right], \tag{2.10}$$

where $\alpha \simeq 0.17$ for Milky Way-mass halos. The slope of the Einasto fit asymptotically approaches zero toward the center, producing a finite density at $r = 0$ (unlike the divergent central density of NFW). Still, the NFW and Einasto profiles are similar over the intermediate scales ($r \sim r_s$, Figure 2.4).

However, the predicted central cusp is not observed in many galaxies. In particular, observations of low surface brightness galaxies indicate inner slopes that are significantly shallower than expected. The isothermal profile [100], in contrast to NFW and Einasto profiles, has a central cored density distribution (Figure 2.4):

$$\rho_{\rm iso} = \rho_s \left[1 + \left(\frac{r}{r_s} \right)^2 \right]^{-1}. \tag{2.11}$$

This discrepancy between the simulations and observations, i.e. cusped versus cored central density, is an issue that is yet to be understood. It may be an indication of some processes that have modified the dark matter distribution in the central region, like interactions with baryons, or WIMPs self-interactions [101]. High-resolution simulations which, constrained and informed by observations, describe and model the dark matter interactions with baryons in cosmological context are needed to fully resolve the core/cusp problem.

The choice of the density profile has direct implications on the expected photon flux, in particular in the case of dark matter annihilation (eq.(2.6)): as J factor is proportional to the density squared, cored central distributions will yield lower fluxes than the cusped ones. This effect is less pronounced for the decaying dark matter, as in that case the flux scales linearly with $\rho(r)$.

Substructures Another factor that may influence the expected photon flux are the substructures: a generic prediction of CDM simulations is that dark matter distribution is not smooth, but rich in density fluctuations with spatial scales smaller than r_s. These substructures are predicted to be gravitationally isolated; their abundance at $z = 0$ depends on the fraction that survives tidal disruptions during the hierarchical mergers and accretion processes [102].

Presence of substructures may significantly enhance the dark matter flux (especially in the annihilation case), compared to the expectations for smooth halo. This contribution is quantified by a boost factor B, such that $J = J_s(1+B)$, where J_s is the line-of-sight integral over the smooth halo distribution. N-body simulations can set a lower limit on the B value by summing the annihilation luminosity from numerically resolved substructures; high resolution simulations of Milky Way-mass halos have found a factor two enhancement [103]. The unresolved substructures could contribute to the value of B more significantly: depending on the halo mass, the boost factor may be in the range $B \simeq 10^2 - 10^3$ for galaxy clusters, $B \sim 10^2$ for Milky Way-mass galaxies and only a factor of few for dSphs (see, e.g. [104] and references within). These estimates, however, heavily rely on the extrapolation of the simulated halo mass spectrum, and thus are subjected to high uncertainties and should be revised once the simulations reach better mass resolution.

2.3.2.2 Annihilation Cross Section and Decay Time

Next, in order to calculate the gamma-ray flux from dark matter annihilation or decay into SM particles, it is necessary to evaluate the $\Phi^{\rm PP}(E)$ contribution. First, the dark matter particle has to be qualified as scalar (of spin 0) or fermion (of spin 1/2); in the case of the latter, it is further identified as either Dirac (has antiparticle) or Majorana (is its own antiparticle). From there, the interaction operators can be constructed between the dark matter and SM particles (for a review, see e.g. [105]), which then leads to calculation of the annihilation cross section or decay time.

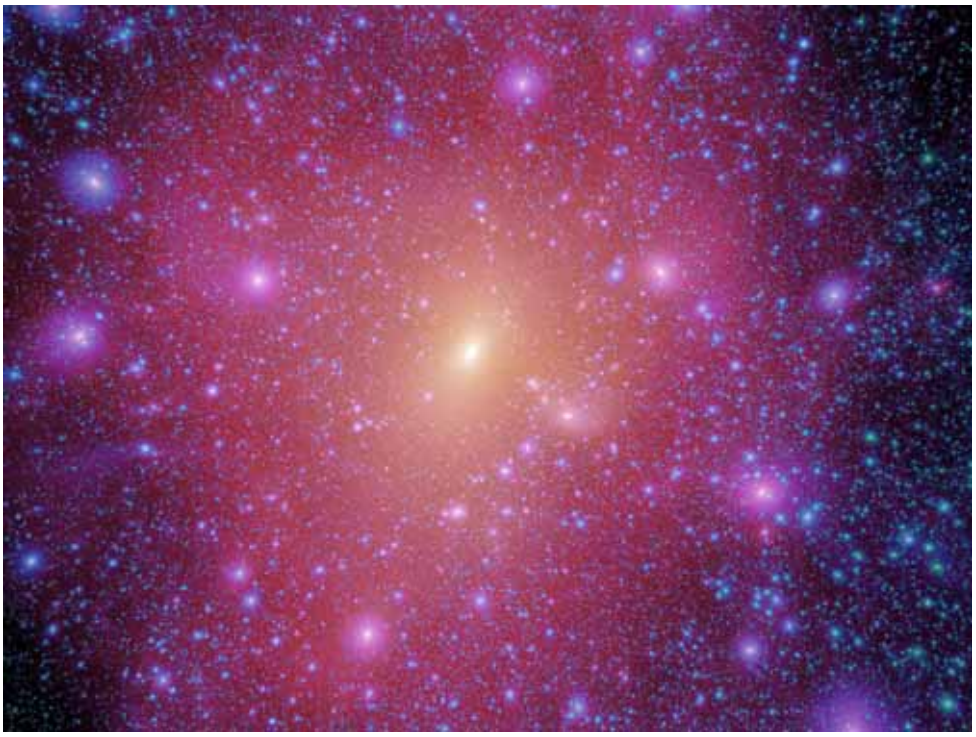

Figure 2.5: Projected dark matter density in high resolution halo at $z = 0$ from Aquarius simulation. The halo is resolved with ~ 1.5 billion particles of 1712 $M_\odot$ each. It contains $\sim$300000 resolved substructures, the largest of which are visible as bright spots on the image. Taken from [102].

The natural value of $\langle \sigma_{\text{ann}} v \rangle \simeq 3 \times 10^{-26} \text{cm}^3 \text{s}^{-1}$ is determined by the requirement to produce the observed dark matter relic abundance during the dark matter freeze-out process in the early Universe [106]. For WIMPs that annihilate at the present time, predominantly through the s-wave processes, $\langle \sigma_{\text{ann}} v \rangle$ is velocity independent and has its natural value. This is the case for dark matter annihilation with pseudoscalar and vector interactions that will be mentioned later. On the other hand, if the cross section depends on the velocity, the $\langle \sigma_{\text{ann}} v \rangle$ would be lower today than in the early Universe, as the typical velocity in a halo at the present is $v/c \simeq 10^{-3}$, opposed to $v/c \simeq 0.1$ at the time of WIMP freeze-out. Some exceptions exist, though: the Sommerfeld enhancement, a non-relativistic quantum mechanical effect, can boost the $\langle \sigma_{\text{ann}} v \rangle$ value, by a factor $\sim 10 - 100$, due to the resonance annihilation for certain, heavy dark matter masses, assuming that the WIMP velocity is small enough [107].

Regarding the decay time, its value depends on the considered model and dark matter particle properties, but, as already mentioned, it has to be longer that the current age of the Universe. For example, in a SUSY extension of the SM with small R-parity violation and gravitino as LSP, decay time into photon and neutrino is calculated to be of order $\tau_{\psi_{3/2} \to \gamma\nu} \simeq 3.8 \times 10^{27}$ s [108].

2.3.2.3 The Photon Spectrum

Spectral distribution of photons emitted in dark matter annihilation or decay is one the decisive factors for detectability of a given model. Characteristic spectral features, that can not be imitated by the conventional mechanisms of gamma-ray production, can be used to distin-

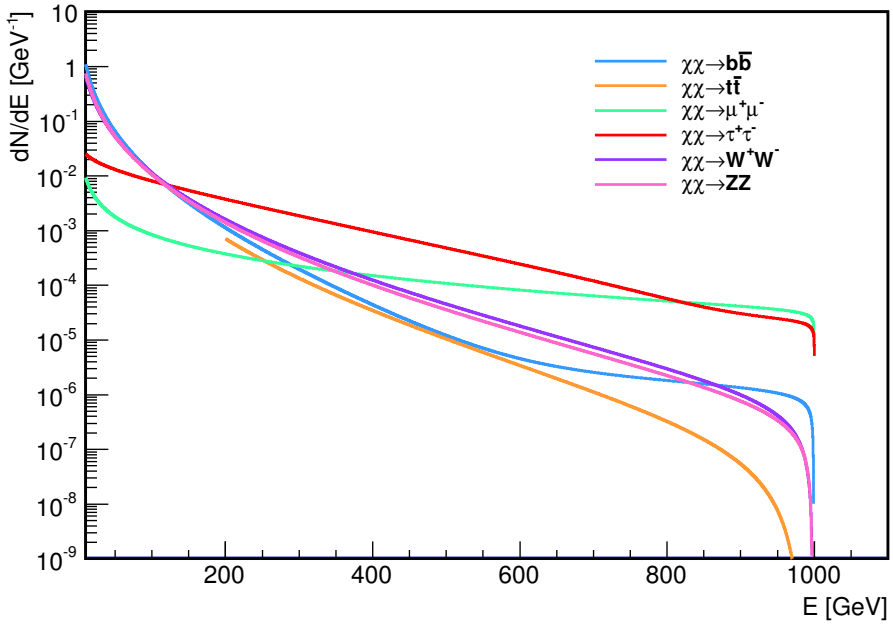

Figure 2.6: Gamma-ray yield from WIMP annihilation into different channels. The assumed dark matter particle mass is $m_\chi = 1$ TeV. When applicable, the FSR is included in the spectrum. For $t\bar{t}$ channel, photon production is assumed only above 200 GeV. Spectral distributions are obtained from the fits provided in [109].

guish the signal of dark matter origin from the astrophysical background, while at the same time revealing information on the dark matter nature itself. The spectral distribution dN/dE is fixed for a chosen model and universal for all dark matter emitters. As given by eq.(2.3), dN/dE is the sum over different final-state contributions; depending on the branching ratio of each of these channels, different features will be more or less pronounced in the spectrum.

Some of the main final-state contributions to dN/dE from dark matter annihilation/decay are listed bellow. In this work, in order to keep the analysis as model-independent as possible, each of these channels is assigned a branching ratio of Br = 100%.

Secondary photons The main photon production channel is through the decay of neutral pions, created in the hadronization of fermion and gauge boson final states. The resulting, *secondary* photons, show a continuous and relatively featureless spectrum with a rather soft cutoff at the kinematical limit $E = m_\chi$ (Figure 2.6). Spectral distributions are very similar for almost all channels and depend very weakly on m_χ. The number of photons produced this way peaks for energies approximately an order of magnitude below m_χ. Still, a convincing claim of dark matter detection based exclusively on this signal, which would show up as a broad bump-like excess over the (often) poorly understood astrophysical background, may be considered rather challenging.

Gamma-ray Line Direct production of gamma-rays through dark matter annihilation (or decay) is a highly suppressed process, as dark matter particles do not couple to photons directly. The branching ratio for such one-loop interactions is completely negligible compared to annihilation to fermions or bosons. Nevertheless, if such process was to occur, the result would be a sharp, monochromatic line-like feature in the photon spectrum – a feature whose detection would represent the *smoking gun* for dark matter indirect searches.

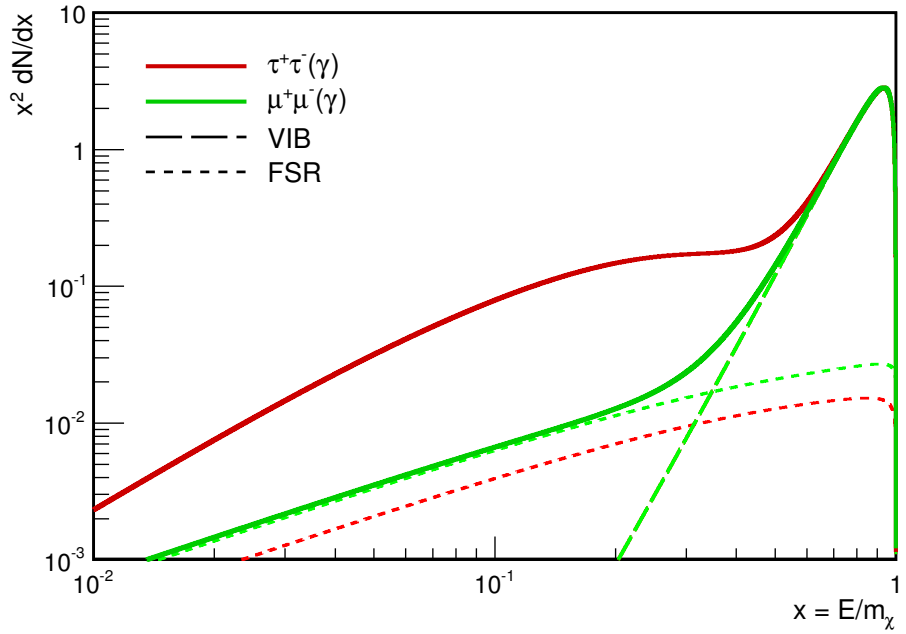

Figure 2.7: Gamma-ray spectrum for different final state fermions, assuming $m_\chi = 100$ GeV and a mass-splitting of $\mu = 1.1$. Solid lines show the full contribution from three-body final states, including the VIB photons close to $x = 1$; short-dashed lines depict the FSR contribution, while the long-dashed ones represent the VIB emission.

Gamma-ray lines are created in direct WIMP annihilation into two photons, $\chi\chi \to \gamma\gamma$, or into photon and a boson, $\chi\chi \to \gamma(Z,h)$; such lines would be located at energies $E = m_\chi$ and $E = m_\chi + (m_{(Z,h)}/m_\chi)^2$, respectively. The $\langle\sigma_{\text{ann}}v\rangle$ needed in these cases, however, is orders of magnitude smaller than for the three-loop channels contributing to the continuum component of the spectrum: $\langle\sigma_{\text{ann}}v\rangle \sim 10^{-29}$ cm^3 s^{-1}. As for the dark matter decay, line production is also a possibility ($\chi \to \gamma\nu$, with $E = m_\chi/2$). It is needed, however, for dark matter particle to have a lifetime τ_χ of 10^{27} s or longer [108].

Internal Bremsstrahlung Whenever dark matter annihilates into pairs of charged particles, the process is accompanied by the internal bremsstrahlung (IB), i.e. emission of an additional photon in the final state. Depending on whether the photon is emitted from the external legs or from virtual charged particles, the two contributions are distinguished as the final state radiation (FSR) and virtual internal bremsstrahlung (VIB).

The FSR spectral distribution is broad, model-independent, and unlike the previously mentioned spectra from secondary photons, it peaks near m_χ and ends with sharp cutoff (Figure 2.7). And although production of FSR photons is suppressed by a factor α ($\approx$1/137) relative to the continuum emission [110], this contribution is the dominant radiation for some channels, like $\chi\chi \to \mu^+\mu^-$, as well as the Kaluza-Klein dark matter.

As for the VIB process, it occurs when the helicity suppression is lifted from the s-wave contribution to σ_{ann} [111, 112]. If dark matter is Majorana (or scalar) particle annihilating into fermion and antifermion ($\chi\chi \to f\bar{f}$), the $\langle\sigma_{\text{ann}}v\rangle$ is quite small, as the s-wave contribution is suppressed by the m_f^2/m_χ^2 term (m_f is the mass of the daughter fermion), while the p-wave contribution is suppressed by the v^2 of the galactic dark matter particles today ($v \sim 10^{-3}$). However, emission of a vector boson ($\chi\chi \to f\bar{f}V$) lifts the suppression of the s-

wave contribution. The resulting 3-body $\sigma_{\rm ann}$ is, unlike FSR, model-dependent: its value is determined by m_χ and the mass splitting parameter μ between the dark matter particle and the t-channel mediator η ($\mu \equiv m_\eta^2/m_\chi^2$). For small values of μ, the VIB contribution becomes very significant, and $(\sigma v)_{\chi\chi\to f\bar{f}\gamma}$ considerably larger than $(\sigma v)_{\chi\chi\to f\bar{f}}$. Furthermore, the VIB spectral shape has a characteristic bump-like feature close to the cutoff ($E \simeq m_\chi$), that, depending on the model, can be quite pronounced (Figure 2.7).

Gamma-ray Boxes If dark matter annihilates into a pair of intermediate, neutral scalar particles ϕ, that in turn decay into a pair of photons, the result from this 1-step cascade is a box-shaped spectrum [113]. Width of such feature is completely determined by the mass of the scalar m_ϕ and m_χ: $\Delta E = \sqrt{m_\chi^2 - m_\phi^2}$ – the smaller the mass difference, the more line-like is the resulting spectrum. On the other hand, when $m_\chi/m_\phi \to 0$, the box-like feature becomes wider in energy and dimmer in amplitude; still, the spectral platou is of non-negligible intensity, it can extend to high energies and its flatness may distinguish it from the exponentially-falling astrophysical backgrounds.

As for the case of dark matter decay, the same considerations apply, but instead of four, two photons are produced: $\chi \to \phi \to \gamma\gamma$.

2.3.3 Review of the Observational Targets

When choosing a target source for indirect dark matter searches, the selection criteria should go in direction of increasing the value of the astrophysical factor J. Therefore, following the prescription from eq.(2.4) and eq.(2.8), suitable target should be a region with high dark matter density, while at the same time its distance from the observer is as (relatively) small as possible. The M/L of the system and the possible background must be regarded as well, since the large baryonic content may cause major drawbacks for dark matter searches: baryonic matter may disrupt the dark matter profile through the dynamical fraction, smoothing the central high dark matter density, and thus reducing the expected flux. Furthermore, baryons may act as strong background to the dark matter signal, as they can produce photons via conventional astrophysical processes in a far more abundant fashion than through the dark matter annihilation or decay.

In practice, a compromise between these selection criteria must be reached. The best dark matter candidate sources proposed so far include the Galactic Center and the Galactic Halo, the dark halo substructures, dSph galaxies and galaxy clusters. This Section briefly reviews their strengths and weaknesses as potential targets for indirect dark matter searches.

The Galactic Center and Galactic Halo The Galactic Center is the closest ($\sim$8.5 pc) astrophysical region highly dominated by dark matter. Theoretical arguments and numerical simulations predict a central dark matter cusp, that would strongly enhance the annihilation signal. However, the Galactic Center is a densely populated region, with large background from conventional sources present at all wavelengths. Furthermore, the great baryonic content in the innermost parts of the Galaxy and the presence of a black hole in its center inevitably lead to the modification of the dark matter profile, making the characterization of the density distribution highly uncertain [114].

Observations of the Galactic Center at the very high energy (VHE) range, where WIMP signatures are expected, have already been carried out by several Cherenkov telescopes (see, e.g. [115, 116]). A non-variable signal was confirmed, with a hard power law spectrum ex-

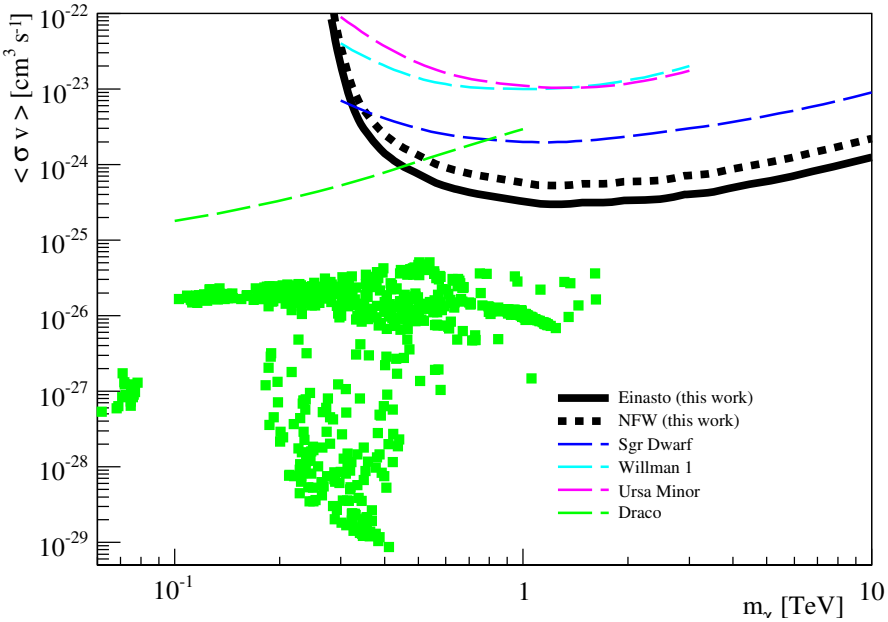

Figure 2.8: Upper limits at the 95% c.l. over the $\langle\sigma_{\text{ann}}v\rangle$ as a function of m_χ from H.E.S.S. observations of the Galactic Halo, considering a fixed dark matter model and Einasto and NFW density profiles. The best sensitivity is achieved at $m_\chi \sim 1$ TeV. For comparison, limits derived from observations of dSph galaxies are also shown. Green points represent different simulated mSUGRA models. Taken from [118].

tending up to 20 TeV, which disfavours its dark matter origin. In addition, the studies of the spatial extension of the source do not agree with the dark matter profile, and the detected flux is several orders of magnitude above the predictions for the pure dark matter emission. More likely origin of this signal were radiations from conventional counterparts in the vicinity of the Galactic Center (the super-massive black hole Sag A*, the supernova remnant Sag A East and the pulsar with nebulae G359.95-0.04), which completely hide the potential dark matter signaturs.

A way to overcome the background contamination is by directing the search to regions which are outside the Galactic plane (and hence unpolluted by astrophysical sources), but, for the annihilation case, still close enough to the Galactic Center to profit from high dark matter density. Such approach has been applied in the observations by the High Energy Spectroscopic System (H.E.S.S.) Telescopes [117], and it provided the currently best limits on the $\langle\sigma_{\text{ann}}v\rangle$ value in the given energy range (Figure 2.8) [118]. On the other hand, if studying the dark matter decay, search should be more effective if carried out in direction of poles, i.e. at higher latitudes [108].

In the past year a hint of a monochromatic gamma-ray signal at around 130 GeV was claimed in the Fermi-LAT data of the Galactic Center region [112, 119]. In numerous interpretations that followed, the signal has been attributed to the VIB contribution, assuming $m_\chi = 149 \pm 4^{+8}_{-15}$ GeV [112]; to $\gamma\gamma$ line, for $m_\chi = 129.8 \pm 2.4^{+7}_{-13}$ GeV [119], and to gamma-ray boxes from axion particles, for $m_\chi = 250$ GeV and $m_\phi = 249.75$ GeV [120]. The decaying dark matter explanations have been postulated as well [121]. The non-dark matter origin of the observed excess is also considered [122]. Still, till date, the Fermi Collaboration has not confirmed the presence of the signal in question [123]. New information is pending the Pass 8 analysis.

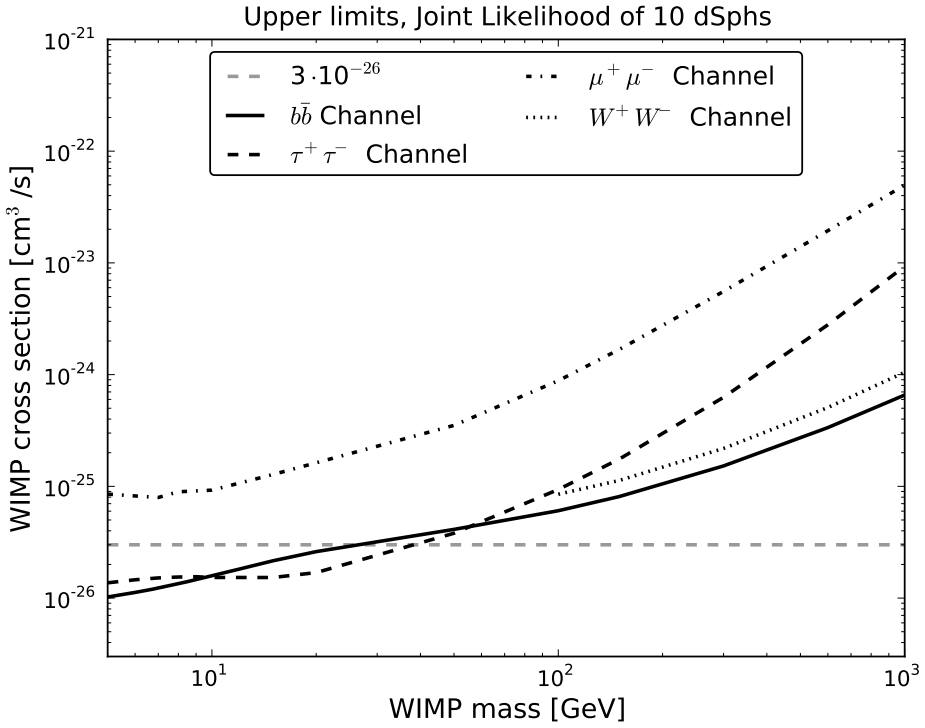

Figure 2.9: Limits on $\langle \sigma_{\text{ann}} v \rangle$ as a function of m_χ for several different final state channels (each with Br = 100%), from the Fermi-LAT joint analysis of data from 10 dSph galaxies. Taken from [125].

Dark Matter Subhalos According to the cosmological N-body simulations, evolution of dark matter distribution in the Universe is marked by hierarchical clustering, that results in formation of dark matter clumps (§2.3.2.1). Larger of these clumps might gather enough mass to attract baryons and commence star formation, while the smaller ones do not have enough gravitational pull and therefore remain completely dark. As a result, dark matter halos are not expected to be smooth, but rich in inner substractures – so-called dark matter subhalos (Figure 2.5). While invisible in the context of conventional emission mechanisms, these subhalos may shine in the energy window where dark matter signal is expected. In the framework of a GeV-mass WIMP, these objects could be gamma-ray emitters. Complete lack of astrophysical background makes the subhalos excellent targets for indirect searches; furthermore, although small, a fraction of them could be relatively nearby. The drawback are their unknown locations; however, subhalos may appear in surveys of gamma-ray sky.

Indeed, Fermi-LAT (§2.3.4.1) has so far detected hundreds of so-called *Unassociated Fermi Objects* (UFOs) – sources that radiate at very-high energies but are without known counterpart at other wavelengths. Some of these UFOs are potential candidates for dark matter subhalos – if their emission is not variable, if their spectra is hard and power-law like (as the dark matter features are predicted at energies above the Fermi range). Furthermore, suitable observational targets are outside the Galactic plaine, as the abundance of astrophysical sources there not only adds large background but also makes potential identification of an object more complicated.

Complementary observations of several subhalo-candidate UFOs have been performed by Cherenkov Telescopes [124] however, no detection has been reported so far.

Dwarf Spheroidal Galaxies Currently the most constraining limits from dSph are set by the Fermi-LAT joinet analysis of observations of 10 dwarf dSph galaxies orbiting the Milky Way are the most dark matter-dominated objects in the Universe known so far [126]. With M/L of order of 100 or even 1000 $M_\odot/L_\odot$, their relative closeness (up to $\sim$ 150 kpc distance from Earth), and almost non-existent gamma-ray background (as there is no gas and no recent star formation), these systems are considered to be excellent targets for indirect dark matter searches. Furthermore, as baryons are the subdominant component in a dSph, and are not expected to significantly alter the dark matter density profile, studies of their stellar kinematics can be used to set relatively robust constraints on the values of the astrophysical factor J [127].

Currently the most constraining limits from dSph are set by the Fermi-LAT joined analysis of observations of 10 dwarf galaxies [125], for m_χ up to 1 TeV (Figure 2.9). As this work presents the results from indirect search in a dSph galaxy, more complete motivation for these objects as good dark matter targets, as well as other competitive results are presented in Chapter 5.

Galaxy Clusters Galaxy clusters are the largest known gravitationally bound systems, with radii of several Mpc and masses of $\sim (10^{14} - 10^{15})$ $M_\odot$. In the hierarchical formation of large scale structures (§1.2.3), these objects represent the top stage as they were the last to form. Galaxy clusters are among the most dark matter dominated object - more than 80% of their total mass is dark, while the remaining percentage is divided among galaxies ($\sim$ 5%) and gas ($\sim$ 15%). High dark matter content makes them attractive targets for indirect searches [128], with significant astrophysical factor values that can be further increased from the presence of substructures (§2.3.2.1) – the boost can be of order of 100-1000 [129]. However, the role of galaxy clusters as good dark matter targets is weakened by the huge background of astrophysical origin, dominantly from the Active Galactic Nuclei (AGN) galaxy population, as well as by the secondary component of cosmic ray-induced radiation.

So far, gamma-ray observations of galaxy clusters Virgo, Coma, Perseus and Fornax have not returned any positive signal of dark matter emission [130, 131]. Campaigns at other wavelengths have not claimed any dark matter hints either [132].

2.3.4 Indirect Search with Gamma-ray Experiments

Annihilation and decay of dark matter particles, whose mass is in a tens of GeV-few TeV range, would result in a production of photons of energies in the high (30 MeV-100 GeV) and very high (100 GeV-30 TeV) subranges of the gamma-ray domain. Seen how the Earth's atmosphere is opaque for such radiation, gamma-rays can not be directly measured from the ground. Instead, detectors have to be placed outside the atmosphere, on the satellites or ballones. Such approach, however, limits the effective area of the detector, which in turn inhibits the measurements of low fluxes beyond the high energy (HE) range. In order to explore the more energetic gamma-rays, different detection approaches are needed – like the Imaging Air Cherenkov technique. Thanks to this technique, the ground-based telescopes can measure the VHE photons indirectly, through the products of interactions induced by gamma-rays entering the atmosphere.

There are many different kinds of experiments (and approaches) used for direct and indirect detection of gamma-rays. However, as this work is about the VHE dark matter searches with Imaging Air Cherenkov Telescopes (IACTs), their detection technique is described in

more detail. Space-based HE gamma-ray observatories are briefly covered as well, as their energy range (and results) complements those of the IACTs of the current generation.

For more complete review of other gamma-ray detection techniques and instruments, refer to e.g. [133].

2.3.4.1 Gamma-ray Satellites

In the HE range, space-based observatories detect gamma-rays through the process of pair production: when an energetic photon penetrates the detector chamber, it interacts with matter creating an electron-positron pair. By measuring the paths and energies of these new particles, properties of the original gamma-ray are reconstructed. Possible background from charged particles is usually reduced by anti-coincidence system surrounding the whole device.

The first gamma-ray satellite, Explorer 11 [134], was launched in 1961, but it was only a decade latter that the first detailed views of the gamma-ray sky were provided (Cos-B [135] and SAS-2 [136]). The first milestone in the field was set by the Energetic Gamma-Ray Experiment Telescope (EGRET, 1991-2000 [137]), that revealed more than 270 galactic and extragalactic objects radiating at energies between 100 MeV and 10 GeV. The most advanced pair-production gamma-ray detector of the current generation is the Large Area Telescope (LAT) on board the Fermi Gamma-ray Space Telescope (Fermi-GST) [138].

Fermi-GST satellite studies the gamma-ray sky with unprecedented sensitivity and angular resolution (Figure 2.10). Launched in 2008, it resides in low-earth circular orbit, at altitude of 550 km, and operates in the all-sky survey mode (a whole sky sweep is performed every three hours). Some of the scientific objectives the Fermi-GST was designed to fulfill include: understanding of acceleration mechanisms in AGNs, pulsars and supernova remnants; understanding of the gamma-ray diffuse emission; characterization of previously unidentified HE emitters, GRBs and other transient sources; search for dark matter signals and study of other questions of the Fundamental Physics.

The principal scientific component of the Fermi-GST is the already mentioned LAT [139], a pair-conversion instrument able to detect photons in the energy range from 30 MeV up to 300 GeV and with a field of view covering $\sim$20% of the sky. Main background for the Fermi-LAT are the charged cosmic rays, but an anti-coincidence detector, covering its top and lateral sides, allows for a 99.97% background rejection (Figure 2.11). As a result, Fermi-LAT has a very fruitful scientific production. Among other, on yearly bases, a comprehensive list of gamma-ray sources (and their properties) detected by the LAT is published; the last edition, the Fermi-LAT Second Source catalog [140], contains 1873 sources, all of them characterized in the 100 MeV to 100 GeV range. More than 500 of those are sources without a known counterpart at other wavelengths – the so-called UFOs (§2.3.3), some of which are potential dark matter targets. Fermi-LAT is contributing to the indirect dark matter searches in other ways as well: one of its first striking results was the discovery that AGNs are not the main source of the diffuse extragalactic background, as it was assumed, but instead can account for just a small fraction of it ($\sim$16%) [141]. This leaves room for an dark matter-based explanation for the dominant portion of the diffuse background, and there are numerous ongoing efforts in this direction. Thanks to its all-sky view, Fermi-LAT can accumulate great amounts of data from the most promising dark matter targets. For instance, this led to limits on dark matter parameter space from stacked galaxy clusters data [142] and from dSphs data [125], latter of which represents the most constraining result for $m_\chi < 1$ TeV (Figure 2.9). More details of

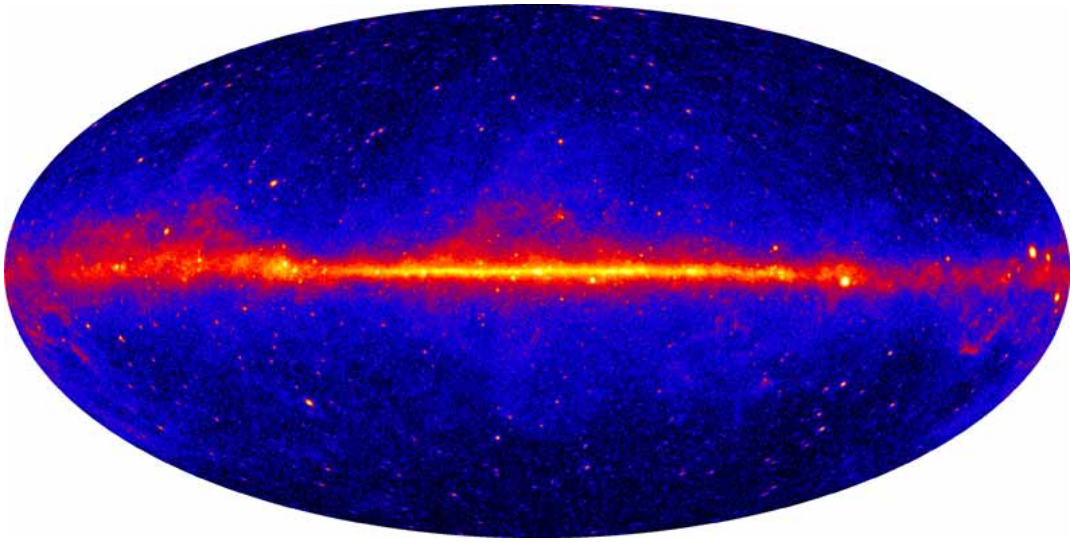

Figure 2.10: Gamma-ray sky as seen by Fermi-GSB. The image is composed from 3 years of data, and it reveals bright emission in the plane of the Milky Way (center), bright pulsars and super-massive black holes. Credit: NASA/DOE/International LAT Team.

Fermi-LAT dark matter searches will be mentioned in Chapter 5.

In addition to the LAT, Fermi-GST also hosts the Gamma-ray Burst Monitor (GBM) [143], designed for detection of bright transient events (particularly gamma-ray bursts (GRBs)), whose sensitivity covers the 150 keV up to 30 MeV energy band. For more details on Fermi satellite and its instruments, refer to [138].

2.3.4.2 Imaging Air Cherenkov Telescopes

When an energetic gamma-ray enters the atmosphere, it interacts with the nuclei of the medium creating an electron-positron pair that inherits its energy. The new particles then loose energy through the emission of bremsstrahlung photons, that in turn create more electron-positron pairs and so on. The process repets itself, with pairs less energetic in every step, until the probability for bremsstrahlung emission becomes smaller than the energy loss through ionization (which becomes the case for critical energy below 83 MeV). This cascade of new particles, originated by the initial gamma-ray, is called the Extended Atmospheric Shower (EAS). It develops over hundreds of meters in width and several kilometers in length, with a maximum of produced particles typically at altitude of 8-12 km. As only photons, electrons and positrons take part in such EAS, it is called the electromagnetic (EM) shower. A large fraction of charged particles of the cascade moves faster than light in the atmosphere, producing Cherenkov radiation – a 'bluish' light emitted within a conic structure, starting at the EAS and ending on the ground with a circle of $\sim$120 m in radius (Figure 2.12). If a parabolic reflector is located within this Cherenkov light pool, it can collect a part of these photons and focus them onto the extremely sensitive camera, composed of high efficiency photodetectors, capable of resolving the image of the shower. From there, by employing the image reconstruction algorithms, the arrival direction and energy of the primary gamma-ray are determined. If two or more of these IACTs record the same event, a stereo image of the shower is obtained, allowing for a better reconstruction of the primary photon.

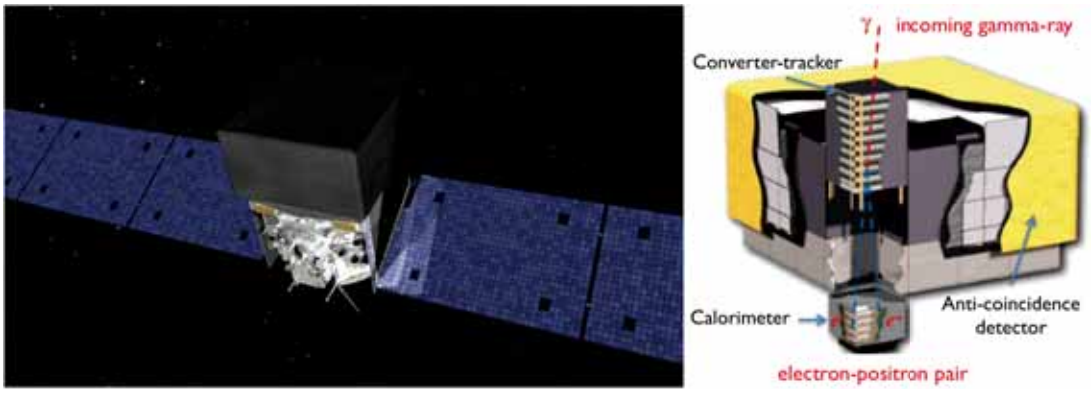

Figure 2.11: Left: simulation still of Fermi-GST in space. **Right**: cutaway of the LAT instrument showing an inside view of one of the towers as an incoming gamma ray interacts producing an electron-positron pair. Credit: LAT Collaboration.

Main issue for this approach is the background. And among different kinds of backgrounds that can affect measurements of gamma-rays are the *hadronic showers* (Figure 2.13). These showers, initiated by cosmic rays, outnumber the EASs created by gamma-rays by order of $\sim$10000. When a cosmic ray hits the atmospheric particle, it generates a shower with neutral pions among its population. These pions immediately decay into pair of gamma-rays, consequently generating secondary EM showers, and the Cherenkov photons that, when recorded, show the hadronic EAS in the camera. The morphology of such image differs from the one of the EM shower (Figure 2.14), and this property is used to discriminate between these two populations of events. Selection algorithms can reject more than 99% of hadron-induced showers.

Another kinds of unwanted events that can trigger an IACT include:

- *electron-induced EM showers*: electrons from the cosmic-ray population can generate purely EM cascades, thus undistinguishable from the gamma-ray induced ones. Consequently, this background cannot be suppressed. On the up side, electron flux (above 100 GeV) is approximately isotropic and much smaller than the gamma-ray flux, which strongly reduced the impact this background has on the observations;

- *diffuse gamma-ray emission*: irreducible and unavoidable background. Strictly speaking, it is not inherent to the method, but to the physics case itself; it is also present in the HE regime. It consists of two components: the extragalactic and the galactic gamma-ray background. Fortunately, neither one is too significant at VHE;

- *muon-induced Cherenkov photons*: muons are habitually produced in hadronic showers, and usually reach the ground before decaying into electron and the corresponding neutrino. Muons do not generate EM showers, but they can radiate Cherenkov photons. If this occurs at moderate altitudes, it mimics the image of a low energy EM shower, while muons reaching the ground near the telescope produce the so-called muon rings in the camera. The incidence of either case is highly suppressed in the stereoscopic observations and by the later analysis;

- *Night-Sky Background* (NSB) *light*: NSB is ambient light, produced by the diffuse scattered light from the stars, the Moon, or human activities in the vicinity of the telescope.

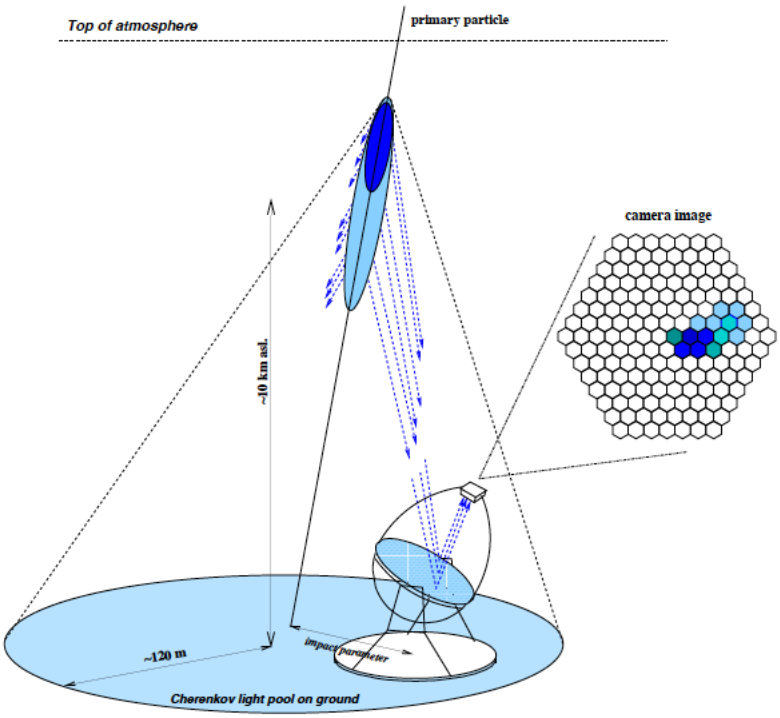

Figure 2.12: Sketch of the principle of the Imaging Air Cherenkov technique, through the formation of the image of an EAS in an IACT pixelized camera. The numbers in the Figure correspond to a typical 1 TeV gamma-ray induced shower.

Fluctuations in NSB are reflected as small images in the camera, in a way that mimics the low energy gamma-ray events. NSB is amplified in the presence of clouds or air pollution;

- *electronic noise*: the camera pixels and the readout chain of the telescope produce an intrinsic electronic noise that must be taken into account in the data analysis. Under certain circumstances, high electronic noise can even trigger the instrument as if it was a low-energy gamma-ray shower. To suppress this kind of background, it is needed to have it well characterized.

The Imaging Air Cherenkov technique is relatively young, compared to other astronomical methods employed in radio and optical telescopes. The first ever detection of a VHE gamma-ray source occurred in 1989 – the Crab Nebula was observed by the pioneering, 10 m diameter Whipple telescope [145]. In the years that followed, the technique was successfully used by other experiments, like HEGRA [146] and CAT [147], increasing the number of detected VHE emitters to ∼10 (mainly nearby AGNs). The current generation of IACTs, represented by MAGIC (Major Atmospheric Gamma-ray Cherenkov Telescope, §3), H.E.S.S. and VERITAS (Very Energetic Radiation Imaging Telescope Array System, [148]), is marked by significant technological improvements with respect to the previous one – this is reflected in a order of magnitude better flux sensitivity and greatly reduced energy threshold. Consequently, the number of detected VHE sources, from both galactic and extragalactic populations, has reached the number of 100. The next step in the field is the construction of the Cherenkov Telescope Array (CTA), observatory of 5-10 times better sensitivity, wider energy

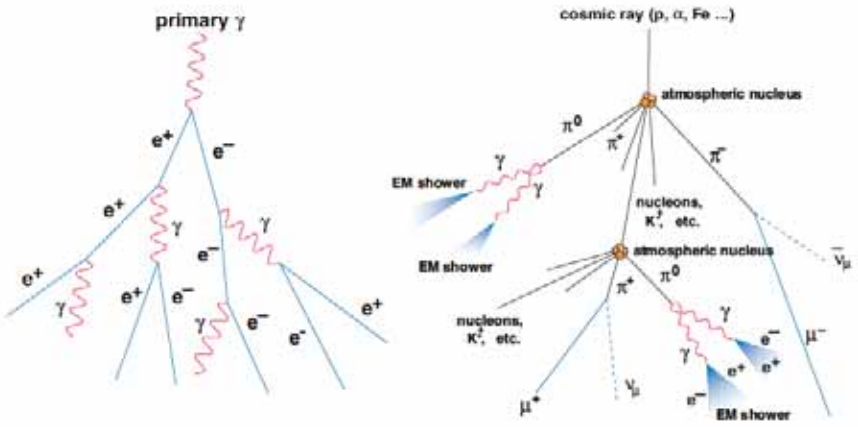

Figure 2.13: Sketch of the structure and the interactions present in an EAS, induced by a γ-ray (**left**) and by a hadron (**right**).

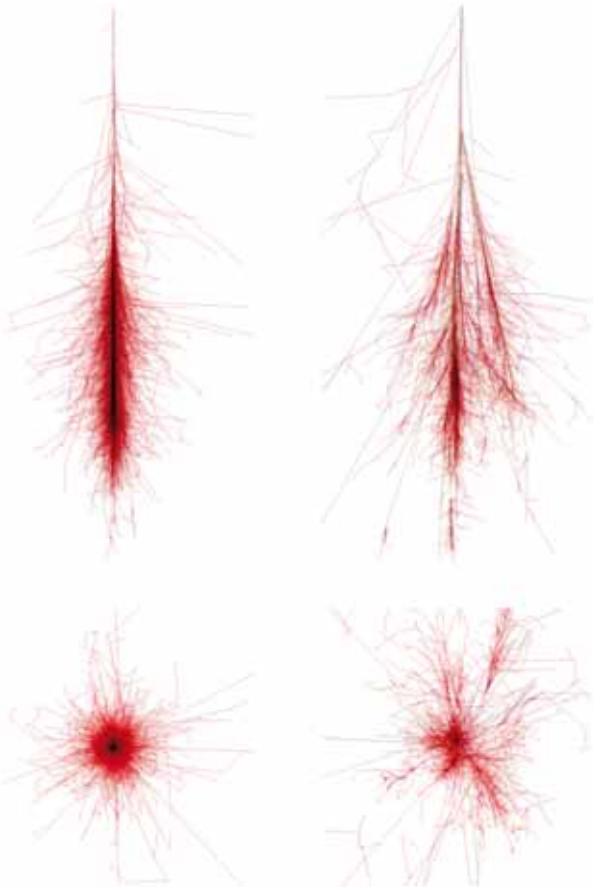

Figure 2.14: Longitudinal (**top**) and lateral (**bottom**) development of an electromagnetic (**left**) and hadronic (**right**) showers with an initial energy of E = 100 GeV simulated with CORSIKA. The longitudinal projection plot has a height of 20 km and a width of 10 km, while the lateral projection plot is 10 km on the side. Taken from [144].

range and increased capability for physics achievements with respect to the current IACTs [149].

Results presented in this work are based on the observations performed with the MAGIC Telescopes. The following Chapter gives details on the technical properties and analysis procedures of MAGIC.

3

The MAGIC Telescopes

The *Florian Goebel* Major Atmospheric Gamma-ray Imaging Cherenkov (MAGIC) Telescopes [150] are located at the Roque de los Muchachos Observatory (28.8° N, 17.9° W; 2200 m a.s.l) in the Canary island of La Palma. The system consists of two, 17 m in diameter telescopes (Figure 3.1), designed to have high sensitivity at low energies and fast response to variable phenomena. The first instrument, MAGIC-I, has been operational since 2004. In 2009, the second telescope, MAGIC-II, was constructed and commissioned, and the system has been successfully running in the stereoscopic mode ever since. During 2011 and 2012, telescopes underwent a major upgrade, aimed at homogenisation and improvement of the performance of both instruments.

This Chapter is devoted to description of technical properties of the MAGIC Telescopes, as well as of the standard observational procedures and of the analysis chain used to process the gathered data.

Figure 3.1: MAGIC Telescopes, Roque de los Muchachos Observatory, La Palma.

3.1 Technical Description

Principles on which MAGIC Telescopes were constructed include large reflector, quick repositioning, prompt and accurate tracking of any source on the sky, fast electronics and highly sensitive sensors able to catch even the faintest flashes of Cherenkov light. As a result, the system can explore the lowest regions of the VHE band, between 30 and 100 GeV, with energy threshold of 50 GeV for the standard observations and corresponding sensitivity of 1.6% of the Crab Nebula flux for a 5σ detection in 50 hours [151]. Moreover, it can move to any position in only tens of seconds, a property that is of great importance when trying to detect extremely short gamma-ray bursts (GRBs). This Section gives some details on technical characteristic of particular subsystems of MAGIC.

3.1.1 Mount, Drive and Mirrors

Mount The mounting structures of MAGIC telescopes, identical for both instruments (Figure 3.2), are made so that they are large, light-weighted and rigid. Large frame is needed for hosting the 17 m reflector, which in turn permits low energy threshold. The three-layer structure is made of light, carbon fiber tubes, that weight about 5.5 tons – one third of the conventional steel-made structure. This permits fast movement. The structure material is also quite resistant to deformations, and as such it prevents significant reflector alterations and worsening of the image quality. Still, some structure bending is inevitable: the camera, located at a focal distance of $\sim$17 m, carried by a single tubular arch and stabilized by thin steel cables anchored to the main dish frame, weights more than half a ton, therefore strain-

Figure 3.2: Frame structure of MAGIC-I with arcs holding the camera (**left**). Elevation motor (**center**). MAGIC-I mirror staggering (**right**).

ing the structure during the telescope tracking. However, the mount deformation is less than 3.5 mm for any orientation of the telescope [152], and its effect on the image can be corrected by an automatic system of mirror re-orientation – Active Mirror Control (AMC).

Drive The mount of the telescope uses Alt-Azimuth drive to track objects during large exposures, like most of the optical telescopes. The continuous observation of a source, without reaching any end position in either altitude or azimuth coordinates, is possible given the wide range of allowed movements: from -90° to +318° in azimuth, and from -70° to +105° in elevation. The motion is powered by two servo-motors for azimutal and one servo-motor for the elevation axis (Figure 3.2), and it is limited by the mechanical end-switches [152]. In speed GRB mode, the telescope can turn 180° in azimuth in ∼20 seconds.

The pointing of the system is constantly cross-checked by three absolute 14-bit shaft-encoders: for 80% of the time, the intrinsic mechanical accuracy of the pointing system is much better than 1' on the sky (1/5 of a pixel diameter). In addition, the pointing precision of the telescope is monitored by a system called Starguider, that allows further, offline correction of misspointing via software. The Starguider system consists of a 4.6° FoV CCD camera installed close to the center of the reflector, that observes the camera of the telescope and determines the exact position of its center by the means of LEDs, placed on the telescope camera frame, and the part of the sky close to the telescope camera (chosen so it contains bright star(s)). Possible offsets are obtained through the comparison of the observed and catalog coordinates of the "guide" stars, thus inferring the actual pointing of the telescope. The reliability of such misspointing measurements depends on the sky visibility (atmospheric conditions), and is estimated using the ratio of the number of observed and expected stars.

Mirrors The 17 m diameter reflector follows a parabolic profile which allows preservation of temporal structure of the Cherenkov photons. The benefit of this shape is two-folded: it reduces the time window required for signal extraction, therefore reducing the integrated noise, and it permits the use of time evolution of the shower as a discrimination parameter between the hadronic and electromagnetic ones (seen how development of the hadronic showers takes longer).

MAGIC-I reflector consists of 956 0.5×0.5 m^2 aluminum honeycomb mirrors of high reflectivity (80%-90%), for a total surface of 239 m^2. Reflector of MAGIC-II is built from 143 full-aluminium and 104 glass-aluminium mirrors, with each panel being of 1 m^2 in size, for a total surface of 247 m^2 [153]. Each mirror can be oriented by the AMC depending on the telescope elevation.

Figure 3.3: (**Left**) Front of the MAGIC-I camera with two types of PMTs visible. (**Right**) Closeup of the MAGIC-II camera.

3.1.2 Camera and Calibration System

When light hits the mirrors of the telescope, it is reflected and focused into the camera. Camera is one of the crucial systems of the telescope, as its performance conditions the sensitivity, energy threshold and signal/background discrimination capacity of the detector. Camera hosts clusters of Photo-Multiplier Tubes (PMTs), that convert photons into electric signal which is then carried to the telescope readout. The key features for PMTs selection were high Quantum Efficiency (QE), fast response and fine pixelization. The photon entrance of each PMT is equipped with a hexagonal light collector (Winston cone), that increases the entry window for each pixel as well as the double-crossing probability of photons with large incidence angles. Furthermore, Winston cone prevents stray light (not coming from the reflector) from entering the PMT. PMTs are double-protected by a transparent Plexiglas window and by two lids that open only during the observations (Figure 3.3). In addition, camera is equipped with an air cooling and heating systems, preventing overheating or moisture accumulation.

Although MAGIC-II was constructed as a mechanical clone of MAGIC-I, camera of the second telescope was built with different structure and using components of improved performance. Its efficiency was cause for an upgrade of the MAGIC-I camera with an exact copy of the MAGIC-II camera, action successfully performed in Summer 2012. However, as the observations analyzed in this work have been recorded with the old MAGIC-I camera, details given below refer to the pre-upgrade systems.

MAGIC-I camera The MAGIC-I camera is of hexagonal shape, and $\sim 3.6^\circ$ FoV (Figure 3.3). It is equipped with 577 PMTs of two types: inner section of the camera (up to 1.2° radius) is made of 397 pixels of 30 mm diameter and 0.1° FoV. This region represents the trigger area. Outer region is composed of the remaining 180 PMTs, of 60 mm diameter and 0.2° FoV. The hemispherical PMT photocatode is coated with a wavelength shifter that decreases the Cherenkov photon frequency and increases the peak QE (up to 28%). The central pixel of the MAGIC-I camera has been specially design to perform optical measurements (mainly the optical pulsations of the Crab Nebula pulsar), and to check the timestamp of the overall system.

Calibration of the MAGIC-I camera is performed by an optical calibration system installed in the center of the reflector. The system employs ultra-fast LEDs (in order to emulate the fast timing behaviour of the Cherenkov pulses) with different characteristic wavelengths (370 nm, 460 nm and 520 nm), able to uniformly illuminate the whole camera with light pulses of custom frequency and intensity.

MAGIC-II camera Camera of MAGIC-II is of roughly circular shape, with 1.2 m diameter and 3.5° FoV (Figure 3.3). It is composed of 1039 PMTs of 30 mm diameter and 0.1° FoV each, grouped in 169 independent clusters. MAGIC-II trigger area is larger than that of MAGIC-I, and it covers the innermost 2.5° region.

The calibration system is installed in the center of the MAGIC-II reflector. It consists of a frequency tripled passively Q-switched Nd-YAG laser, whose beam passes through two filter wheels with different attenuations, allowing for easy adjustment of the pulse intensity. After the attenuation, the laser beam is diffused via an integrating (Ulbricht) sphere, providing a homogeneous illumination of the camera.

3.1.3 Readout System

Following the conversion of Cherenkov photons into electric pulses in the PMTs, the electric signal is amplified and converted into optical signal by the Vertical Cavity SurfacE Laser diodes (VCSELs), located at the base of the PMTs. The VCSELs are coupled to optic fibers which transmit the signal over ∼80 m to the *Counting House*, a building hosting the rest of the electronics and the operations center. This way of analog optical transmission protects the signal from ambient electromagnetic noise in the line and reduces the signal losses from the camera to the readout. In the Counting House, optical signals are back-converted into electric pulses in the receivers boards and split in two branches, by means of fast GaAs PIN diodes. One branch goes into the trigger system, while the other is passed to the Data Acquisition System (DAQ). DAQ, through the use of Flash Analogical to Digital Converters (FACDs), digitizes the electric pulses at speed of 2 GSamples/s. When trigger arrives, the sampling stops and the digitized signal is recorded into raw data file.

When MAGIC-II was built, its readout system differed from that of MAGIC-I. In Autumn 2011, a partial upgrade of the telescopes was performed, including replacement of both readout systems with the new ones, identical for the two instruments. As this change affects the observations presented in this work, the pre-upgrade as well as the post-upgrade readout systems are described in detail below.

3.1.3.1 Pre-Upgrade

MAGIC-I When the optical signal reaches the MAGIC-I readout, it is split in two branches before reaching the receiver boards. One half of the signal is sent to the trigger, where it is converted back into an analog electric pulse. The other half is forwarded to the fiber-optic multiplexing readout system (MUX) [154], where pulses from every 16 channels are linked together. This is done by delaying the optical signal of each channel by multiples of 40 ns before converting them back into electric pulses by means of fast GaAs PIN diodes. The signal is then digitized by 2 GSamples/s FADCs and written to a ring buffer. When trigger is issued, the corresponding part of the buffer is written to the disk. The bandwidth of the whole DAQ chain is about 250 Hz, and the deadtime is ∼16 μs.

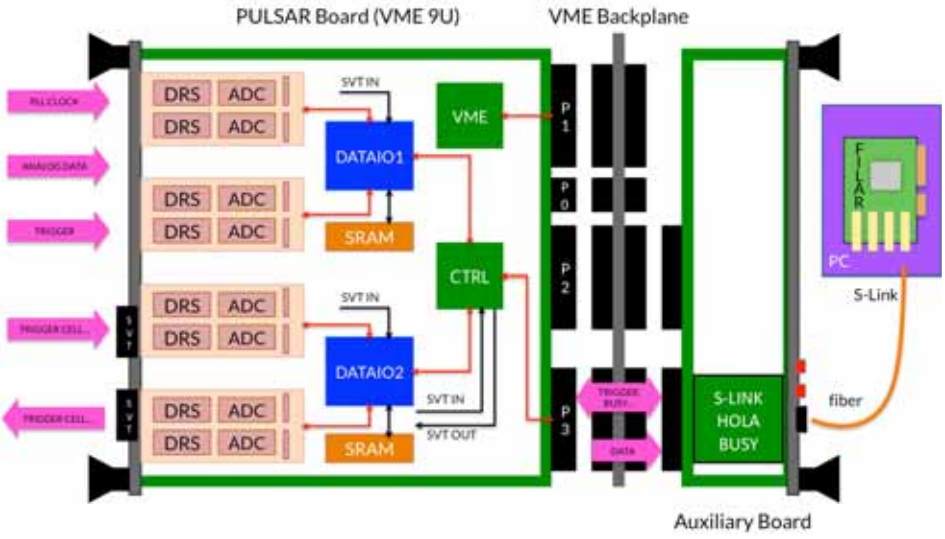

Figure 3.4: Partial schematics of the MAGIC-II pre-upgrade DAQ system.

MAGIC-II The readout of MAGIC-II first converts the optical back into electric signal in the high bandwidth and fully programmable receiver boards called MONSTER (Magic Optical NanoSecond Trigger and Event Receiver), and then splits the signal in two branches. One branch is sent to a discriminator with a software adjustable threshold, and the signal that surpasses the chosen threshold is digitized and routed to the trigger system. The other branch of the signal is passed to the digitizing units. The core of the MAGIC-II DAQ is an ultra fast analog sampler, called Domino Ring Sampler, version 2 (DRS2) [155]. A single Domino chip hosts 10 input analog channels, each associated with one pixel in the camera. One DRS2 channel is equipped with 1024 capacitive cells, organized as a ring buffer where signal is continuously recorded. When trigger arrives, the sampling is stoppes and the signal currently stored in the capacitors is frozen, then read out and digitized at 40 MHz rate. DRS2 chips are installed in pairs on custom made mezzanine cards, that in turn are mounted (in groups of 4) on the PULSAR (PULSer And Recorder) boards. PULSAR reads out the analog input signal which is then transmitted to the HOLA (High Optical Link for Atlas) board, and from there forwarded via optical S-Link to the FILAR (Four Input Links for Atlas Readout) board. FILARs are installed in DAQ pc that interfaces with user and where the readout system ends. Schematic representation of a fully equipped analog PULSAR is shown on Figure 3.4.

In addition to 14 analog PULSAR boards, there are two special PULSARs that belong to the DAQ system: the DIGITAL PULSAR, implemented to add digital information to the data (such as absolute time and the trigger number), and BUSY PULSAR that stops the triggers when the readout is already processing one event or when an error occurs.

3.1.3.2 Post-Upgrade

By the end of 2011, as part of the planned improvements of both telescopes, the readouts of MAGIC-I and MAGIC-II have been replaced by upgraded systems, largely based on the previous DRS2 readout [156]. The main change is the use of an more sophisticated digitizing unit, DRS4. The new chip has several important advantages over DRS2: a completely linear behavior as well as the option to operate in the limited, Region-Of-Interest (ROI) readout mode, which significantly reduces the dead time (to less than 1%).

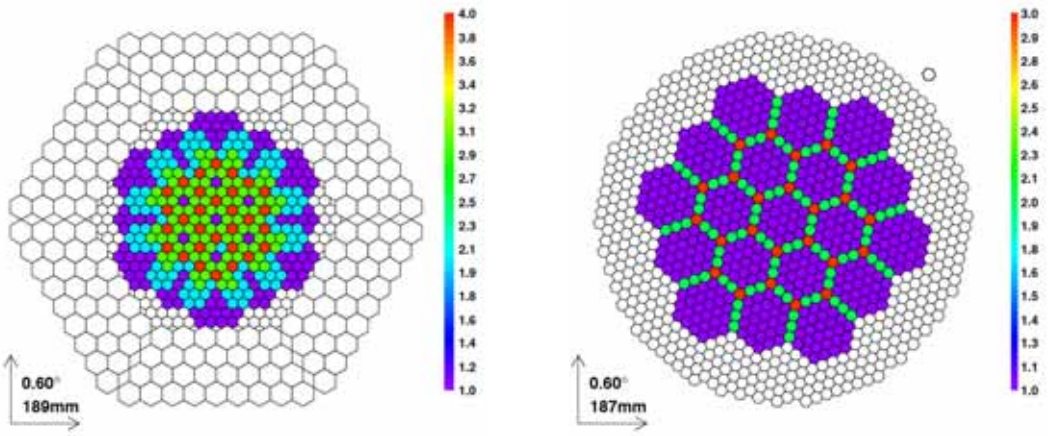

Figure 3.5: Schematic representation of the MAGIC-I (pre-upgrade, **left**) and MAGIC-II (**right**) cameras with L1 trigger areas marked with colored pixels. The color coding indicates the number of macrocells each pixel belongs to, illustrating the overlapping level.

3.1.4 Trigger

The trigger system discriminates Cherenkov showers from the NSB, by selecting only fast pulses ($<$5 ns) detected simultaneously in several neighbouring pixels. Trigger is composed of four different trigger levels: the first three work over the individual telescope data, while the fourth is shared by both instruments.

- Level 0 (L0): hosted on the receiver boards, it evaluates every channel and digitizes its signal only if it exceeds a certain amplitude – discriminator threshold (DT). DTs are programmable by the software.
- Level 1 (L1): digitized signals from L0 are sent to L1, which examines the channels in search for spatial and temporal correlation over the decomposition of the trigger region in 19 overlapping macrocells. This topological condition is based on the Close Compact Next Neighbor (CCNN) logic, that is, only events present in N adjacent pixels are accepted by the L1 trigger. The standard CCNN setup applied in MAGIC observations is that of 4NN, with 2NN, 3NN and 5NN also available.
- Level 2 (L2): in the first version of the MAGIC-I trigger, events triggered by L1 entered L2 for further, shape-based discrimination. L2 was never enabled for standard data taking, but its unit is used for event rate monitoring, rate scaling and integration of L1, calibration and stereo triggers.
- Level 3 (L3 - Stereo trigger): selects only those events that have triggered both telescopes within a certain time interval. In order to minimize the coincidence time window, the arrival times of L1 events of each telescope are delayed, depending on the pointing positions of the telescopes.

Aside from these trigger levels that are considered standard in MAGIC observations, there is another trigger concept – the Sum Trigger – specifically designed to lower the trigger threshold by a factor of 2, down to $\sim$25 GeV. Sum Trigger logic is based on sum of several analog signals, in such a way that the signal-to-noise ratio of low energy showers is minimized over the NSB light. Sum Trigger was implemented in the pre-upgrade MAGIC-I and used only for a limited set of data, so it will not be further discussed here; for more information, see [157].

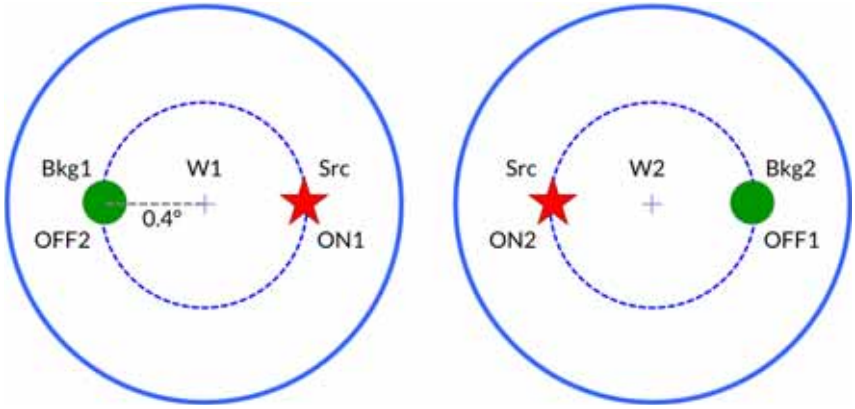

Figure 3.6: Wobble observation mode: the background in the source region of W1 is estimated from the background region of W2 and vice versa.

3.2 Data Taking Procedure

All subsystems of MAGIC Telescopes are controlled and monitored from the Central Control (CC) program [158]. The CC defines standards for all observational procedures, and this Section briefly describes what observation modes can be used and what types of data can be taken with MAGIC Telescopes.

3.2.1 Source Pointing Models

There are two observation settings used by MAGIC: the *tracking* (*ON/OFF*) mode and the *wobble* mode.

In *tracking* mode telescopes are pointing directly to the source, in such a way that nominal position of the target is located at the center of each camera. Data recorded in this configuration are called *ON* data. In order to properly estimate the background in *ON* sample, additional, dedicated observations of so-called *OFF* region(s) are required. *OFF* data are recorded from areas where no significant gamma-ray emission is expected, under the same circumstances as the *ON* observations (same zenith angle (*ZA*) range, level of background light, atmospheric conditions and so on).

Wobble, or the *false source tracking* mode [159], consists of observations where telescopes are alternatively tracking (at least) two directions on the sky, located with a slight offset with respect to the nominal position of the source (Figure 3.6). For MAGIC, the default offset is 0.4°, with wobble positions changing every 20 minutes to ensure uniform (azimuthal) coverage of the sky and avoid possible bias. The main advantage of this technique is that it does not require any additional *OFF* data, seen how the signal and the background are simultaneously measured. Background in every wobble is extracted from the opposite region to the source position in the camera, also called the anti-source. Such position is the source nominal position rotated by 180° around the camera center, and works as the equivalent to the OFF region in the *tracking* mode observations. Number of used background regions can be increased according to the user's needs, as long as these regions do not overlap with the signal region.

Still, *wobble* mode observations have two main drawbacks: loss in the gamma-ray efficiency (by 15%-20%), due to the smaller effective trigger area around the source, and a pos-

sible bias introduced by the off-center source position, consequence of the camera inhomogeneities.

Furthermore, stereo observations originate an irregular feature, referred to as the "stereo blob", that represents the uneven acceptance in the FoV, caused by the broken azimuthal symmetry due to the relative orientations of the telescopes. The presence of the "blob" can have significant effect at lowest energies, and it is most pronounced for observations carried out by only two instruments: the greater the number of telescopes in the system, the smaller the area affected by the "blob".

3.2.2 Types of Data

Independently on the observation mode, MAGIC data is classified according to the kind of the events that are recorded. Three kinds are always taken during the standard observations:

- *Pedestal run*: randomly triggered events (usually 2000 per run), digitized and recorded for evaluation of the effects the NSB light and the readout electronics noise have. The contribution of both components is further extracted, pixel-by-pixel, in the calibration of the data (§3.3.1). Probability of recording an actual shower is negligible.
- *Calibration run*: events triggered by the calibration system of each telescope (§3.1.2), through generation of light pulses that mimic Cherenkov showers in terms of duration and wavelength. The calibration events are further applied in the calibration of the data (§3.3.1) – they are used to calculate the arrival time offsets as well as the conversion factor between the FADC counts and photoelectrons (ph.e.).
- *Data run*: events triggered by the cosmic showers. Data run also includes pedestal and calibration events, interleaved with the cosmic events at a rate of 25 Hz. The interleaved events are further used to maintain the pedestal values and calibration constants updated during the sequential calibration of the data (§3.3.1).

Each telescope records, for every source, its own pedestal, calibration and data runs, under the common identifying run numbers assigned by the CC. In addition to these, in the case of MAGIC-II, a special kind of run is taken at the beginning of every night – the *Domino Calibration run* [155], used for correction of the non-linearity of the DRS2-based readout (§3.1.3.1). After the upgrade, this kind of run is no longer necessary.

3.3 Data Analysis

The main objectives in every analysis of MAGIC Telescopes are to distinguish between the gamma-ray and hadron events, to determine the primary energies of the gamma-ray photons and to precisely induce their incoming directions.

The standard MAGIC analysis relies on programs and classes of the official MAGIC Analysis and Reconstruction Software (MARS) [160, 161], a dedicated software package written in C++ language and embedded in the framework of ROOT [162]. The philosophy of MARS is to create an analysis chain, where each program produces the input for the subsequent step. The final output is the list of events that is used for production of higher level results, like spectra and skymaps. Main links of the analysis chain are described in more detail in the following Sections; this is their brief summary:

- *Data calibration*: for each pixel in the camera, charge (in ph.e.) and the arrival time of Cherenkov pulse are determined.
- *Image cleaning and parametrization*: pixels that contain noise (and no signal) are removed from further analysis, after which parameters describing the shower image are computed.
- *Data selection*: quality control of the data is performed, based on acquisition rate stability, atmospheric conditions, values of the image parameters, etc.
- *Data merger*: data streams from both telescopes are combined together and the corresponding stereo parameters are calculated.
- *Event characterization*: for each event, its energy, arrival direction and likelihood to be a gamma-ray induced shower are estimated.
- *Calculation of the signal significance*: excess gamma-ray and background events are used to determine the significance of the observed gamma-ray signal.
- *Higher level products generation*: depending on the significance of the signal, differential and integral fluxes, the Spectral Energy Distribution (SED) and light curves (in the case of the detection) or differential and integral upper limits to the flux (in the case of no detection) can be obtained. Skymaps can be created in either case.

The analysis chain depends heavily on Monte Carlo (MC) simulations for background rejection and determination of the response function of the telescopes. Simulations include development of extensive air showers, propagation of Cherenkov light through the atmosphere, response of the telescope mirrors and distribution of the photons on the camera plain, as well the response of the PMTs for a given NSB light and behaviour of the readout [163, 164]. The gamma-ray source can be simulated as either point-like or diffuse, and its emission is usually approximated by a power law.

Additionally, if possible, analysis of the chosen source is always accompanied by a parallel analysis of a Crab Nebula data sample. Such sample must coincide with the principal source observations as much as possible, mainly in the atmospheric conditions and *ZA* range. The purpose of this complementary analysis is to examine the overall performance of the analysis chain. Crab Nebula data are used since this object is considered to be the standard candle of the VHE astronomy, given its large and stable flux for the energy range of IACTs [165].

3.3.1 Data Calibration

This link of the analysis chain can be divided into several steps:

Conversion into ROOT format MAGIC raw data consist of digitized pulses, recorded for every event and every pixel, with amplitudes expressed in arbitrary FADC units. Originally stored in the binary form, these data are translated to ROOT format by means of MERging and Preprocessing Program (`merpp`). Aside from the format conversion, `merpp` is also responsable for injection of relevant reports from the telescope subsystems into data files. That way, all the information regarding the conditions and performance of the subsystems during data taking are easily accessible.

Signal reconstruction For each pixel, the recorded signal of each event is sampled in 80, 0.5 ns-wide, FADC capacitors[1]. Every sample is analyzed by the *signal extractor*, a program that provides information on the arrival time of the signal as well as its amplitude and charge in FADC counts. Among various algorithms that can be used for the signal extraction [166], two are adopted in MAGIC analysis: the *cubic spline extractor* (for pre-upgrade MAGIC-I data) and the *sliding window extractor* (for the pre-upgrade MAGIC-II and both telescopes post-upgrade). In the pre-upgrade MAGIC-II analysis, the signal extraction is always preceded by the correction of the data for the nonlinearity of the DRS2 chip (§3.1.3.1).

The *cubic spline extractor* works in the following way: after the pedestal subtraction, the FADC counts are interpolated by the cubic spline algorithm, and the maximum of the interpolation function is adopted as the signal amplitude. The signal charge is calculated as the integral of the interpolation function, computed in a fixed-width interval with limits dependent on the position of the maximum. Lastly, the location of the half maximum at the rising edge of the pulse gives the signal arrival time.

The *sliding window extractor* calculates the signal charge as the maximum integral content of 6 consecutive FADC capacitors, over a fixed time window and after the pedestal extraction. The signal arrival time is defined as the average of the FADC capacitors time, weighted by the counts content in each of them.

FADC count to photoelectron conversion Once the signal is reconstructed, its charge in FADC counts is translated into the equivalent number of ph.e., through the use of *F-factor* method [167]. This approach makes the conversion based on the proportion ratio obtained from the calibration events. *F-factor* method assumes an uniform photon detection efficiency over the entire camera, a number of incoming photons that follows the Poisson statistics, and the readout noise independent of signal amplitude. If, on one hand, the distribution of the number of calibration events in each pixel has mean N and RMS of $\sqrt{N}$, let the distribution describing the charge measured in FADC counts be of mean $\langle Q \rangle$ and RMS σ. The latter distribution is broader than the pure Poisson one, and their relative widths are related by the *F-factor* as:

$$F \frac{1}{\sqrt{N}} = \frac{\sigma}{\langle Q \rangle}. \tag{3.1}$$

The broadening of the measured distribution is a consequence of electron multiplication in the PMTs, and it has to be individually quantified for each PMT in the laboratory. In case of the pre-upgrade MAGIC-I, an averaged *F-factor* used for all PMTs was 1.14. For the pre-upgrade MAGIC-II and for both instruments after the upgrade, *F-factor* is 1.095.

With known *F-factor* and measured $\langle Q \rangle$ and σ, eq.(3.1) can be used to compute the mean number of ph.e. in calibration events:

$$C = \frac{N}{\langle Q \rangle} = F^2 \frac{\langle Q \rangle}{\sigma^2}, \tag{3.2}$$

where C is the conversion factor from FADC counts to ph.e. During the regular observations, mainly due to thermal sensitivity of analog to optical converters, the values of the conversion factor change, and therefore have to be constantly updated. This is accomplished thought the interleaved calibration events (§3.2.2).

[1] The pre-upgrade DAQ of MAGIC-I was actually recording 50 out of 80 capacitors: the first and the last 15 capacitors only contained the "switching noise".

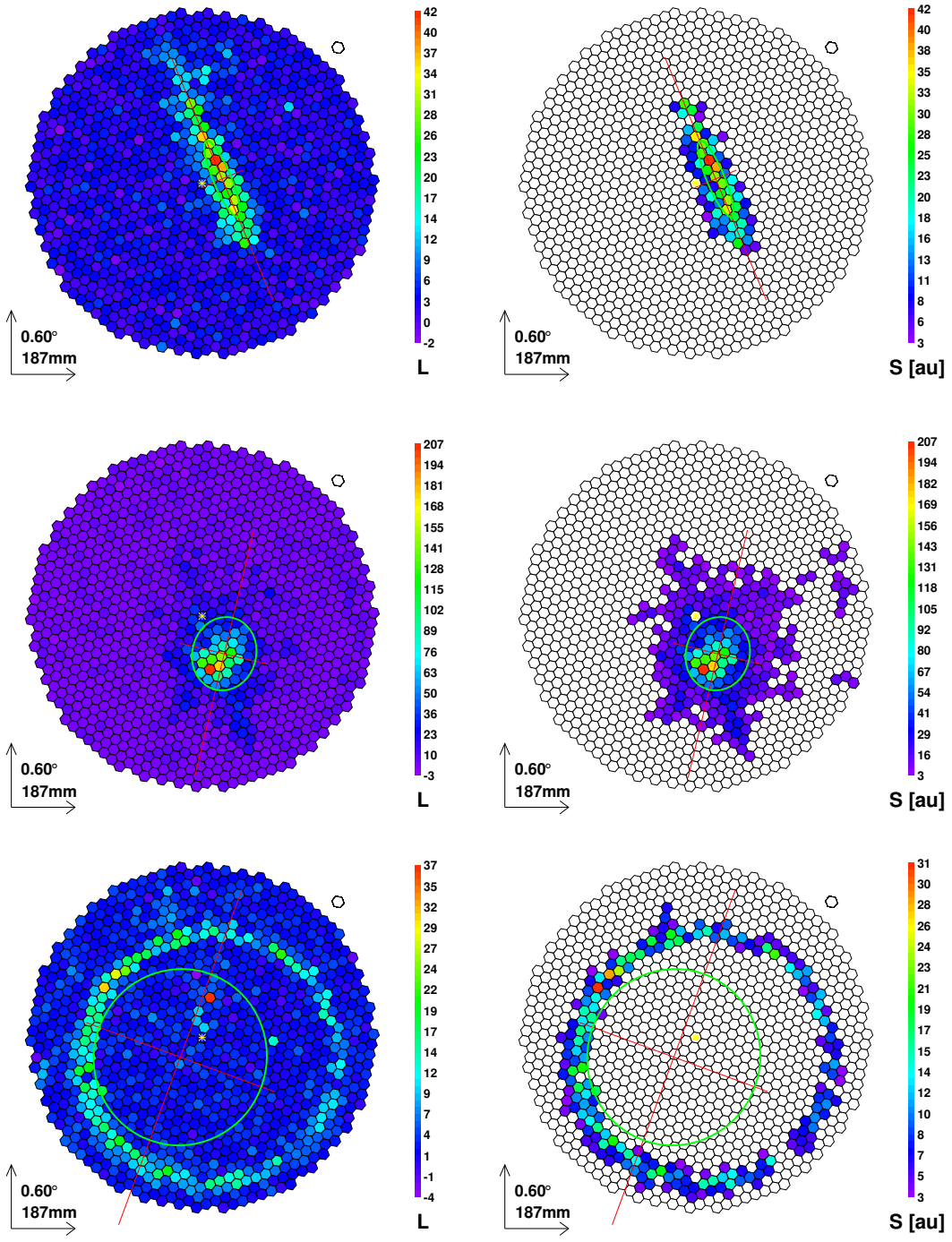

Figure 3.7: Real events recorded with MAGIC-II, before (**left panels**) and after the image cleaning (**right panels**). **Top row**: Gamma-like events. **Middle row**: Hadron-like events. **Bottom row**: Muon-like events.

Calibration of the MAGIC pre-upgrade data is performed by the program called `callisto` (CALibrate LIght Signals and Time Offsets), while after the upgrade this task is done by `sorcerer` (Simple, Outright Raw Calibration; Easy, Reliable Extraction Routines).

3.3.2 Image cleaning and parametrization

Cleaning After the calibration, the charge and arrival time information of each event in each pixel are used to identify noise generated by the NSB light and remove it from the shower image. This process is referred to as the *image cleaning*, and there are many algorithms that can fulfill this objective (for e.g., see [168, 169]). Performance of these algorithms, however, has a significant impact on the sensitivity of the analysis, especially at lowest energies, so the choice of the approach to be applied to the data has to be carefully considered.

Standard image cleaning of MAGIC analysis removes pixels containing the noise and divides the remaining ones, that actually form the shower image, into two populations: the core and boundary pixels. A pixel is identified as of one or the other population if its charge exceeds a certain threshold of number of ph.e. (q_c for core, q_b for boundary pixels, with $q_c > q_b$) and if it is adjacent to at least one another pixel of the same population. Additionally, the individual arrival time of core pixel can not differ from the mean arrival time of the core of the image by more than Δt_c, while for boundary pixels arrival time has to be less than Δt_b disagreeing from the arrival time of its core pixel neighbour. The standard values for the image cleaning parameters are:

- MAGIC-I (pre-upgrade): $q_c = 6$ ph.e., $q_b = 3$ ph.e., $\Delta t_c = 4.5$ ns, $\Delta t_b = 1.5$ ns;
- MAGIC-II (pre-upgrade): $q_c = 9$ ph.e., $q_b = 4.5$ ph.e., $\Delta t_c = 4.5$ ns, $\Delta t_b = 1.5$ ns;
- MAGIC-II (post-upgrade): $q_c = 8$ ph.e., $q_b = 4$ ph.e., $\Delta t_c = 4.5$ ns, $\Delta t_b = 1.5$ ns.

Figure 3.7 shows the effects of image cleaning applied to the actual MAGIC-II events.

Parametrization Image cleaning is followed by reduction of each shower to a set of parameters quantifying its shape, orientation and timing. Based on their function, these parameters can be sorted as:

- **Hillas Parameters**, or the momenta of the 2-dimensional distribution of charge surviving the image cleaning [170]. The most relevant ones are:
  - *Size*: total charge (in ph.e.) of the full clean image. It is strongly correlated with the energy of the primary gamma-ray event.
  - *Width*: the RMS spread of the light along the minor axis of the image. It is a measure of the lateral development of the shower (Figure 3.8).
  - *Length*: the RMS spread of the light along the major axis of the image. It is a measure of the longitudinal development of the shower (Figure 3.8).
  - *Conc(N)*: fraction of the image charge concentrated in the N brightest pixels. It is an estimate of the compactness of the shower image, being usually larger for gamma-ray showers than for the hadronic ones.
- **Timing Parameters** exploit temporal properties of the shower:
  - *Time RMS*: the RMS spread of the arrival times of all the pixels that survived the image cleaning. It is a discriminator between the gamma-ray and hadronic showers, as their development times differ.

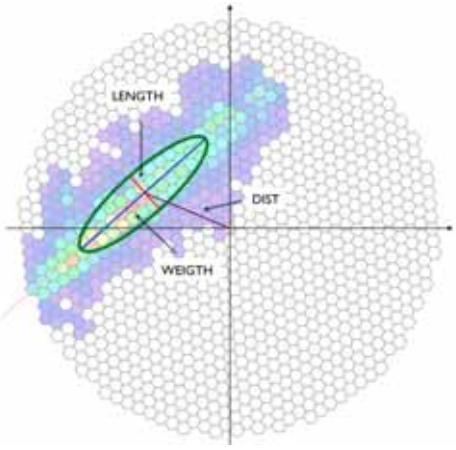

Figure 3.8: Image of an actual shower in MAGIC-II camera after the cleaning, superimposed with the Hillas ellipse parametrization.

- ✧ *Time gradient*: slope of the linear fit to the arrival time projection along the major axis line. It is a source-dependent parameter, adopting negative value if the arrival time increases when moving towards the location of the source in the camera, and positive otherwise.

❖ **Quality parameters** asses the image reconstruction accuracy:

- ✧ *LeakageN*: fraction of the charge contained in the *N* outermost pixel rings of the camera. It serves as an estimator of the portion of the shower image that spills over the camera. Events with large *leakageN* are likely to undergo a bad reconstruction.
- ✧ *Number of islands*: number of isolated groups of pixels that survive the image cleaning procedure. Gamma-ray showers generate a single island image, while the hadronic ones may produce several islands in a single event image (Figure 3.7).

The image cleaning and parametrization of the single telescope data is performed by the STandard Analysis and Reconstruction (`Star`) program.

3.3.3 Data Selection

Purpose of data selection is to discard those data whose inadequate quality may jeopardize the sensitivity of the analysis. Main criteria in data selection are the atmospheric conditions and hardware performance during the observations.

Integrity of the hardware is constantly monitored by the subsystems of the telescopes, and possible malfunctions are reported in electronic runbooks of every observational night, or detected from the daily checks of the subsystems. Data taken with erroneous hardware, with problems that can not be corrected via software, are normally discarded from further analysis.

Atmospheric conditions are the main source of data degradation, as transparency of the atmosphere has significant impact on the propagation of Cherenkov light, and therefore on the resulting observations. A dedicated weather station, a lidar and a pyrometer operate at MAGIC site in parallel with observations and provide more detail on the current atmospheric

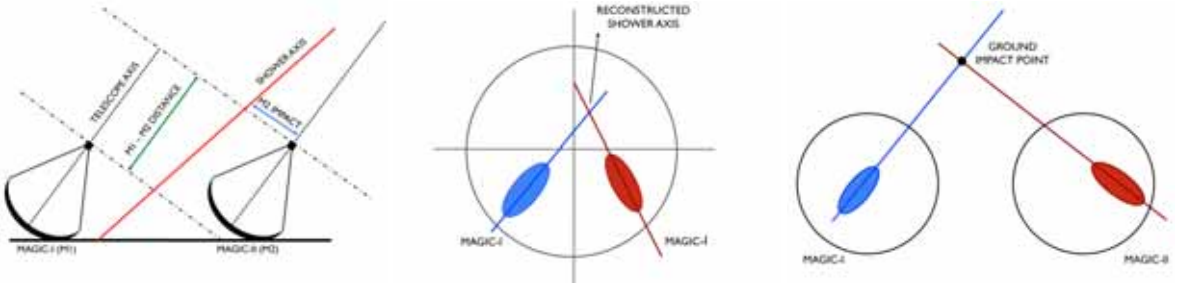

Figure 3.9: Shower axis reconstruction in a stereoscopic view. (**Left**) Geometrical definition. (**Center**) Reconstruction of the shower direction as the intersection of the image major axes, once superimposed the images. (**Right**) Reconstruction of the shower impact point at ground.

circumstances. Nevertheless, the correlation between data quality and weather parameters is not conclusive, and there is not a sharply defined rule for data exclusion based on the atmospheric situation.

The most robust, systematic way for data quality check is monitoring of the events analysis rate r (after the image cleaning and above a certain *size* cut). It only depends on the observation zenith angle ZA as:

$$r = r_0 \sqrt{\cos ZA}. \tag{3.3}$$

Thus, deviations from the expected value usually indicate some problem, and data whose rates differ for more than 15%-20% from the mean value are discarded.

Data quality can also be estimated from some other image parameter distributions, like *size*, *length* and *width*, seen how their values are expected to be constant during the stable observations.

3.3.4 Data Merger and Stereo Parameter Reconstruction

Up to this point the analysis is applied to data of each telescope separately, but after the image parametrization and data cleaning, information about the same event recorded by individual telescopes are combined into a single set. This is performed by a program named `SuperStar`. Aside from data merger, `SuperStar` also calculates stereo parameters describing the 3-dimensional development of the shower [171], the most relevant of which are:

- *Shower axis*: information about the direction of the shower and its impact point on the ground. The arrival direction is defined as the intersection of two major axes of two images, once superimposed in the camera plain. The impact point on the ground is determined from the intersection of the major axes of two images with respect to the telescope positions (Figure 3.9). The accuracy of estimating the shower axis depends on the relative positions of the telescopes and the shower: the more parallel the two images on the camera planes are, the larger the uncertainties.

- *Impact parameter*: the perpendicular distance between the shower axis and the telescope pointing axis (Figure 3.9).

- *Shower maximum height*: estimate of the height at which the maximum development of the shower occurred. It is based on the shower axis characterization as the 3-dimensional geometrical location of the Center of Gravity (CoG) of the image. The shower

maximum height is strongly correlated to the energy of the primary gamma-ray and is a powerful discriminator at low energies.

- *Cherenkov radius* and *Cherenkov photon density*: radius and density of the Cherenkov light pool on the ground. They are calculated assuming Cherenkov emission from a single electron at the shower maximum height and with energy equal to the critical energy, of 86 MeV.

3.3.5 Event Characterization

Event characterization is aimed at determining the nature and properties of the primary particle that originated the shower. In particular, the energy and the arrival direction of the particle are of the greatest interest for the analysis. These values are estimated from the image parameters described in §3.3.2, following several different algorithms: the *Random Forest* (RF) type decision trees [172], parameterizations and *Look-Up Tables* (LUTs).

The characterization requires a MC dataset of simulated gamma-ray events, as it is not feasible to acquire pure gamma-ray sample from the observations. For the analysis purposes, the MC simulations are split into two subsets: one, called the *training* sample, used for preparation and tuning of the characterization algorithms, and the other, the *test* sample, used for evaluation of the performance of the trained algorithms. Both *train* and *test* samples are independent, thus avoiding biased results.

Before the actual characterization of the events, certain event-based quality cuts are applied. For instance, events with *size* lower than some minimum charge value are discarded; same goes for events with too great *leakage*, too many *islands* and too few core pixels. Additionally, events that recorded sparks generated by electric discharges between the PMT cathodes and Winston cones are removed from the further analysis.

The estimation of the nature of the particle, its energy and its arrival direction are explained in more detail in the following. Program in charge of those tasks is called `Melibea` (MErge and Link Image parameter Before Energy Analysis).

3.3.5.1 γ/hadron Separation

The IACTs data are dominated by the background. Unwanted triggers are produced by fluctuations in the NSB light, Cherenkov light of individual muons, and showers originated by the cosmic rays, so called *hadronic showers* (Figure 3.7).

Hadronic showers are the most numerous population of recorded triggers: for observations of a typical VHE gamma-ray source, there are $\sim 10^4$ more hadronic that gamma-ray events. With a signal to noise ratio that small, sensitive measurements are only achievable if a highly effective hadron suppression is applied. In MAGIC analysis, this suppression is called γ/*hadron separation*, and there are several methods that provide it. The one used in this work (and by default in the MAGIC standard analysis) is the *RF method*, a multi-dimensional classification algorithm based on decision trees [173]. These trees are trained with a sample of MC simulated gamma-ray events and a sample of hadronic events from the actual observations. Trees grow in the space of image parameters, through dynamical evolution of the cuts. The final set of classification trees, defined as the mean classification from all trees, is referred to as *hadronness* - a likelihood that event is of hadronic origin. *Hadronness* takes

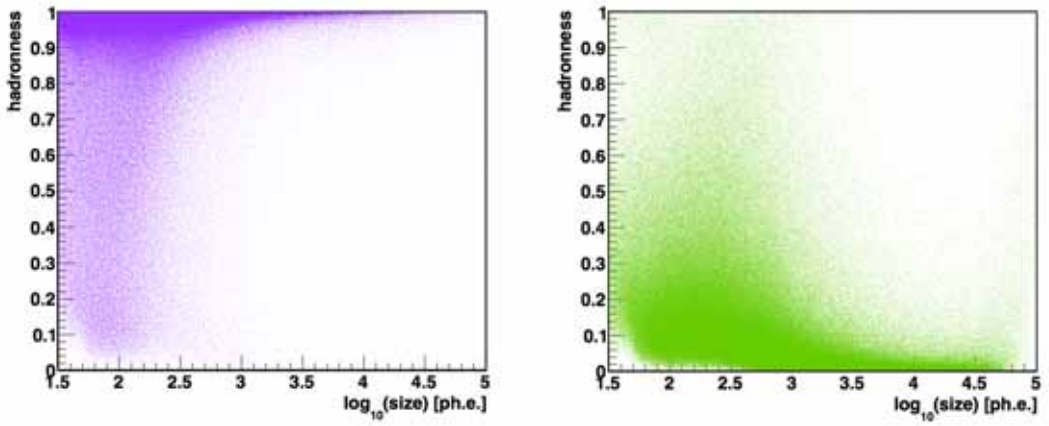

Figure 3.10: Distribution of *hadronness* as a function of *size*, for a data sample (**left**) and for simulated MC gamma-ray events (**right**).

values between 0 and 1: for the gamma-like events, *hadronness* is closer to 0, while for the hadronic ones it assumes greater values.

γ/*hadron separation* for a given data set is performed by applying a cut in *hadronness* parameter. The resulting hadron suppression is about 90%-99% (improving with increasing *size* of the events).

Figure 3.9 illustrates the separation power of the *hadronness* parameter as a function of *size*.

3.3.5.2 Arrival Direction Estimation

As already mentioned in §3.3.4, direction of the shower can be calculated geometrically, but with some uncertainties dependent on the mutual positions of the telescopes. More accurate estimate of the arrival detection is achieved through the definition of a new parameter, called *disp*, that represents the angular distance between the image CoG and impact point in the camera. There are several methods that can be applied to estimate the value of *disp*. The one used in MAGIC stereo analysis, and in this work, is called *Disp RF*, and it consists of introducing all image parameters that may influence the *disp* value in a dedicated RF algorithm [174]. The *Disp RF* is trained with a sample of simulated gamma-ray events of known source position, and it grows the corresponding decisional trees to evaluate the correlation between the *disp* and the input parameters. The value of *disp* is estimated for events from each telescope separately, and for the shower in each camera there are two possible reconstructed source positions along the image major

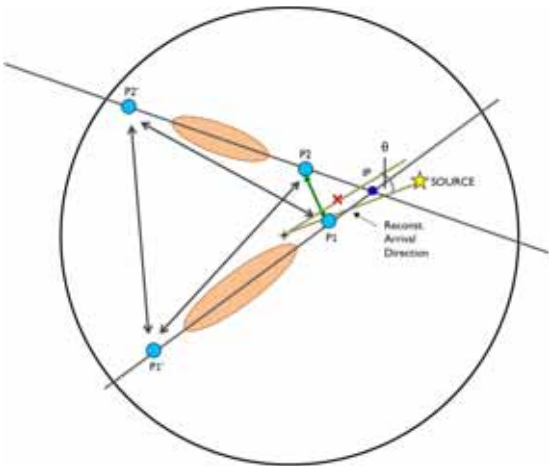

Figure 3.11: Sketch of the stereo *Disp* algorithm. Each of the two superimposed images has two possible reconstructed source positions. The favoured one is drawn in green (P1-P2). The arrival direction (red cross) is reconstructed as the weighted average of P1, P2 and the point of intersection (IP) of two major axes.

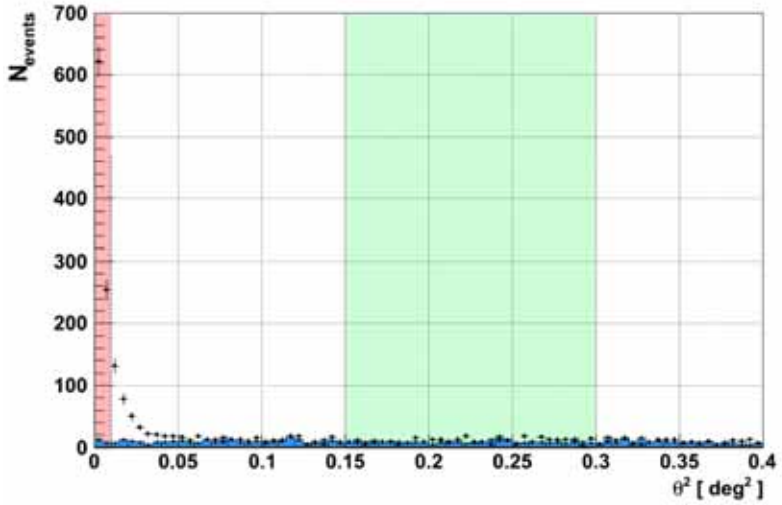

Figure 3.12: Example of a signal detection from Crab Nebula with a θ^2-plot. Excess gamma-ray events are given as points, while the background events are represented in blue. Red shaded area is the signal region, and the green one the normalization region.

axis (Figure 3.11). When events are merged, the distances between all possible combinations of position pairs are calculated. The closest pair is chosen as the correct one, and the arrival direction is determined as the weighted average of such positions together with the crossing point of the main axes of the images.

The use of *disp* parameter provides an unbiased way for estimation of the source position on the camera, as it does not require any previous assumption on its location. In addition, it allows for introduction of a new, powerful discriminator between the gamma-ray events coming from the observed source and the rest of the background: the θ^2 parameter. The θ is defined as the angular distance between the reconstructed arrival direction of the event and the nominal source position on the camera plane (Figure 3.11). For gamma-ray events from the source, θ^2 distribution peaks toward zero values, while for hadronic and diffuse gamma-ray events, that are expected to fall isotropically, this distribution is flat (Figure 3.12).

3.3.5.3 Energy Estimation

In the MAGIC standard analysis chain, energy of each event is estimated through the use of LUTs. The LUTs are based on a simple model describing the distribution of the Cherenkov photons on the ground, by relying on the parameters *impact*, *Cherenkov radius* (r_c) and *Cherenkov density* (ρ_c), introduced in §3.3.4. LUTs are built for each telescope independently, by dividing a sample of simulated gamma-ray events in bins of *size* and in bins of *impact*/r_c ratio. Since the energy of the primary gamma-ray is proportional to *size*/ρ_c, each of the table bins contains the mean value of the distribution of $E' \times \rho_c/$*size*, where E' is the true energy, with an error given by the RMS of the distribution. The final energy estimation, E, is the average value obtained from both telescopes, weighted according to their errors, and corrected for the *ZA* dependence through the empirical factor $0.4 \times \cos(ZA)$.

3.3.6 Signal Estimation

After applying the *hadronness* cut, further background suppression can be achieved through the use of θ^2 parameter. As already mentioned, the θ^2 distribution peaks close to zero values

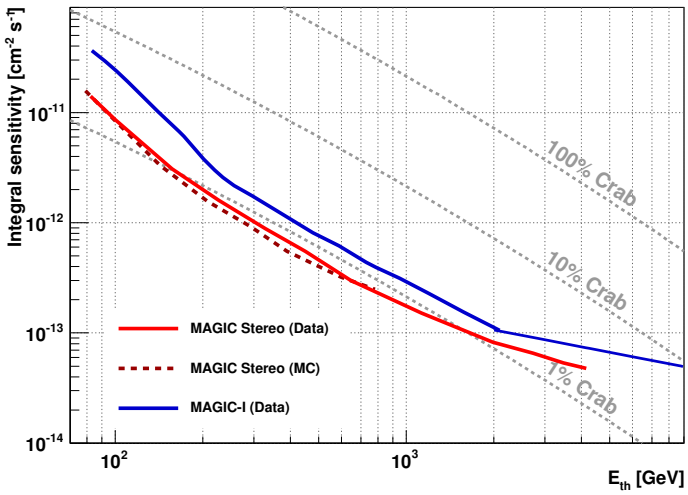

Figure 3.13: Integral sensitivity of stereo observations as a function of $E_{\rm th}$, predicted from MC simulations (dark red dashed line) and measured from observations of the Crab Nebula (solid red line). Blue line represents the sensitivity achieved with MAGIC-I in standalone mode. For reference, different fractions of the Crab Nebula flux are represented as gray dashed lines. Taken from [151].

for gamma-ray events from the source, whereas for the background events, whose arrival directions are isotropic, the θ^2 distribution is flat. Consequently, by choosing a θ^2 value bellow which the signal/background discrimination is good, geometrical space limited by that cut represents the signal (*ON*) region in the analysis (Figure 3.12).

The events in *ON* region are of both gamma-ray and hadronic origin. To estimate the background in the *ON* region, an independent data sample from the region with no expected gamma-ray signal (*OFF*) is used (see §3.2.1). The treatment of both background and signal regions, in sense of analysis methods and applied cuts, is the same. From measured number of events in *ON* and *OFF* regions, $N_{\rm ON}$ and $N_{\rm OFF}$, respectively, number of excess events $N_{\rm ex}$ is calculated as:

$$N_{\rm ex} = N_{\rm ON} - \frac{N_{\rm OFF}}{\tau}, \tag{3.4}$$

where τ is the normalization factor between the *ON* and *OFF* samples, calculated as a fraction of $N_{\rm OFF}$ over $N_{\rm ON}$ events in a region far away from the peak of θ^2 distribution (Figure 3.12).

For a given source, the significance level of detection (S) is computed by means of a statistical test, with null hypotheses assuming that the expected signal is no different from the background, i.e. all observed photons are from the background emission. The significance is calculated from the following expression [175]:

$$S = \sqrt{2}\left\{ N_{\rm ON} \cdot \ln\left[(1+\tau)\left(\frac{N_{\rm ON}}{\tau N_{\rm ON} + N_{\rm OFF}}\right)\right] + \frac{N_{\rm OFF}}{\tau} \cdot \ln\left[(1+\tau)\left(\frac{N_{\rm OFF}}{\tau N_{\rm ON} + N_{\rm OFF}}\right)\right]\right\}^{1/2}. \tag{3.5}$$

As a convention, the detection of a source can be claimed if its significance level equals or surpasses the 5σ value[2]. This significance has to be corrected for the number of trials generated if different sets of cuts were used in the analysis, in order to avoid false detections caused by the possible background fluctuations.

[2] A 5σ detection means that the probability of detected signal being false and result of background fluctuations is 3×10^{-7}.

The applied *hadronness* and θ^2 cuts are previously optimized on a reference Crab Nebula sample (§3.3), by maximizing its signal significance in the 2-dimensional parameter space.

Sensitivity The analysis can also be quantified in tearms of its sensitivity, usually expressed as a minimum flux that would be measured above a certain energy threshold $E_{\rm th}$, with 5σ significance in 50 hours of observations, for a source whose spectrum is of the same shape as the one of the Crab Nebula. This *integral sensitivity* is calculated assuming a Gaussian approximation of the significance level (eq.(3.5)) and a normalization factor $\tau = 1$:

$$\Phi^{\rm min}_{>E_{\rm th}} = 5 \cdot \frac{\sqrt{N_{\rm OFF}}}{N_{\rm ex}} \sqrt{\frac{T_{\rm OBS}\ [h]}{50\ h}} \cdot \Phi^{Crab}_{>E_{\rm th}}, \tag{3.6}$$

with $\Phi^{Crab}_{>E_{\rm th}}$ being the Crab Nebula integral flux obtained from $T_{\rm OBS}$ hours of observations. The integral sensitivity is usually expressed as a total fraction of $\Phi^{Crab}_{>E_{\rm th}}$, also called the Crab Nebula units (C.U.). Figure 3.13 shows the integral sensitivity of MAGIC Telescopes.

Differential sensitivity is calculated in the same way, but with $N_{\rm ON}$ and $N_{\rm OFF}$ extracted in bins of estimated energy E. For a sufficiently fine binning, the spectral dependence disappears.

3.3.7 Higher Level Products

Once the data has been cleaned, parametrized and reduced with the optimized analysis cuts, higher level results can be generated. For MAGIC, that means skymaps, light curves, integral and differential spectra, in the case of signal detection, or, otherwise, integral and differential upper limits. For the production of these results, however, it is necessary to know the response of the telescopes for gamma-rays of properties defined by the applied analysis cuts. Before describing in more detail higher level results of MAGIC Telescopes, properties of its *Response Function* (R) are briefly explained in the following Section.

3.3.7.1 Response Function

The response function of an IACT is governed by its hardware design, reconstruction algorithms, selection criteria for quality of the events and for discrimination between gamma-rays and hadrons. It is computed by means of full MC simulations and for each analysis separately, as it depends on the particular cuts applied to the data as well as on the overall technical settings and performance of the instrument at the time of the observations.

Response function is typically represented as a product of three different functions describing, for the given circumstances, the effective collection area $A_{\rm eff}$, angular resolution Σ and energy reconstruction parameters G:

$$R(E, \hat{p}; E', \hat{p'}, t) = A_{\rm eff}(E', \hat{p}, t) \times \Sigma(\hat{p}; E', \hat{p'}, t) \times G(E; E', \hat{p'}, t), \tag{3.7}$$

where E' and E are true and estimated energy, $\hat{p'}$ and $\hat{p}$ are the true and estimated direction of the incoming particle, and t refers to the time of the detection.

Effective Collection Area is the geometrical area around the telescope where gamma-ray shower produces a trigger ($A_{\rm sim}$), folded with the gamma-ray efficiency ε_γ of all the cuts

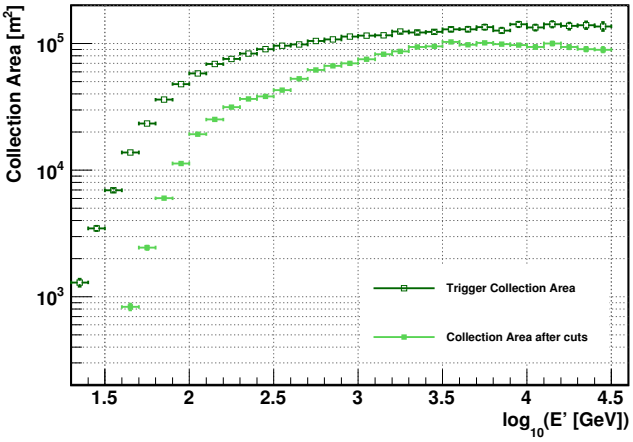

Figure 3.14: MAGIC effective collection area for stereoscopic observations and at $ZA < 30^\circ$. Dark green open squares show the collection area when only trigger efficiency is considered, while the light green full squares show the case when analysis cuts have been applied. Taken from [151].

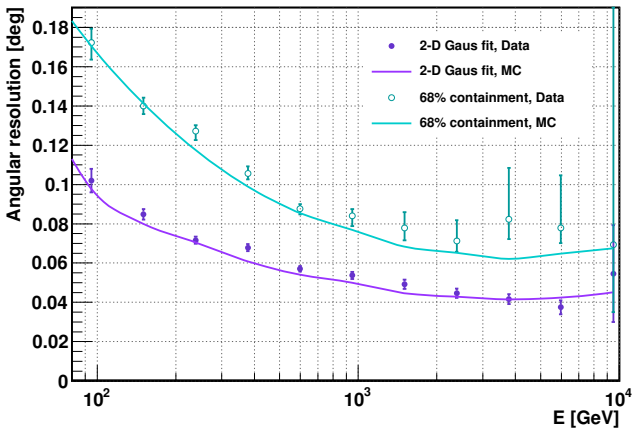

Figure 3.15: MAGIC angular resolution (violet) and 68% containment radius (cyan), as computed from a MC-simulated point-like source (lines) as well as from a Crab Nebula sample (circles). Taken from [151].

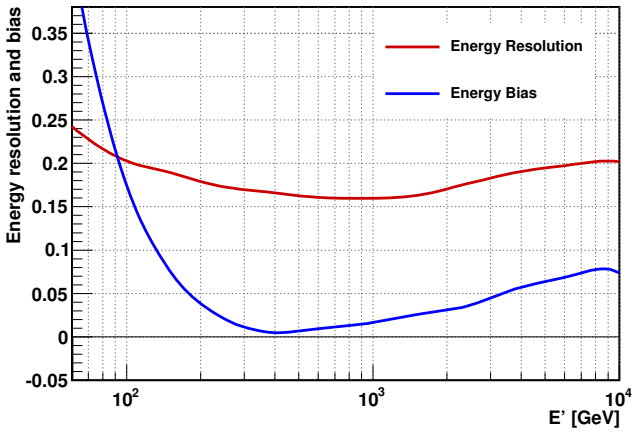

Figure 3.16: MAGIC energy reconstruction function, estimated by the means of LUTs. Red line represents the energy resolution, the blue one the energy bias. Taken from [151].

applied in the analysis. It mainly depends on the energy of the primary gamma-ray particles and the *ZA* of the observations:

$$A_{\text{eff}}(E', ZA) = A_{\text{sim}}\varepsilon_{\gamma} = A_{\text{sim}}\frac{N_{\gamma\text{AfterCuts}}}{N_{\gamma\text{Total}}}, \tag{3.8}$$

with ε_{γ} defined as the fraction of simulated MC gama-ray events that survive all the analysis cuts ($N_{\gamma\text{AfterCuts}}$) and the total number of produced events ($N_{\gamma\text{Total}}$). The more constraining the cuts, the lower the ε_{γ}.

A_{eff} is computed from MC sample and E' of the gamma-rays, and it is expressed in units of m^2. Figure 3.14 shows an example of A_{eff} for the MAGIC stereoscopic observations: probability to get a tigger increases very rapidly at low energies until all the showers in the light pool generate enough light to induce triggers, after which A_{eff} remains almost constant.

Angular Resolution is also referred to as the PSF of the telescope: it is the standard deviation of the 2-dimensional Gaussian fit to the sky distribution of a point-like source. The PSF corresponds to the radius containing 39% of the gamma-ray events from the source. Figure 3.15 shows the stereo angular resolution of MAGIC: for 300 GeV it is good as 0.07°, and even better at higher energies. For the sake of completeness, also shown is the 68% containment radius.

Energy Reconstruction is described by the *energy resolution* and *energy bias*. Energy resolution σ is defined as the width of a Gaussian fit to the $(E - E')/E'$ distribution, while the mean of that fit is the relative energy bias μ. The energy reconstruction is as good as it is close to the zero value. Distributions of σ and μ for MAGIC stereo observations are shown on Figure 3.17.

Additionally, E_{th} of the analysis is conventionally defined as the maximum peak of the energy distribution from the simulated gamma-ray *test* sample, once the background rejection and analysis cuts are applied. E_{th} strongly depends on the minimum cut in the *size* image parameter.

3.3.7.2 Skymap

Skymap refers to a 2-dimensional histogram that contains arrival directions, in sky coordinates, of all gamma-ray events that remain after the analysis cuts and after the subtraction of the expected background, smoothed with a Gaussian of width equal to the angular resolution at a given energy (Figure 3.17).

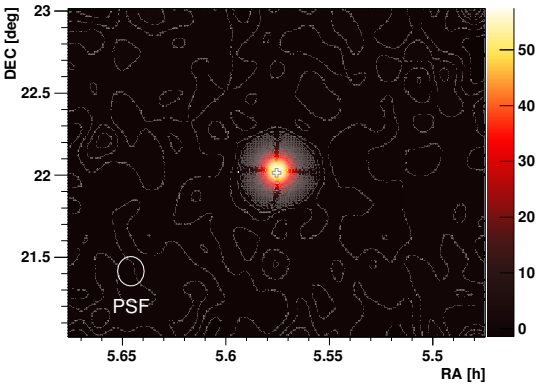

Figure 3.17: Example of the skymap obtained from the Crab Nebula data sample.

Skymap production relies on unbiased reconstruction of the arrival time provided by the *disp* parameter (§3.3.5.2), as well as on the correct modeling of the background, which often is not a straightforward task. The camera acceptance in general is not homogeneous, and this irregularity is additionally boosted by factors like field stars, malfunctioning pixels and trigger inefficiencies. Furthermore, dependence the sensitivity of the instrument has on the *ZA* must be taken into

account. For different observation modes (§3.2.1), background is estimated differently. For the *tracking* mode, background is built from the *OFF* sample, assuming an isotropic arrival direction of the events. In the *wobble* mode, the camera inhomogeneities are somewhat smoothed: for each wobble position, the camera is divided into two halves, one containing the source position and the other background events. From there, background is modeled only from the events whose arrival directions do not lie in the source part of the camera [176].

Skymaps of well-known sources are also used to check the mispointing of the instrument.

3.3.7.3 Spectra

The differential gamma-ray spectrum is defined as the total number of photons coming from the source and reaching the observer, in unit of energy, area and time:

$$\phi(E) = \frac{dN_\gamma}{dt_{\text{eff}} dA_{\text{eff}}(E) dE}, \tag{3.9}$$

where t_{eff} is the *effective observation time*, i.e. time during which telescope has been recording events, corrected for the dead time of the readout.

From the computational point of view, the differential treatment of A_{eff} in eq.(3.9) translates into fine energy binning. As for the dt_{eff} term, it is replaced by a single temporal bin, encompassing all the observation and of duration t_{eff}, when the emission from the source is considered to be steady.

Spectrum Unfolding is applied as a correction for the effects the finite energy resolution of the telescope and the existence of energy biases have on the obtained spectrum. It enables estimation of the true observable through the modification of the value of the measured one. There are different unfolding approaches implemented in the MAGIC analysis chain, namely, forward unfolding [177], Tikhonov [178], Bertero [179] and Schmelling [180] methods.

3.3.7.4 Light Curve

The variability of a source is estimated in terms of a light curve – the integral flux of the source presented in different time bins. All points of the light curve cover the same energy interval, $[E_{\text{min}} - E_{\text{max}}]$. For bin i, spanning over time interval $[t_m^i - t_n^i]$, the corresponding integral flux is calculated as:

$$\Phi^i(E) = \int_{t_m^i}^{t_n^i} \int_{E_{\text{min}}}^{E_{\text{max}}} \phi(E) dE dt. \tag{3.10}$$

This way of computing a light curve point only applies if the source is detected with enough significance in the given energy range and time interval. Otherwise, the calculated value is not the integral flux but an upper limit to the integral flux.

3.3.7.5 Upper Limits

Whenever no significant detection can be claimed, upper limits to the differential or integral flux of the source can be derived, with a certain confidence level (c.l.).

For the upper limit calculations, necessary input includes measured number of events from the source and background regions (N_{ON} and N_{OFF}, respectively), as well as the assumption on the energy differential spectrum, in simple form given as $\phi(E) = K \cdot S(E)$, where K is the normalization constant. Additionally, the time evolution of the possible emission is presumed to be constant over the period of observations.

In MAGIC analysis, the standard way to calculate upper limits is by estimating the number of gamma-ray events g in the *ON* region through the so-called Rolke method [181], also referred to throughout this work as the conventional approach (§4.1.1; eq.(4.1)). In addition, the expected differential spectrum is approximated by a simple power law of spectral slope α = -2.6 (Crab-like spectrum). From there, the integral flux upper limit can be expressed through the normalization constant K as:

$$K^{\mathrm{UL}} < \frac{g^{\mathrm{UL}}}{t_{\mathrm{eff}} \int\limits_{E_{\mathrm{min}}}^{E_{\mathrm{max}}} S(E) A_{\mathrm{eff}}(E) dE}. \tag{3.11}$$

As conventional method is a fully frequentist approach, uncertainties in the background estimation are treated as nuisance parameters. In MAGIC standard analysis chain, these uncertainties are set to 30%, based on the systematic errors of the analysis method whose efficiency is taken to be constant and equal to 1. The c.l. is by default chosen to be 95%.

However, the conventional method is only optimized for emissions with power law-like spectra. As a part of this work, a dedicated approach has been developed to maximize the analysis sensitivity for spectra with features; for detailed explanation, refer to Chapter 4.

It should be noted that the flux upper limit depends on the significance of the detection, given how the significance strongly dictates the upper limit to the number of estimated gamma-ray events, g^{UL} (for more details, see §4.1.1). Quantitatively, lower significance corresponds to lower (and therefore more constraining) upper limit.

3.3.8 Systematic Uncertainties

While for the weak sources main uncertainty in the analysis is caused by low statistics of excess gamma-ray events, for strong sources the systematic errors become the dominant ones. Principal factors contributing to systematic uncertainties can be grouped as:

- *Sources of systematic uncertainties on energy scale*: atmospheric transmission, insufficiently good knowledge on the current state of the hardware components (mirror reflectivity, QE of the PMTs, photon losses on the camera entrance (§3.1.1)) and effectiveness of analysis methods (signal extraction, calculation of the *F-factor* (§3.3.1), etc.).

- *Sources of systematic uncertainty on the flux normalization*: small discrepancies between the MC simulations and the data, background subtraction, camera inhomogeneities and faulty pixels, misspointing, NSB, dead time of the readout.

- *Sources of systematic uncertainty on spectral slope*: different efficiencies of various approaches applied in the analysis (different unfolding methods (§3.3.7.3), different efficiencies of the selection cuts (§3.3.3) and different *ZA* ranges). Also, it includes the uncertainties caused by the non-linearity of the pre-upgrade MAGIC-II readout (§3.1.3.1).

The overall systematic uncertainty depends on the energy. The precision of energy scale is 17% at low energies ($E \leq 100$ GeV) and ∼15% at medium ones ($E \geq 300$ GeV). For flux normalization, for low and medium energies, precision is 19% and 11%, respectively. As for the slope of the differential spectra, it is affected by the systematic uncertainty of 0.15.

3.3.9 Accessibility of the Analysis Results

Once the analysis has been completed, and its outcome cross-checked by other member(s) of the MAGIC Collaboration, the final results are made public. They can be accessed either in the printed form, through scientific journals, or in a digital form, as FITS files.

This Section describes in more detail the latter way of presenting MAGIC results, as the Author of this work has been the principle responsable for the development of the tools and maintenance of the database of the MAGIC results in FITS form.

3.3.9.1 FITS File Format

FITS stands for "Flexible Image Transport System" [182], and it is a digital file format used to store, transmit and manipulate scientific data sets. The format is created as self-defining and adaptable to changing needs that may arise from different applications. One of the FITS main features is that it can carry any number of n-dimensional data arrays (like 1-dimensional spectra, 2-dimensional images, 3-dimensional data cubes, ...). Furthermore, FITS stores all the metadata information associated with such matrices in a human-readable headers.

FITS structure is based on so-called Header and Data Units (HDUs), that contain the metadata information written as ASCII text, followed by an integer number of binary data records. The FITS file itself may be composed out of any number of HDUs, out of which the first one is the Primary header (PHDU) and the rest are the extensions. HDUs are defined based on their content and can be of the type IMAGE or BINTABLE.

The ASCII cards contained in the headers are 80 character fixed-length strings that carry keyword/value pairs. The keywords are used to provide information related to the data, such as its size, origin, coordinates, analysis details or anything else the creator might want to include. Some keywords are defined by the FITS standars (reserved keywords), while others may be generated according to the needs of the user.

3.3.9.2 FITS Format for MAGIC Data

First standardized in 1981, FITS is the most generally used format in the astronomy today. However, within the VHE astronomical community (and especially among the international collaborations operating the IACTs), it is not as popular. Reason for this probably lies in the fact that, historically, this field has been more close to the particle physics and its way of presenting the data. Nevertheless, in the last few years this trend has been gradually changing, particularly in the light of projected construction of the next generation IACT – the CTA. CTA is intended to operate as a "standard" astronomical observatory and to provide public access to significant portion of its data in the FITS form [183]. In the meantime, the IACTs of the current generation have been working, each one in their own way, on reproducing their results in the FITS format.

MAGIC Collaboration has its public FITS Database since 2008 [184]. It is based on a principle that for each scientific work, published by the Collaboration in a refereed international journal, there is one FITS file associated to it. The information contained in such FITS file are exactly the same, higher level results, as in the printed publication. The exception are the publications from some multi-wavelength or joint IACTs campaigns, where results from other observatories are presented as well. MAGIC does not publicly distribute such information, so the corresponding FITS files will only contain MAGIC data. Also, some particular, telescope-specific findings that, although present in the publication, are considered to be of no relevance for an external analyser, are excluded from the FITS file as well.

According to the MAGIC Standard [185], structure of the FITS file consists of the compulsory PHDU, followed by any number of extensions. The extension HDUs may contain skymaps (§3.3.7.2), integral and differential spectra (§3.3.7.3), integral and differential upper limits (§3.3.7.5), SEDs, light curves (§3.3.7.4), alpha-[3] and θ^2-plots (§3.3.5.3), and even other kinds of 1- or 2-dimensional distributions with user-defined magnitudes presented on the x and y axes.

Keywords that can be used in the PHDU and HDUs are defined in accordance with the MAGIC observations and analyses. Apart from some required and reserved words, some new, MAGIC (or IACT) specific variables are generated as well. For instance, PHDU contains general information about the FITS file itself: when and by whom it was created, to which publication it refers to, and what is its current version. Furthermore, it gives details about the observations (when did they take place, with which instrument and at which *ZA* range), about the source (its name, coordinates, periodicity and phase,...) and some global characteristics of the performed analysis (which energy range was considered, which cuts were used, what is the assumed c.l., t_{eff}, gamma-ray efficiency, etc). PHDU only contains information that is common for the entire file; everything that applies only to a certain higher level product(s) is written in the header of the corresponding extension(s) instead. Furthermore, aside from these general keywords, there are some that are specific for the given extension (like whether the spectrum is differential or integral, has the skymap been smeared with a Gaussian function and of what width...).

For the creation of MAGIC FITS files, a tool called `MFits` is used. `MFits` is written as a class of MARS (§3.3), and it relies on public libraries `CCfits` [186] and `cfitsio` [187]. Aside from creation of FITS files for the Database, `MFits` can also process the lower level results of MAGIC analysis, as well as make the two-way conversions between the FITS and ROOT format. At the moment, `MFits` is only available to the members of the MAGIC Collaboration.

3.3.9.3 MAGIC Data at the Virtual Observatory

Over the years, amount (and size) of data gathered by astronomical facilities was increasing, together with variety of scientific tools needed for the interpretation and analysis of different datasets. It was becoming evermore difficult for the astronomers to cope with such an overwhelming abundance. The issue was addressed through the creation of the Virtual Observatory (VO) - a collection of interoperating data archives and software tools which utilizes the internet to form a scientific research environment in which astronomical research programs can be conducted [188].

[3] Alpha-plot may be considered an mono-observations-equivalent to the θ^2-plot. As it is not used in this work, its details are omitted. More information can be found at [158].

The core components of the VO are finding what data is available and getting access to that data through simple requests. For this concepts to function, data has to be published in a VO-compliant form – that is, according to VO standards that make the data readable to many of the commonly used scientific tools. VO standards are set by the International Virtual Observatory Alliance (IVOA) [189], an organization that defines the protocols and coordinates the efforts of different VOs. At the moment, the VO standards are not adapted for the needs of IACTs: for instance, some of the required fields in the VO searches are not optimized for Cherenkov observatories, and some data types (like θ^2-plots) are not supported. However, these standards are constantly evolving in accordance with the needs of the astronomical community.

MAGIC public data is available in a VO-compliant form, either through the registry of the European Virtual Observatory [188] or directly from the MAGIC VO server [190]. For the time being, only spectrum and light curve protocols are supported, with the one for the skymaps being implemented. Data is provided to the user in the FITS format, with one file created for each search result. Tools that manage VO requests are also incorporated in the `MFits` class.

4

Full Likelihood Method

Cherenkov Telescopes are observatories that deal with great variety of scientific objectives – from detection and study of galactic and extragalactic gamma-ray sources to probing some of the most intriguing questions of the fundamental physics and cosmology. However, the duty cycles of these instruments are limited, and not all of the issues can be properly covered. The preference is usually given to the astrophysical objects of conventional origin, with spectral distributions nicely fitted, in the majority of cases, by a simple power law. As a consequence, standard analysis tools and methods are adapted for such signals, at the expense of sources whose emissions are predicted to contain some distinctive spectral features.

This Chapter is devoted to introduction of an alternative analysis method, *full likelihood*, optimized for recognition of spectral features in IACT observations. In the upcoming sections concepts and characterization of the full likelihood will be presented, as well as the comparisons of its performance with respect to the standard, *conventional* approach, currently deployed in the IACT analyses.

4.1 The Method

Observations with IACTs are dominated by the background. For each gamma-ray photon from the source (*ON*) region one may expect thousands of unwanted cosmic ray protons, majority of which are later removed through the analysis cuts (§3.3.5.1). The number of background events that remain in the data sample is estimated with high precision from the synchronous, or very similar (to the source) observations of control (*OFF*) regions from which no gamma-ray emission is expected (§3.2.1).

This Section describes how the acquired data are analysed by the conventional and by the full likelihood methods.

4.1.1 Conventional Analysis Approach

In the standard analysis chain of IACTs, the existence of a source is established by a mere comparison of the integrated number of events detected from the *ON* region (N_{ON}) with the integrated number of events from the *OFF* region(s) (N_{OFF}) (see §3.3.6, eq.(3.5)). Both N_{ON} and N_{OFF} are random variables that obey Poisson statistics; therefore, the actual number of gamma-ray (g) and background events (b) present in the *ON* region can be estimated through maximization of the following likelihood function [181]:

$$\mathscr{L}(g,b|N_{\mathrm{ON}},N_{\mathrm{OFF}}) = \frac{(g+b)^{N_{\mathrm{ON}}}}{N_{\mathrm{ON}}!}e^{-(g+b)} \times \frac{(\tau b)^{N_{\mathrm{OFF}}}}{N_{\mathrm{OFF}}!}e^{-\tau b}, \tag{4.1}$$

with τ denoting the normalization between the *ON* and *OFF* regions (e.g. ratio of their associated observation times).

This approach is what is currently used in the standard analysis of the IACTs (§3.3.7.5) and which is referred to, in this work, as the *conventional* approach. Whilst acceptable for sources of astrophysical origin, this method makes no distinction of the potential features present in the gamma-ray spectrum, and as such, it is suboptimal for studies where such features play a significant role (e.g. dark matter searches, §2.3.2.3).

4.1.2 Full Likelihood Method

As an alternative to the conventional approach, the *full likelihood* method is based on making an a priori assumption on the expected spectral shape (which is fixed for the chosen signal model), and including it in the maximum likelihood analysis. That way, the spectral information of the signal events if completely exploited, and the achieved sensitivity of the analysis increased with respect to that of the conventional method.

The full likelihood function has, for a given signal model M with parameters θ, the following form:

$$\mathscr{L}(N_{\mathrm{EST}},M(\theta)|N_{\mathrm{OBS}},E_1,...,E_{N_{\mathrm{OBS}}}) = \frac{{N_{\mathrm{EST}}}^{N_{\mathrm{OBS}}}}{N_{\mathrm{OBS}}!}e^{-N_{\mathrm{EST}}} \times \prod_{i=1}^{N_{\mathrm{OBS}}} \mathscr{P}(E_i;M(\theta)), \tag{4.2}$$

with N_{OBS} ($= N_{\mathrm{ON}} + N_{\mathrm{OFF}}$) and N_{EST} denoting the total number of observed and estimated events, respectively, in *ON* and *OFF* regions.

$\mathscr{P}(E_i;M(\theta))$ is the value of the probability density function (PDF) of the event i with *measured* energy E_i. In general, $\mathscr{P}$ can also depend on the measured arrival time and direction

of the photon. However, for the purposes of this work, contributions of those parameters are integrated out in the analysis (for more details, see §4.2.1.1). Therefore, the PDF is defined as a function of measured energy only:

$$\mathscr{P}(E;M(\theta)) = \frac{P(E;M(\theta))}{\int_{E_{\min}}^{E_{\max}} P(E;M(\theta))dE}, \tag{4.3}$$

where $E_{\min}$ and $E_{\max}$ are the lower and upper limits of the considered energy range. $P(E;M(\theta))$ represents the differential rate of the events, such that:

$$P(E;M(\theta)) = \begin{cases} P_{\mathrm{OFF}}(E_i), & i \in OFF \\ P_{\mathrm{ON}}(E_i;M(\theta)), & i \in ON \end{cases}, \tag{4.4}$$

with $P_{\mathrm{OFF}}(E)$ and $P_{\mathrm{ON}}(E;M(\theta))$ being the expected differential rates from the *OFF* and *ON* regions, respectively:

$$P_{\mathrm{OFF}}(E) = \tau \int_0^\infty \frac{d\Phi_B}{dE'} R_B(E;E')dE' \tag{4.5}$$

and

$$P_{\mathrm{ON}}(E;M(\theta)) = \int_0^\infty \frac{d\Phi_B}{dE'} R_B(E;E')dE' + \int_0^\infty \frac{d\Phi_G(M(\theta))}{dE'} R_G(E;E')dE'. \tag{4.6}$$

True energy is denoted with E'. $d\Phi_B/dE'$ and $d\Phi_G/dE'$ are the differential fluxes of cosmic (background) and gamma-ray (signal) emissions, and $R_B(E;E')$ and $R_G(E;E')$ are the telescope response functions to each of them (§4.2.1.1). In practice, the response of the instrument can be different for the background events coming from the *ON* and from the *OFF* regions (see §4.2.7). $d\Phi_G/dE'$ contains the dependencies on the model parameters θ.

Apart from the shape of the spectral distribution, the given signal model $M(\theta)$ also predicts the expected number of detected events for a given observation time T_{OBS}:

$$N_{\mathrm{EST}} = T_{\mathrm{OBS}} \int_{E_{\min}}^{E_{\max}} P(E;M(\theta))dE, \tag{4.7}$$

included in the full likelihood function (eq.(4.2)) through the Poisson term.

4.1.2.1 Full vs. Conventional Likelihood Approach

Primary difference between the conventional and full likelihood methods can be illustrated with Figure 4.1: both likelihoods are based on comparisons of the collected data with the predictions from the signal and background models. However, while the conventional approach integrates the spectral information in a pre-optimized energy range (for more details, see §4.2.3), and compares the expected and measured *number of events*, the full likelihood compares the expected and measured *energy distributions*, thus completely profiting from the potential presence of spectral features.

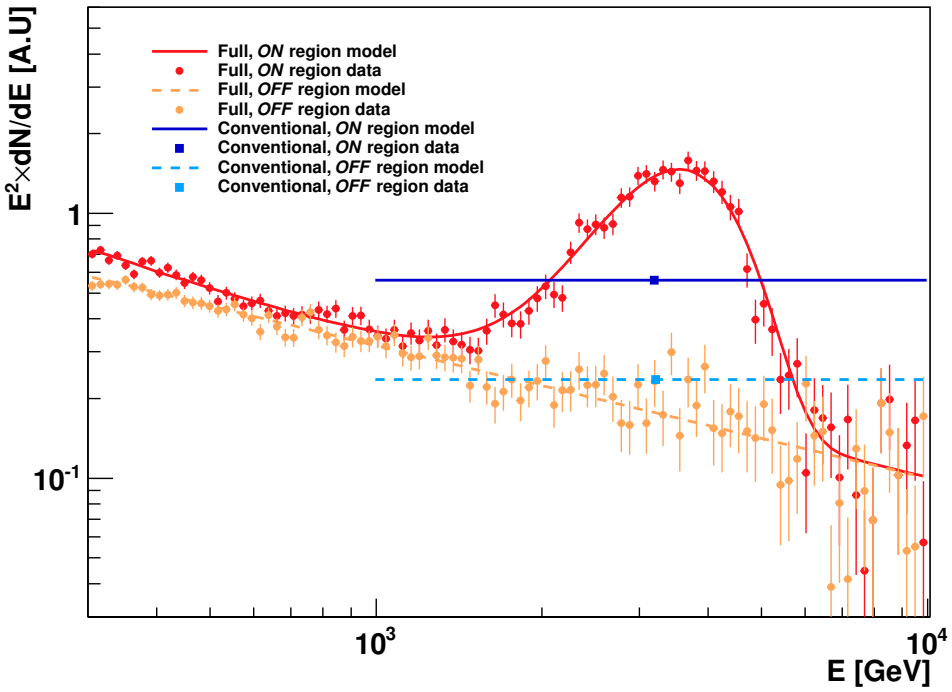

Figure 4.1: Illustration of the advantage the full likelihood method has over the conventional one. Red and orange lines show the assumed spectral energy distributions of the *ON* and *OFF* regions, respectively, while the data points, with the same color code, represent the measured events (fine binning is used for the demonstration purposes only – the full likelihood is unbinned). The levels of horizontal blue and cyan lines correspond to the average value within the energy range considered in the conventional method, with points referring to the measurements. See the main text for more details.

Lastly, for the comparison of the full likelihood with the conventional analysis, it should be noted that their parameters relate as:

$$b = \frac{T_{\mathrm{OBS}}}{\tau} \int_{E_{\mathrm{min}}}^{E_{\mathrm{max}}} P_{\mathrm{OFF}}(E) dE \tag{4.8}$$

and

$$g(\theta) = T_{\mathrm{OBS}} \int_{E_{\mathrm{min}}}^{E_{\mathrm{max}}} P_{\mathrm{ON}}(E; M(\theta)) dE - b. \tag{4.9}$$

4.2 Characterization

In this Section, in order to evaluate the performance of the proposed full likelihood concept, its properties are tested using fast simulations produced under a predefined set of conditions, and the results compared to those of the conventional method obtained under the exact same circumstances.

4.2.1 The setup

4.2.1.1 Response Functions

As already described in §3.3.7.1, the response functions of an IACT for the background and gamma-ray events (R_B and R_G, respectively), depend on the properties of the instrument itself, on the effectiveness of its analysis procedures and on the analysis cuts applied in the given case.

Response function is usually depicted as the combination of the effective area $A_{\rm eff}(E', \hat{p}', t)$, angular $\Sigma(\hat{p}; E', \hat{p}', t)$ and energy $G(E; E', \hat{p}', t)$ reconstruction functions (eq.(3.7)). However, the focus of this work is on potential dark matter sources, that are expected to be steady, so the time component can be integrated out. As for the spatial signatures, they may have a more relevant role for, e.g. galaxy clusters [128, 191], as they can be predicted from the halo simulations (although, usually with great uncertainties). Still, the analysis presented here is oriented towards source-candidates of angular size smaller or comparable to the typical PSF of the IACTs ($\sim 0.1^\circ$) – hence, the contribution of the likelihood function dependent on the direction is not expeced, and can be integrated out as well. Therefore, the response function depends on the energy only:

$$R_{B,G}(E; E') = A_{\rm eff_{B,G}}(E') \times G_{B,G}(E; E'). \tag{4.10}$$

For the characterization of the full likelihood method, as representative response function of a current-generation IACT, the approximation of the corresponding functions of the MAGIC Telescopes (§3.3.7.1) is used.

Background uncertainties As already mentioned, the R_B functions entering eq.(4.5) and eq.(4.6) may differ – this is due to their dependencies on the direction of the incoming particles. Such discrepancies are measurable by the telescopes with relatively high precision, and the residual and systematic uncertainties can be taken into account in the likelihood function through inclusion of the relevant nuisance parameters.

For the characterization purposes, it is assumed that the background is known without the uncertainties. However, the effects those uncertainties may have on the results are studied in §4.2.7.

4.2.1.2 Spectral Functions

Spectral distributions needed for the full likelihood maximization are the ones of the background, $d\Phi_B/dE'$, and of the signal, $d\Phi_G/dE'$ (eq.(4.5) and eq.(4.6)).

Background The background emission is produced by the cosmic rays, with a flux well described by a simple power law:

$$\frac{d\Phi_B}{dE'} = A_B E'^{-\alpha}, \tag{4.11}$$

with spectral index α and intensity A_B. In practice, however, the exact values of these parameters are not strictly necessary, since the needed value of $P_{\rm OFF}(E)$ (eq.(4.5)) is directly measured by the IACTs (or computed from Monte Carlo simulations for projected instruments).

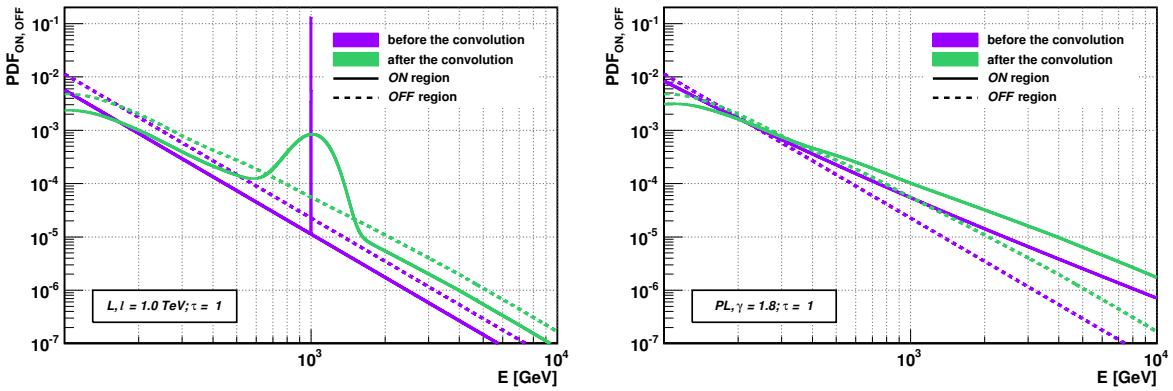

Figure 4.2: Contributions of the *ON* (full line) and *OFF* regions (dashed line) to the PDF, before (purple) and after the convolution (green) of the spectral function with the response function of the telescope. **Left**: A monochromatic line is smoothed and widened due to the finite energy resolution. **Right**: The spectral slope of a power law-shaped signal is harder after the convolution. Shape of the background (**left** and **right**) is also affected by the response function.

Signal For the characterization purposes, two simple cases of signal emission are considered:

- a monochromatic line (L) at energy l and of intensity A_L:

$$\frac{d\Phi_G}{dE'} = A_L \delta(E' - l); \tag{4.12}$$

- power law (PL) of spectral index γ and intensity A_{PL}:

$$\frac{d\Phi_G}{dE'} = A_{PL} E'^{-\gamma}. \tag{4.13}$$

The convolution of the spectral and response functions yields the form of the PDF. As seen in Figure 4.2, the original spectral shapes are modified by the imperfect instrument, with features like line being smoothed and hardness of the power law being altered.

4.2.1.3 Improvement Factor

In order to quantify the performance of the full likelihood with respect to that of the conventional approach, the *Improvement Factor* (IF) is defined as

$$IF(M(\theta)) = \langle CI_{\text{cnvn}} / CI_{\text{full}} \rangle, \tag{4.14}$$

i. e. the average ratio of the widths of the confidence intervals, CI_{cnvn} and CI_{full}, each calculated by the corresponding method.The CIs are estimated as two-sided and following the "$ln\mathscr{L} + 1/2$" rule, assuming a common c.l. and one unconstrained degree of freedom. In this work, the free parameter is chosen to be the signal intensity – for the characterization, that is A_L for the monochromatic line signal, and A_{PL} for the power law-shaped emission.

By construction, Improvement Factor is the *improvement in the sensitivity* of a given search expected from the use of full likelihood over the conventional approach. In practice, this can be translated to, e.g. total observational time: an 40% sensitivity gain achieved through the full likelihood method is equivalent to the results of the conventional analysis applied to twice as much data.

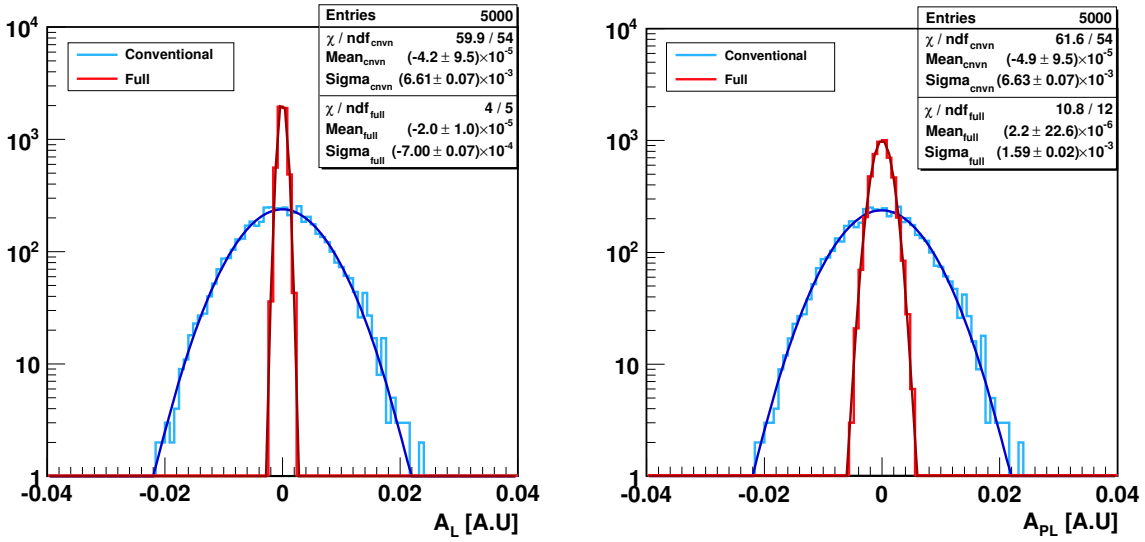

Figure 4.3: Distribution of the free parameter values estimated by the conventional (blue) and full likelihood methods (red), for line at energy $l = 1$ TeV (**left**) and power law of spectral slope $\gamma = 1.8$ (**right**) signal emission models.

4.2.1.4 Experimental conditions

For the characterization of the method, unless specified otherwise, the confidence intervals are calculated with 95% c.l., and their ratio averaged from 25 fast-simulated experiments. Each simulations consists of 10^5 events, randomly generated according to the PDF describing the expected background (i.e. the expected value of the signal intensity is zero). The background normalization is set to $\tau = 2$, and the considered energy range is between $E_{\min} = 100$ GeV and $E_{\max} = 10$ TeV. The maximization of the likelihood functions (eq.(4.1) and eq.(4.2)) is performed using the `TMinuit` class incorporated in the framework of ROOT [192, 193].

4.2.2 Bias

The concept of the Improvement Factor makes sense only if both full likelihood and conventional approach produce unbiased estimators. This can be tested by checking how well results of each of the methods approximate to the actual value of the free parameter used for the simulation of the events. Figure 4.3 shows the distributions of the free parameter values, A_L for the line signal model and A_{PL} for the power law-shaped one, calculated from 5000 experiments each. The events were generated assuming that there is only background in the data sample – therefore, having the distributions of the signal amplitudes peak at zero indicates that the analyses are unbiased.

4.2.3 Optimization of the Integration Range

In order to make a fair comparison of the performances of the full likelihood and conventional approaches, only the most constraining results from each method should be taken into the account. By definition, the full likelihood takes complete advantage of the signal spectral information; therefore, it makes sense to expect that maximal sensitivity with this method is achieved when the whole energy range is considered. For the conventional con-

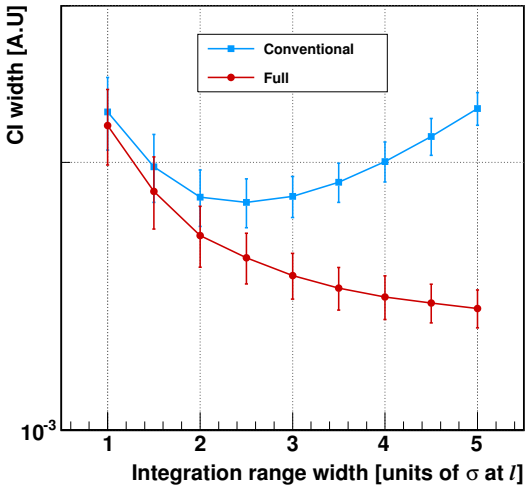

Figure 4.4: Mean widths of the *CI*s, calculated by the conventional (blue) and the full likelihood (red) methods, as a function of the integration range given in units of σ around the line energy $l = 1$ TeV. Error bars are the RMS of the *CI* distributions.

cept, however, this does not have to be the case, especially if some distinctive features are expected in the spectra.

The following tests are devoted to the estimation of the performances of each of the two approaches for different energy integration ranges. For a chosen model and a given method, the optimal integration range is the one resulting in the best sensitivity.

4.2.3.1 Line

In the case of a line signal model, the sensitivity of likelihood analyses is optimized by restricting to those events in the vicinity of the peak. Figure 4.4 shows the *CI* widths of the conventional and full likelihood approaches, as a function of the integration range width centered at l. Given how the ability of the instrument to distinguish characteristic spectral features, like lines, are determined by its resolution at the corresponding energies, the integration range width is expressed in units of σ.

As expected, the full likelihood is best favoured when the entire energy range is considered (out of the range in Figure 4.4). On the other hand, the conventional approach is most sensitive for a particular, limited range: in the case of a line at $l = 1$ TeV, the optimal integration range is 2.5σs wide.

4.2.3.2 Power Law

For the power law-shaped signal models, the optimization can be done by fixing one integration limit while varying the other. Figure 4.5 shows the mean values of *CI*s, calculated by each method, for a signal model of spectral slope $\gamma = 1.8$ and the integration range of fixed E_{min} (left) or fixed E_{max} (right). Again, in both cases, the full likelihood is best favoured when the entire energy range is considered. As for the conventional approach, the scenario with fixed E_{max} and optimized E_{min} yields the best sensitivity.

Power Law with the cutoff Regarding the models where continuous, power law-shaped emission abruptly ceases at a certain energy, the usual practice is to set the upper limit of the

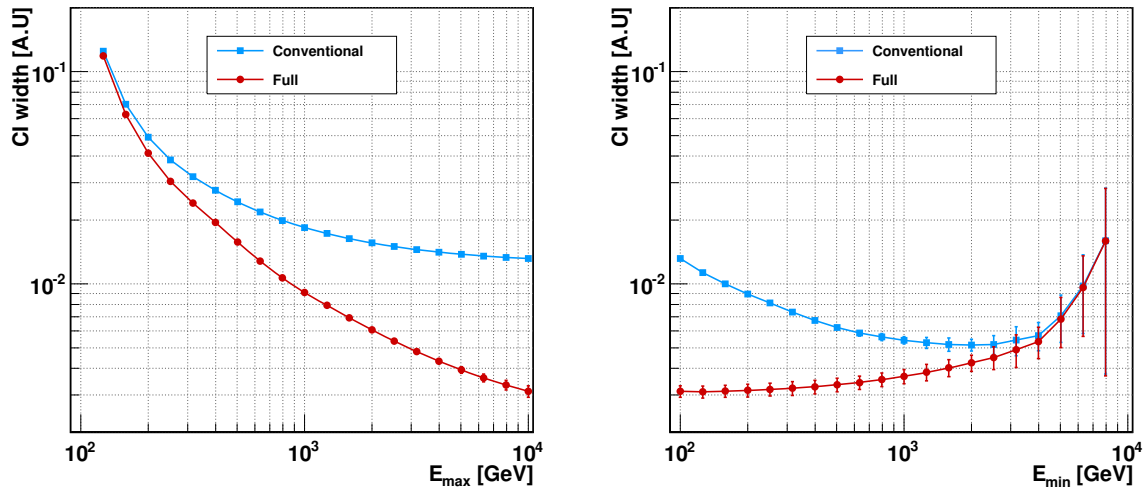

Figure 4.5: Mean widths of the *CI*s, calculated by the conventional (blue) and full likelihood approach (red), as a function of integration range when E_{min} (**left**) or E_{max} (**right**) is fixed. The considered signal model is a *PL* of spectral slope $\gamma = 1.8$. Error bars are the RMS of the *CI*s distributions.

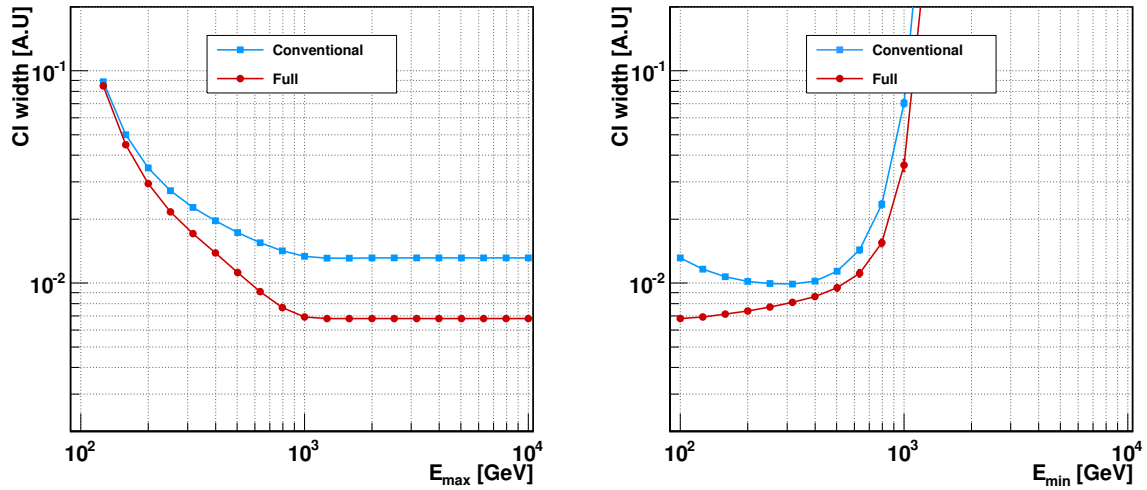

Figure 4.6: Mean widths of the *CI*s, calculated by the conventional (blue) and full likelihood approach (red), as a function of integration range when E_{min} (**left**) or E_{max} (**right**) is fixed. The considered signal model is a *PL* of spectral slope $\gamma = 1.8$ and with an energy cutoff at 1 TeV. Error bars are the RMS of the *CI*s distributions.

integration range to the energy of the cutoff. However, as seen in Figure 4.6, the conventional method is more constraining if this limit is just above the cutoff, and the lower one is again optimized for the given signal model. The full likelihood is again the most sensitive for the integration of the entire available energy range.

The Improvement Factor values given in the following Sections are always calculated from the most constraining upper limits of both methods, using the entire energy range for the full likelihood and the optimized one for the conventional approach.

4.2.4 Improvement Factor for different signal models

The following tests compare the sensitivities of the conventional and full likelihood methods for various power law and line-shaped signal models.

4.2.4.1 Line

For the line models, depending on the line energy l, the Improvement Factor values range between 40% and 65% (Figure 4.7). The dashed line refers to the optimal integration range width for the conventional approach (in units of σ at l). It is interesting to note that this width is almost constant for all the models and of order of 2.5-3 (Figure 4.8).

4.2.4.2 Power Law

The Improvement Factor values for *PL* signal models depend on the slope of the spectral index γ (Figure 4.9). The softer the spectrum, the lower the gain full likelihood provides over the conventional approach. For instance, for the chosen characterization setup, for the case when $\gamma \approx 3.6$, the shapes of signal and background differential rates are very alike, and therefore the improvement one achieves from the use of the full likelihood is almost negligible. For the harder spectral slopes the advantage of the full likelihood over the conventional one is far more significant, with Improvement Factor values of up to $\sim 70\%$. The dashed line indicates the value of E_{min} for which the conventional method yields the most constraining limit for a given model. As seen in Figure 4.10, for expected signal emissions of harder spectral indices, that dominate over the background radiation at higher energies, the conventional approach is optimized for the upper end of the energy range. For increased γ, differences between the signal and background concentrate at lower energies, so integration of the entire energy range is preferred.

4.2.4.3 Additional Features

The spectral shape of the signal can be further elaborated by including additional features of physical interest. For instance, there can be a sharp cutoff in the spectral distribution, smoothed by the response function of the detector. Figure 4.11 considers the case of *PL* models with different spectral slopes γ that all have a cutoff at a fixed energy of 1 TeV. In the presence of a cutoff, the Improvement Factor is lower than in the case of uninterrupted *PL* emission. This is especially noticeable for those signal models that dominate at high energies ($\gamma > \alpha$), since their distinction from the background is partially erased by the cutoff. For the softer spectra, this effect is not that evident, as for those cases signal is more distinguishable from the background at lower energies, i.e. well bellow the cutoff.

The dependency of the Improvement Factor value on the position of the cutoff itself is shown on Figure 4.12: for hard spectra, the higher the cutoff, the greater the gain from the use of the full likelihood. Nevertheless, loss of the signal events due to the cutoff always keeps the Improvement Factor below the value of that for the corresponding *PL* model without the cutoff. As for the softer spectra, the improvement is enhanced by low-energy cutoffs to levels comparable to those obtained for spectral lines at similar energies.

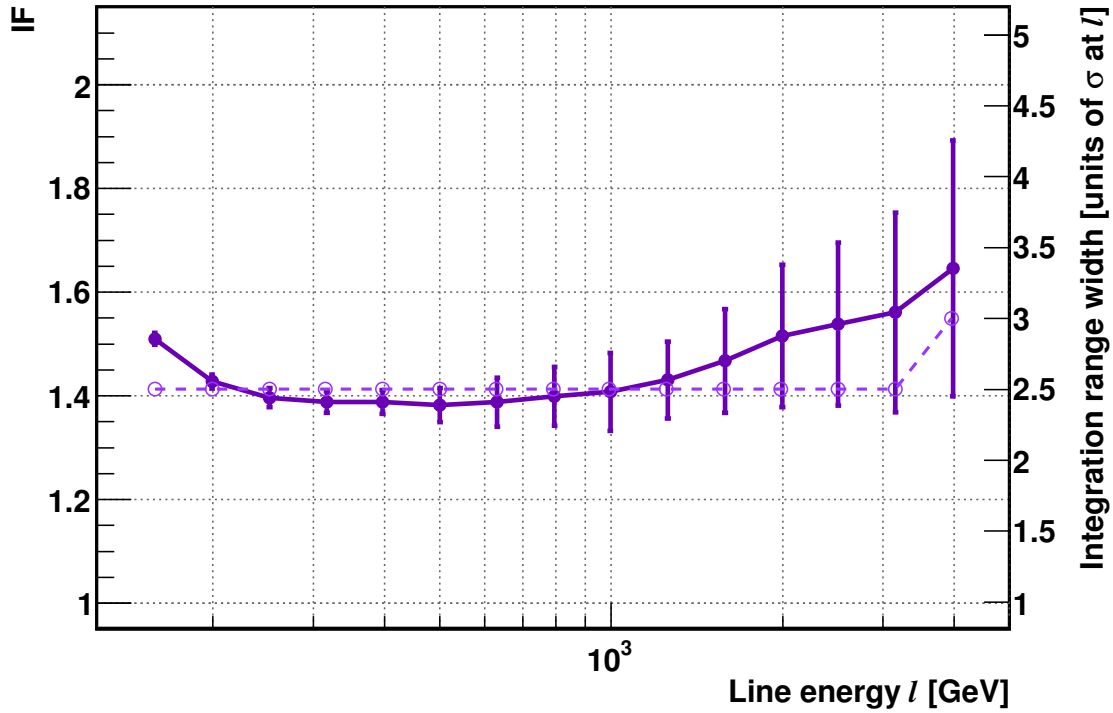

Figure 4.7: Improvement Factor for different L signal models (full line). Also shown are the optimal integration range widths for the conventional approach for the considered models (dashed line, right-hand axis). Error bars are the RMS of the IF distributions.

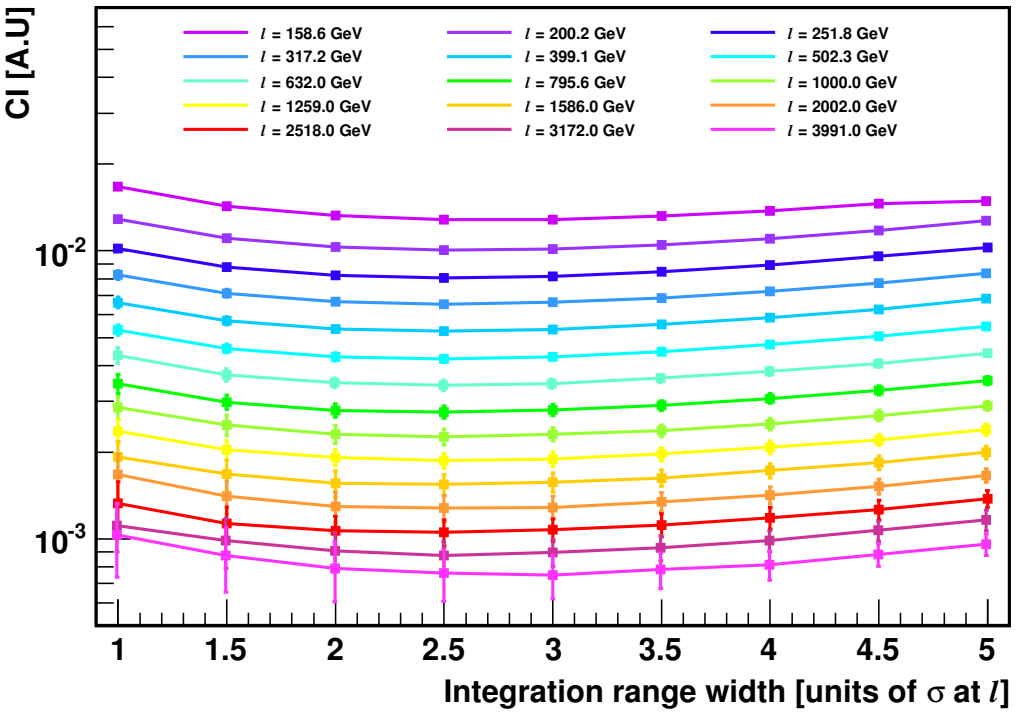

Figure 4.8: Widths of the CIs, calculated by the conventional method as a function of the integration range width, for different L signal models. Error bars are the RMS of the CIs distributions.

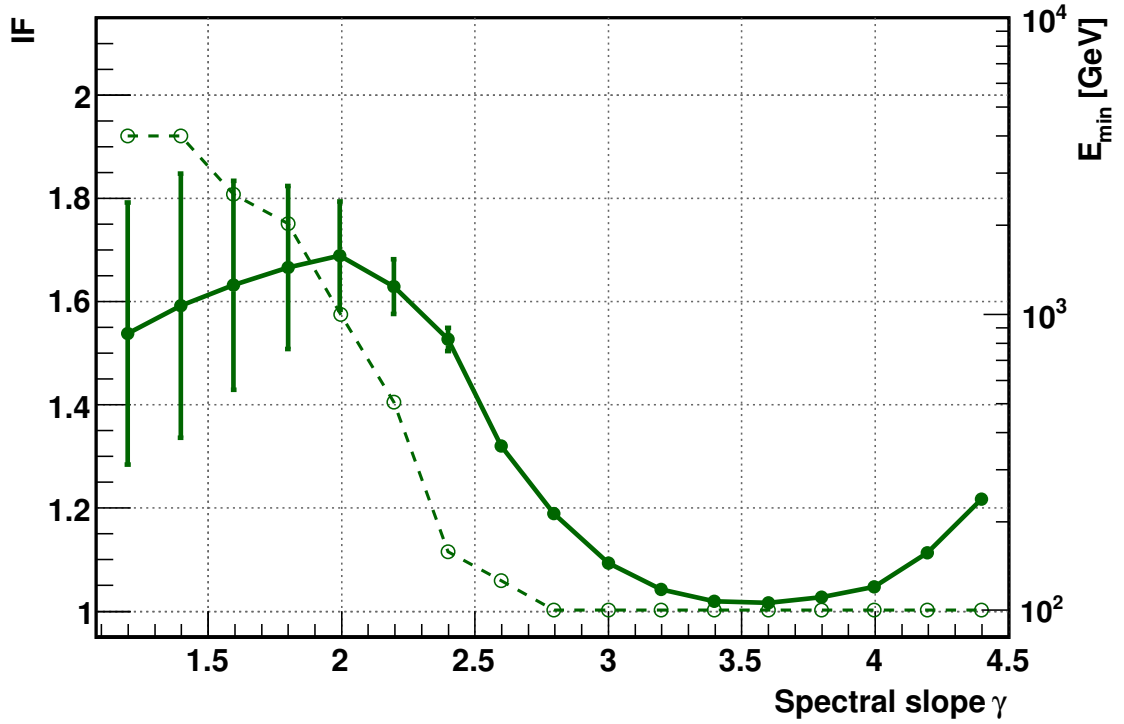

Figure 4.9: Improvement Factor for different *PL* signal models (full line). Also shown are the optimal values of E_{min} for the conventional approach for the considered models (dashed line, right-hand axis). Error bars are the RMS of the IF distributions.

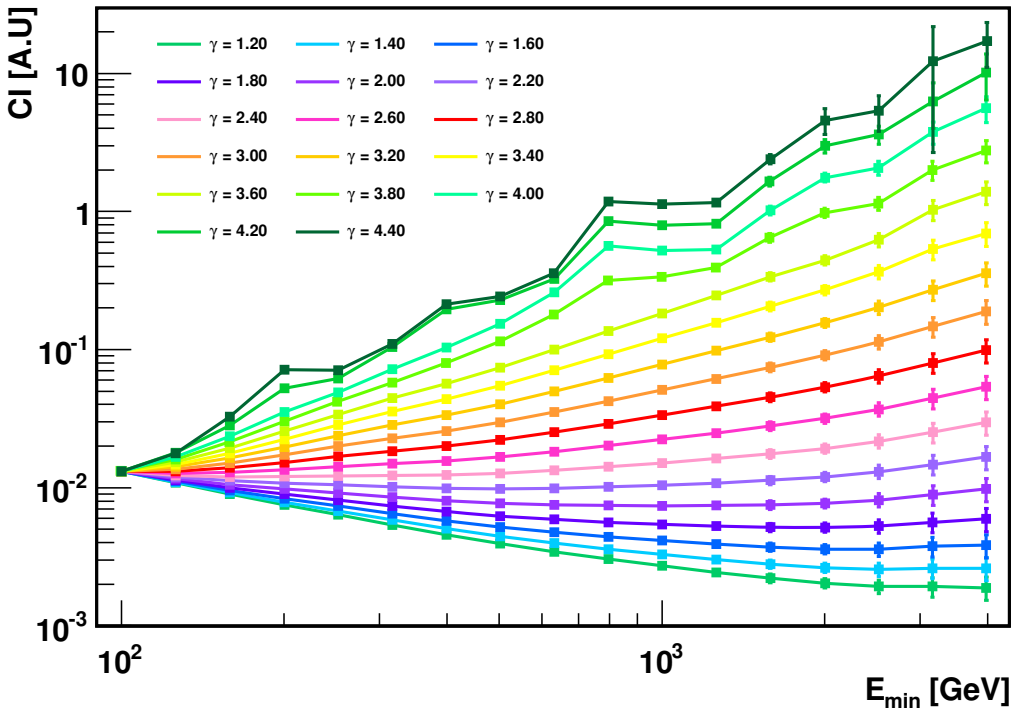

Figure 4.10: Widths of the *CI*s, calculated by the conventional method as a function of the lower integration range limit, for different *PL* signal models. Error bars are the RMS of the *CI*s distributions.

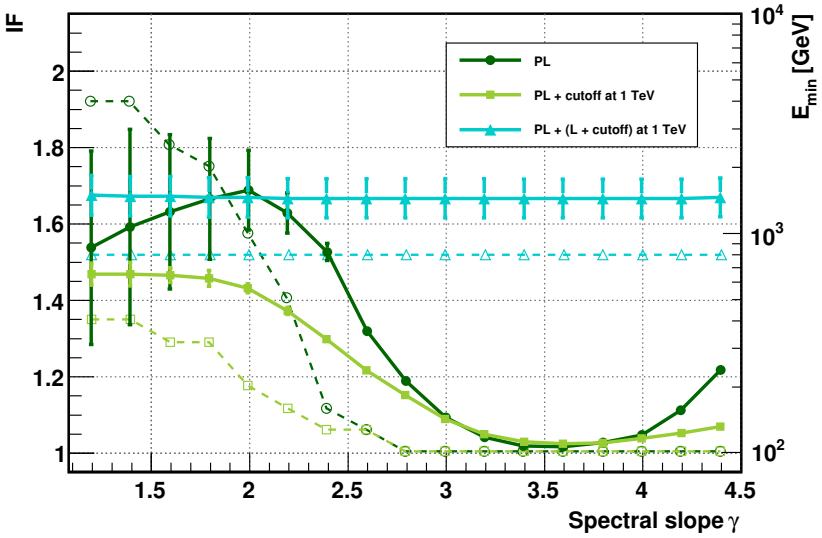

Figure 4.11: Improvement Factor as a function of spectral slope γ for different signal models (full line). Also shown are the optimal values of E_{min} for the conventional approach for the considered models (dashed line, right-hand axis). Error bars are the RMS of the IF distributions.

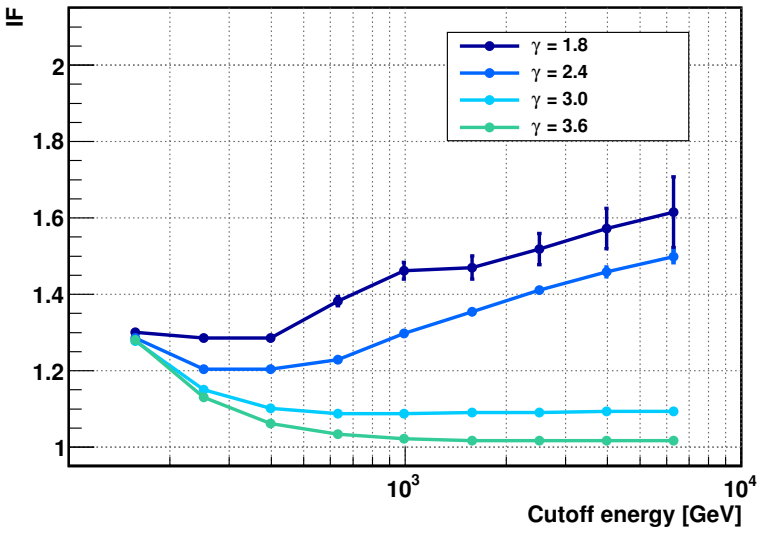

Figure 4.12: Improvement Factor as a function of cutoff energy for different *PL* signal models. Error bars are the RMS of the IF distributions.

Lastly, the effect of adding a line to a power law-with-the-cutoff spectral distribution is examined. For such models, the overall signal intensity is taken as the free parameter, while the individual amplitudes of the power law (A_{PL}) and line contributions (A_L) are set in such a manner that the integrated areas corresponding to those emissions in the PDF are equal. As shown in Figure 4.11, presence of a line at the same energy as the cutoff ($l = 1$ TeV) significantly boosts the Improvement Factor value, especially for soft spectra. Its contribution is obvious from the optimal E_{min} distribution as well: regardless of the value of γ, the most constraining limits from the conventional method are achieved when E_{min} is just below the line, seeing how this feature is the one dominating the Improvement Factor value.

4.2.5 Stability

Previous Sections dealt with variations of the signal models; this one examines the dependence of the Improvement Factor value on parameters not affiliated with the model itself, but, instead, with experimental conditions, like observational setup, characteristics of the instrument and choice of the analysis cuts. Also, powers of the full likelihood and the conventional one are tested and compared for the situation when there is a signal in the data.

Background normalization τ refers to the ratio between the number of events from *ON* and *OFF* regions. In the first approximation, it can simply be the number of *OFF* regions chosen (in the observational scheme or in the analysis (§3.2.1, §3.3.6)) for the estimation of the background emission in the *ON* region. More *OFF* regions means greater statistics, and consequently, one can also expect more constraining results from the analyses. Figure 4.13 shows the dependence of the Improvement Factor on the value of τ, for the case of hard power law-shaped spectrum ($\gamma = 1.8$). As it can be seen, the greater the τ, the lower the gain provided by the full likelihood method. The same conclusion applies to the line signal models. On the other hand, soft power law-shaped signals are not significantly affected by the τ (Table 4.1).

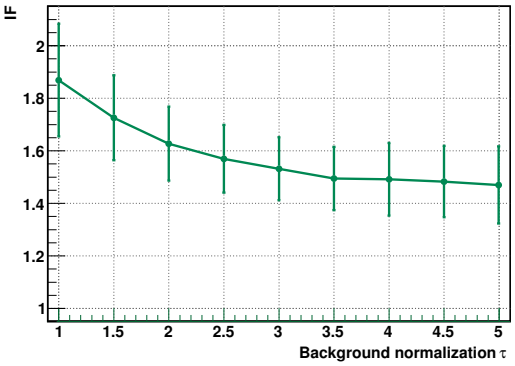

Figure 4.13: Improvement Factor dependence on the background normalization τ value, for a *PL* signal model of spectral slope $\gamma = 1.8$. Error bars are the RMS of the IF distributions.

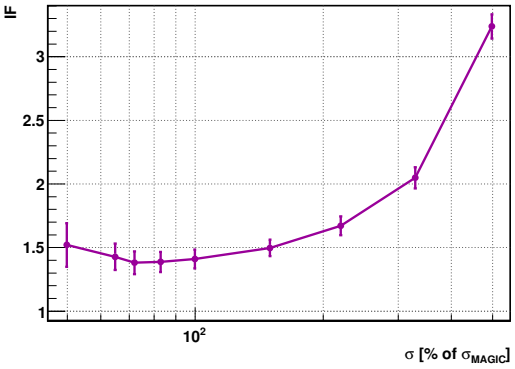

Figure 4.14: Improvement Factor dependence on the energy resolution σ of the instrument, for *L* signal model centered at energy $l = 1$ TeV. Error bars are the RMS of the IF distributions.

Number of events chosen for the characterization (10^5 events) translates to $\sim$200 hours of data, assuming the described setup (§4.2.1). This number, however, strongly depends on the chosen instrument and applied analysis cuts (in particular, on the energy threshold of the analysis (§3.3.5.3)). Nevertheless, the number of the events included in the likelihood functions does not play a significant part in the overall Improvement Factor value (Table 4.1).

Energy resolution σ of a given instrument reflects its ability to distinguish characteristic spectral features. It is therefore expected to have the value of the Improvement Factor for line signal models dependent on the σ of the detector. As seen from Figure 4.14, the worse the σ, the greater the improvement. It must be clarified, however, that this does not imply that a poor resolution yields more constraining results (for neither of the studied likelihoods), but that the advantage of the full likelihood over the conventional one is more significant.

Parameter	Variation Range [units of the parameter]	IF PL, $\gamma = 1.8$	IF PL, $\gamma = 3.6$	IF L, $l = 1$ TeV
τ	1 - 5	1.91 - 1.47	1.02 - 1.01	1.63 - 1.26
Number of events	5×10^4 - 5×10^6	1.66 - 1.62	1.03 - 1.02	1.43 - 1.41
σ [% of σ_{MAGIC}]	50 - 500	1.65 - 1.66	1.01 - 1.11	1.37 - 3.23
E_{max} [TeV]	10 - 50	1.65 - 1.82	1.01 - 1.02	1.40 - 1.41
S [standard deviations]	0 - 5	1.65 - 1.75	1.01 - 1.01	1.40 - 1.42

Table 4.1: Dependence of the Improvement Factor on different experimental parameters for three different representative signal models.

Regarding the power law-shaped emissions, as they have no relevant features that might be subjected to the effects of energy resolution, the Improvement Factor values do not significantly depend on σ (Table 4.1).

Energy range maximum E_{max} of the given analysis depends on the chosen cuts. For the line signal models, expansion of the total energy range only adds more background, and the Improvement Factor value is not significantly affected (Table 4.1). Same goes for soft power law-shaped spectra, that are distinguished from the background only at lower end of the energy range. Hard spectral emission, however, dominate at high energies, and the increase of the energy range also means the greater Improvement Factor.

Significance of the detection S is considered as another variable that may influence the Improvement Factor value. The presence of a signal sufficiently strong to be detected with significance of up to 5 standard deviations, yields, for line and soft power law models, no relevant change in the Improvement Factor value. For the hard power law-shaped spectra, there is some effect: increase in the signal intensity allows for an up to 10% increase in the Improvement Factor as well (Table 4.1). This can be understood from the fact that, as a consequence of the energy range optimization (performed over the sample containing only the background events), conventional method may lose some gamma-ray events that, on the other hand, are by default included in the full likelihood maximization (§4.2.3.2).

4.2.6 Robustness

The robustness of the full likelihood is questioned by assuming that the response function of the instrument is not precisely known. For the following tests, the events are simulated with one response function, R_0, while a different (wrong) one, R_W is used for the likelihood maximization. Data are generated so that they contain a gamma-ray signal of intensity that yields a 5σ detection for $R_0 = R_W$. Studies below describe how the significance of the detection by the full likelihood degrades when $R_0 \neq R_W$.

Effective area A_{eff} Let the effective area function, assumed to describe the response of the detector, be shifted for a fixed energy interval with respect to the actual A_{eff}. As a result, the sensitivity of the detection is decreased, for power law-shaped signal models, by up to 5% for a 50 GeV shift. The effect on the line-like models is not significant (less than 1%, Figure 4.15).

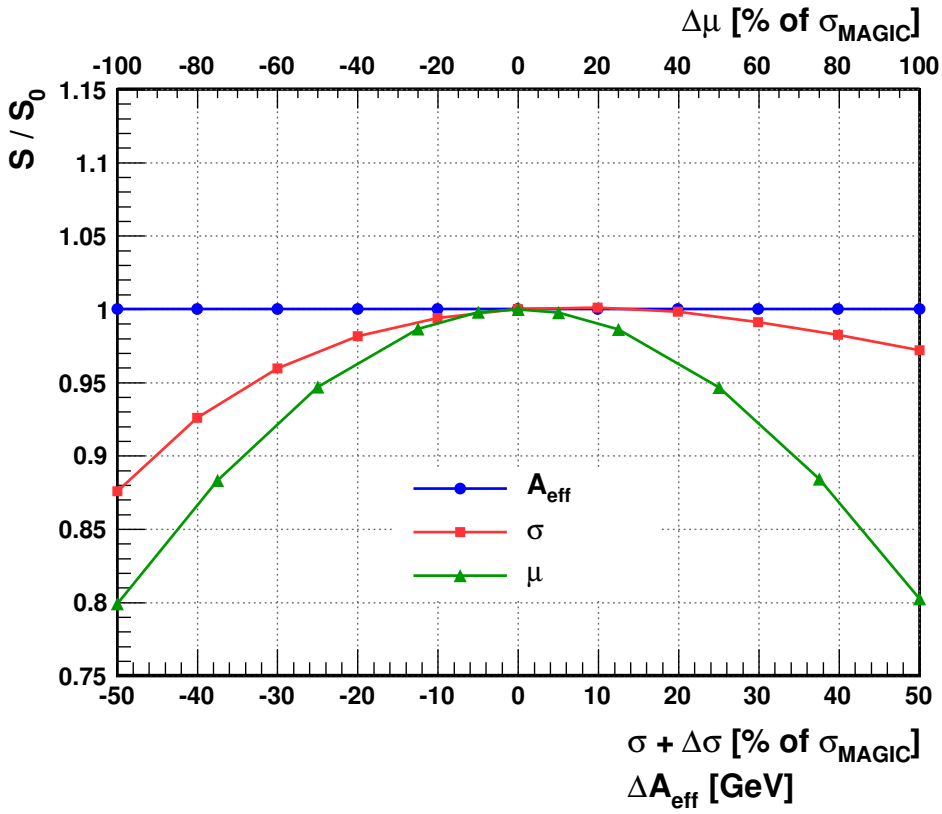

Figure 4.15: The full likelihood sensitivity decrease as a result of not precisely known effective area (blue), energy resolution (red) or energy bias (green) of the detector. The considered case is of the line signal model, with $l = 1$ TeV.

Energy resolution σ Next, the case of unknown σ is considered: a factor 2 mistake in the estimate of the energy resolution leads to up to $\sim$10% worst sensitivity for line-like models (Figure 4.15). For power law spectra, a σ wrong by the same factor has no significant effect – less than 1% sensitivity decline.

Energy bias μ Lastly, different μ functions are presumed for the simulation and for the likelihood analysis. Findings show that, for μ values shifted from the actual ones by 1σ at a given energy, the sensitivity of the analysis decreases $\sim$5% (Figure 4.15). If the shift is 2σ, the decline is up to 20%. This means that, for instance, when searching for a line in the spectrum, steps wide as up to 1σ can be made in the scan without risking a significant sensitivity degradation.

Having in mind that even under these extreme and conservative conditions, the worsening in the sensitivity of the full likelihood method is still smaller than the gain its use provides, it may be concluded that this method is robust.

4.2.7 Background

As mentioned in §4.2.1.1, background in the *ON* region may be known within some uncertainties. This Section estimates the effect these uncertainties can have on the results of the conventional and full likelihood methods.

First, the energy-dependent differences between the R_B functions for *ON* and *OFF* regions are considered. For their parametrization, an extra power law term multiplying the first in-

tegral in eq.(4.6) is added. Its index is introduced in the likelihood functions as a nuisance parameter, with Gaussian probability distribution of mean 0 and width 0.04 (so that maximum deviation of 5% is achieved at any energy). This results in the sensitivity decrease for both the full likelihood and the conventional method, but more drastically for the latter one: for the case of line-like models, as well as the hard power law-shaped spectra, results from the conventional approach are up to $\sim$ 50% less constraining. For the full likelihood, the corresponding sensitivity losses are smaller: $\sim$ 5% for line and $\sim$25% for power law signal models. Soft power law-shaped spectra are not affected (less than 1%), for either of the analysis methods.

The case of global (normalization) differences is examined by treating τ as a nuisance parameter, with a Gaussian probability distribution of a 5% width. The result are the significant sensitivity losses for the conventional method: $\sim$30% for the line-like models and $\sim$10% for the hard power law signals. The full likelihood is again far more robust, exhibiting almost negligible worsening – less than 2% for both kinds of signal models. On the other hand, soft power law models result problematic for both approaches, especially when the spectral shape of the signal is similar to that of the convoluted background. The conventional approach suffers from an up to factor $\sim$8 worse sensitivity, also for all softer models. For the full likelihood this is less pronounced (up to a factor $\sim$4 sensitivity degradation), and the power of the method is recovered as soon as the shape of the expected signal distribution becomes different from that of the background. This is caused, for both approaches, by high correlation (up to 0.99) between τ and signal intensity, when signal and background are of similar spectral shapes. For other signal models the correlation is low, due to the energy range optimization applied in the conventional approach (§4.2.3) and the presence of the spectral term in the full likelihood expression (eq.(4.2)).

4.3 Overview of the Full Likelihood Method

In this Chapter, the concept of the full likelihood method has been introduced, and its performance characterized. As shown, this method is constructed to take the maximal advantage of the spectral information, and almost solely through the inclusion of the a priori knowledge on the expected gamma-ray spectrum in the likelihood, it achieves significantly better sensitivity than the conventional method.

Furthermore, it has been demonstrated that the full likelihood is unbiased and robust; the sensitivity gain from its use is rather independent on other analysis characteristics, like the background estimation or signal-to-background discrimination. As a result, the full likelihood method can be combined to any other analysis development aimed at further sensitivity enhancements.

Another very important characteristics of the full likelihood (and any likelihood-based analysis) is that it allows a rather straightforward combination of the results obtained by different instruments and from different targets. For a given model $M(\theta))$ and $N_{\rm inst}$ different instruments (or measurements), a global likelihood function can be simply written as:

$$\mathscr{L}(M(\theta)) = \prod_{i=1}^{N_{\rm inst}} \mathscr{L}_i(M(\theta)). \tag{4.15}$$

This approach eliminates the complexity required for a common treatment of data and response functions of different telescopes or analyses: within the likelihood scheme, the de-

tails of each experiment do not need to be combined or averaged. The only necessary information is the value of the likelihood, expressed as a function of the free parameter of a given model for different instruments.

Considering all of the above, the full likelihood method is a logical choice for the analysis in the dark matter searches with IACTs: following Chapters present the results of this approach applied to the actual MAGIC observations, as well as the predictions on the sensitivity achievable with the future CTA.

5

Dark Matter Searches in Dwarf Spheroidal Galaxy Segue 1 with MAGIC

This Chapter sums up the results of this work – the search for signals of dark matter in dSph galaxy Segue 1. The long-term observational campaign was carried out with the MAGIC Telescopes between January 2011 and March 2013. With 158 hours of good-quality data, this is the deepest survey of any dwarf galaxy by any IACT so far. No significant gamma-ray signal has been found. Using the full likelihood approach, limits have been set assuming different models of dark matter annihilation and decay. At the moment, those limits are the most constraining results for the considered scenarios obtained from dSphs observations with IACTs.

This Chapter begins with motivation behind the choice of Segue 1 as suitable dark matter target, followed by the details of its observations with MAGIC and the subsequent analysis. Finally, results from the full likelihood method and their interpretation in the light of various dark matter models are described.

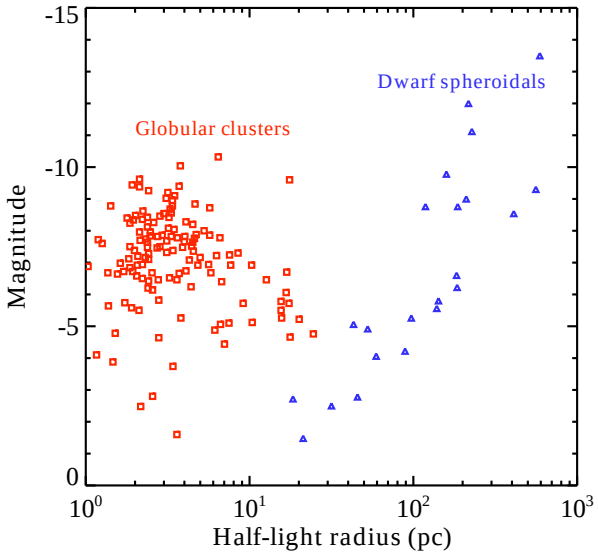

Figure 5.1: Relationship between the apparent magnitude and the half-light radius for Milky Way globular clusters (red squares, left side) and dSphs (blue triangles, right side). The ultra-faint satellites appear as the blue triangles in the lower portion of the figure. Taken from [105].

5.1 Segue 1 as Target for Dark Matter Searches

5.1.1 Introduction to Dwarf Spheroidal Galaxies

In the context of ΛCDM, dark matter structures form by hierarchical collapse of small overdensities and are presumed to extend in mass down to the scale of the Earth, or even bellow [102]. Some of these substructures may have attracted enough baryonic matter along their evolutionary road to commence the star creation. This hypothesis has been used to explain the dSph satellite galaxies of the Milky Way, proposed to have formed within the substructures of the Galactic dark matter halo [194, 195].

The first galaxies identified as dSphs were Sculptor and Fornax, in 1938 [196]. By the end of the 20th century, due to their faint nature, only seven more of these objects were discovered. Given how the number of known dSphs was orders of magnitude lower that the one predicted by the N-body simulations (the so-called *missing satellite problem*, [103], it was reasonable to assume that the existing census of Milky Way satellites was incomplete, and that new detections may be expected from the more sophisticated photometric surveys.

Indeed, since 2004, with the advent of the Sloan Digital Sky Survey (SDSS, [197]), dozen of new dSph galaxies have been identified. The newly-discovered dSphs, however, are not just significantly fainter than their predecessors, which was expected, but also posses certain properties more akin to the globular clusters than to dwarfs. It is why the distinction is made between the *classical* dSphs, detected in the pre-SDSS era, and the *ultra-faint* ones, discovered since 2004.

The classical dSphs are by now the well-established sources, with hundreds of identified member stars, and located at distances from 70-250 kpc (Table 5.1). They are more extended and more luminous than their ultra-faint counterparts, with half-light radii typically of the order of few hundreds of parsecs, and luminosities spread over nearly two orders of magnitude ($10^5 - 10^7 L_\odot$). Thanks to their many bright giant constituents, velocities of the member

Name	**Distance** [kpc]	**Magnitude**	**Half-light radius** [pc]	$\langle\sigma^2\rangle$ [km/s]
Sculptor	80	-9.8	283	9.0
Fornax	138	-13.1	710	10.7
Leo I	250	-11.9	251	9.0
Leo II	205	-10.1	176	6.6
Draco	80	-9.4	221	10.1
Ursa Minor	69	-8.9	181	11.5
Carina	101	-9.4	250	6.4
Sextans	86	-9.5	695	7.1
Willman 1	38	-2.7	25	4.0
Ursa Major I	106	-5.5	319	7.6
Ursa Major II	32	-4.2	149	6.7
Hercules	138	-6.6	330	5.1
Leo IV	158	-5.0	206	3.3
Canes Venatici I	224	-8.6	564	7.6
Canes Venatici II	151	-4.9	74	4.6
Coma Berenices	44	-4.1	77	4.6
Segue 1	23	-1.5	29	4.3
Bootes I	60	-6.3	242	9.0

Table 5.1: Compilation of properties of Milky Way satellites. Classical dSphs are above the horizontal line, while the ultra-faints are below. The table only shows galaxies with well-measured kinematic data, in which cases the mass can be determined from the velocity dispersion and half-light radius. Taken from [105].

stars can be measured to a precision of a few km/s, or less [198].

On the other hand, all of the known ultra-faint dSphs have total luminosities lower than the faintest classical satellite ($L \simeq 10^3 L_\odot$). Their stellar population is small, consisting of only tens of very faint stars (with typical magnitudes of 20-21). This affects the precisions of velocity dispersion measurements (uncertainties are 2-3 km/s, which is about a factor of two of the intrinsic velocity dispersion of the system), as well as the total luminosity estimation (which can be inflated if not all of the interloping stars are removed from the dSph sample [199]). The half-light radii of some ultra-faints are in the 30-100 pc range (Table 5.1), which is more typical for globular clusters than for galaxies (Figure 5.1). Furthermore, the velocity dispersions of both dwarfs and clusters are similar (5-15 km/s, [29]). With ultra-faints behaving as 'in-between' the classical dSphs and globular clusters, it is very important to correctly derive the properties and make a classification of the newly discovered object as either globular cluster, for which the dynamical mass within the half-light radius is dominated by stars, or as a dSph galaxy, for which dark matter will be the principal component. Distinction between the two kinds of systems is based on their different chemical compositions: the globular clusters are on average metal-rich, [Fe/H]> -2, and show a small amount of internal metallically spread, unlike the metal-poor dSphs [200]. In addition, the clusters largely formed their star population in a single burst, while in a galaxy there could be member stars formed at different stages of dSph evolution.

The currently known classical and ultra-faint dSph galaxies with well measured kinematic data, together with some of their basic properties, are listed in Table 5.1.

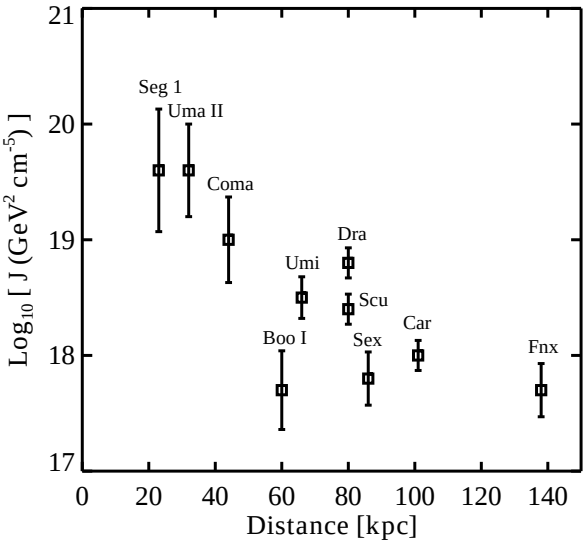

Figure 5.2: Astrophysical factor J values for dSphs, integrated with 0.5° radius, as a function of their galactocentric distance. The assumed dark matter density profile is NFW. Taken from [105].

5.1.2 Dwarf Spheroidal Galaxies as the Dark Matter Candidates

From the measurements of the velocities of member stars in dSphs, it has been estimated that M/L ratio for this class of objects is of order of hundred, or even thousand $M_\odot/L_\odot$ for some ultra-faint dwarfs, which makes these galaxies the most dark matter dominated objects in the Universe [201, 202]. Furthermore, given their extreme total M/L ratios, it is unlikely that the luminous material has altered the distribution of dark matter in these systems [203]. The gamma-ray background expected from dwarfs is very low: the low baryonic content disfavors presence of conventional gamma-ray emitters (such are supernova remnants, pulsars of binary systems); there are no indications of the recent star formation history; there is little or no gas in their interstellar medium to serve as target material for cosmic rays [204]. Locations of dSphs are well known and many of these galaxies are within 100 kpc distance from Earth. Finally, some of the dwarfs are located at high galactic latitudes, where contamination form the Galactic background is subdominant.

Given some of their above mentioned properties, the astrophysical factor J of dSphs is usually quite high (Figure 5.2) and, thanks to the studies of their stellar dynamics, more constrained than for some other classes of sources [127]. Still, due to the relatively small kinematic samples (especially for the ultra-faint dwarfs), it is not possible to determine whether their central dark matter distributions are cusped or cored. However, the uncertainty on the mass profiles is minimized at about the half-light radius: the best constrained integrated half-light radius for a classical satellite is determined to approximately 5% (Fornax), to be compared to lowest uncertainty of 20% for the best constrained ultra-faint dwarf (Canes Venatici I, [205]). There are hints of dark matter cores in classical dSphs [206], but more definitive affirmation will have to wait for complete measurements of proper motions of the individual member stars, as well as higher-quality photometric data sets in the central regions.

As for the potential boost of the expected gamma-ray flux due to the presence of substructures, in the case of dSphs it is predicted to be negligible (factor of few at most, [104]), which leads to rather straightforward interpretation of the no-detection result as a limit on $\langle \sigma_{\mathrm{ann}} v \rangle$

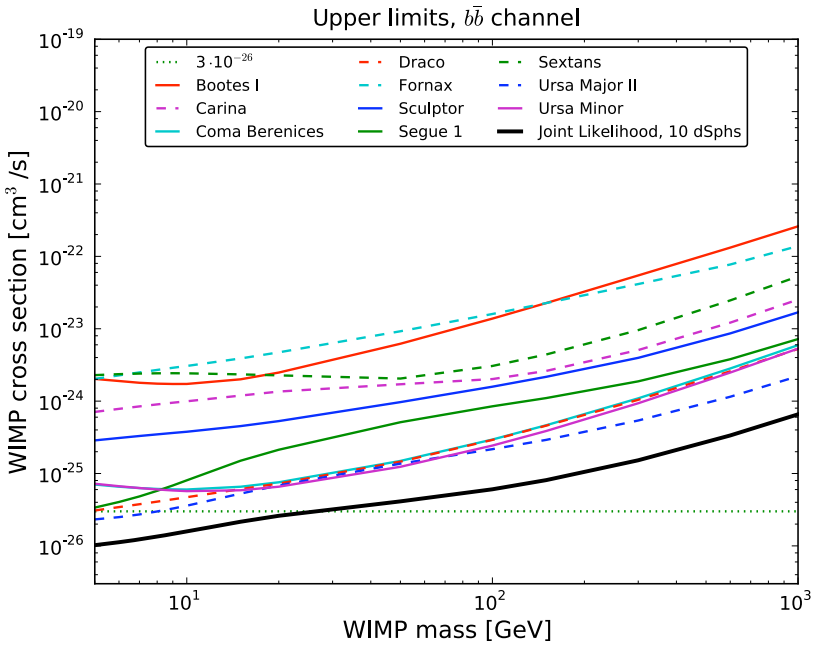

Figure 5.3: Individual and combined limits from 10 dSphs observed by Fermi-LAT, on the annihilation cross section as a function of the WIMP mass, assuming 100% annihilation to $b\bar{b}$. Taken from [125].

(with respect to some other sources, like Galactic Center or galaxy clusters).

Overall, dSph galaxies can be considered excellent targets for indirect dark matter searches. In the last couple of years, several of these satellites have been observed by the IACTs: Draco, Willman 1 and Segue 1 by MAGIC (all in mono mode, [207, 208]), Draco, Bootes, Willman 1 and Segue 1 by VERITAS [209] and Sagittarius, Carina, Canis Major, Sculptor and Fornax by HESS [210]. So far, no signal has been reported. Additionally, Fermi-LAT has combined the observations of 10 dSphs into the currently most constraining limits on $\langle \sigma_{\text{ann}} v \rangle$ (Figure 5.3, [125]).

5.1.3 Segue 1

This works sums up the 3-years long observational campaign of the MAGIC Telescopes directed to dark matter searches. The goal of this program was to perform deep survey of the best available (to MAGIC) dark matter candidate, and accumulate many hours of good quality data. In case of no detection, the sample is to be used for deriving limits for annihilation or decay for different dark matter models. The source chosen for the observations is dSph galaxy Segue 1.

Segue 1 was discovered in 2006 as an overdensity of resolved stars in imaging data from the SDSS (Figure 5.3). Located towards the Sagittarius constellation, at a distance of 23±2 kpc, it was originally identified as a large globular cluster [1] [212], given its compactness and low absolute magnitude ($M_V = -1.5^{+0.6}_{-0.8}$), more characteristic for clusters than for dwarfs. This claim, however, was contested by the Keck/DEIMOS [213] spectroscopic measurements of the radial velocities of 24 of the Segue 1 member stars: with mean heliocentric velocity estimated

[1] Thus the name Segue 1, after the survey SEGUE (Sloan Extension for Galaxy Understanding and Exploration, [211]), as conventional for globular clusters, instead after the constellation towards which it lies.

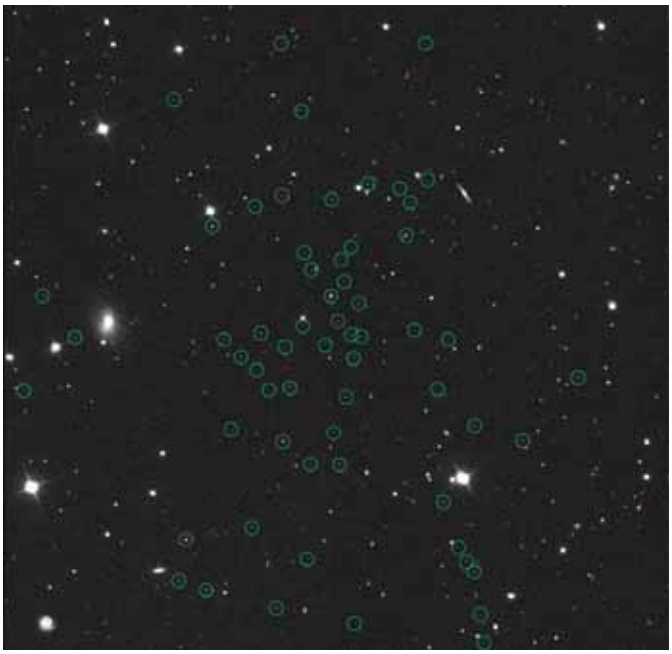

Figure 5.4: Segue 1 as seen by the II 10-m telescope. The image accounts for a total exposure of 5400 s in the 6400-9100 $\mathring{A}$ waveband. Segue 1 stars are circled in green. Credit: M. Geha and W. M. Keck Observatory.

to 206 km/s and velocity dispersion of 4.2 ± 1.2 km/s, it was concluded that Segue 1 was actually an ultra-faint dwarf galaxy, and a highly dark matter dominated one at that [214]. There were several consequent attempts to dispute these results and classify the source as a globular cluster again (see, e.g. [215]), but, in 2011, a more comprehensive Keck/DEIMOS spectroscopic survey was conducted, increasing the number of member stars to 71. Analysis of this new data set allowed for a clearer identification of Segue 1 as a least-luminous dSph galaxy, with the highest known M/L, estimated to 3400 $M_{\odot}/L_{\odot}$ [202].

It should be clear that, despite this impressive M/L, its value has to be treated with caution. Although the mean velocity of Segue 1 member stars allows their clear separation from the foreground ones of the Milky Way, special care must be taken that make sure no interloping star is included in the mass characterization of the system, as it can significantly inflate the total luminosity and therefore the M/L value. Some more extensive future study of kinematic properties of the member stars should be able to address these uncertainties.

Some basic measured (or estimated) properties of Segue 1 are given in Table 5.2. As it can be seen, this dSph is relatively close, highly dark matter dominated and with almost no background of conventional origin at very high energies. In addition, it is located outside of the Galactic plain, it is in the Northern hemisphere and visible to MAGIC for about 370 hours of dark time per year at low ZA. From the comparison with other potential dark matter sources, Segue 1 has been chosen as the best (currently) available target for indirect dark matter searches with MAGIC, and the following Sections present the results of extensive observations of this dSph performed over the course of 3 years.

Segue 1	
Coordinates	$10^{h}\,07^{m}\,04^{s}$, $+16^{\circ}\,04'\,55''$
Distance	23 ± 2 kpc
Number of resolved stars	71
Magnitude	$-1.5^{+0.6}_{-0.8}$
Apparent magnitude	13.8 ± 0.5
Luminosity	$340\,L_{\odot}$
Mass	$5.8^{+8.2}_{-3.1}\times10^{5}M_{\odot}$
M/L	$\sim3400\,M_{\odot}/L_{\odot}$
Half-light radius	29^{+8}_{-5} pc
System velocity	208.5 ± 0.9 km/s
Velocity dispersion	$3.7^{+1.4}_{-1.1}$ km/s
Mean [Fe/H]	-2.5

Table 5.2: Segue 1 main characteristics. Extracted from [202, 214].

5.2 Observations and Data Reduction

The observations of Segue 1 were performed with MAGIC, in stereoscopic mode, between January 2011 and March 2013. During this time, the telescopes underwent series of significant changes: at the end of 2011, the readout systems of both instruments were replaced by the more advanced, DRS4-based configurations (§3.1.3.2); by the end of 2012, among other improvements, the camera of MAGIC-I was upgraded to the exact replica of that of MAGIC-II (§3.1.2). As a result, performance of the system varied during the total period of Segue 1 observations; therefore, data from each of the different telescopes states are analysed and described separately. Basic details are summed in Table 5.3.

5.2.1 Sample A: 2011 Data

Data sample A referes to Segue 1 observations from January to May 2011, carried out under dark night conditions, for total of 64 hours. The *ZA* range extended from 13° (corresponding to the source culmination at MAGIC latitude) and 33.7°, thus ensuring low energy threshold of the analysis.

Observational Setup The observations were performed in a false tracking (wobble) mode (§3.2.1). However, instead of the standard observational setup (source at a 0.4° offset from the camera center), special wobble configuration was devised for this case. Namely, there is a 3.5-apparent magnitude star, Eta Leonis (η Leo), located at a 0.68° angular distance from Segue 1, and as such, in the FoV of MAGIC cameras. Every time the star enters the trigger area of the cameras (Figure 3.5), it causes an increase in the charge of the corresponding PMTs and in the rate of data acquisition. To solve this problem, the trigger threshold of the affected pixels has to be dynamically augmented (since the star moves in the camera). This in particular was an issue for MAGIC-I, as the electronics of its camera were not fast enough to quickly correct for the presence of η Leo.

In order to deal with the problem, wobbling scheme was chosen in such a way that the star

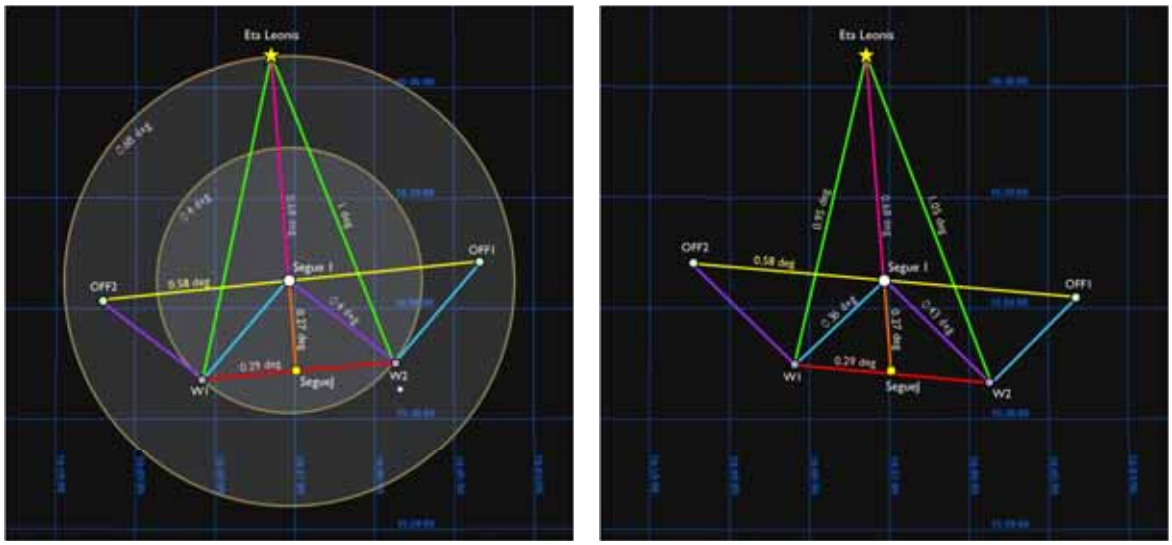

Figure 5.5: Observational scheme devised to exclude the η Leo star from the MAGIC-I trigger area (**left**) differs from the one actually used in the observations (**right**) due to different conventions applied in coordinate calculations. Nevertheless, the sensitivity was not affected. This configuration was used in Segue 1 observations from January 2011 to May 2012 (samples A, B1 and B2). See the main text for more details.

was always outside the trigger region of MAGIC-I: instead of wobbling around the nominal position of the actual source, the tracking was done with respect to a fake target, dubbed SegueJ, located 0.27° away from Segue 1 and on the opposite side from η Leo (Figure 5.4). The wobble offset of 0.29° and wobble angles of 175° and 355° were chosen so that the star is always at 1° distance from the center of the camera and therefore outside of the MAGIC-I trigger region. Also, with such configuration, Segue 1 is 0.4° away from the camera center (as in the standard observational configuration), with residual background estimated from positions 0.58° away, thus preserving both the homogeneity of the camera exposure and sensitivity for the analysis.

Unfortunately, due to different conventions (regarding the direction of right ascension increase) applied in the calculations of wobble scheme by the analysers and by the Central Control of the telescopes, instead of 175° and 355° wobble angles, 5° and 185° were used. This altered the desired configuration, with angular distances between the wobble positions and Segue 1 being 0.36° and 0.43° instead of 0.4° (Figure 5.4). However, these differences are not sufficiently big to affect the sensitivity of the analysis (for instance, the misspointing of the telescopes can be as big as 0.1°). In any case, the background estimation is done correctly, from positions that are at the same distances from the camera center as the source, and the distances between these *OFF* positions and Segue 1 are the same, and remain 0.58°.

In order to avoid possible effects of the L3 blob (§3.2.1), special care was taken to ensure that both wobble positions were observed for similar amounts of time and with similar azimuthal coverage (Figure 5.5). For this, observations were reviewed on daily bases, faulty subruns rejected, and calculations made on how the new data (to be taken the following night) would contribute to the existing azimuth distribution.

Data Reduction Data reduction was performed following the steps of the standard MAGIC procedures described in §3.3. After the calibration (§3.3.1), the absolute image cleaning

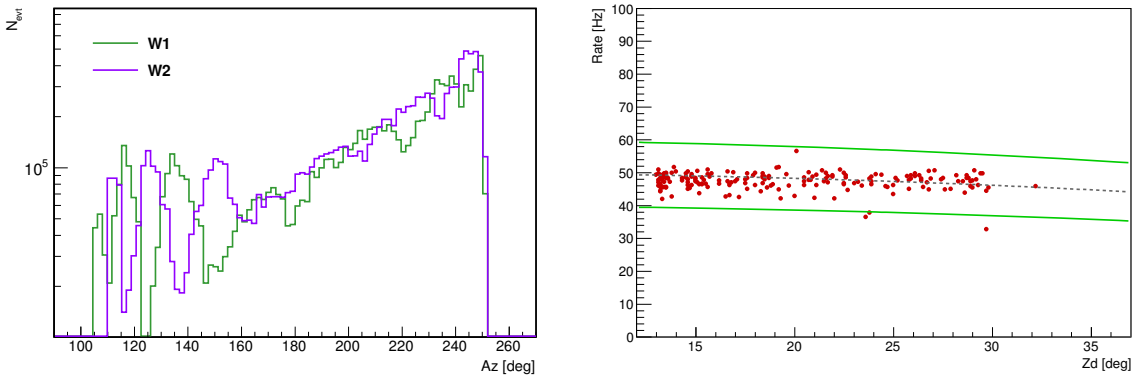

Figure 5.6: Left: Azimuth distribution for the sample A observations for both wobble positions. **Right**: Distribution of rates for the same period as a function of *ZA*. Full line represent the reference rate and dashed lines its ±20% values, marking the area outside of which the data is excluded. Each point represents a single data run.

was applied using the standard values for the pre-upgrade configuration (§3.3.2): for MAGIC-I, a minimum of $q_c = 6$ ph.e and $q_b = 3$ ph.e for the core/boundary pixels was required, while for MAGIC-II those numbers were $q_c = 9$ ph.e and $q_b = 4.5$ ph.e. At the same time, individual core pixels whose signal arrival time differed from the mean core time by more than $\Delta t_c = 4.5$ ns were rejected, as well as the individual boundary pixels with arrival time difference with respect to that of their core neighbours greater than $\Delta t_c = 1.5$ ns. This cleaning was followed by the image parametrization.

Next, quality selection was performed (§3.3.3), first individually for data of each telescope and each observational day. Criteria for rejection of a given subrun was deviation for more than 20% with respect to average (for the day in question) value of event rate, and 5% deviation from the mean of *length* and *width* parameter values. This way, 12.3 hours of data were excluded, mainly due to the bad meteorological conditions and subsystem failures. After this individual quality selection, data from both instruments were merged and stereo parameters reconstructed (§3.3.4). This was followed by another quality check, but this time encompassing the entire sample: runs whose event rates differed by more than 20% from the mean rate of the whole data set were excluded from the further analysis (Figure 5.6).

The events characterization – γ/hadron separation, energy and arrival direction estimation – were performed following the procedures outlined in §3.3.5. The *hadronness* calculation (§3.3.5.1) was done by means of the RF method; the corresponding matrices were trained over a subset of MC gamma-ray events and ∼16 hours-sample composed of observations where no significant gamma-ray emission was found. These datasets were chosen so they share (or are simulated with) similar observational conditions with Segue 1 (*ZA*, instrument PSF). The energy estimation (§3.3.5.3) was derived from LUTs constructed from MC gamma-ray events. As for the arrival direction, it was calculated with *Disp RF* method (§3.3.5.2), trained using the image and shower parameters, as well as the *ZA* of observations.

The validity of the created RF matrices and energy LUTs was first verified on a 4.8 hours of Crab Nebula sample, contemporaneous to sample A observations and of same *ZA* range, before being used in the characterization of the events of the source. The same Crab Nebula sample was latter used for optimization of the cuts for Segue 1 analysis (§5.3.1).

Finally, after the correction for the dead time of the system (0.5 ns), the effective obser-

	Sample A	**Sample B1**	**Sample B2**	**Sample C**
Readout	DRS2	DRS4	DRS 4	DRS 4
MAGIC-I camera	old	old	old	new
Obs. period	Jan - May 2011	Jan - Feb 2012	Mar - May 2012	Nov 2012 - Feb 2013
Obs. time [h]	64	24.28	59.77	55.05
ZA range [deg]	13-33.7	13-32.5	13-35.7	13-37
Az range [deg]	104.8-250.2	120.2-252.0	115.4-257.2	103.8-259.4
Wobble source	SegueJ	SegueJ	SegueJ	Segue 1
Wobble offset [deg]	0.29	0.29	0.29	0.40
Wobble angles [deg]	5, 185	5, 185	5, 185	5, 185
Image cleaning	absolute	absolute	absolute	dynamic sum
q_c/q_b [ph.e] (M-I)	6/3	6/3	6/3	6/3.5
q_c/q_b [ph.e] (M-II)	9/4.5	8/4	8/4	6/3.5
Δt_c [ns]	4.5	4.5	4.5	4.5
Δt_b [ns]	1.5	1.5	1.5	1.5
W1 EOT [h]	22.66	6.07	25.02	23.71
W2 EOT [h]	24.35	6.20	26.11	23.80
EOT [h]	47.00	12.26	51.13	47.51
Total EOT [h]				**157.9**

Table 5.3: Basic observations and data reduction details for four samples of Segue 1 data. Refer to main text for additional explanations.

vation time (EOT) of the Segue 1 sample A was reduced to 47.0 hours of good-quality data.

5.2.2 Sample B: 2012 Data

Segue 1 was observed with MAGIC between January and May 2012. Since December of 2011, the telescopes were operating with improved, DRS4-based readout systems, which resulted in dead time reduction from 0.5 ns to only $2.6e^{-5}$ ns. However, the beginning of the post-upgrade period was marked buy many hardware problems and analysis issues. In particular, the Segue 1 data taken during January and February was affected by several faulty mezzanines in MAGIC-I (total of 24 bad channels), which was seen in the camera as 3 big 'holes'. Furthermore, due to a bug in the AMC system of MAGIC-I, the PSF of this telescope was increased. Posteriori, data taken in such conditions could be salvaged through software, but it needed special attention and designated MC files simulated with the mentioned defects taken into the account. The issues were solved for observations from March onwards; however, as the treatment and MC sets for these data are different, this 2012 Segue 1 data is divided into two samples, analysed separately: sample B1 (pre-March) and sample B2 (post-March data).

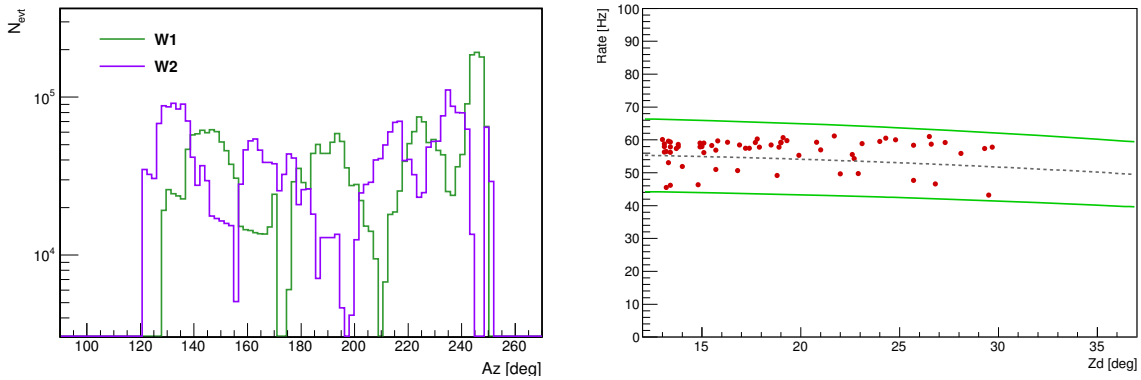

Figure 5.7: Left: Azimuth distribution for the sample B1 observations for both wobble positions. **Right**: Distribution of rates for the same period as a function of *ZA*. Full line represent the reference rate and dashed lines its ±20% values, marking the area outside of which the data is excluded. Each point represents a single data run.

5.2.2.1 Sample B1: Pre-March Data

This data was taken from end of January to the end of February 2012, for total of 24.3 hours, under dark night conditions and for *ZA* range between 13° and 32.5°.

Observational Setup Observations were performed in the wobble mode, using the same configuration as in the sample A (§5.2.1, Figure 5.5). Due to the very harsh weather conditions in this period, and a rather unstable system, data taking and balancing of azimuthal coverages for both wobbles was complicated (Figure 5.7).

Data Reduction Data reduction followed the standard steps described in §3.3. After the calibration (from this period on done by the program `sorcerer`), absolute image cleaning was applied, with parameters $q_c = 6$ ph.e and $q_b = 3$ ph.e for MAGIC-I and $q_c = 8$ ph.e and $q_b = 4$ ph.e for MAGIC-II (Table 5.3), and $\Delta t_c = 4.5$ ns and $\Delta t_c = 1.5$ ns for time cleaning. Image parametrization was followed by data selection on daily level for each instrument (with allowed deviations of the individual parameters from the daily mean up 20% for the rate and 5% for *length* and *width* parameters. This resulted in rejection of almost half of the sample (∼12 hours), which was expected given very bad weather and frequent system failures during this period. After the merger of data and reconstruction of stereo parameters, another quality control was performed, excluding all runs with rates exceeding 20% of the mean rate value of the whole dataset (Figure 5.7).

Processes of the event reconstruction were done with matrices and LUTs trained with ∼2 hours of data where no gamma-ray signal was found, and with MC sample simulated so the hardware issues of the MAGIC-I (the increased PSF and 'holes' in the camera) were taken into the account. Validity of reconstruction matrices and tables was verified on ∼4 hours of Crab Nebula sample, taken in the same period as Segue 1 data, and under the similar conditions. This sample was later used in the analysis for the cuts optimization (§5.3.1).

After the dead time correction, the EOT of the Segue 1 B1 sample amounted to 12.26 hours of good-quality data.

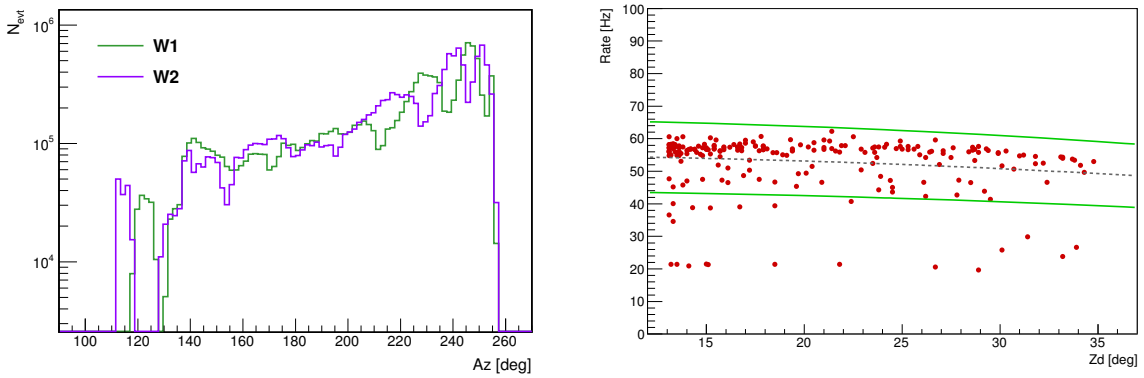

Figure 5.8: Left: Azimuth distribution for the sample B2 observations for both wobble positions. **Right**: Distribution of rates for the same period as a function of *ZA*. Full line represent the reference rate and dashed lines its ±20% values, marking the area outside of which the data is excluded. Each point represents a single data run.

5.2.2.2 Sample B2: Post-March Data

Between March and May 2012, Segue 1 was observed for 59.8 hours, under dark conditions and for *ZA* range from 13° to 35.7°, thus ensuring the low energy threshold.

Observational Setup Same wobble configuration as in samples A and B1 was used (5.2.1, Figure 5.5). Azimuthal coverage of each of the wobble positions was carefully controlled during the data taking (Figure 5.8).

Data Reduction After the calibration, absolute image cleaning was applied with same parameter values as for the B2 sample: $q_c = 6$ ph.e and $q_b = 3$ ph.e for MAGIC-I, $q_c = 8$ ph.e and $q_b = 4$ ph.e for MAGIC-II, and for time cleaning $\Delta t_c = 4.5$ ns and $\Delta t_c = 1.5$ ns (Table 5.3). Data selection was performed on the same principles as described before: allowed deviations were 20% for the rate values and 5% for *length* and *width* parameters, on the daily level for each telescope, and after the merger of the data, 20% rate differences from the mean of the whole sample (Figure 5.8). These quality checks resulted in rejection of 6.9 hours of data.

Matrices and LUTs for event characterization were obtained from MC sample, simulated under the similar conditions as the Segue 1 data taking in this period, and from $\sim$ 6 hours of actual data that contained no signal. Out of this 6 hours, $\sim$1.5 hours are of Segue1 itself: this measure was necessary since there was no data from other sources, taken in the same period and under the same conditions as Segue 1, and surviving the quality checks, that covered the zenith range between 17° and 28°. To make sure that the matrices for these angles were properly calculated, a fraction of Segue 1 sample, overlapping the mentioned range, was added for the training. This data was not considered in the further analysis. Generated LUTs and matrices were first tested on 6.2 hours of Crab Nebula data, taken contemporaneously with Segue 1 and under the same conditions, before being used in the event reconstruction of the source data. The Crab Nebula sample was also used for the optimization of the cuts later on (§5.3.1).

After the described quality selection, dead time correction and removal of $\sim$1.5 hours of data used for RF training, the EOT of the Segue 1 B2 sample was 51.13 hours of good-quality data.

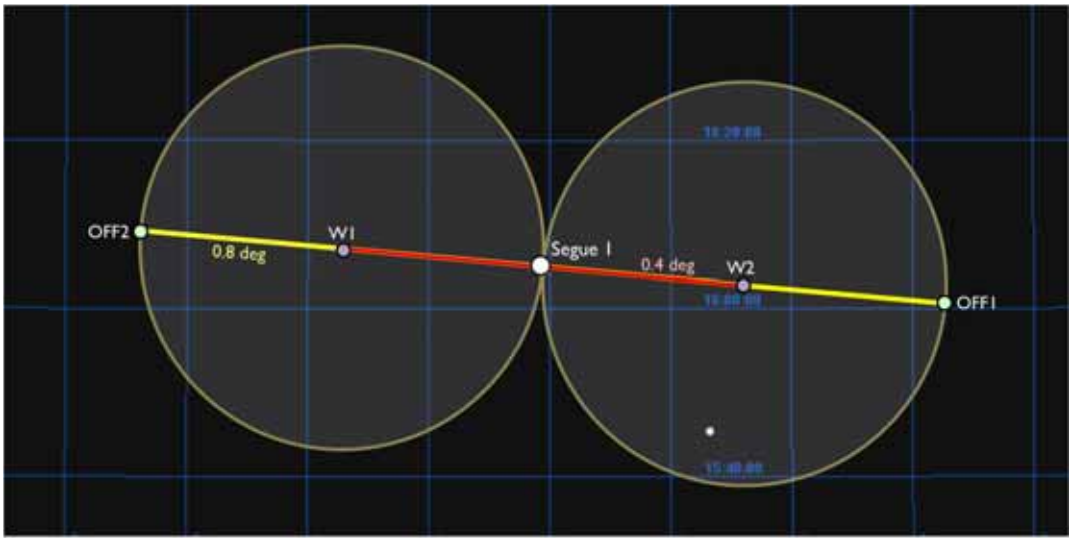

Figure 5.9: Observational scheme for the sample C observations. The wobbling is done around Segue 1, at standard offset of 0.4° and wit wobble angles of 5° and 185° (so that the maximal symmetry between the source, pointing and η Leo star is achieved). See the main text for more details.

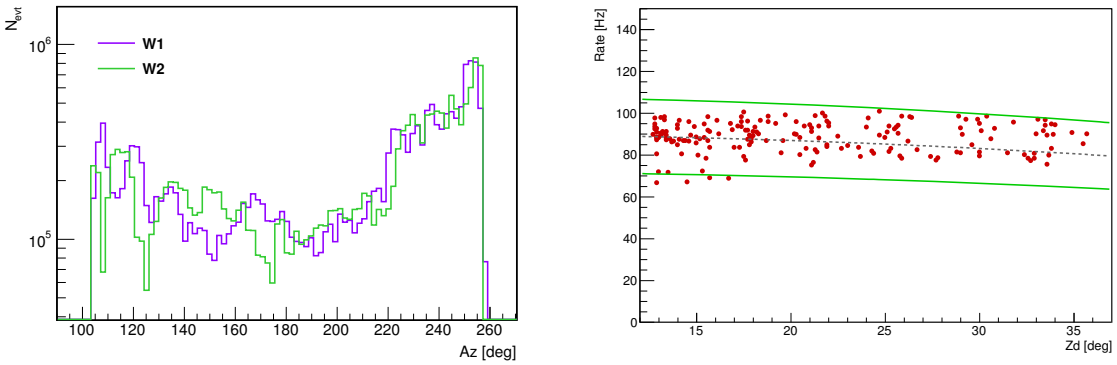

Figure 5.10: Left: Azimuth distribution for the sample C observation for both wobble positions. **Right**: Distribution of rates for the same period as a function of *ZA*. Full line represent the reference rate and dashed lines its ±20% values, marking the area outside of which the data is excluded. Each point represents a data run.

5.2.3 Sample C: 2012-2013 Data

By November 2012, the planned improvements of the MAGIC Telescopes were successfully completed. Most notably, the camera of MAGIC-I was replaced with an exact replica of the MAGIC-II camera. The changes made in the upgrade were followed by some changes in the analysis chain and MC production.

The sample C refers to the observations of Segue 1 from November 2012 to February 2013. For total of 55 hours, under dark night conditions, Segue 1 was observed in the $13^\circ - 37^\circ$ *ZA* range.

Observational Setup The upgraded MAGIC-I camera has greater trigger area and faster electronic than the old one. In particular case of Segue 1 observations, this means that the η

Leo is always inside the trigger region (as in the case of MAGIC-II), but also that the camera electronics are now capable to swiftly correct the trigger thresholds of the PMTs affected by the star. It was, therefore, opted to observe Segue 1 in the wobble mode, but with the standard settings: 0.4° angular distance between the source and camera center and 0.8° between the source and OFF region in both wobble positions (Figure 5.9). The offset angles remained 5° and 185°, in order to keep the symmetry between the positions of the source, pointings and η Leo at maximum. The azimuth coverage of both wobble positions was again carefully monitored during the course of observations (Figure 5.10).

Data Reduction Since 2013, standard image cleaning in the data reduction chain is the dynamical sum cleaning (§3.3.2). In dynamical cleaning, the cleaning level is adapted for each event in dependence of the *size* of the shower, in order to preserve as much signal as possible at low energies and only the relevant signal at high ones. In practice, the cleaning level values for individual core pixels, $q_c = 6$ ph.e (same for both telescopes) are dynamically scaled as a function of total clipped sum of the charge in all core pixels: bellow the basic threshold of 750 phe, the scaling factor is 1, while for greater *size* values the scaling factor and cleaning level value increase. But first, for pixels to qualify as core, the thresholds for summed charge in 2NN, 3NN and 4NN multiplicities must be reached: 21.6, 24.6 and 25.2 ph.e, respectively. For boundary pixels, the minimum charge of the individual pixel is $q_b = 3.5$ ph.e. Regarding the time windows, pixel is accepted as cored if its arrival time is within 0.5, 0.7 and 1.1 ns from the mean arrival time of its 2NN, 3NN or 4NN group, respectively. Further more, there is an additional condition that the individual arrival time of a core pixel can not differ more than $\Delta t_c = 4.5$ ns from the mean arrival time of the shower core. For boundary pixel, the arrival time difference with respect to its core neighbour must be smaller than $\Delta t_c = 1.5$ ns; otherwise, that pixel is removed from the image.

Following the image cleaning and parametrization, data selection is performed for each day and for each telescope individually (based on rate, *length* and *width* values), and, after the data merger and stereo reconstruction, quality of each run is established based on the comparison of its rate and the mean rate of the whole sample (Figure 5.10). This way, 6.65 hours of data were rejected from the sample C.

For event characterization training was done using a MC sample and $\sim$10 hours of observations of sources where no significant excess was found. Both sets were chosen so they coincide with Segue 1 sample C in *ZA* range and PSF. The validity of generated matrices and LUTs was verified on $\sim$30 hours of Crab Nebula data, taken in the same period as Segue 1 and under the same observational conditions. The Crab sample was used latter on for the cuts optimization.

The EOT of sample C, after the dead time correction, was reduced to 47.51 hours of good-quality data.

5.3 Analysis

This Section describes the analysis of Segue 1 data using the full likelihood. Following the prescription of this method, presented in Chapter 4 (§4.2.1), the response function of the telescopes is determined, the background is modeled, and the spectral functions depicting the expected signal distributions are decided upon (by choosing certain dark matter models). But first, the analysis cuts optimal for a source such as Segue 1 are defined. In addition, for

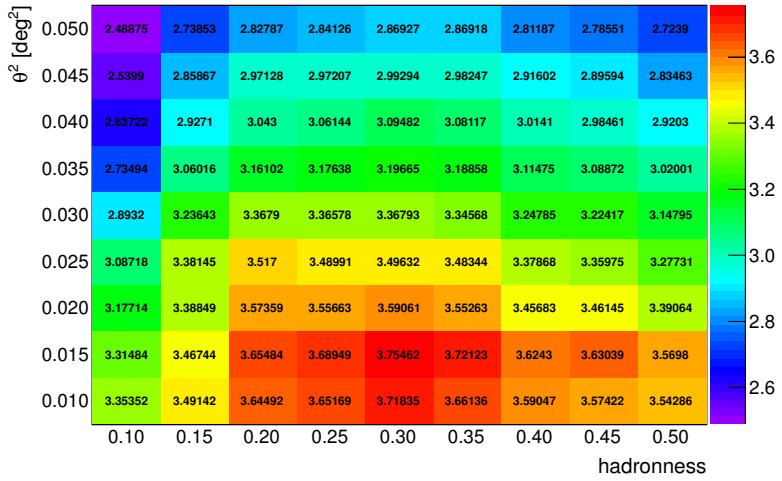

Figure 5.11: Significance scan over the different values of θ^2 (y-axis) and *hadronness* cuts (x-axis), for *size*>50 ph.e and energy between 59.2 GeV and 10 TeV. The color scale refers to the significance, obtained after the cuts are applied, for a weak source with signal expected to be 5% of that of the Crab Nebula. This particular case refers to the sample A. See the main text for more details.

the sake of completeness, high-level products of the MAGIC standard analysis chain (§3.3.7) are shown; however, those limits will not be used at the end of this Chapter for the interpretation of Segue 1 results in context of dark matter searches.

5.3.1 Cuts Optimization

Choice of cuts to be applied in the analysis is very important, as it directly influences the prospects for detection. Segue 1 is assumed to be a weak source, therefore the cuts for this analysis are rather tight, selected to ensure the best possible background rejection.

The main cuts applied in this work are:

- *size*: given how it is in the intrest of this analysis to cover the low energy range, the *size* cut (for both telescopes) requires minimum of only 50 ph.e for event not to be rejected;
- *hadronness*: maximal exclusion of the background implies low hadronness. This cut is optimized on a Crab Nebula sample, assuming a weak source such as Segue 1;
- θ^2: radius of *ON* and *OFF* regions (given as θ) defines how big are the areas from which events are considered in the analysis. It is also optimized on the Crab Nebula sample;
- $E_{\rm min}$ and $E_{\rm max}$: as shown in §4.2.3, the full likelihood method takes advantage of the entire energy range available. Therefore, the lower and upper cuts in energy for this analysis are set to $E_{\rm min} = 59.2$ GeV and $E_{\rm max} = 10$ TeV, respectively. The value for $E_{\rm min}$ does not go down to even lower energies since the response of the detector becomes unreliable; $E_{\rm max}$ does not exceed 10 TeV as there are no events above this limit (after *hadronness* and θ^2 cuts are applied).

As already mentioned in the previous Section, the Crab Nebula sample is used for the optimization of the analysis cuts of a given observational period. In this work, this is done in the

Cuts	Sample A	Sample B1	Sample B2	Sample C
$E_{\rm min} - E_{\rm max}$ [GeV]	59.2 - 10000.0	59.2 - 10000.0	59.2 - 10000.0	59.2 - 10000.0
size [ph.e]	50	50	50	50
hadronness	0.30	0.30	0.25	0.25
θ^2 [deg^2]	0.015	0.015	0.015	0.015

Table 5.4: Segue 1 optimized analysis cuts for different observational periods. See the main text for more details.

following way: sets of cuts are defined, with fixed *size* and energy, and θ^2 and *hadronness* that can adopt values from certain ranges (from 0.01 to 0.05 degrees squared for the θ^2 cut, and from 0.1 to 0.5 for hadronness). Each set of cuts is applied to the Crab Nebula sample, and the surviving signal and background events ($N_{\rm ON}$ and $N_{\rm OFF}$, respectively) are then used to calculate the significance following the LiMa prescription (eq.(3.5)). However, as Segue 1 is expected to be a much weaker source than Crab Nebula, its signal is assumed to be only 5% of that of the Crab, and $N_{\rm ON}$ is scaled down to 5%. The resulting significances for different sets of cuts from θ^2 - *hadronness* space are compared, an the cuts corresponding to the highest value are chosen as optimal (Figure 5.11).

Given that both θ^2 and *hadronness* cuts are energy-dependent, the correct course would be to optimize these cuts for different energy bins. Indeed, this was originally done for the analysis presented here. However, the binned approach led to distributions of events from *ON* and *OFF* regions that were more step-like than continuous, with 'steps' appearing at bin edges. Such distributions are likely to cause practical problems in the computation of the full likelihood, as 'step' could be mistaken for a feature. Therefore, it was opted to go for a more global set of cuts, optimized for the entire energy range. This does not affect the sensitivity in a major way: it has been verified that, for the Crab Nebula sample, when both the optimal and global cuts are applied for each energy bin, the resulting sensitivities and significances are compatible.

The complete list of the cuts, optimized for each of the four observational periods, is listed in Table 5.4. Aside from being used on the Segue 1 data, the same cuts are also applied to the MC gamma-ray events for the calculations of the response functions (§5.3.3).

5.3.2 Results of the Standard Analysis

As already explained, the conventional analysis approach, currently the standard for IACTs, is not optimal for signals with some characteristic features, as expected from dark matter annihilation or decay. Thus, in this work, the full likelihood is used instead. Still, for the sake of completeness, some of the high level products of the MAGIC analysis chain are presented.

Figure 5.12 shows the θ^2-plot for the 158 hours of Segue 1 data. The distributions of events from *ON* (red) and *OFF* regions (gray) are first calculated for each wobble position of each observational period, before being combined in the final result. As it can be seen, no significant excess of gamma-ray events is found. However, there appears to be, however, a negative excess, but it is $\sim$1.5% of the residual background, and given that the systematics in background estimation, expected at lowest energies are $\sim$5%, this excess is within the expected error.

Figure 5.13 is the total skymap for the Segue 1 observations. Again, each of the four periods

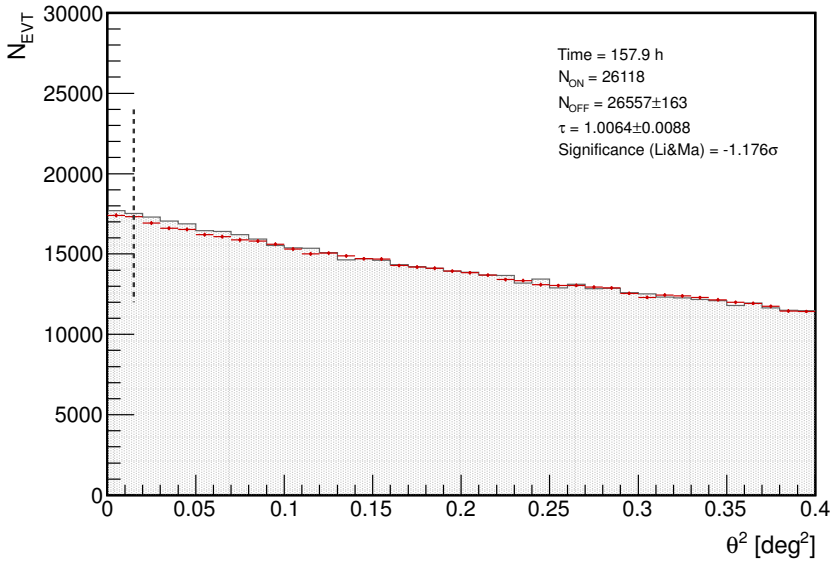

Figure 5.12: Segue 1 cumulative θ^2 distribution from 157.9 hours of observations. The signal (*ON* region) is presented by red points, while the background (*OFF* region) is the shaded gray area. The *OFF* sample was normalized to the *ON* sample in the region where no signal is expected, for θ^2 between 0.15 and 0.4 degrees squared. The vertical dashed line shows the θ^2 cut.

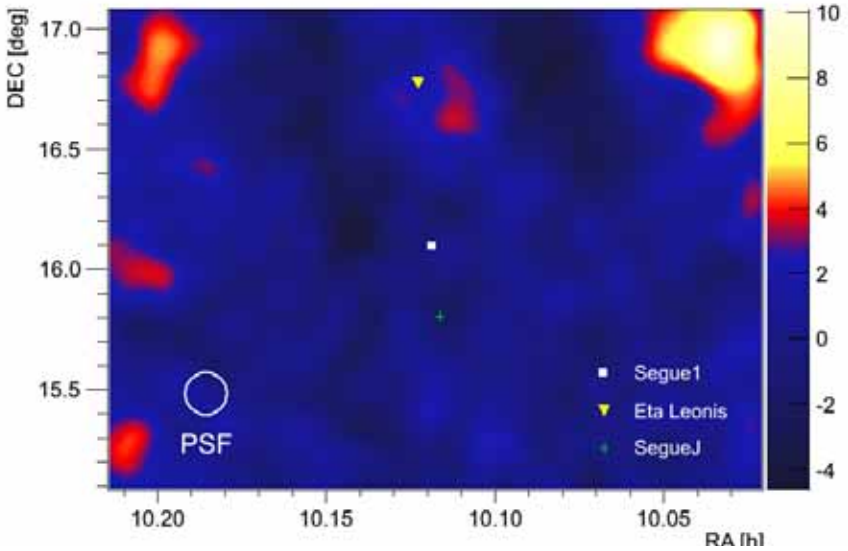

Figure 5.13: Segue 1 cumulative significance skymap, for 157.9 hours of data and energies above 100 GeV. The spots around the edges of the map are artifacts of background estimation, and should not be misanken for signal. Positions of Segue 1, η Leo and SegueJ are shown with white square, yellow triangle and green cross, respectively.

(A, B1, B2 and C) are first obtained with their own cuts, before being combined. The lower energy cut is (for all samples) set to $E_{\text{min}} = 100$ GeV, to avoid some known difficulties related to skymap production and lowest energies. The bright spots close to the borders of the map are artifacts of background estimation and should not be mistaken for signal. As seen from the Figure 5.13, there is no significan excess at the Segue 1 position.

5.3.3 Response Function

In context of this work, the response function refers to the effective area A_{eff}, energy resolution σ and energy bias μ of the telescopes. For each of the four observational periods discussed in Section 5.2, performance of the system is estimated separately, from their corresponding MC *test* samples (§3.3.5). Each *test* MC set is first subjected to the processes of event characterization, using the same matrices and LUTs as for Segue 1 data, after which the cuts optimized for the source are applied (Table 5.4).

The effective area is calculated following the eq.(3.8). Given its dependence on the *ZA*, for the particular case of Segue 1 observations, A_{eff} distributions are first calculated for two bins in zenith: 13.0°-25.8° and 25.8°-35°, after which they are combined in the A_{eff} actually used for the analysis. Figure 5.14 shows effective areas for the four different observational periods, as a function of the true energy E'. Also shown are the trigger areas of each period (i.e. A_{eff} before any kind of cuts are applied), illustrating how big were (are) the surfaces within which a photon of certain energy would have to fall in order to trigger the system.

Energy resolution and bias are obtained in the following way: MC gamma-ray events that survived the cuts are divided in a certain number of energy bins. For each bin, distribution $(E - E')/E'$ is fitted with a gaussian. Width of that fit is the energy resolution σ, and mean of the fit is the bias μ, for the energy range covered by the given bin. Final distributions of σ and μ as a function of E' for the four observational periods are shown in Figure 5.14.

5.3.4 Background Modeling

In order to recognize a possible gamma-ray signal coming from Segue 1, it is necessary to know well enough the background in the *ON* region. As there is no possible way to measure this background directly, it is estimated from the simultaneously observed *OFF* region, where no gamma-ray sources are expected.

For the full likelihood analysis, it is needed to make an *a priori* assumption on the spectral shape of the emission from the *ON* region, for both its signal and background components. For the signal contribution, this is rather straightforward; for the background, the issue is more complicated. The main obstacle is that the response of the telescopes to the background emission is not known. A way around this problem is to estimate the shape of background distribution as expected to be measured by the system, i.e. as a function of measured energy E.

As background in the *ON* region is approximated with the observations from the *OFF* region, it is the latter that has to be modeled for the purposes of the full likelihood calculations. In this work, it is done in the following way: four zones are defined, of the same size and at the same angular distances from the camera center as the *OFF* region (Figure 5.15). These zones are located adjacently to the *OFF*, two on each side, to ensure maximal agreement between them (in sense of the camera homogeneity). Then, by the means of Kolmogorov-Smirnov test (K-S), events from each of these zones, separately and together, are compared to the events from the *OFF* region. The K-S statistics tests whether the events from two different sets come from the same parent distribution. If the calculated confidence level for their compatibility is close to 1 (with possible values between 0 and 1), the zone (or sum of several zones) in question is suitable for modeling the *OFF* region. The most compatible zone is then fitted with a continuous function, which is then used to model the background component in the full likelihood.

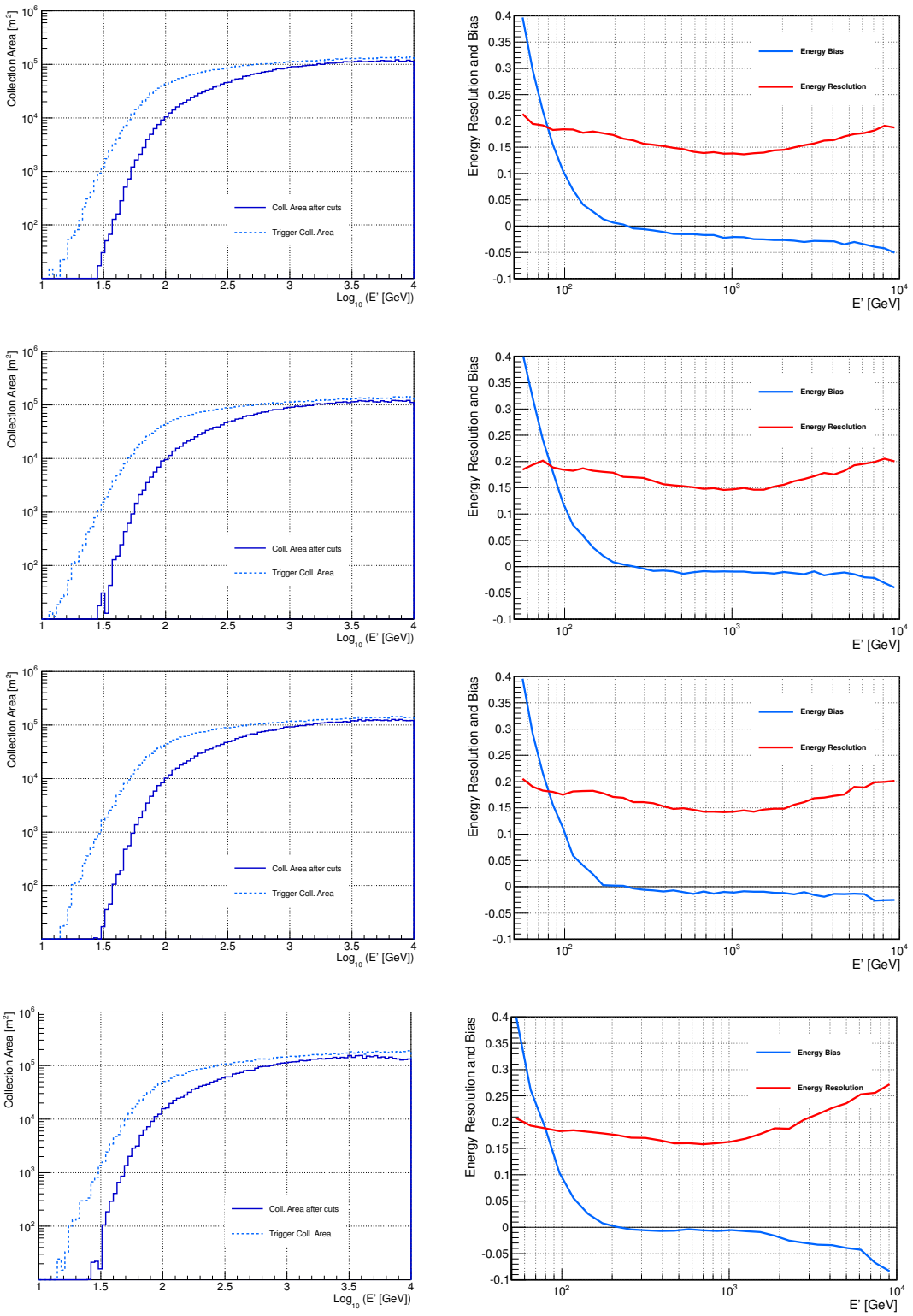

Figure 5.14: Effective area A_{eff} (**left column**) and energy resolution σ and bias μ (**right column**) for different periods of Segue 1 observations: sample A (**first row**), sample A (**second row**), sample A (**third row**) and sample C (**fourth row**).

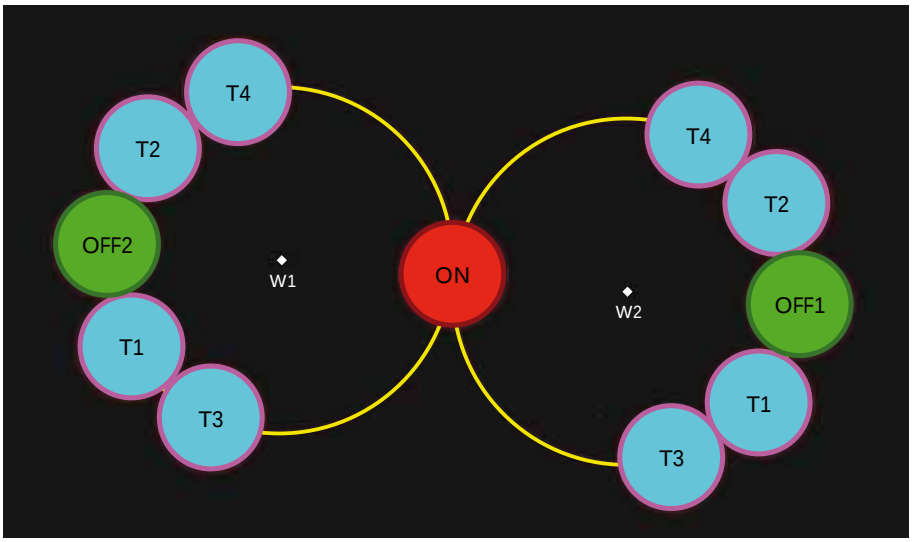

Figure 5.15: Illustration of different zones used for modeling of the background in the *OFF* regions. This particular scheme corresponds to sample C wobble configuration. See the main text for more details.

	Sample A		**Sample B1**		**Sample B2**	
	W1	**W2**	**W1**	**W2**	**W1**	**W2**
Zone	T1	T2	T1+T2+T3	T1+T2+T3	T1+T2	T1+T2
K-S prob.	0.749	0.122	0.760	0.366	0.098	0.754
A_0	0.063	0.0600	0.111	0.073	0.144	0.158
E_b [GeV]	73.57±4.08	73.71±3.25	71.97±6.71	74.72±2.88	72.94±0.46	72.28±0.53
c_1	3.87±2.46	3.58±2.42	5.16±2.13	4.59±2.22	6.00±0.25	6.00±0.37
c_2	-2.66±0.04	-2.78±0.04	-2.67±0.04	-2.73±0.04	-2.68±0.02	-2.81±0.03
β	0.39±0.26	0.36±0.21	0.46±0.53	0.27±0.23	0.77±0.06	0.61±0.08
χ^2	99.655	78.413	60.325	66.452	94.924	79.12
NDF	95	95	95	95	95	95
χ^2/NDF	1.049	0.825	0.635	0.699	0.999	0.832
Probability	0.491	0.891	0.998	0.988	0.624	0.939

Table 5.5: Details of the background modeling for Segue 1 data samples A, B1 and B2. Horizontal lines separate information regarding selection of the zone(s) used for modeling, sets of parameters obtained from the likelihood fit of the events from the zone(s), and values describing the validity of the fit.

In this work, background is modeled for each wobble of each observational period: when telescopes are pointing to W1, data is gathered for *OFF2* and for the zones used to model *OFF2*, and vice versa for W2 (Figure 5.15). The -S statistics is calculated comparing the *OFF* with each of its four zones (T1, T2, T3 and T4), as well as with the sums of two (T1+T2), three (T1+T2+T3, T1+T2+T4) and all four zones (T1+T2+T3+T4). The events from the most compatible zone(s), according to the K-S statistics (Table 5.5), are then used to model the background. The distribution of those events is nicely fitted by a smooth broken power law

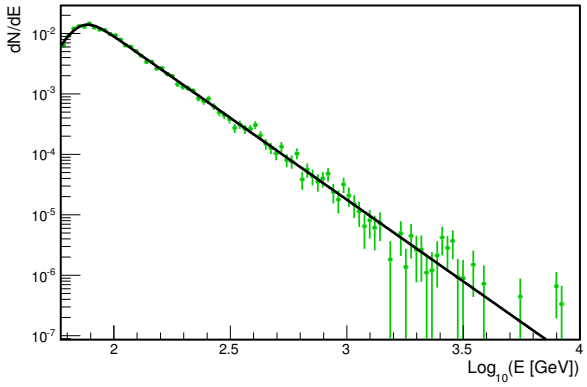

Figure 5.16: Example of background modeling applied in this analysis. The green points represent the events from the zone(s) that is most compatible with the *OFF* region, and the black line is the fit to their distribution. This particular case represents the background modeling of *OFF2* region for the sample B2.

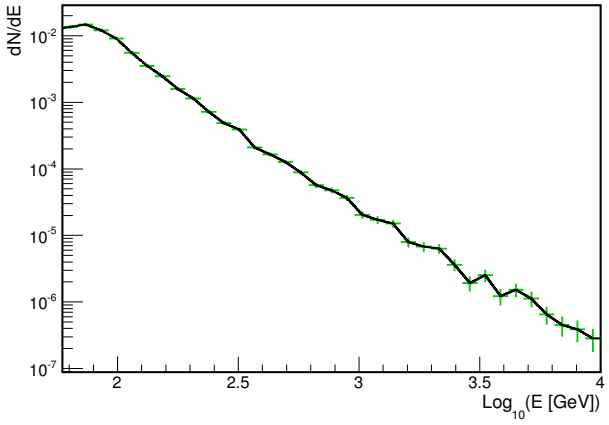

Figure 5.17: Example of background modeling for the sample C data. The green points represent the events from the zone(s) that is most compatible with the *OFF* region, and the black line, used for the background modeling, is obtained from the extrapolation of these points. This particular case represents the background modeling of *OFF1* region. See the main text for more details.

function (Figure 5.16):

$$\frac{dN}{dE} = A_0 \left(\frac{E}{100\text{GeV}} \right)^{c_1} \left(1 + \left(\frac{E}{E_b} \right)^{\frac{c_1 - c_2}{\beta}} \right)^{-\beta}, \tag{5.1}$$

where A_0 is a normalization constant, E_b is the break energy, β is the curvature of the transition between the low energy power law and high energy power law, whose respective indices are c_1 and c_2. Values of these parameters are estimated by maximization of the likelihood, performed by the `TMinuit` class of ROOT [192]. The resulting values, as well as the χ^2 estimates of such fit are listed in Table 5.5, for models of both *OFF* regions of all of the observational periods, except for the sample C data. Namely, due to the dynamical sum cleaning applied for this sample, the smooth broken power law no longer represents the optimal fit at the highest energies[2]. Instead, background is modeled directly from the continuous, binned

[2]The dynamical sum cleaning was not the best solution for the Segue 1 data of sample C, however, by the time

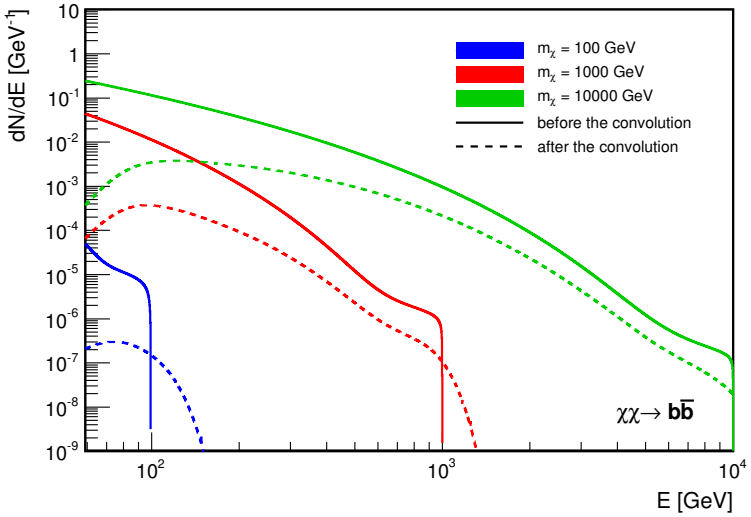

Figure 5.18: Gamma-ray spectrum from dark matter annihilation into $b\bar{b}$ channel (full lines) for m_χ = 100, 1000 and 10000 GeV (blue, red and green lines, respectively). The dashed lines represent the shape of the spectrum convoluted with the response function of MAGIC Telescopes.

distribution of the events (Figure 5.17) from the most compatible zone(s) (the K-S tests favour (T1+T2+T3+T4) for *OFF1* and (T1+T2+T3) for the modeling of *OFF2*).

5.3.5 Signal

Lastly, for the full likelihood analysis, the spectral function of the expected gamma-ray emission from the source has to be defined. For the work presented here, this means selecting a certain model of dark matter annihilation or decay for which investigation with MAGIC makes sense. Once the model is chosen, the spectral shape of the signal is fixed by the dN/dE' term of the particle physics flux contribution Φ^{PP} (eq.(2.2,2.7)). This spectral shape, however, is defined as a function of true energy E'; to transform it to the function of measured energy E, it has to be convoluted with the response function of the telescopes (eq(4.6)).

Some of the mechanisms for the production of gamma-rays through the annihilation or decay of dark matter particles have already been presented in §2.3.2.3. This Section lists the particular models that will be considered in this work, and presents some more technical aspects regarding their analysis. For all of the models, the branching ratio Br is taken to be Br = 100%, and the dark matter particle mass m_χ is considered to be in the 100 GeV - 10 TeV range.

Secondary photons, produced from annihilation or decay of dark matter into SM particles, have continuous and rather featureless spectral distributions, with a soft cutoff at kinematical limit $E_\gamma = m_\chi$. Thus, after the convolution with the response function, the principal change in their spectra is the alteration of the spectral slope and slight extension beyond the energy of m_χ (Figure 5.18). The following final state products are considered:

- ❖ quarks: $b\bar{b}$ and $t\bar{t}$;
- ❖ leptons: $\mu^+\mu^-$ and $\tau^+\tau^-$; and

this work was finished, production of MC files with different cleaning was not possible.

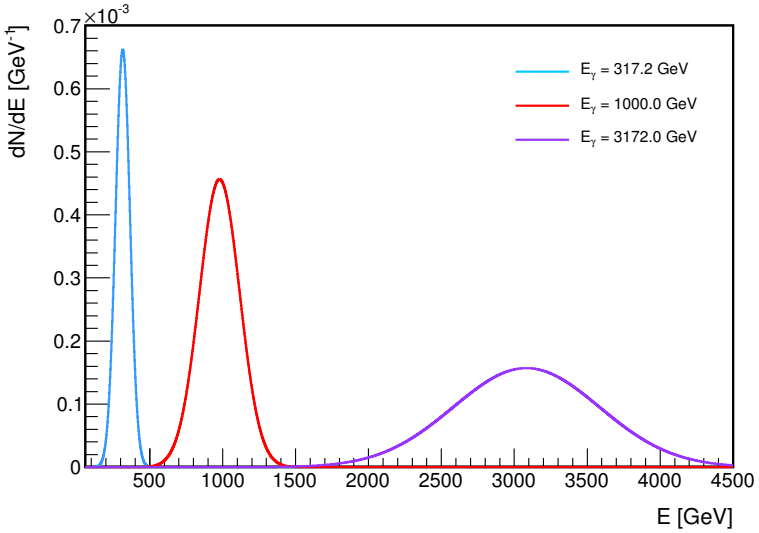

Figure 5.19: Aspect of gamma-ray lines after the convolution with the MAGIC response function. The shown example assumes direct dark matter annihilation into two photons, with m_χ taking values of 317.2, 1000 and 3172 GeV (blue, red and violet lines, respectively).

- gauge bosons: W^+W^- and ZZ.

Their modeling is done from the fit functions presented in [109].

Gamma-ray lines, from direct annihilation or decay of dark matter particles into photon(s), are expected to be the 'smoking guns' of indirect searches. The monochromatic line is in practice modeled as a very narrow gaussian centered at m_χ. However, due to finite energy resolution of the instruments, if detected, line would be seen as widened and smoothed (Figure 5.19). In this work, line is expected from the following annihilation processes:

- $\chi\chi \to \gamma\gamma$, with $E_\gamma = m_\chi$ and
- $\chi\chi \to Z\gamma$, with $E_\gamma = m_\chi\left(1 - m_Z^2/4m_\chi^2\right)$.

For the case of the decay into $\gamma\gamma$ or $Z\gamma$, the line is expected at energy of $E_\gamma = m_\chi/2$ and $E_\gamma = m_\chi/2\left(1 - m_Z^2/4m_\chi^2\right)$, respectively.

Virtual Internal Bremsstrahlung photons have spectral distribution characterized by the prominent peak at energies close to the m_χ, and by the sharp cutoff at $E_\gamma = m_\chi$ (Figure 2.7). As these photons are emitted in the dark matter annihilation into charged SM particles, the total spectrum is composed of continuous distributions of secondary photons and FSR, plus the VIB bump; therefore, in this work, limits are set on the total 3-body annihilation cross section. The shape of the VIB part of the spectra is widened by the energy resolution of the telescopes; the cutoff is softened and spectrum extended a bit above m_χ.

In this work, the following annihilation cases are considered:

- $\chi\chi \to \mu^+\mu^-(\gamma)$, and
- $\chi\chi \to \tau^+\tau^-(\gamma)$.

How pronounced is the VIB bump depends on the mass-splitting parameter $\mu(\equiv m_\eta^2/m_\chi^2$, where η is the t-channel mediator, §2.3.2.3). Here are considered contributions for $1 < \mu \leq 2$, as the VIB feature is the most important in nearly degenerate case.

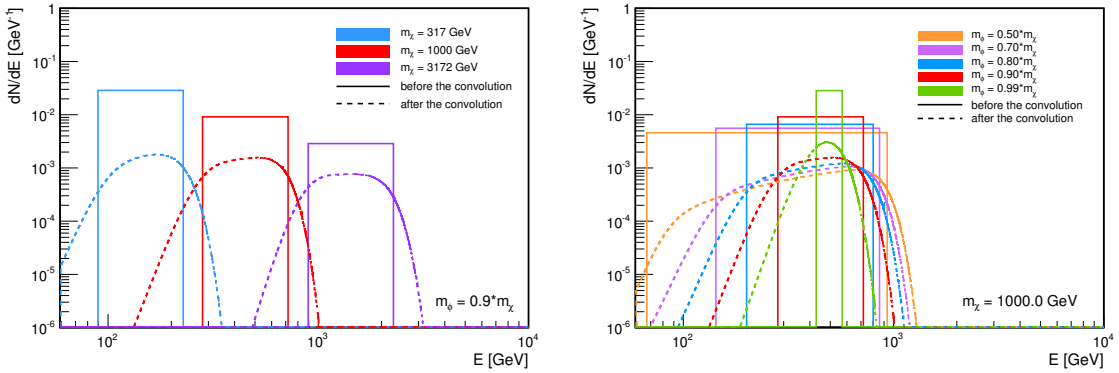

Figure 5.20: Box-like gamma-ray spectra from dark matter annihilation, when m_χ takes values of 317.2, 1000.0 and 3172.0 GeV (blue, red and violet lines, respectively) and $m_\phi = 0.90 * m_\chi$ (**left**), and when $m_\chi = 1000$ GeV while the mass of the scalar ϕ varies as $m_\chi/m_\phi = 0.5$, 0.7, 0.8, 0.9 and 0.99 (orange, violet, blue, red and green lines, respectively; **right**). Full lines represent the spectra before, and dashed lines after the convolution with the response function of MAGIC.

Gamma-ray boxes are another possibly pronounced spectral features in dark matter annihilation or decay. Depending on the mass of the intermediate scalar Φ, the width of the 'boxy' shape is wider and dimmer ($m_\phi < m_\chi$) or intense and almost line-like ($m_\phi \approx m_\chi$). Convolution with the response function smoothens the edges and broadens the signal distribution (Figure 5.20).

Here is considered that the scalar ϕ decays into two photons ($\phi \to \gamma\gamma$), meaning that annihilation of two dark matter particles results in production of 4 photons, while for the case of dark matter decay the outcome are 2γ.

5.3.6 Analysis Technicalities

For each of the two wobbles of each of the four Segue 1 observational periods with MAGIC (§5.2), a PDF for the full likelihood analysis is constructed from the corresponding background model (§5.3.4) and the signal spectral function (§5.3.5) convoluted with the appropriate response of the telescopes (§5.3.3). Each PDF is then used to calculate the likelihood of the corresponding data set of Segue 1 observations, already reduced by the application of optimized cuts (§5.3.1).

The full likelihood calculations are performed for the 95% c.l. and one-sided confidence intervals by the `TMinuit` class of ROOT. Gamma-ray signal intensity θ is included as a free parameter, and its value is obtained as a sum of its minimum $\theta_{\rm min}$ (that corresponds to the maximum likelihood) plus the width of the confidence interval $\theta_{\rm CI}$. A limitation is set, so that θ can only assume values from the physical sector, i.e. it can not be negative. If the calculated $\theta_{\rm min}$ is negative, its value is set to zero; that way, $\theta = \theta_{\rm min} + \theta_{\rm CI} > 0$ always applies. Additionally, number of estimated background events b (related to the number of estimated gamma-ray events g through eq.(4.9)) and background normalization τ are treated as the nuisance parameters in the likelihood maximization.

These calculations are made for each of the two wobble positions of each of the four observational samples, but also for the entire Segue 1 data sample. The latter is done by combining the above mentioned 8 individual likelihoods, following the eq.(4.15).

Lastly, the conversion of the θ value into $\langle\sigma_{\rm ann}v\rangle$ or τ_χ is rather straightforward: from

eq.(4.3-4.6), θ can be expressed as a function of $d\Phi/dE$, which is then replaced by the corresponding form of the expected gamma-ray flux (eq.(2.1)).

5.4 Results

Finally, this Section presents the results of this work: 157.9 hours of good-quality data from observations of dSph galaxy Segue 1 with MAGIC are analysed using the full likelihood method, an approach optimized for spectra with some characteristic features.

Results are presented in the following way: for each of the dark matter models listed in §5.3.5, the result from Segue 1 data is given by an exclusion curve obtained through the combination of likelihood analyses of each of the two wobbles of each of the four observational samples. This joint limits is first compared with the expectations (from toy MC for the given model) for the case when there is no signal, as well as for the scenarios when signal is present and detectable with 1σ or 2σ significance. Additionally, when applicable, the results of this work are shown in light of the most constraining limits from other gamma-ray observatories.

As for the astrophysical factor J, for the cuts used in this analysis, and assuming Einasto dark matter density profile, its value has been calculated to be $J = 1.051 \times 10^{19}$ GeV^2 cm^{-5} for the annihilation scenarios.

5.4.1 Secondary photons from annihilation into SM particles

The results for each of the six considered models ($b\bar{b}$, $t\bar{t}$, $\mu^+\mu^-$, $\tau^+\tau^-$, W^+W^- and ZZ) are presented separately, and compared with the latest limits from Fermi-LAT, VERITAS and H.E.S.S.

The Fermi-LAT results are obtained from the already mentioned joint analysis of 10 dSphs ([125], Figures 2.9 and 5.3). The limits were obtained from two years of data, assuming dark matter annihilation into $b\bar{b}$, $\mu^+\mu^-$, $\tau^+\tau^-$ and W^+W^- final states, all with branching ratios of 100% and for m_χ in the 5 GeV - 1 TeV range (and 100 GeV - 1 TeV for W^+W^-). For $b\bar{b}$ and $\tau^+\tau^-$ channels, for WIMP particle lighter than 25 GeV and 40 GeV, respectively, Fermi-LAT limits on $\langle\sigma_{\rm ann}v\rangle$ are actually stronger than the thermal rate of $\langle\sigma_{\rm ann}v\rangle \sim 3 \times 10^{-26}$ cm^3 s^{-1} (Figure 2.9).

Fermi-LAT constraints weaken significantly for higher energies, and for $m_\chi > 500$ GeV, the currently strongest limits come from H.E.S.S.: from 112 hours of Galactic Halo observations, and assuming a generic model of dark matter annihilation into quarks, the most stringent limit (for $m_\chi = 1$ TeV) is about a factor 10 weaker than the termal value ([118], Figure 2.8). Still, when comparing limits from different targets, one should always keep in mind that the underlying astrophysical uncertainties in calculation of the factor J may be quite different: for instance, predictions for integrated signal fluxes are much more robust for dSphs than for the Galactic Center.

Additionally, the VERITAS Collaboration has published the results from $\sim$50 hours of Segue 1 observations [216]. Among others, exclusion limits were derived for annihilation and decay into for $b\bar{b}$, $\mu^+\mu^-$, $\tau^+\tau^-$ and W^+W^- channels, for m_χ in the 100-11000 GeV range. However, these results show some inconsistencies that can be traced back to the probable overestimation of the VERITAS performance assumed for the analysis presented in [216]. The cross-check of these results by the Author of this work and her colleges shows that, for even the most conservative assumptions, values provided in [216] imply a VERITAS sensitivity of

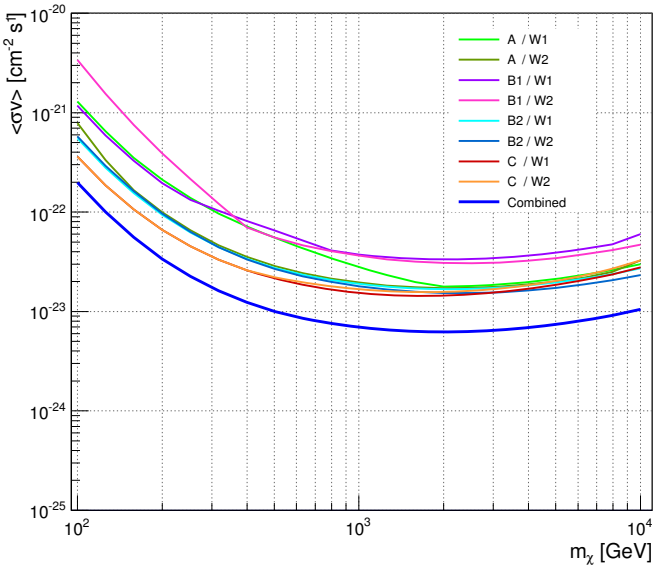

Figure 5.21: Individual limits from different wobble positions from different observational samples, for $b\bar{b}$ channel. Also show is the limit from the combined likelihood analysis.

0.32% of Crab flux above 165 GeV, more than a factor 2 better than reported by the VERITAS Collaboration [217]. This discrepancy is currently under revision by the VERITAS Collaboration. And although their limits from Segue 1 will be shown in the following plots together with results from Fermi-LAT and from this work, they will not be discussed and the Reader should regard them with serious reservs.

Lastly, constrains from ∼30 hours of the 2009 observations of Segue 1 with MAGIC in the single telescope mode (MAGIC-II was still under commissioning at this period) are considered [208]. Limits were derived for dark matter annihilation into $b\bar{b}$, $\tau^+\tau^-$ and $\mu^+\mu^-$ channels, with m_χ between 200 and 1350 GeV. These results are included in this Section in order to illustrate the advance that has been achieved in dark matter searches with MAGIC since four years ago, by means of deeper observations, more sensitive instruments and dedicated analysis method.

- $\chi\chi \to b\bar{b}$

As already mentioned, the $\langle\sigma_{\rm ann}v\rangle$ limits is obtained by combining the full likelihood analyses of each of the wobbles of each of the four observational periods. For the illustration purposes, these individual limits are shown on Figure 5.21. As it can be seen, the weakest constrains come from the statistically 'poor' B1 samples, while the fully upgraded system (sample C) yields the best limits[3]. Also shown is the combined limit on $\langle\sigma_{\rm ann}v\rangle$ – it is stronger, by at least a factor ∼2, than the most constraining individual limit at any energy. Figure 5.22 shows the combined limit (from now on, limit) on the $\langle\sigma_{\rm ann}v\rangle$ calculated from the data (full line), together with the expectations from simulations for the cases where there is no signal (dashed line), and when there is 1σ (shaded gray area) and 2σ (shaded light blue area; the same color/line coding will be applied for all the other dark matter models) significant

[3]Above 2 TeV, the dynamic sum image cleaning is no longer optimal for this analysis, but it has to be used due to the lack (at the time this work was finished) of MC samples with other cleaning settings.

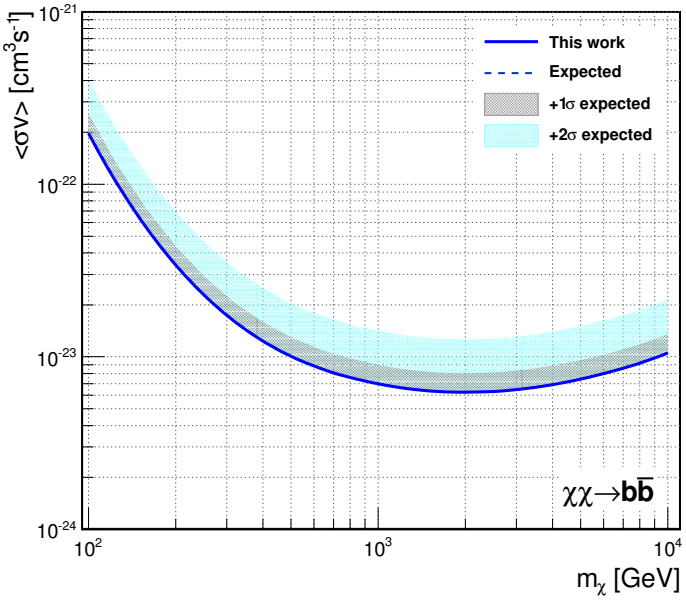

Figure 5.22: Limit on $\langle\sigma_{\rm ann}v\rangle$ for $b\bar{b}$ channel, from Segue 1 observations (full line) and as expected for the case of no signal (dashed line), or signal with 1σ or 2σ significance (gray and light blue shaded areas, respectively).

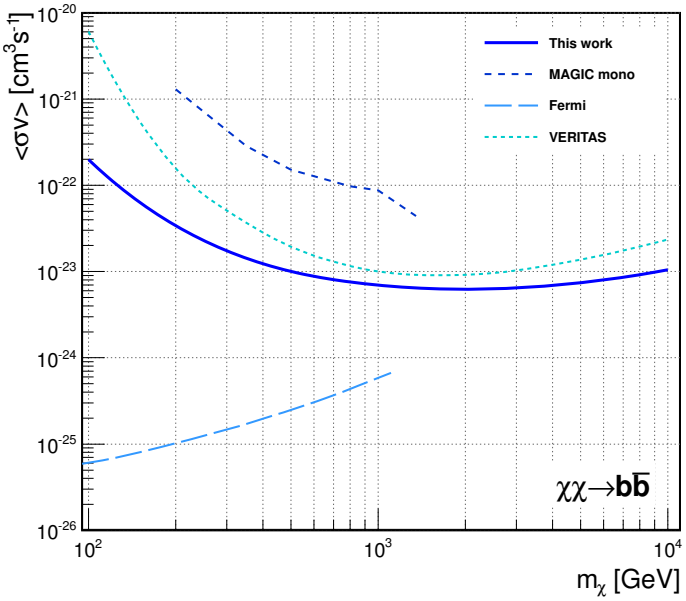

Figure 5.23: Limits on $\langle\sigma_{\rm ann}v\rangle$ for $b\bar{b}$ channel, from this work (full line) and from previously published results from MAGIC-I [208], Fermi-Lat [125] and VERITAS [216].

signal. As seen from the Figure 5.22, limit from this work is consistent with no-detection scenario.

This limit is compared to the constrains from other experiments in Figure 5.23: it is the most constraining result from dSph observations by IACTs, reaching minimum of $\langle\sigma_{\rm ann}v\rangle = 6\times10^{-24}$ cm^3 s^{-1} for $m_\chi = 2$ TeV. It complements the Fermi exclusion line above 1 TeV, and it is more than an order of magnitude better than the previos MAGIC limit from mono observations.

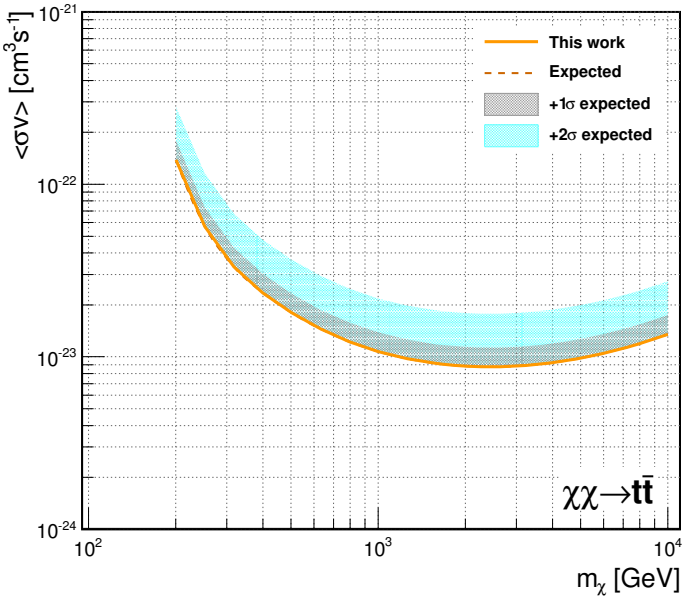

Figure 5.24: Limit on $\langle\sigma_{\rm ann}v\rangle$ for $t\bar{t}$ channel, from Segue 1 observations (full line) and as expected for the case of no signal (dashed line), or signal with 1σ or 2σ significance (gray and light blue shaded areas, respectively).

✧ $\chi\chi \to t\bar{t}$

This annihilation channel becomes an option for $m_\chi > m_{\rm t} = 173.5\pm0.6$ GeV. In this work, limit for $t\bar{t}$ is calculated for $m_\chi >$200 GeV. Figure 5.24 compares the result from observations with the expectations; again, there is no hint of a signal. No experimental results from other gamma-ray observatories have been found for this channel. The strongest limit is calculated for $m_\chi = 2$ TeV, and is of order $\langle\sigma_{\rm ann}v\rangle = 9\times10^{-24}$ cm^3 s^{-1}.

✧ $\chi\chi \to \mu^+\mu^-$

As μ-lepton is not massive enough for the hadronization, photons are emitted from the FSR process. As a consequence, their spectral distribution is of rather hard slope and peaks near kinematical limit. Figure 5.25 shows limit from this work versus expectations. As it can be seen, there are some statistical fluctuations for lowest dark matter particle masses and m_χ between 1 and 5 TeV. This however, is all within the expectations, and no signal can be claimed from this limit.

Figure 5.26 compares result from this work with those from Fermi, and for $m_\chi >$300 GeV, MAGIC limit becomes the most constraining, with strongest value $\langle\sigma_{\rm ann}v\rangle = 4\times10^{-24}$ cm^3 s^{-1} corresponding to $m_\chi = 400$ GeV. This, however, is still a factor $\sim$100 above the thermal value. Improvement with respect to the MAGIC mono result is of one order of magnitude.

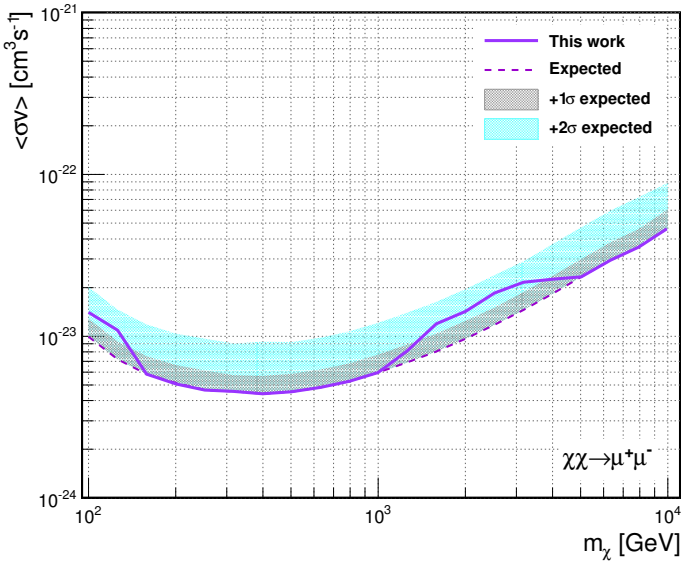

Figure 5.25: Limit on $\langle\sigma_{\rm ann}v\rangle$ for $\mu^+\mu^-$ channel, from Segue 1 observations (full line) and as expected for the case of no signal (dashed line), or signal with 1σ or 2σ significance (gray and light blue shaded areas, respectively).

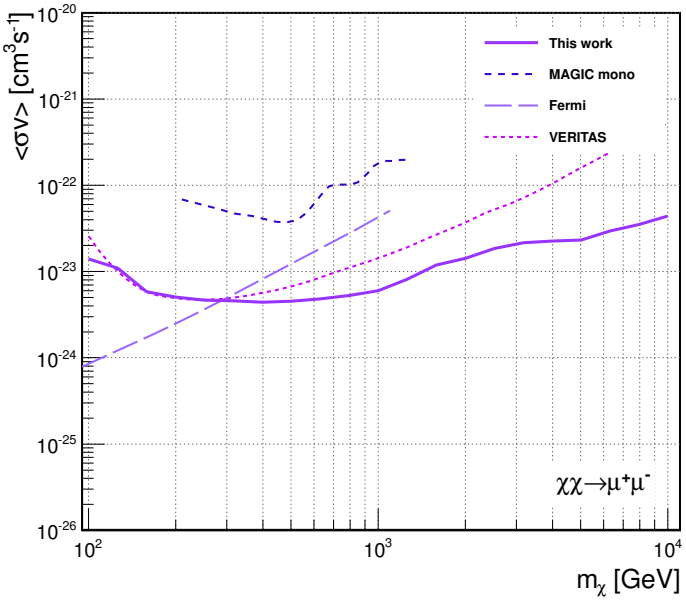

Figure 5.26: Limits on $\langle\sigma_{\rm ann}v\rangle$ for $mu^+\mu^-$ channel, from this work (full line) and from previously published results from MAGIC-I [208], Fermi-Lat [125] and VERITAS [216].

✧ $\chi\chi \to \tau^+\tau^-$

Limit for this channel shows some statistical fluctuations at highest energies, but no hint of a signal (Figure 5.27). This limit becomes stronger than the Fermi constraint for m_χ above

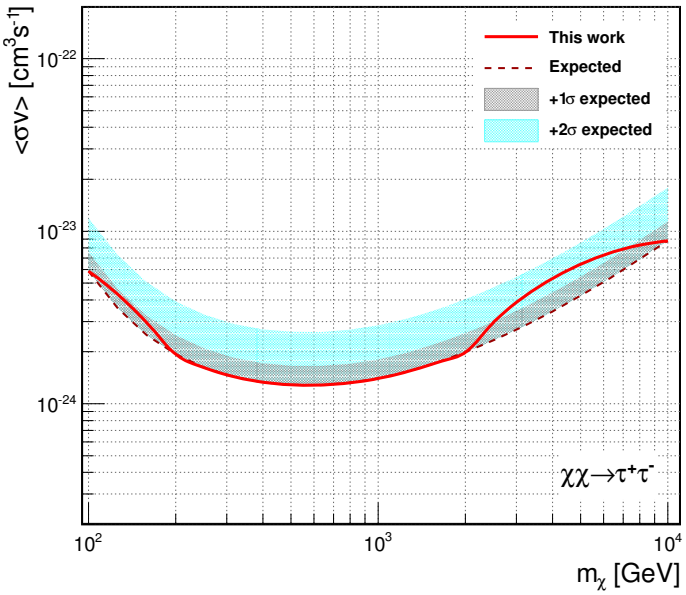

Figure 5.27: Limit on $\langle\sigma_{\rm ann}v\rangle$ for $\tau^+\tau^-$ channel, from Segue 1 observations (full line) and as expected for the case of no signal (dashed line), or signal with 1σ or 2σ significance (gray and light blue shaded areas, respectively).

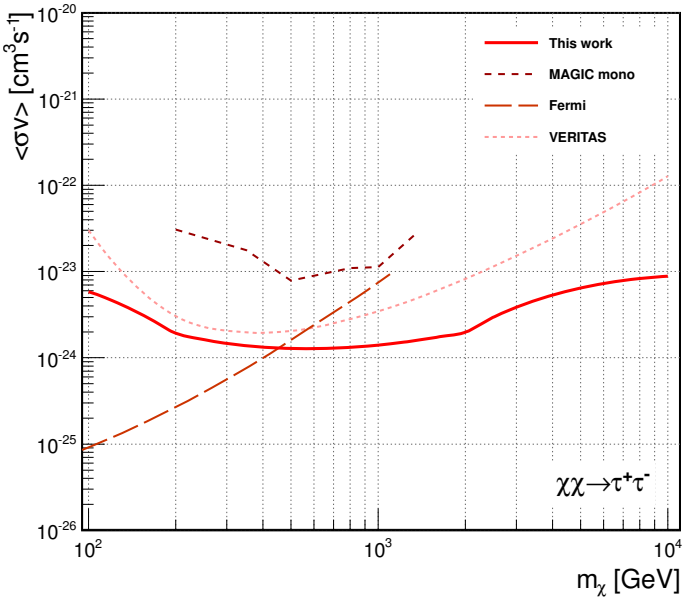

Figure 5.28: Limits on $\langle\sigma_{\rm ann}v\rangle$ for $\tau^+\tau^-$ channel, from this work (full line) and from previously published results from MAGIC-I [208], Fermi-Lat [125] and VERITAS [216].

450 GeV (Figure 5.28. It is at the same time the most stringent result from dSph observations with IACTs till date, and the lowest limit from this work for secondary photons, with best $\langle\sigma_{\rm ann}v\rangle$ value of 1×10^{-24} cm^3 s^{-1} for $m_\chi = 500$ GeV, a factor ~ 30 above the thermal rate of 3×10^{-26} cm^3 s^{-1}.

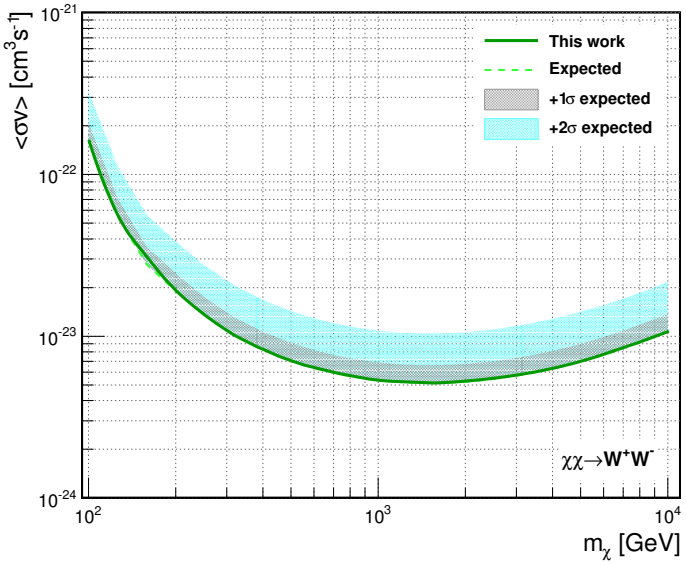

Figure 5.29: Limit on $\langle\sigma_{\rm ann}v\rangle$ for W^+W^- channel, from Segue 1 observations (full line) and as expected for the case of no signal (dashed line), or signal with 1σ or 2σ significance (gray and light blue shaded areas, respectively).

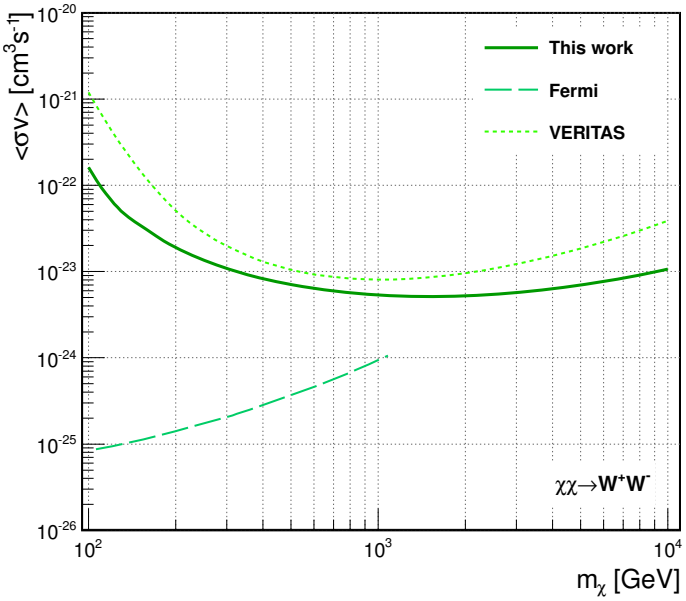

Figure 5.30: Limits on $\langle\sigma_{\rm ann}v\rangle$ for W^+W^- channel, from this work (full line) and from previously published results from Fermi-Lat [125] and VERITAS [216].

✧ $\chi\chi \to W^+W^-$

Limit for W^+W^- final state is shown in comparison with different expectations in Figure 5.29, and with results from different experiments in Figure 5.30. It is the most constraining result from dSphs observations for this channel above 1 TeV, with the most stringent value $\langle\sigma_{\rm ann}v\rangle = 5\times10^{-24}$ cm^3 s^{-1} for $m_\chi = 1.5$ TeV.

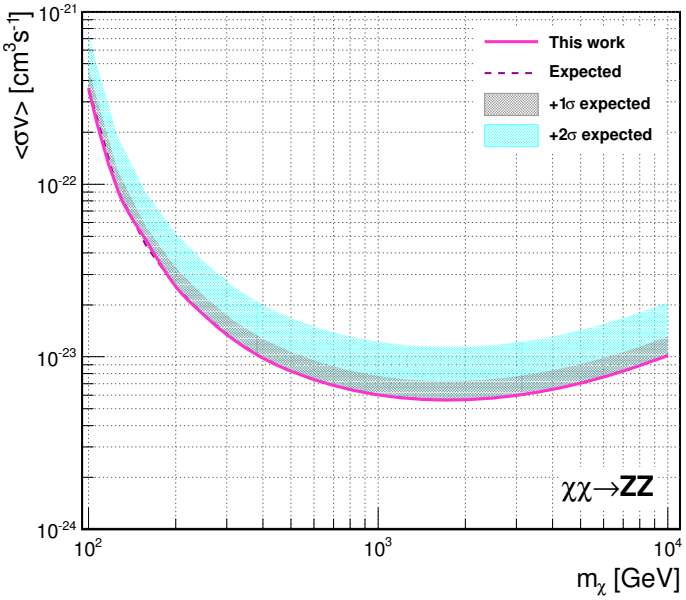

Figure 5.31: Limit on $\langle\sigma_{\rm ann}v\rangle$ for ZZ channel, from Segue 1 observations (full line) and as expected for the case of no signal (dashed line), or signal with 1σ or 2σ significance (gray and light blue shaded areas, respectively).

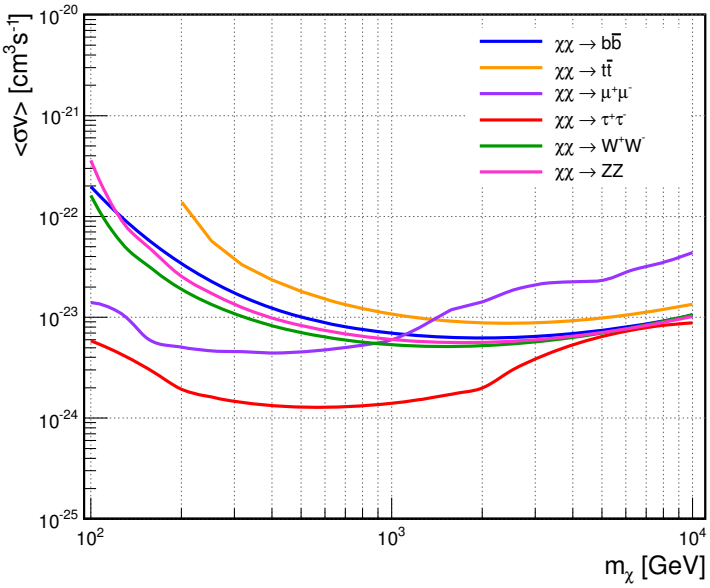

Figure 5.32: Limits on $\langle\sigma_{\rm ann}v\rangle$, for different final channels, from Segue 1 observations analyzed with the full likelihood method.

✧ $\chi\chi \to ZZ$

The spectral shape of ZZ channel is very similar to that of W^+W^-, thus it is not surprising that their limits are similar as well. Figure 5.31 shows the ZZ limit versus expectations. The most stringent $\langle\sigma_{\rm ann}v\rangle$ value is $\sim 5.5\times10^{-24}$ cm^3 s^{-1} for $m_\chi = 1.5$ TeV.

Lastly, for a more comprensive overview, all of the $\langle\sigma_{\rm ann}v\rangle$ limits obtained from this work for the considered final state channels are plotted in Figure 5.32.

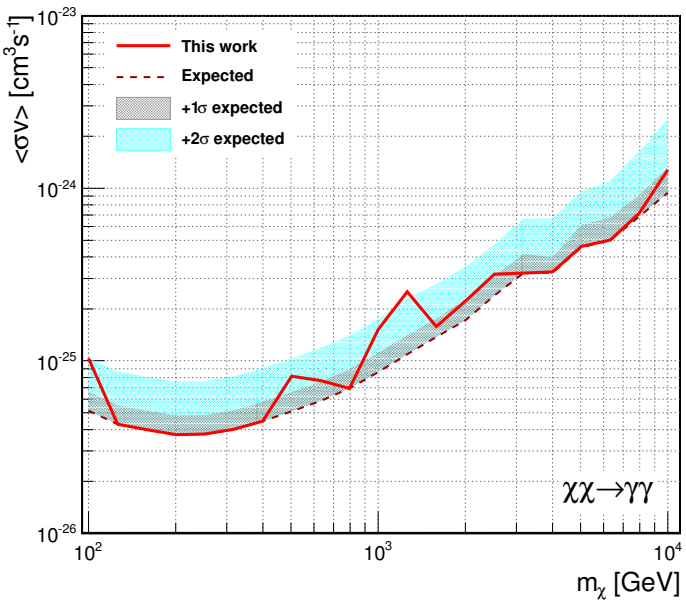

Figure 5.33: Limit on $\langle\sigma_{\text{ann}}v\rangle$ for direct annihilation into $\gamma\gamma$, from Segue 1 observations (full line) and as expected for the case of no signal (dashed line), or signal with 1σ or 2σ significance (gray and light blue shaded areas, respectively).

5.4.2 Gamma-ray Line

Although direct annihilation of dark matter particles into photons and the subsequent line emission is highly suppressed ($\mathscr{O} \sim 1/\alpha^2$), importance of detection of such feature can not be overestimated: not only such a line would be firm proof of dark matter existence, it would also reveal some information about the nature of its particle (as line energy corresponds to m_χ. It is why many searches for hint of a line have been conducted so far, in galaxy clusters, Milky Way satellite dwarf galaxies, the Galactic Center and Halo.

The currently strongest limits presented by the Fermi-LAT follow from 2 years of observations of Galactic Center region [123] and extend from $\langle\sigma_{\text{ann}}v\rangle \leq 3\times10^{-29}$ cm^3 s^{-1} at $m_\chi =$ 10 GeV to $\langle\sigma_{\text{ann}}v\rangle \leq 4\times10^{-27}$ cm$^{3]}$ s^{-1} at $m_\chi = 200$ GeV. At higher energies, above 500 GeV, results from H.E.S.S. observations of Galactic Halo set constraints of $\langle\sigma_{\text{ann}}v\rangle \sim 2\times10^{-27}$ cm^3 s^{-1} [218].

Limit from this work, for direct annihilation $\chi\chi \to \gamma\gamma$ is shown in Figure 5.33: as it can be seen, for the considered range of m_χ, $\langle\sigma_{\text{ann}}v\rangle$ constraints are between $\sim 4\times10^{-26}$ cm$^{3]}$ s^{-1} (for $m_\chi = 200$ GeV) and $\sim 1\times10^{-24}$ cm$^{3]}$ s^{-1} (for $m_\chi = 1000$ GeV). This result is compared with expectations for the no-signal scenario (dashed line), as well as with 1σ and 2σ significant excess (shaded gray and light blue areas, respectively).

Comparison of the results from Galactic Center region with those from dSphs is not very competitive, as the high astrophysical factor J of the former ones will always make them stronger. Still, as already mentioned, there are significant uncertainties in J estimate, and thus it is interesting to see how limits from different targets compare. Figure 5.34 shows the limit from this work versus constraints from the above cited Fermi-LAT and H.E.S.S line searches. At $m_\chi = 200$ GeV, MAGIC result is about an order of magnitude away from Fermi-LAT, while the difference with H.E.S.S. limit is almost order of two. Again, given different targets, this is expected.

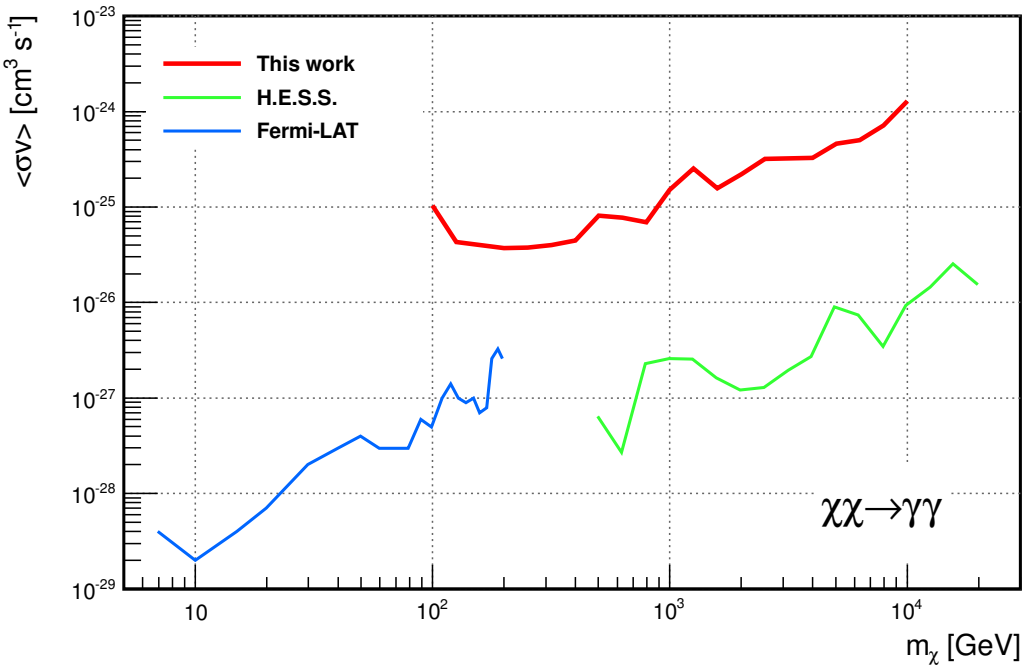

Figure 5.34: Limits on $\langle \sigma_{\mathrm{ann}} v \rangle$ for dark matter annihilation into two photons, calculated from the Segue 1 observations presented in this work (red line). Limits obtained by Fermi-LAT [123] 2-year observations of Galactic Center region (blue line) and H.E.S.S 112 hours of observations of the Galactic Halo [218] (green line) are shown for comparison.

Conclusions

The presented work reports on indirect dark matter searches in dSph galaxy Segue 1. The observations with the MAGIC Telescopes, performed between January 2011 and February 2013, have resulted in 157.9 hours of good-quality data, thus making this observational campaign the deepest survey of any dSph by any IACT so far.

A sound case has been made in favour of Segue 1 as the best (at the moment) dark matter target for MAGIC. With mass-to-light ratio of order of 1000, this galaxy is the most dark matter-dominated object known so far. In addition, its relative closeness, lack of baryonic content and astrophysical background at very high energies, establish Segue 1 as an excellent candidate for indirect searches.

Data have been analyzed by means of the *full likelihood method*, an optimized analysis approach developed as a part of this work. The full likelihood takes complete advantage of the distinct features expected in the gamma-ray spectrum of dark matter origin, achieving significantly better sensitivity with respect to the standard analysis chains of IACTs. Additionally, it is robust, unbiased and stable, and it has a potential for a global, sensitivity-optimized indirect dark matter search by combining the results of all Cherenkov observatories of the present generation.

Given that the analyzed data show no significant gamma-ray excess, the obtained results are translated into limits for various channels of dark matter annihilation. In particular, constraints for various final state channels are the strongest limits from IACT observations of dSphs. For $m_\chi = 2$ TeV, the $\langle\sigma_{\rm ann}v\rangle$ exclusion line is set to $\sim 6\times10^{-24}$ cm^3 s^{-1} for $b\bar{b}$ and $\langle\sigma_{\rm ann}v\rangle \sim 9\times10^{-24}$ cm^3 s^{-1} for $t\bar{t}$. For leptonic channels, best limits are achieved for $m_\chi = 400$ GeV ($\langle\sigma_{\rm ann}v\rangle \sim 4\times10^{-24}$ cm^3 s^{-1}) and $m_\chi = 450$ GeV ($\langle\sigma_{\rm ann}v\rangle \sim 1\times10^{-24}$ cm^3 s^{-1}), for $\mu^+\mu^-$ and $\tau^+\tau^-$, respectively. In fact, above $\sim$300 GeV and $\sim$450 GeV, respectively, these results become more stringent that the Fermi-LAT limits from combined analysis of 10 dSphs. Lastly, for gauge boson channels W^+W^- and ZZ, the strongest limits correspond to $m_\chi = \sim$1.5 TeV and are of order $\langle\sigma_{\rm ann}v\rangle \sim 5.5\times10^{-24}$ cm^3 s^{-1}.

Gamma-ray line has been considered as well: although direct dark matter annihilation into photons is highly suppressed, even the slightest possibility for the detection of this feature is extremely exciting. MAGIC observations of Segue 1 have been used to set $\langle\sigma_{\rm ann}v\rangle$ limits for such process; the strongest result corresponds to $m_\chi = 200$ GeV, and is of order of $\sim 4\times10^{-24}$ cm^3 s^{-1}. Still, these observations are not competitive in line searches with other gamma-ray observatories that can take advantage of observations of the Galactic Center vicinity.

The results presented in this work will for sure represent an important landmark in the field before the next generation of Cherenkov Telescopes – the CTA – becomes operational in 2017. The CTA will be the most powerful instrument for dark matter searches in the VHE gamma-ray band, promising us all very exciting times ahead.

References

[1] E. Öpik, *An Estimate of the Distance of the Andromeda Nebula*, *Astrophys. J.* **55** (1922) pp. 406–410.

[2] J. H. Oort, *The Force Exerted by the Stellar System in the Direction Perpendicular to the Galactic Plane and Some Related Problems*, *Bull. Astron. Inst. Neth.* **6** (1932) pp. 249–287.

[3] F. Zwicky, *Rotation of the Andromeda Nebula from a Spectroscopic Survey of Emission Regions*, *Helv. Phys. Acta* **6** (1933) pp. 110–127.

[4] V. Rubin and W.K.Jr. Ford, *Die Rotverschieb ung von extragalaktischen Nebeln*, *Astorphys. J.* **159** (1970) pp. 397–403.

[5] K.G. Begeman, A.H. Broeils, and R.H. Sanders, *Extended rotation curves of spiral galaxies - Dark haloes and modified dynamics*, *Mon. Not. Roy. Astron. Soc.* **149** (1991) pp. 523–537.

[6] P.Schneider, J. Ehlers, and E. E. Falco. *Gravitational Lenses*, Study ed., *Springer-Verlag*, Berlin (1992) ISBN: 978-3540665069.

[7] R. Gavazzi et al., *The Sloan Lens ACS Survey. IV: the mass density profile of early-type galaxies out to 100 effective radii*, *Astrophys. J* **667** (2007) pp. 176–190 [arXiv:astro-ph/0701589].

[8] N. Kaiser and G. Squires, *Mapping the dark matter with weak gravitational lensing*, *Astrophys. J* **404** (1993) pp. 441–450.

[9] M. Bradač et al., *Strong and weak lensing united III: Measuring the mass distribution of the merging galaxy cluster 1E0657-56*, *Astrophys. J.* **652** (2006) pp. 937–947 [arXiv:astro-ph/0608408].

[10] D. Clowe, *A direct empirical proof of the existence of dark matter*, *Astrophys. J.* **648** (2006) pp. L109–L113 [arXiv:astro-ph/0608407].

[11] J. Wambsganss, *Microlensing Search for Dark Matter at all Mass Scales*. Proceedings of the 225$^{\text{th}}$ International Astronomical Union, Lausanne, Switzerland (2004).

[12] S. Weinberg. *Cosmology*, 1$^{\text{st}}$ ed., *Oxford University Press Inc.* New York (2008) ISBN: 978-0198526827.

[13] G. Hinshaw et al., *Nine-Year Wilkinson Microwave Anisotropy Probe (WMAP) Observations: Cosmological Parameter Results*, (2012) [arXiv:1212.5226].

[14] A. A. Penzias and R. W. Wilson, *A Measurement of Excess Antenna Temperature at 4080 Mc/s*, *Astrophys. J.* **142** (1965) pp. 419–421.

[15] C. L. Bennett et al., *Nine-Year Wilkinson Microwave Anisotropy Probe (WMAP) Observations: Final Maps and Results*, (2012) [arXiv:1212.5225].

[16] National Aeronautics and Space Administration, *Wilkinson Microwave Anisotropy Probe (WMAP),* http://map.gsfc.nasa.gov (January, 2013).

[17] S. Dodelson. *Modern Cosmology*, 1st ed., *Academic Press*, San Diego (2003) ISBN: 978-0122191411.

[18] J. R. Primack, *Whatever Happened to Hot Dark Matter?*, *SLAC beam Line* **31** (2001) pp. 50–57 [arXiv:astro-ph/0112336].

[19] V. Springel, C. S. Frenk, and S. D. M. White, *The large-scale structure of the Universe*, *Nature* **440** (2006) pp. 1137–1144 [arXiv:astro-ph/0604561].

[20] P. Colin, V. Avila-Reese, and O. Valenzuela, *Substructure and halo density profiles in a Warm Dark Matter Cosmology*, *Astrophys. J.* **542** (2000) pp. 622–630 [arXiv:astro-ph/0004115].

[21] The 2dF Galaxy Redshift Survey Collaboration, *The 2dF Galaxy Redshift Survey Homepage,* http://magnum.anu.edu.au/~TDFgg (January, 2013).

[22] The Sloan Digital Sky Survey Collaboration, *Sloan Digital Sky Survey Homepage,* http://www.sdss.org (January, 2013).

[23] J. Huchra et al., *A survey of galaxy redshifts. IV - The data*, *Astrophys. J. Supp.* **52** (1983) pp. 89–119.

[24] The Virgo Consortium, *The Millennium Simulation Project Homepage,* http://www.mpa-garching.mpg.de/galform/virgo/millennium (January, 2013).

[25] L. Perivolaropoulos, *LCDM: Triumphs, Puzzles and Remedies*. Proceedings of Lorenz Center Workshop, Leiden, Netherlands (2010) [arXiv:1104.0539].

[26] P. Salucci, *The mass distribution in Spiral galaxies*. Proceedings of the 244th International Astronomical Union Symposium, Cardiff, UK (2008) [arXiv:0707.4370].

[27] C. Trachternach et al., *Dynamical Centers and Noncircular Motions in THINGS Galaxies: Implications for Dark Matter Halos*, *Astron. J.* **136** (2008) 2720–2760 [arXiv:0810.2116].

[28] J. S. Bullock, *Notes on the Missing Satellites Problem*. Proceedings of the XX Canary Islands Winter School of Astrophysics, Tenerife, Spain (2008) [arXiv:1009.4505].

[29] J. D. Simon and M. Geha, *The Kinematics of the Ultra-Faint Milky Way Satellites: Solving the Missing Satellite Problem*, *Astrophys. J.* **670** (2007) 313–331 [arXiv:0706.0516].

[30] M. Milgrom, *A modification of the Newtonian dynamics as a possible alternative to the hidden mass hypothesis*, *Astrophys. J.* **170** (1983) pp. 365–370.

[31] J. D. Bekenstein, *Relativistic gravitation theory for the modified Newtonian dynamics paradigm*, *Phys. Rev. D* **70** (2004) 083509, Erratum-ibid. D71 (2005) 069901 [arXiv:astro-ph/0403694].

[32] K. Gödel, *An Example of a New Type of Cosmological Solutions of Einstein's Field Equations of Gravitation*, *Rev. Mod. Phys.* **21** (1949) pp. 447–450.

[33] F. Hoyle, G. Burbidge, and J. V. Narlikar, *The Basic Theory Underlying the Quasi-Steady-State Cosmology*, *Proc. R. Soc. Lond. A* **21** (1995) pp. 191–212.

[34] C. H. Brans, *The roots of scalar-tensor theory: an approximate history*, (2005) [arXiv:gr-qc/0506063].

[35] A. Blanchard et al., *An alternative to the cosmological "concordance model"*, *A&A* **412** (2003) pp. 35–44 [arXiv:astro-ph/0304237].

[36] P. Hut, *Limits on masses and number of neutral weakly interacting particles*, *Phys. Lett. B* **69** (1977) pp. 85–88.

[37] G. Gelmini and P. Gondolo. *DM production mechanisms*. In: G. Bertone (ed.), *Particle Dark Matter: Observations, Models and Searches*, pp. 121–141. 1st ed., *Cambridge University Press*, Cambridge, UK (2010) ISBN: 978-0521763684.

[38] P. Fayet and S. Ferrara, *Supersymmetry*, *Phys. Rept.* **32** (1977) pp. 249–334.

[39] H. P. Nilles, *Supersymmetry, Supergravity and Particle Physics*, *Phys. Rept.* **110** (1984) pp. 1–162.

[40] E. Witten, *Mass hierarchies in supersymmetric theories*, *Phys. Lett. B* **105** (1981) pp. 267–271.

[41] J. Ellis, S. Kelley, and D. V. Nanopoulos, *Constraints from gauge coupling unification on the scale of supersymmetry breaking*, *Phys. Lett. B* **287** (1992) pp. 95–100 [arXiv:hep-ph/9206203].

[42] J. R. Ellis et al., *Supersymmetric Relics from the Big Bang*, *Nucl. Phys. B* **238** (1984) pp. 453–476.

[43] P. Fayet, *Supersymmetry and weak, electromagnetic and strong interactions*, *Phys. Lett. B* **64** (1976) pp. 159–162.

[44] J. Wess and J. Bagger. *Supersymmetry and Supergravity*, 2nd revised ed., *Princeton University Press*, New Jersey (1992) ISBN: 978-0691025308.

[45] A. H. Chamseddine, R. L. Arnowitt, and P. Nath, *Locally Supersymmetric Grand Unification*, *Phys. Rev. Lett* **59** (1982) 970974.

[46] J. Ellis et al., *Exploration of the MSSM with non-universal Higgs masses*, *Nucl. Phys. B* **652** (2003) pp. 259–347 [arXiv:hep-ph/0210205].

[47] C. F. Berger et al., *Supersymmetry without prejudice*, *JHEP* **02** (2009) 23 [arXiv:0812.0980].

[48] T. Bringmann, L. Bergstrom, and J. Edsjo, *New Gamma-Ray Contributions to Supersymmetric Dark Matter Annihilation*, *JHEP* **10** (2008) 049 [arXiv:0710.3169].

[49] CERN European Organization for Nuclear Research, *The Large Hadron Collider Homepage*, http://public.web.cern.ch/public/en/LHC/LHC-en.html (January, 2013).

[50] S. Chatrchyan et al., *Observation of a new boson at a mass of 125 GeV with the CMS experiment at the LHC*, *Phys. Lett. B* **716** (2012) pp. 30–61 [arXiv:1207.7235].

[51] R. Aaij et al., *First Evidence for the Decay $B_s^0 \to \mu^+\mu^-$*, *Phys. Rev. Lett.* **110** (2013) 021801 [arXiv:1211.2674].

[52] CERN Courier, *Work for the LHCs first long shutdown gets under way* (March, 2013).

[53] T. Kaluza, *On the problem of unity in physics*, *Sitzungsber.Preuss.Akad.Wiss.Berlin (Math.Phys.)* (1921) pp. 966–972.

[54] O. Klein, *Quantum theory and five-dimensional theory of relativity*, *Z. Phys.* **37** (1926) pp. 895–906.

[55] T. Appelquist, H.C. Cheng, and B.A. Dobrescu, *Bounds on universal extra dimensions*, *Phys. Rev. D* **64** (2001) 035002 [arXiv:hep-ph/0012100].

[56] J.A.R. Cembranos, A. Dobado, and A.L. Maroto, *Brane-World Dark Matter*, *Phys. Rev. Lett.* **90** (2003) 241301 [arXiv:hep-ph/0302041].

[57] M. Schmaltz and D. Tucker-Smith, *Little Higgs review*, *Ann. Rev. Nucl. Part. Sci.* **55** (2005) pp. 229–270 [arXiv:hep-ph/0502182].

[58] K. Agashe and G. Servant, *Warped Unification, Proton Stability, and Dark Matter*, *Phys. Rev. Lett.* **93** (2004) 231805 [arXiv:hep-ph/0403143].

[59] T. Asaka and M. Shaposhnikov, *The νMSM, dark matter and baryon asymmetry of the universe*, *Phys. Lett. B* **620** (2005) pp. 17–26 [arXiv:hep-ph/0505013].

[60] M. G otz and J. Sommer-Larsen, *Galaxy formation: Warm dark matter, missing satellites, and the angular momentum problem*, *Astrophys.Space Sci.* **284** (2003) pp. 341–344 [arXiv:astro-ph/0210599].

[61] A. Dolgov and S. Hansen, *Massive sterile neutrinos as warm dark matter*, *Astropart. Phys.* **16** (2002) pp. 339–344 [arXiv:hep-ph/0009083].

[62] J. L. Feng, A. Rajaraman, and F. Takayama, *SuperWIMP Dark Matter Signals from the Early Universe*, *Phys. Rev. D* **68** (2003) 063504 [arXiv:hep-ph/0306024].

[63] R.D. Peccei and H. R. Quinn, *CP conservation in the presence of pseudoparticles*, *Phys. Rev. Lett.* **38** (1977) pp. 1440–1443.

[64] J. L. Feng and J. Kumar, *Dark-Matter Particles without Weak-Scale Masses or Weak Interactions*, *Phys. Rev. Lett.* **101** (2008) 231301 [arXiv:0803.4196].

[65] M. Battaglia and M. E. Peskin. *Supersymmetric dark matter at colliders*. In: G. Bertone (ed.), *Particle Dark Matter: Observations, Models and Searches*, pp. 276–305. 1st ed., *Cambridge University Press*, Cambridge, UK (2010) ISBN: 978-0521763684.

[66] CERN European Organization for Nuclear Research, *The ATLAS Experiment Homepage*, http://atlas.web.cern.ch/Atlas/Collaboration (March, 2013).

[67] CERN European Organization for Nuclear Research, *The CMS Experiment Homepage*, http://cms.web.cern.ch/ (March, 2013).

[68] L. Roszkowski K. Kowalska and E. M. Sessolo, *Two ultimate tests of constrained supersymmetry*, (2013) [arXiv:1302.5956].

[69] ATLAS Collaboration, *Search for strongly produced supersymmetric particles in final states with two same-sign leptons and jets with the ATLAS detector using 21 fb^{-1} of proton-proton collisions at $\sqrt{s} = 8$ TeV*, ATLAS note ATLAS-CONF-2013-007, CERN, Geneve, Switzerland (2013).

[70] S. Chatrchyan et al., *Search for dark matter and large extra dimensions in monojet events in pp collisions at $\sqrt{s} = 7$ TeV, JHEP* **09** (2012) 094 [arXiv:1206.5663].

[71] D. G. Cerdeno and A. M. Green. *Direct detection of WIMPs*. In: G. Bertone (ed.), *Particle Dark Matter: Observations, Models and Searches*, pp. 347–369. 1st ed., *Cambridge University Press*, Cambridge, UK (2010) ISBN: 978-0521763684.

[72] R. Bernabei et al., *First results from DAMA/LIBRA and the combined results with DAMA /NaI, Eur. Phys. J. C* **56** (2008) pp. 333–355 [arXiv:0804.2741].

[73] C. E. Aalseth et al., *Results from a Search for Light-Mass Dark Matter with a P-type Point Contact Germanium Detector, Phys.Rev.Lett.* **106** (2011) 31301 [arXiv:1002.4703].

[74] The XENON Dark Matter Project, *XENON100 Experiment*, http://xenon.astro.columbia.edu/XENON100Experiment (April, 2013).

[75] E. Aprile et al., *Dark Matter Results from 225 Live Days of XENON100 Data, Phys. Rev. Lett.* **109** (2012) 181301 [arXiv:1207.5988].

[76] E. Aprile et al., *Limits on spin-dependent WIMP-nucleon cross sections from 225 live days of XENON100 data*, (2013) [arXiv:1301.6620].

[77] E. Armengau et al., *Radiopure Scintillators for EURECA*. Proceedings of the 1st International Workshop RPScint, Kyiv, Ukraine (2009) [arXiv:0903.1539].

[78] L. Baudis, *DARWIN: dark matter WIMP search with noble liquids*. Proceedings of Indentification of Dark Matter, Montpellier, France (2010) [arXiv:1012.4764].

[79] E. Aprile et al., *Performance of a cryogenic system prototype for the XENON1T Detector, Journal of Instrumentation* **7** (2012) p. 10001 [arXiv:1208.2001].

[80] Kamioka Observatory, *Super-Kamiokande Official Homepage*, http://www-sk.icrr.u-tokyo.ac.jp/sk/index-e (April, 2013).

[81] ANTARES Collaboration, *ANTARES homepage,* http://antares.in2p3.fr/ (April, 2013).

[82] University of Wisconsin-Madison, *IceCube Neutrino Observatory,* http://icecube.wisc.edu/ (April, 2013).

[83] F. Halzen and D. Hooper. *High-energy neutrinos from WIMP annihilations in the Sun.* In: G. Bertone (ed.), *Particle Dark Matter: Observations, Models and Searches*, pp. 507–520. 1st ed., *Cambridge University Press*, Cambridge, UK (2010) ISBN: 978-0521763684.

[84] R. Abbasi et al., *Search for Neutrinos from Annihilating Dark Matter in the Direction of the Galactic Center with the 40-String IceCube Neutrino Observatory*, (2012) [arXiv:1210.3557].

[85] O. Adriani et al., *An anomalous positron abundance in cosmic rays with energies 1.5-100 GeV, Nature* **458** (2009) pp. 607–609 [arXiv:0810.4995].

[86] A. A. Abdo et al., *Measurement of the Cosmic Ray e+ plus e- spectrum from 20 GeV to 1 TeV with the Fermi Large Area Telescope, Phys. Rev. Lett.* **102** (2009) 181101 [arXiv:0905.0025].

[87] I. Moskalenko and A. Strong, *Production and Propagation of Cosmic-Ray Positrons and Electrons, ApJ* **493** (1998) pp. 694–707 [arXiv:astro-ph/9710124].

[88] M. Aguilar et al., *First Result from the Alpha Magnetic Spectrometer on the International Space Station: Precision Measurement of the Positron Fraction in Primary Cosmic Rays of 0.5350 GeV, Phys. Rev. Lett.* **110** (2013) 141102.

[89] PAMELA Mission, *A Payload for Antimatter Exploration and Light-nuclei Astrophysics Mission Official Website,* http://pamela.roma2.infn.it/ (April, 2013).

[90] AMS-02 Collaboration, *The Alpha Magnetic Spectrometer Experiment,* http://www.ams02.org (April, 2013).

[91] M. Cirelli et al., *Model-independent implications of the e^+, e^-, anti-proton cosmic ray spectra on properties of Dark Matter, Nucl. Phys. B* **813** (2009) 1–21 [arXiv:0809.2409].

[92] A. Ibarra, D. Tran, and C. Weniger, *Decaying Dark Matter in Light of the PAMELA and Fermi LAT Data, JCAP* **01** (2010) 009 [arXiv:0906.1571].

[93] D. Hooper, P. Blasi, and P. Dario Serpico, *Pulsars as the sources of high energy cosmic ray positrons, JCAP* **01** (2009) 025 [arXiv:0810.1527].

[94] O. Adriani et al., *A new measurement of the antiproton-to-proton flux ratio up to 100 GeV in the cosmic radiation, Phys. Rev. Lett.* **102** (2009) 051101 [arXiv:0810.4994].

[95] P. Salati, F. Donato, and N. Fornengo. *Indirect dark matter detection with cosmic antimatter.* In: G. Bertone (ed.), *Particle Dark Matter: Observations, Models and Searches*, pp. 521–546. 1st ed., *Cambridge University Press*, Cambridge, UK (2010) ISBN: 978-0521763684.

[96] A. Ibarra, D. Tran, and C. Weniger, *Detecting gamma-ray anisotropies from decaying dark matter: Prospects for Fermi LAT*, *Phys. Rev. D* **81** (2010) 023529 [arXiv:0909.3514].

[97] J. F. Navarro, C. S. Frenk, and S. D. White, *The Structure of cold dark matter halos*, *ApJ* **462** (1996) pp. 563–575 [arXiv:astro-ph/9508025].

[98] C. A. Vera-Ciro et al., *Not too big, not too small: the dark halos of the dwarf spheroidals in the Milky Way*, *Mon. Not. Roy. Astron. Soc.* **428** (2013) 1696–1703 [arXiv:1202.6061].

[99] J. F. Navarro et al., *The diversity and similarity of simulated cold dark matter haloes*, *Mon. Not. Roy. Astron. Soc.* **402** (2010) pp. 21–34 [arXiv:0810.1522].

[100] A. V. Kravtsov et al., *The Cores of Dark Matter Dominated Galaxies: theory vs. observations*, *ApJ* **502** (1998) pp. 48–58 [arXiv:astro-ph/9708176].

[101] N. W. Evans, J. An, and M. G. Walker, *Cores and cusps in the dwarf spheroidals*, *Mon. Not. Roy. Astron. Soc. Lett.* **393** (2009) pp. L50–L54 [arXiv:0811.1488].

[102] V. Springel et al., *The Aquarius Project: the subhaloes of galactic haloes*, *Mon. Not. Roy. Astron. Soc* **391** (2008) pp. 1685–1711 [arXiv:0809.0898].

[103] J. Diemand, M. Kuhlen, and P. Madau, *Dark Matter Substructure and Gamma-Ray Annihilation in the Milky Way Halo*, *ApJ* **657** (2007) 262–270 [arXiv:astro-ph/0611370].

[104] L. E. Strigari et al., *Precise constraints on the dark matter content of Milky Way dwarf galaxies for gamma-ray experiments*, *Phys. Rev. D* **75** (2007) 083526 [arXiv:astro-ph/0611925].

[105] L. E. Strigari, *Galactic Searches for Dark Matter*, (2012) [arXiv:1211.7090].

[106] E. W. Kolb and M. S. Turner, *The Early Universe*, *Front. Phys* **69** (1990) 1.

[107] J. Hisano, S. Matsumoto, and M. M. Nojiri, *Explosive Dark Matter Annihilation*, *Phys. Rev. Lett.* **92** (2004) 031303 [arXiv:hep-ph/0307216].

[108] G. Bertone et al., *Gamma-Rays from Decaying Dark Matter*, *JCAP* **11** (2012) 003 [arXiv:0709.2299].

[109] J. Cembranos et al., *Photon spectra from WIMP annihilation*, *Phys. Rev. D* **83** (2011) 083507 [arXiv:1009.4936].

[110] A. Birkedal et al., *Robust gamma ray signature of WIMP dark matter*, (2005) [arXiv:hep-ph/0507194].

[111] T. Bringmann, L. Bergström, and J. Edsjö, *New Gamma-Ray Contributions to Supersymmetric Dark Matter Annihilation*, *JHEP* **01** (2008) 049 [arXiv:0710.3169].

[112] T. Bringmann et al., *Fermi LAT Search for Internal Bremsstrahlung Signatures from Dark Matter Annihilation*, *JCAP* **07** (2012) 054 [arXiv:1203.1312].

[113] A. Ibarra, S. Lopez Gehler, and M. Pato, *Dark matter constraints from box-shaped gam-ma-ray features*, *JCAP* **07** (2012) 043 [arXiv:1205.0007].

[114] D. Merritt et al., *Dark Matter Spikes and Annihilation Radiation from the Galactic Center*, *Phys.Rev.Lett.* **88** (2002) 191301 [arXiv:astro-ph/0201376].

[115] F. Aharonian et al., *H.E.S.S. observations of the Galactic Center region and their possible dark matter interpretation*, *Phys. Rev. Lett.* **97** (2006) 221102 [arXiv:astro-ph/0610509].

[116] J. Albert et al., *Observations of Gamma Rays from the Galactic Center with the MAGIC Telescope*, *ApJ* **638** (2006) pp. L101–L104 [arXiv:astro-ph/0512469].

[117] H.E.S.S. Collaboration, *H.E.S.S. - The Highly Energy Spectroscopic System,* http://www.mpi-hd.mpg.de/hfm/HESS (April, 2013).

[118] A. Abramowski et al., *Search for a Dark Matter Annihilation Signal from the Galactic Center Halo with H.E.S.S*, *Phys. Rev. Lett.* **106** (2011) 161301 [arXiv:1103.3266].

[119] C. Weniger, *A tentative gamma-ray line from Dark Matter annihilation at the Fermi Large Area Telescope*, *JCAP* **08** (2012) 007 [arXiv:1204.2797].

[120] A. Ibarra et al., *Gamma-ray boxes from axion-mediated dark matter*, (2013) [arXiv:1303.6632].

[121] W. Buchmuller and M. Garny, *Decaying vs Annihilating Dark Matter in Light of a Tentative Gamma-Ray Line*, *JCAP* **08** (2012) 035 [arXiv:1206.7056].

[122] A. Hektor, M. Raidal, and E. Tempel, *Double gamma-ray lines from unassociated Fermi-LAT sources revisited*, (2012) [arXiv:1208.1996].

[123] M. Ackermann et al., *Fermi LAT Search for Dark Matter in Gamma-ray Lines and the Inclusive Photon Spectrum*, *Phys. Rev. D* **86** (2012) 022002 [arXiv:1205.2739].

[124] D. Nieto. *Dark Matter Constrains from High Energy Astrophysical Observations*. PhD thesis. Universidad Complutense de Madrid, Spain (2012).

[125] M. Ackermann et al., *Constraining Dark Matter Models from a Combined Analysis of Milky Way Satellites with the Fermi Large Area Telescope*, *Phys. Rev. Lett.* **107** (2011) 241302 [arXiv:1108.3546].

[126] L. E. Strigari et al., *The Most Dark-Matter-dominated Galaxies: Predicted Gamma-Ray Signals from the Faintest Milky Way Dwarfs*, *ApJ* **678** (2008) 614–620 [arXiv:0709.1510].

[127] N. Evans, F. Ferrer, and S. Sarkar, *A Baedecker for the dark matter annihilation signal*, *Phys. Rev. D* **69** (2004) 123501 [arXiv:astro-ph/0311145].

[128] A. Pinzke, C. Pfrommer, and L. Bergström, *Prospects of detecting γ-ray emission from galaxy clusters: cosmic rays and dark matter annihilations*, *Phys. Rev. D* **84** (2011) 123509 [arXiv:1105.3240].

[129] M. A. Sanchez-Conde et al., *Dark matter searches with Cherenkov telescopes: nearby dwarf galaxies or local galaxy clusters?*, *JCAP* **12** (2011) 011 [arXiv:1104.3530].

[130] M. Ackermann et al., *Constraints on Dark Matter Annihilation in Clusters of Galaxies with the Fermi Large Area Telescope*, *JCAP* **05** (2010) 025 [arXiv:1002.2239].

[131] J. Aleksić et al., *MAGIC Gamma-ray Telescope Observation of the Perseus Cluster of Galaxies: Implications for Cosmic Rays, Dark Matter, and NGC 1275*, *ApJ* **710** (2010) pp. 634–647 [arXiv:0909.3267].

[132] A. Boyarsky et al., *Restrictions on parameters of sterile neutrino dark matter from observations of galaxy clusters*, *Phys. Rev. D* **74** (2006) 103506 [arXiv:astro-ph/0603368].

[133] V. Schönfelder (ed.) *The Universe in Gamma Rays*, *Springer-Verlag*, Hamburg (2001) ISBN: 978-3540678748.

[134] NASA Goddard Space Flight Center, *The Explorer-11 Satellite,* http://heasarc.gsfc.nasa.gov/docs/heasarc/missions/explorer11 (April 2013).

[135] European Space Agency, *Cos-B Overview,* http://www.esa.int/Our˙Activities/Space˙Science/Cos-B˙overview2 (April 2013).

[136] NASA Goddard Space Flight Center, *The Small Astronomy Satellite 2,* http://heasarc.gsfc.nasa.gov/docs/sas2/sas2 (April 2013).

[137] NASA Goddard Space Flight Center, *The Energetic Gamma Ray Experiment Telescope (EGRET),* http://heasarc.gsfc.nasa.gov/docs/cgro/egret (April 2013).

[138] NASA Goddard Space Flight Center, *The Fermi Gamma-Ray Space Telescope,* http://fermi.gsfc.nasa.gov (April 2013).

[139] W. B. Atwood et al., *The Large Area Telescope on the Fermi Gamma-Ray Space Telescope Mission*, *ApJ* **697** (2009) pp. 1071–1102 [arXiv:0902.1089].

[140] P. L. Nolan et al., *Fermi Large Area Telescope Second Source Catalog*, *ApJ Supp.* **199** (2012) p. 46 [arXiv:0902.1089].

[141] A. A. Abdo et al., *The Fermi-LAT high-latitude Survey: Source Count Distributions and the Origin of the Extragalactic Diffuse Background*, *ApJ* **720** (2010) pp. 435–453 [arXiv:1003.0895].

[142] M. Ackermann et al., *Constraints on dark matter annihilation in clusters of galaxies with the Fermi large area telescope*, *JCAP* **05** (2010) 025 [arXiv:1002.2239].

[143] C. A. Meegan et al., *The Fermi Gamma-ray Burst Monitor*, *ApJ* **702** (2009) pp. 791–804 [arXiv:0908.0450].

[144] F. Schmidt, *CORSIKA Shower Images* http://www.ast.leeds.ac.uk/~fs (April 2013).

[145] T. S. Weeks et al., *Observations of TeV gamma rays from the Crab nebula using the atmospheric Cherenkov imaging technique*, *ApJ* **342** (1989) pp. 379–395.

[146] Max-Planck-Institut für Kernphysik, *The HEGRA Atmospheric Cherenkov Telescope System,* http://www.mpi-hd.mpg.de/hfm/CT (April 2013).

[147] A. Barrau et al., *The CAT Imaging Telescope for Very-High-Energy Gamma-Ray Astronom*, *Nucl. Instrum. Meth. A* **416** (1998) pp. 278–292 [arXiv:astro-ph/9804046].

[148] VERITAS Collaboration, *VERITAS Homepage,* http://veritas.sao.arizona.edu/ (April 2013).

[149] The CTA Consortium, *The Cherenkov Telescope Array Homepage,* https://www.cta-observatory.org/ (April 2013).

[150] MAGIC Collaboration, *MAGIC Telescopes Homepage,* http://magic.mppmu.mpg.de (December, 2012).

[151] J. Aleksić et al., *Performance of the MAGIC stereo system obtained with the Crab Nebula data*, *Astropart. Phys.* **35** (2012) pp. 435–448 [arXiv:1108.1477].

[152] T. Bretz et al., *The drive system of the major atmospheric gamma-ray imaging Cherenkov telescope*, *Astropart. Phys.* **31** (2009) pp. 92–101 [arXiv:0810.4593].

[153] M. Doro. *Novel reflective elements and indirect dark matter searches for MAGIC II and future IACTs*. PhD thesis. Universitá degli Studi di Padova, Italy (2009).

[154] F. Goebel et al., *Upgrade of the MAGIC Telescope with a Multiplexed Fiber-Optic 2 GSamples/s FADC Data Acquisition system*. Proceedings of the 30$^{\text{th}}$ International Cosmic Ray Conference, Mérida, México (2007) [arXiv:0709.2363].

[155] J. Aleksić. *Characterization of the MAGIC II Data Acquisition System*. MA thesis. Universitat Autonoma de Barcelona, Spain (2009).

[156] D. Tescaro, *The Upgraded Readout System of the MAGIC Telescopes*. To appear in the Proceedings of the IEEE Nuclear Science Symposium, Anaheim, California (2012).

[157] M. Rissi et al., *A new sum trigger to provide a lower energy threshold for the MAGIC telescope*, *IEEE Transactions on Nuclear Science* **56** (2009) pp. 3840–3843.

[158] R. Zanin and J. Cortina, *The central control of the MAGIC telescopes*. Proceedings of the 31$^{\text{st}}$ International Cosmic Ray Conference, Łódź, Poland (2009) [arXiv:0907.0946].

[159] V. P. Fomin et al., *New methods for atmospheric Cherenkov imaging for gamma-ray astronomy 1: The False source method*, *Astropart. Phys.* **2** (1994) pp. 137–150.

[160] A. Moralejo et al., *MARS, the MAGIC Analysis and Reconstruction Software*. Proceedings of the 31$^{\text{st}}$ International Cosmic Ray Conference, Łódź, Poland (2009) [arXiv:0907.0943].

[161] S. Lombardi et al., *Advanced stereoscopic gamma-ray shower analysis with the MAGIC Telescopes*. Proceedings of the 32$^{\text{nd}}$ International Cosmic Ray Conference, Beijing, Chi-na (2011) [arXiv:1109.6195].

[162] ROOT, *A Data Analysis Framework,* http://root.cern.ch/drupal (December, 2012).

[163] P. Majumdar et al., *Monte Carlo simulation for the MAGIC Telescope*. Proceedings of the 29th International Cosmic Ray Conference, Pune, India (2005).

[164] E. Carmona et al., *Monte Carlo simulation for the MAGIC-II System*. Proceedings of the 30th International Cosmic Ray Conference, Merida, Mexico (2007) [arXiv:0709.2959].

[165] R. Zanin. *Observations of the Crab Nebula pulsar wind nebula and microquasar candidates with MAGIC*. PhD thesis. Univeristat Autónoma de Barcelona, Spain (2011).

[166] J. Albert et al., *FADC signal reconstruction for the MAGIC telescope*, *Nucl. Instrum. Meth. A* **594** (2008) pp. 407–419 [arXiv:astro-ph/0612385].

[167] R. Mirzoyan, *On the calibration accuracy of light sensors in atmospheric Cherenkov fluorescence and neutrino experiments*. Proceedings of the 25th International Cosmic Ray Conference, Durban, South Africa (1997).

[168] M. Shayduk et al., *A new image cleaning method for the MAGIC Telescope*. Proceedings of the 29th International Cosmic Ray Conference, Pune, India (2005).

[169] E. Aliu et al., *Improving the performance of the single-dish Cherenkov telescope MAGIC through the use of signal timing*, *Astropart. Phys.* **30** (2009) pp. 293–305 [arXiv:0810.3568].

[170] A. M. Hillas, *Cherenkov light images of EAS produced by primary gamma rays and by nuclei*. Proceedings of the 19th International Cosmic Ray Conference, La Jola, USA (1985).

[171] A. Kohnle et al., *Stereoscopic imaging of air showers with the first two HEGRA Cherenkov Telescopes*, *Astropart. Phys.* **5** (1996) pp. 119–131.

[172] L. Breiman, *Random Forests*, *Machine Learning* **45** (2001) pp. 5–32.

[173] J. Albert et al., *Implementation of the Random Forest Method for the Imaging Atmospheric Cherenkov Telescope MAGIC*, *Nucl. Instrum. Meth. A* **588** (2008) pp. 424–432 [arXiv:0709.3719].

[174] J. Aleksić et al., *Search for an extended VHE -ray emission from Mrk 421 and Mrk 501 with the MAGIC Telescope*, *A&A* **524** (2010) A77 [arXiv:1004.1093].

[175] T. P. Li and Y. Q. Ma, *Analysis Methods for results in gamma-ray astronomy*, *Astrophys. J* **272** (1983) pp. 317–324.

[176] M. Errando. *Discovery of very high energy gamma-ray emission from 3c 279 and 3c 66A/B with the MAGIC telescope*. PhD thesis. Univeristat Autónoma de Barcelona, Spain (2009).

[177] W. Wittek, *Unfolding (revised)*, MAGIC internal note TDAS 05-05, Max-Planck-Institut for Physics, Munich, Germany (2005).

[178] A. N. Tikhonov and V. Y. Arsenin. *Solutions of ill posed problems*, 1st ed., *V. H. Winston*, New York (1977) ISBN: 978-0470991244.

[179] M. Bertero. *Linear inverse and ill-posed problems*. In: P. W. Hawkes (ed.), *Advances in Electronics and Electron Physics* **75**, pp. 1–120. *Academic Press INC.* San Diego (1989) ISBN: 978-0120146758.

[180] M. Schmelling, *Numerische Methoden der Datenanalyse*, Blockkurs Winter Semester 1997/1998, MPI-K Heidelberg, Germany (1998).

[181] W. A. Rolke, A. M. López, and J. Conrad, *Limits and confidence intervals in the presence of nuisance parameters*, *Nucl. Instrum. Meth. A* **551** (2005) pp. 493–503 [arXiv:physics/0403059].

[182] R. J. Hanisch et al., *Definition of the Flexible Image Transport System (FITS), A&A* **376** (2001) pp. 359–380.

[183] CTA Collaboration, *CTA Data and e-Infrastructure,* https://www.cta-observatory.org/?q=node/178 (December, 2012).

[184] MAGIC Collaboration, *MAGIC Datacenter @ PIC - FITS database,* http://magic.pic.es/pub/fits (December, 2012).

[185] J. Aleksić and J. Rico, *FITS format for MAGIC data*, MAGIC internal note TDAS 09-05, Institut de Física d'Altes Energies, Barcelona, Spain (2009).

[186] NASA Goddard Space Flight Center, *CCfits: Wrappers for the cfitsio library,* http://heasarc.gsfc.nasa.gov/fitsio/CCfits (December, 2012).

[187] NASA Goddard Space Flight Center, *FITSIO Home Page,* http://heasarc.gsfc.nasa.gov/fitsio (December, 2012).

[188] EURO-VO, *European Virtual Observatory,* http://www.euro-vo.org/pub/general/qa.html (December, 2012).

[189] IVOA, *International Virtual Observatory Alliance,* http://www.ivoa.net (December, 2012).

[190] MAGIC Collaboration, *MAGIC Data Virtual Observatory Search,* http:/vobs.magic.pic.es (December, 2012).

[191] M. A. Sanchez-Conde, *Dark matter searches with Cherenkov telescopes: nearby dwarf galaxies or local galaxy clusters?*, *JCAP* **12** (2011) 011 [arXiv:104.3530].

[192] F. James, *MINUIT. Function minimization and error analysis, reference manual version 94.1*, CERN Program Library Long Writeup D506, CERN, Geneva, Switzerland (1994).

[193] ROOT, *TMinuit,* http://root.cern.ch/root/html/TMinuit.html (January, 2013).

[194] B. Moore et al., *Cold collapse and the core catastrophe*, *Mon. Not. Roy. Astron. Soc.* **310** (1999) pp. 1147–1151 [arXiv:astro-ph/9903164].

[195] G. Gilmore et al., *The Observed properties of Dark Matter on small spatial scales*, *ApJ* **663** (2007) pp. 948–959 [arXiv:astro-ph/0703308].

[196] H. Shapley, *A stellar system of a new type*, *Harvard College Obs. Bull* **908** (1938) pp. 1–11.

[197] The Sloan Digital Sky Survey Collaboration, *The SDSS Home Page*, http://www.sdss.org (April, 2013).

[198] M. G. Walker, M. Mateo, and E. W. Olszewski, *Stellar Velocities in the Carina, Fornax, Sculptor, and Sextans dSph Galaxies: Data From the Magellan/MMFS Survey*, *AJ* **137** (2009) pp. 3100–3108 [arXiv:0811.0118].

[199] J. Klimentowski et al., *Mass modelling of dwarf spheroidal galaxies: The effect of unbound stars from tidal tails and the Milky Way*, *Mon. Not. Roy. Astron. Soc.* **378** (2007) pp. 353–368 [arXiv:astro-ph/0611296].

[200] B. J. Pritzl, K. A. Venn, and M. Irwin, *A Comparison of Elemental Abundance Ratios in Globular Clusters, Field Stars, and Dwarf Spheroidal Galaxies*, *ApJ* **130** (2005) pp. 2140–2165 [arXiv:astro-ph/0506238].

[201] M. Mateo et al., *The Carina dwarf spheroidal galaxy – How dark is it?*, *AJ* **105** (1993) pp. 510–526.

[202] J. Simon et al., *A Complete Spectroscopic Survey of the Milky Way Satellite Segue 1: The Darkest Galaxy*, *ApJ* **733** (2011) pp. 46–66 [arXiv:1007.4198].

[203] C. J. Hogan and J. J. Dalcanton, *New dark matter physics: clues from halo structure*, *Phys. Rev. D* **63** (2000) 063511 [arXiv:astro-ph/0002330].

[204] M. Mateo, *Dwarf galaxies of the local group*, *Ann. Rev. A&A* **36** (1998) pp. 435–506 [arXiv:astro-ph/9810070].

[205] J. Wolf et al., *Accurate Masses for Dispersion-supported Galaxies*, *Mon. Not. Roy. Astron. Soc.* **406** (2010) pp. 1220–1237 [arXiv:0908.2995].

[206] J. Jardel and K. Gebhardt, *The Dark Matter Density Profile of the Fornax Dwarf*, *ApJ* **746** (2012) pp. 89–97 [arXiv:1112.0319].

[207] J. Aleksić et al., *Segue 1: the best dark matter candidate dwarf galaxy surveyed by MAGIC*. Proceedings of the 32$^{\text{nd}}$ International Cosmic Ray Conference, Beijing, China (2011) [arXiv:1109.6781].

[208] J. Aleksić et al., *Searches for dark matter annihilation signatures in the Segue 1 satellite galaxy with the MAGIC-I telescope*, *JCAP* **06** (2011) 035 [arXiv:1103.0477].

[209] A. W. Smith et al., *CF2 White Paper: Status and Prospects of The VERITAS Indirect Dark Matter Detection Program*. To appear in Proceedings of the Snowmass on the Mississipi, Minneapolis, USA (2013) [arXiv:1304.6367].

[210] A. Viana, *Dark Matter searches with H.E.S.S. towards dwarf spheroidal galaxies*. Proceedings of Indentification of Dark Matter, Montpellier, France (2010) [arXiv:1111.5781].

[211] Sloan Digital Sky Survey Collaboration, *SEGUE: Sloan Extension for Galactic Understanding and Exploration* http://www.sdss.org/segue/aboutsegue (May 2013).

[212] V. Belokurov et al., *Cats and Dogs, Hair and a Hero: A Quintet of New Milky Way Companions*, *ApJ* **654** (2007) pp. 897–906 [arXiv:astro-ph/0608448].

[213] Keck Observatory, *DEIMOS Homepage,* http://www2.keck.hawaii.edu/inst/deimos (May 2013).

[214] M. Geha et al., *The Least Luminous Galaxy: Spectroscopy of the Milky Way Satellite Segue 1*, *ApJ* **692** (2009) pp. 1464–1475 [arXiv:0809.2781].

[215] M. Niederste-Ostholt et al., *The origin of Segue 1*, *Mon. Not. Roy. Astron. Soc.* **398** (2009) pp. 1771–1781 [arXiv:0906.3669].

[216] E. Aliu et al., *VERITAS Deep Observations of the Dwarf Spheroidal Galaxy Segue 1*, *Phys. Rev. D* **85** (2012) 062001 [arXiv:1202.2144].

[217] VERITAS Collaboration, *VERITAS Specifications,* http://veritas.sao.arizona.edu/about-veritas-mainmenu-81/veritas-specifica-tions-mainmenu-111 (May, 2013).

[218] A. Abramowski et al., *Search for photon line-like signatures from Dark Matter annihilations with H.E.S.S*, *Phys. Rev. Lett.* **110** (2013) 041301 [arXiv:1301.1173].

[219] G. Bertone, D. Hooper, and J. Silk, *Particle Dark Matter: Evidence, candidates and constrains*, *Phys. Rept.* **405** (2005) pp. 279–390 [arXiv:hep-ph/0404175].